Development of a Calibration Stand for Photosensors for Extremely High-Energy Cosmic Ray Research

Zur Erlangung des akademischen Grades eines

Doktors der Naturwissenschaften

von der Fakultät für Physik des
Karlsruher Instituts für Technologie (KIT)

genehmigte

Dissertation

von

Michael Karus

aus Karlsruhe (Baden)

Tag der mündlichen Prüfung: 22. Januar 2016

Referent: Prof. Dr. Johannes Blümer, KIT

Korreferent: Prof. Dr. Marc Weber, KIT

07. Januar 2016

SUPERVISORS:
Prof. Dr. Johannes Blümer
Prof. Dr. Marc Weber
Dr. Andreas Haungs

LOCATION:
Karlsruhe (Baden)

TIME FRAME:
May 2012 - January 2016

There is something in this world that nobody has seen yet.
It's something gentle, and very sweet.

And if you ever laid eyes on it, you would yearn for it.
That's why no one has ever seen it.

The world hid it so that no one could get their hands on it easily.
However, someday, someone will find it.

The person who deserves it the most will definitely find it.
This is how its created.

—Opening dialogue of 'Toradora'

ABSTRACT

This work is about the development of a single photon calibration stand for photosensors that are used for the detection of cosmic rays of highest energies. First the basics of cosmic rays and the related formation of extensive air showers in Earth's atmosphere is recapitulated. Here the main focus is set on the origin of fluorescence and Cherenkov light in these air showers and their detection via the emitted light. Further the *Extreme Universe Space Observatory onboard the Japanese Experiment Module* (JEM-EUSO) is presented. It is a next-generation experiment for the detection of cosmic rays of highest energies, using fluorescence and Cherenkov light. The calibration stand, which was designed, built, and improved during this work, is presented in detail. The calibration measurements of every single component are introduced and their results are recorded. The reference light source can send single photons as well as several ten thousands of photons, each mode with different wavelengths, onto a photodetector with up to 64 channels. With this, several calibration modes are possible and were tested, e. g. single photon calibration, gain measurements, illumination of large sensor areas, and dynamic range measurements. Two types of photodetectors, namely *multianode photomultiplier tubes* (MAPMTs) and *silicon photomultipliers* (SiPMs) are presented. MAPMTs are used in the baseline design of JEM-EUSO. SiPMs are an interesting alternative because of their characteristics, in particular their more compact form, their smaller mass, and their lower power consumption. Calibration measurements were conducted under comparable systematics and are presented for both detector types. The systematic uncertainties of the calibration stand are in the range of 3.1 % to 4.1 % for the photo detection efficiency. The gain can be determined with systematic uncertainties of 3.9 %. These values are comparable to the uncertainties of previous calibration stands, but are now applicable to larger focal surfaces and different wavelengths.

ZUSAMMENFASSUNG

Diese Arbeit befasst sich mit dem Aufbau eines Teststands zur Kalibration von Photosensoren im Einzelphotonenmodus, die zur Messung kosmischer Strahlung höchster Energien Verwendung finden. Zu diesem Zweck werden zuerst die Grundlagen der kosmischen Strahlung und die damit verbundene Entstehung von ausgedehnten Luftschauern in der Erdatmosphäre eingeführt. Das Hauptaugenmerk liegt hierbei auf der Entstehung von Fluoreszens- und Cherenkov-Licht in Luftschauern und deren Detektion über dieses ausgesandte Licht. Im Weiteren wird das *Extreme Universe Space Observatory onboard Japanese Experiment Module* (JEM-EUSO) vorgestellt. Es handelt sich hierbei um ein Experiment der nächsten Generation zur Detektion kosmischer Strahlung höchster Energien über das emittierte Fluoreszens- und Cherenkov-Licht. Der während dieser Arbeit entworfene, aufgebaute und verbesserte Teststand wird im Detail beschrieben. Die Kalibrationsmessungen der einzelnen Komponenten werden vorgestellt und deren Ergebnisse festgehalten. Die Referenzlichtquelle ist sowohl in der Lage einzelne Photonen als auch mehrere Zehntausend Photonen, jeweils mit verschiedenen Wellenlängen, zu erzeugen und auf einen Photodetektor mit bis zu 64 Kanälen zu senden. Damit sind verschiedene Messmodi, wie z. B. die Einzelphotonenkalibration oder die Messung des dynamischen Bereichs von Photodetektoren möglich und wurden durchgeführt. Zwei Arten von Photodetektoren, und zwar *multianode photomultiplier tubes* (MAPMTs) und *silicon photomultipliers* (SiPMs) werden vorgestellt. Hierbei sind MAPMTs im Basisdesign von JEM-EUSO vorgesehen. SiPMs sind neuerdings aufgrund ihrer kompakteren Bauweise, ihrer geringeren Masse und ihrem geringeren Leistungsverbrauch eine interessante Alternative zu MAPMTs. Kalibrationsmessungen an diesen zwei Detektortypen wurden unter vergleichbaren Bedingungen durchgeführt und werden vorgestellt und diskutiert. Die systematischen Unsicherheiten des Kalibrationsstands liegen für die Photodetektionseffizienz im Bereich von 3.1 % bis 4.1 %. Der Verstärkungsfaktor der Detektoren kann mit systematischen Unsicherheiten von 3.9 % angegeben werden. Diese Werte sind vergleichbar mit bisherigen Kalibrationsmöglichkeiten und sind nun aber auch für großflächige Fokalebenen und verschiedene Wellenlängen anwendbar.

CONTENTS

1

PREAMBLE

Astroparticle physics is a relatively young field of physics, nonetheless it is very fascinating. This maybe stems from the fact that this particular field in physics exists at the boundary of particle physics, astrophysics, astronomy and cosmology. Therefore it is a quite dynamic and interdisciplinary field of physics. The focus of research within astroparticle physics is to study particles originating from energetic sources in the Universe and to discover their connection to astrophysical and cosmological processes. A strong driver of the present research field of astroparticle physics was the discovery of neutrino oscillations. For that the Nobel price in physics was given to Takaaki Kajita and Arthur B. McDonald in 2015 [1]. Further research topics include the search for dark matter in the Universe and the measurement of gravitational waves that might for example result from the merger of two black holes. However, this does not mean that experiments in astroparticle physics are only looking towards space. There are also research interests in fundamental particle interactions at the Large Hadron Collider (LHC) at European Organization for Nuclear Research (CERN) with the goal to tune particle interaction models to LHC-energies and beyond. Especially the part with "beyond" is very interesting, since here the goal is to understand the energetic processes in the sources of cosmic rays (CR). Today this energy region can only be examined via CR which expand over a very wide range of energies, covering several magnitudes [2]. Although CR have been a big research topic over the past 100 years, many questions are still not answered. For example the origin of CR, in particular for high energies, is still unknown. Further, the mechanisms accelerating particles to such high energies are an enigma. One would also like to know if there is an upper energy limit to the spectrum of CR and, if there is one, its cause.

To unveil these mysteries, many CR observatories were built in the past, e. g. the Pierre Auger Observatory or the Telescope Array (TA), both for higher energy CR, or the Karlsruhe Shower Core and Array Detector (KASCADE) at Karlsruhe Institute of Technology (KIT), for lower and medium energies [3–5]. The observation of CR in these energy ranges are done indirectly by observing extensive air showers (EAS). For that CR observatories use an array of Cherenkov water or scintillator detectors, which are distributed in a ground array, to measure the lateral particle distribution of EAS on ground. To get an observation of the shower development, the observatories use telescopes, to observe fluorescence and Cherenkov light emitted from EAS. Both detection techniques are used in conjunction with each other. The flux of highest energy CR is around one particle per square kilometer per century [2]. This drives the need for big ground arrays in the range of thousands of square kilometers.

An idea for a next generation experiment is to use the fluorescence detection technique with a telescope that is looking down on Earth from space to increase the observation area significantly. The Extreme Universe Space Observatory onboard the Japanese Experiment Module (JEM-EUSO) mission plans to do exactly that. The telescope is planned to be attached to the International Space Station (ISS). With a wide field of view and an orbit with an altitude around $400\,km$ the observed area can easily reach $1 \times 10^5\,km^2$. The detectors for the telescope will altogether have around $300\,000$ channels, allowing for the measurement of a shower track on the focal surface. The direction of the air shower and thus the arrival direction of the primary particle can be estimated via the timing information of the track. The number of detected photons gives an estimation of the total shower energy. Of course, the photodetectors for this telescope need to be very sensitive, to be able to see direct fluorescence light and reflected Cherenkov light from EAS developing in the Earth's atmosphere. To correctly estimate the shower energy, the number of incoming photons needs to be known very well. This goes hand in hand with knowing the detector answer to incoming signals, especially the photo detection efficiency of the detectors. Further, the sensitive detector area should also have a uniform photo detection efficiency. Prototype experiments for JEM-EUSO are already operational and further ones are under development.

For the calibration and sorting of photosensors, Single PhOton Calibration stand at KIT (SPOCK) was designed, built, and improved during this work. It serves as a multipurpose calibration stand for all kinds of photodetectors. It is used for the precise measurement of the photo detection efficiency and the gain of the detectors. This is achieved via a reference light source with known optical output power and output wavelength. The reference light source can operate in different modes. Because of the universality of the read-out electronics, the calibration stand built during this work is usable as a test stand for different photosensors.

This work is structured in the following way: Chapter 2 will shortly introduce the basics of CR and EAS. Afterwards, Chapter 3 will present the JEM-EUSO mission with its baseline design, goals, and pathfinder experiments. The in-flight calibration will be briefly discussed. Chapter 4 holds the main part of this work. The working principle and the design of SPOCK is explained in detail. The calibration measurements of its components are also shown there. The end of that chapter holds implications and ideas for the inflight-calibration of JEM-EUSO, which stem from experiences gained during the course of this work. Chapter 5 shows the photodetectors that are planned to use for the JEM-EUSO mission and how they can be calibrated with SPOCK. Measurement results of the photo detection efficiency (PDE) and the gain are also shown. An alternative to multianode photomultiplier tubes (MAPMTs) are silicon photomultipliers (SiPMs). They are introduced in Chapter 6. The calibration process for these novel types of photodetectors is explained and measurements of the PDE and the gain are shown. The conclusion of this work is given in Chapter 7. Further material like detailed measurement data, uncertainty calculations, pictures, and technical information can be found in the appendix.

<div style="text-align: right; font-size: 3em;">2</div>

COSMIC RAYS AND EXTENSIVE AIR SHOWERS

A brief introduction to the field of astroparticle physics was given in the preamble. In the following, this thesis will constrain itself to the CR part of the vast field of astroparticle physics. Since the ultimate goal for calibrated photodetectors is to measure photons emitted from extensive air showers (EAS), the physics behind that goal need to be defined.

For that purpose this chapter briefly introduces CR and their interactions with the Earth's atmosphere resulting in EAS. Furthermore a short overview of detection techniques for EAS is given. Within the scope of this work ultraviolet (UV)-light emission processes from EAS are explained.

2.1 COSMIC RAYS

Charged particles, primarily fully ionized atomic nuclei that come from the cosmos and continuously impact on the Earth are called cosmic rays (CR). Their energy spectrum ranges from 10^9 eV to 10^{20} eV and probably beyond. These are the highest energies that where ever observed in the Universe [2]. Furthermore the CR flux is declining with energy over several orders of magnitude. A fitting description is a power law of the the form:

$$\frac{dN}{dE} \propto E^{-\gamma} \quad ,$$

with the number of particles N, the nucleus energy E, and the spectral index $\gamma \approx 2.7$. In Figure 2.1 the scaled CR flux is shown versus the energy per nucleus. The spectrum has four distinct features that are more clearly visible because of the scaling with $E^{2.5}$. Around 10^{15} eV the *knee*, a steepening of the spectrum is visible. To slightly higher energies, around 8×10^{16} eV, the spectrum further steepens with the *second knee* [5–7]. At the *ankle*, around 3×10^{18} eV, the spectrum flattens. Above 5×10^{19} eV the flux is highly suppressed. This is known as *GZK-effect* or *GZK-suppression* (Greisen-Zatsepin-Kuz'min (GZK)) [8, 9].

Below primary energies of 1×10^{15} eV CR were measured directly with balloon and space-based experiments [11–13]. From these direct calorimetric measurements the abundance of individual chemical elements has been measured. It mimics the solar systems element abundance with the exception of a few light elements like Lithium, Beryllium, and Boron that exceed the solar average. Also elements below iron are more abundant in CR because these elements are produced via the interaction of those heavy elements with the interstellar medium during their propagation
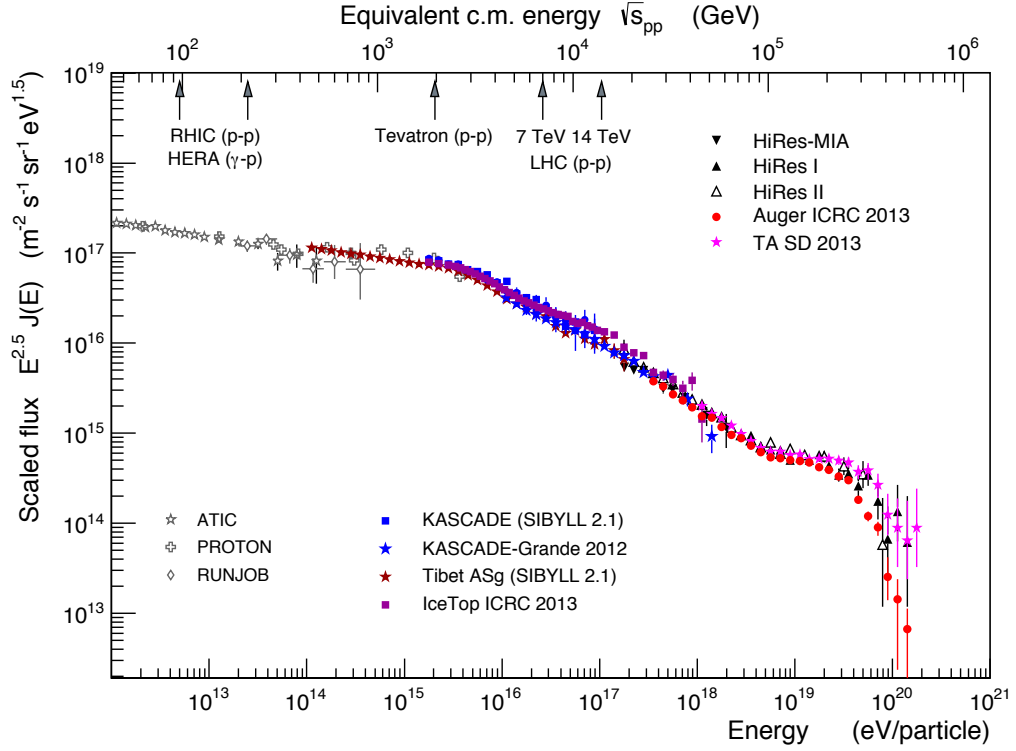
Figure 2.1: All particle spectrum of the CR flux scaled by $E^{2.5}$ versus the energy per primary particle (bottom) and versus the equivalent center of mass energy (top). Around 10^{15} eV a steepening of the spectrum is visible (knee). Around 3×10^{18} eV the spectrum flattens (ankle). Above 5×10^{19} eV the flux is highly suppressed [2] (updated [10]).

(spallation processes). Hence, CR in this energy regime are accelerated ordinary galactic matter [14]. For higher energies these direct measurements become insufficient, because the flux gets too low (on particle per square meter per year) and detectors would have to become unreasonable big [2].

Primary energies between the *knee* and the *ankle* are called high energy cosmic rays (HECR). One simple explanation for the *knee* and the *second knee* are HECR of galactic origin using a leaky box model (rigidity-dependent escape) [15, 16]: Charged particles that are being accelerated in the galaxy are influenced by the galactic magnetic field B, their own atomic mass A, and their charge Z. The resulting Larmor radius r_L for a charged particle with a velocity $v_\perp$ that is perpendicular to the galactic magnetic field is:

$$r_L = \frac{A \cdot v_\perp}{Z \cdot B} \quad . \tag{2.1}$$

At a critical momentum the Larmor radius starts exceeding the thickness of the galaxy and the charged particle escapes from the galaxy. On Earth this is seen as a flux suppression. However the maximum acceleration energy of the sources is not known yet. The *knee* is a result of the suppression of the lighter components

(protons) whereas the *second knee* is attributed to the suppression of heavier components [5, 6]. When going to the *ankle* the flux recovers again. This is most likely due to a transition to high energetic extragalactic CR that are called ultra-high energy cosmic rays (UHECR). There are different models that can all explain the spectrum in the *ankle* region and the associated transition from galactic to extragalactic CR [17]. Since the different models assume different compositions of the CR-spectrum in that region, detailed composition studies should be able to provide further information on the sources. However, for that better statistics are needed in a regime where the flux is as "big" as one particle per square kilometer per century [2].

Going hand in hand with composition studies, the identification of UHECR sources would also help to better understand the CR spectrum. A simple requirement for astrophysical sources of CR, deduced via the Larmor radius given in Equation 2.1, has been formulated by Hillas [18]:
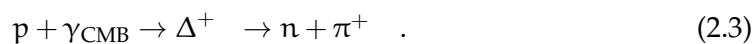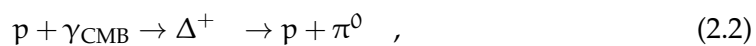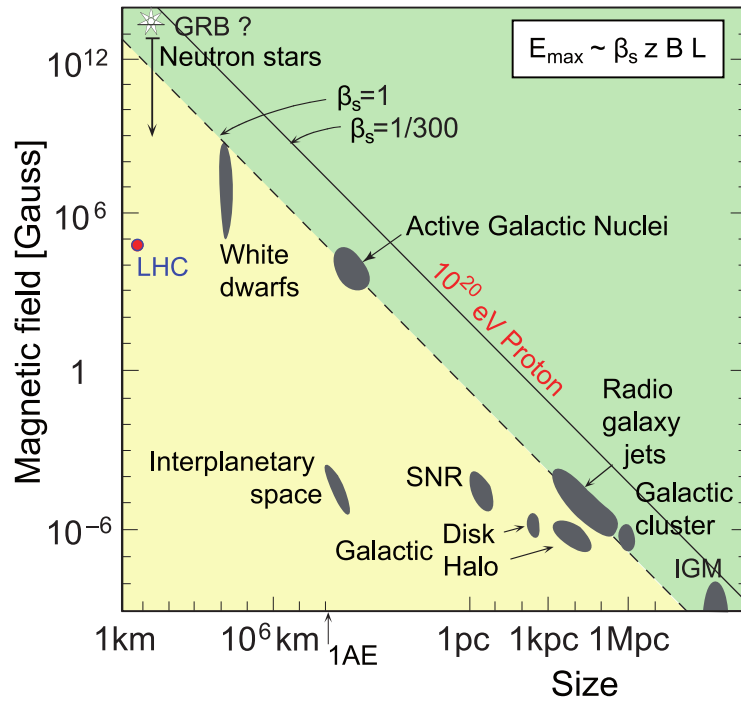
$$B \cdot L > \frac{2 \cdot E}{Z \cdot \beta} \quad,$$

where

B	is the normal component of the galactic magnetic field in µG,
L	is the size of the source candidate in pc,
E	is the particle energy in PeV,
Z	is the charge of the particle, and
$\beta = \frac{v}{c}$	is the velocity in natural units
	(particles velocity v and the speed of light c).

Based on this equation, Figure 2.2 shows the magnetic field versus the size of astrophysical objects. Inside this so called Hilas plot, there are source candidates shown, such as Gamma Ray Bursts (GRB), neutron stars, Active Galactic Nuclei (AGN), radio galaxy jets, and supernova remnants (SNR). The plot also contains constraints on proton (solid line) and iron nuclei (dashed line) acceleration, both to energies of 1×10^{20} eV. Objects below the respective lines are not capable of accelerating protons or iron nuclei above that energy. The parameter β_S gives the ratio of the accelerated shock front velocity to the speed of light. The plot clearly shows that there are not many source candidates for UHECR comprised of iron nuclei and no ones for protons above 1×10^{20} eV. It is also clear that possible messengers for the search for UHECR sources that avoid deflection in galactic and intergalactic magnetic fields would be neutral particles like neutrinos or high energy photons [19].

The highest energy part of the CR-spectrum above the ankle region (1×10^{18} eV) is suppressed, as has been seen experimentally [20]. An explanation for this suppression is the GZK effect. It describes the energy loss of UHECR via the interaction with photons of the cosmic microwave background (CMB) [8, 21]. The energy loss of protons is due to continuous *photo-pion production*:

$$p + \gamma_{CMB} \rightarrow \Delta^+ \quad \rightarrow p + \pi^0 \quad, \tag{2.2}$$

$$p + \gamma_{CMB} \rightarrow \Delta^+ \quad \rightarrow n + \pi^+ \quad. \tag{2.3}$$

Figure 2.2: Hillas plot with the estimated magnetic field strength versus characteristic sizes of source candidates. Objects below the solid line are not capable of accelerating protons above 10^{20} eV. For iron nuclei the dashed line is the limit for the same energy. The parameter β_S is the ratio of the velocity of the accelerated shock front relative to the speed of light [19] (updated [10]). Original: Hillas [18]).

For heavier elements the energy loss can be explained with photo-disintegration due to giant dipole resonances at similar energies. From this the assumption is drawn that there is a GZK horizon at around $100\,\text{Mpc}$. That means that sources for UHECR with more than 6×10^{19} eV have to be within that horizon [22]. However, signals in that energy range are still too scarce to have good statistics and thus it is still not clear if the suppression is only due to the GZK effect or if this is a characteristic of the sources which just do not accelerate particles faster than that. Nevertheless, particles that are near the limit of the GZK effect or beyond are called extreme energy cosmic ray (EECR).

The energies towards the end of the CR spectrum are comparable to macroscopic energies, e. g. a tennis ball (57 g) with the speed of $85\,\text{km}\,\text{h}^{-1}$ has an kinetic energy of roughly 1×10^{20} eV. However, the probability of encountering a CR primary particle with that energy is in the range of one particle per square kilometer per century. Since the flux cannot be changed and time is also more or less moving forward with a fixed "speed" (at least for experimental physics), the only option for detecting these EECR events is to have a huge detector size, if one does not want to wait for many centuries, to have enough statistics. Therefore, several current experiments use EAS that are produced by HECR and above. The CR primary particles hit the Earth's atmosphere and after interaction with molecules in the atmosphere a shower of secondary particles is produced. So HECR, UHECR, and EECR are measured indirectly via their secondary particle showers while using the Earth's

atmosphere as a calorimeter. The two most prominent current experiments are the Pierre Auger Observatory in Argentina [23] and the Telescope Array in Utah (USA) [24]. Both experiments use a hybrid detection technique, employing surface detectors that measure Cherenkov light or scintillation light, and employing fluorescence telescopes that measure fluorescence light from excited nitrogen molecules in the EAS. The Pierre Auger Observatory uses on the surface an array of around 1600 water Cherenkov detectors and 27 fluorescence telescopes. The covered area is around 3000 km^2. The TA covers an area of 777 km^2 with about 500 scintillation detectors on the surface and 38 fluorescence telescopes. Latest publications from both experiments show a similar shape of the CR spectrum for UHECR, but also slight discrepancies in the energies and spectral indices where the GZK suppression occurs [25, 26]. Joint working groups were formed to investigate these differences between results from Pierre Auger Observatory and TA. They are mainly checking for the energy, where the suppression occurs and for the composition of UHECR primary nuclei [27, 28].

2.2 EXTENSIVE AIR SHOWERS

To get a better understanding of the detection techniques for UHECR, the physics behind EAS will be explained shortly. These EAS are generated, when primary CR hit the Earth's atmosphere. The primary CR interacts with molecules of the atmosphere and induces a cascade of secondary particles that is called EAS. The indirect detection of UHECR becomes possible by measuring the secondary particles on ground or by detecting emitted light or radio emission during the EAS. The three components of an EAS are shown in Figure 2.3.

The first nuclear interaction of the primary particle with air molecules produces mainly pions and kaons [29]. This *hadronic component* of the air shower generates new hadronic particles via inelastic scattering and further hadronic interactions, providing source material for the other two components of the EAS. Before further interactions, charged pions and kaons can decay into muons and neutrinos, forming the *muonic component* of the EAS. Because of their small cross-section these are the most penetrating component of an air shower and at sea level the muonic component is the most abundant. The fast decay of neutral pions into photons builds the *electromagnetic component*. It consists of mainly electrons and photons and distributes the energy of the primary particle over millions of secondary particles. Photons, electrons, and positrons are the majority of secondary particles, but they also get absorbed by the atmosphere quite fast if below critical energy.

The *Heitler model* describes the growth of the *electromagnetic component* [30]. An electromagnetic cascade is driven by two radiative processes (bremsstrahlung and pair production), and suffers energy loss due to ionization. The number of particles doubles after each interaction, producing 2^n particles after n interactions. The photon production due to bremsstrahlung and the electron positron production due to pair production continues during the shower development until ionization energy losses exceed the radiative losses. Then the multiplication of particles stops and the particle number decreases with increasing longitude. The critical energy
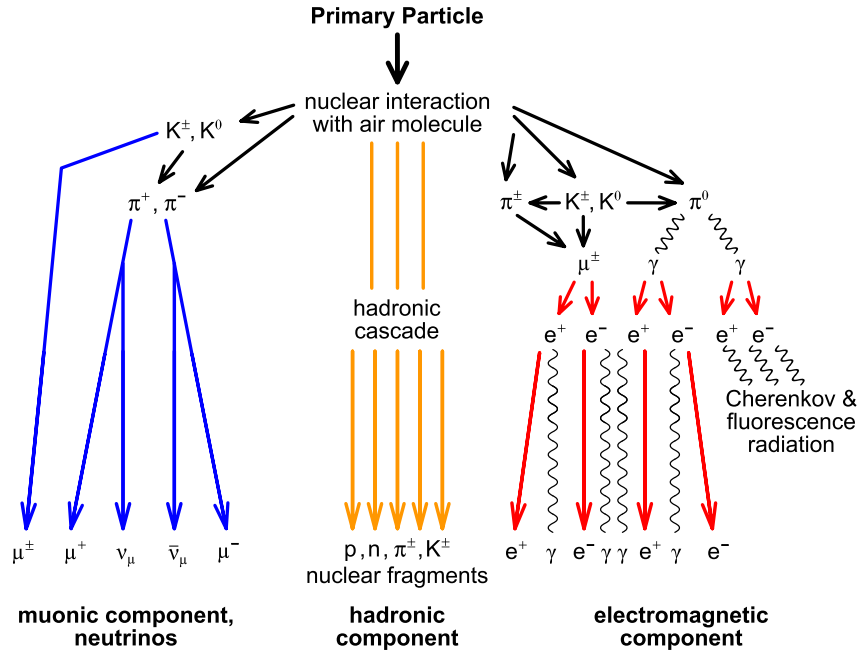
Figure 2.3: Schematic EAS development. The primary particle has a nuclear interaction with an air molecule and a hadronic shower is produced via inelastic scattering. Charged and neutral pions are produced through decay. The charged pions decay further to muons and neutrinos (muonic component). The neutral pions start an electromagnetic cascade which emitts radiation at various wavelengths (adopted from [29]).

E_c is around $85 \, \text{MeV}$ in air. The characteristic parameters defining the longitudinal shower evolution in terms of particle numbers versus the atmospheric depth X (defined as atmospheric path length already crossed by the shower), are the depth X_0 of the first interaction, the depth of the shower maximum X_{max}, and the interaction length λ_{em} of the particles. In this simple model, the total number N_{max} of particles is given by the ratio of the total energy E_0 of the primary particle and the critical energy E_c. Although the *Heitler model* is a very simple estimation for an electromagnetic shower, it still gives good estimates for two very important features. First, the total number N_{max} of particles (electrons, positrons, and photons) in the *electromagnetic component* is proportional to the total energy E_0 of the primary particle. Second, the atmospheric depth of the shower maximum X_{max} is logarithmically proportional to E_0.

For heavier primaries, the *superposition model* is used [29]. It replaces a single heavier nucleus with an ensemble of m single particles, leading to a distribution of the primary energy E_0 onto m single particles. This results in an shift of X_{max} proportional to $\ln(m)$, decreasing X_{max} for heavier primaries, e. g. when comparing the depths of the shower maxima for proton and iron induced showers, a shift in the order of $100 \, \text{g} \, \text{cm}^{-2}$ can be expected for X_{max}. This is the key feature for mass composition studies.

The width of the lateral distributions and the size (number of particles) of the three shower components are very different [29]. The *electromagnetic component* is the most abundant, with the highest particle density in the showers lateral distribution. The *muonic component* and the *hadronic component* have roughly the same

particle density as each other, but are around 1 % of the electromagnetic particle density. Therefore, the spread of the *hadronic component* in the shower footprint is much smaller than the spread of the *electromagnetic component*. The *muonic component* shows the biggest spread, since it is mostly produced high up in the atmosphere and thus even very small lateral impulses are translated to huge muonic footprints.

2.3 DETECTION TECHNIQUES

The detection techniques for EAS can be divided into two groups: particle detectors and detectors for radiative emission. The former can be Cherenkov water or scintillator detectors, which are distributed in a ground array, to measure the lateral particle distribution of the EAS on ground. The latter measure radiative emission caused by charged secondary particles in air, during the shower development. The associated emissions can be UV-light (fluorescence- and Cherenkov-light) [31], radio emission (MHz range) [32–34], and microwave emission (GHz range) [35]. The used detectors are either telescopes or antennas. For this work the focus lies on the UV-light emission from EAS, since this will be the technique used by JEM-EUSO. The two most important processes for the UV-light emission from EAS are isotropically emitted fluorescence light and forward beamed Cherenkov light.

CHERENKOV RADIATION FROM EAS: Cherenkov radiation is a forward beamed light emission with a continuous spectrum [31]. It is produced, when charged particles move through a dielectric medium with a velocity that is higher than the phase velocity of light in that medium. If that is the case, the particle ionizes the medium in its path, leaving a locally excited path behind. The following relaxation is done via the emission of light. Since the velocity of the particle was higher than the phase velocity, the interference of the electromagnetic waves is constructive and a net cone-shaped wave front is generated. The opening angle of the cone is dependent on the spectral index of the medium and the speed of the particle. In a sense, Cherenkov radiation is the optical analogon to the sonic boom. The emission spectrum of Cherenkov radiation is continuous and the photon yield is higher for shorter frequencies, resulting in higher intensities for UV-light than for visible light.

FLUORESCENCE LIGHT FROM EAS: Fluorescence light from EAS is isotropically emitted light in the UV-regime. It is a consequence of the relaxation of nitrogen molecules that have been excited by the interaction with mainly electrons and positrons from an air shower. Therefore, the energy deposit is proportional to the number of electrons and positrons in the air shower. Since the energy deposit is stored in different oscillation and rotation modes of the molecule, the spectrum is comprised of discrete wavelengths in the range of 290 nm to 430 nm. The most intense emission is around 377.1 nm (Figure 2.4) [36].
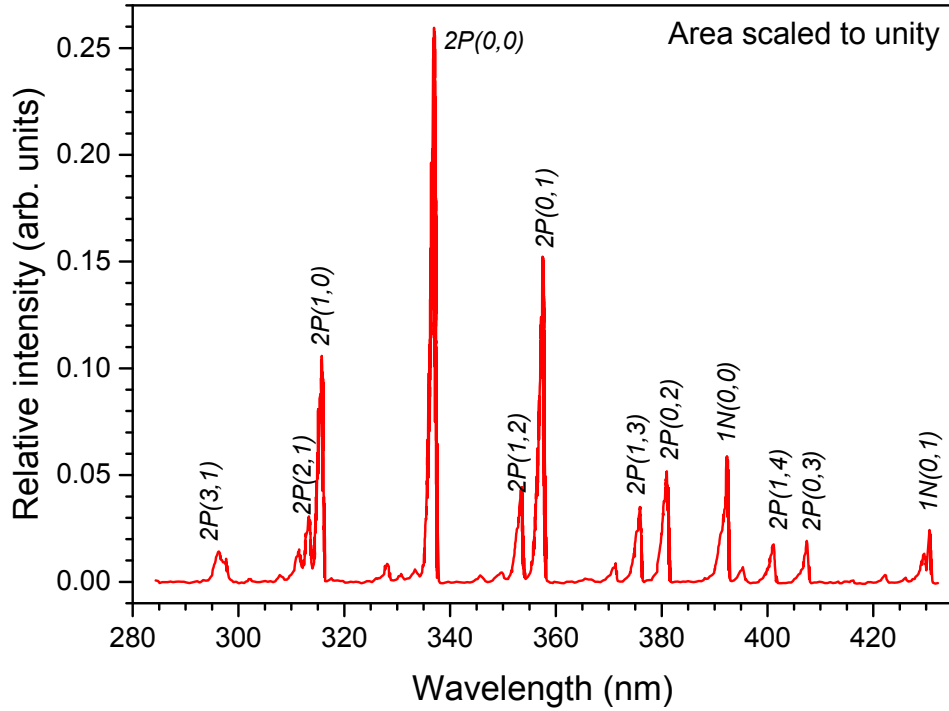
Figure 2.4: Air fluorescence spectrum of nitrogen relaxation in the UV band from 280 nm to 435 nm at 800 hPa (about 2 km) measured by the AIRFLY collaboration. The area was scaled to unity. This shows that 25 % of the spectrum's intensity is due to the main band at 337.1 nm (adopted from [36]).

The two groups for EAS detection techniques have different advantages and disadvantages. The ground array of particle detectors only sees a developed state of the shower [29]. In every station of an array, the shower footprint is sampled. Observables are the extrapolated particle numbers of the three components, energy distributions, and arrival time profiles. These are used to draw inferences about the energy, mass, composition, and arrival direction of the primary particle. Their duty cycle is basically 100 %. The fluorescence detection images an EAS during its longitudinal development, yielding a direct observation of the shower maximum, specifically X_{max}, and a calorimetric measurement of the primary particles energy in a model independent way [29, 37]. In general the duty cycle of fluorescence detectors is very short, since they can only be operated during clear and dark nights with low background light. To get the advantages of both groups of detection techniques, they are used in hybrid mode, where fluorescence telescopes survey the volume above an ground array of particle detectors. The two most prominent current experiments employing these techniques are the aforementioned Pierre Auger Observatory in Argentinia [23] and the TA in Utah (USA) [24].

2.3.1 Details on fluorescence light

For the calorimetric measurement of the shower and the corresponding primary particles energy, it is essential to know the fluorescence yield in order to get a good

estimate of the particle number in the shower, since the energy deposit is proportional to the number of electrons and positrons in the EAS. It is the observable of fluorescence telescopes and gives the rate of emitted photons per meter of traversed air [38]. However, the fluorescence yield is sensitive to atmospheric conditions, since the relaxation of nitrogen molecules via fluorescence light is competing with non-radiative processes, like collisional quenching with other molecules. Further more, the emitted fluorescence photons are attenuated and scattered (wavelength dependent) on their path to the telescopes, which themselves have a certain spectral sensitivity that cannot be neglected [36]. Also the different band heads of the emission spectrum vary in their intensity (Figure 2.4). In general, the fluorescence efficiency (energy deposit as photons per MeV) increases with altitude, since the competing quenching collision process becomes more unlikely, due to fewer targets [38]. The increase of this efficiency is different for the diverse band systems. The overall fluorescence yield (sum of all bands) increases slightly from $0\,\text{km}$ to $10\,\text{km}$ altitude, because the energy deposit (fluorescence efficiency) is increasing. Above an altitude of $10\,\text{km}$, the overall fluorescence yield starts to decrease. This is because the number of nitrogen molecules starts to decrease and the increase in efficiency of the process cannot keep up with that.
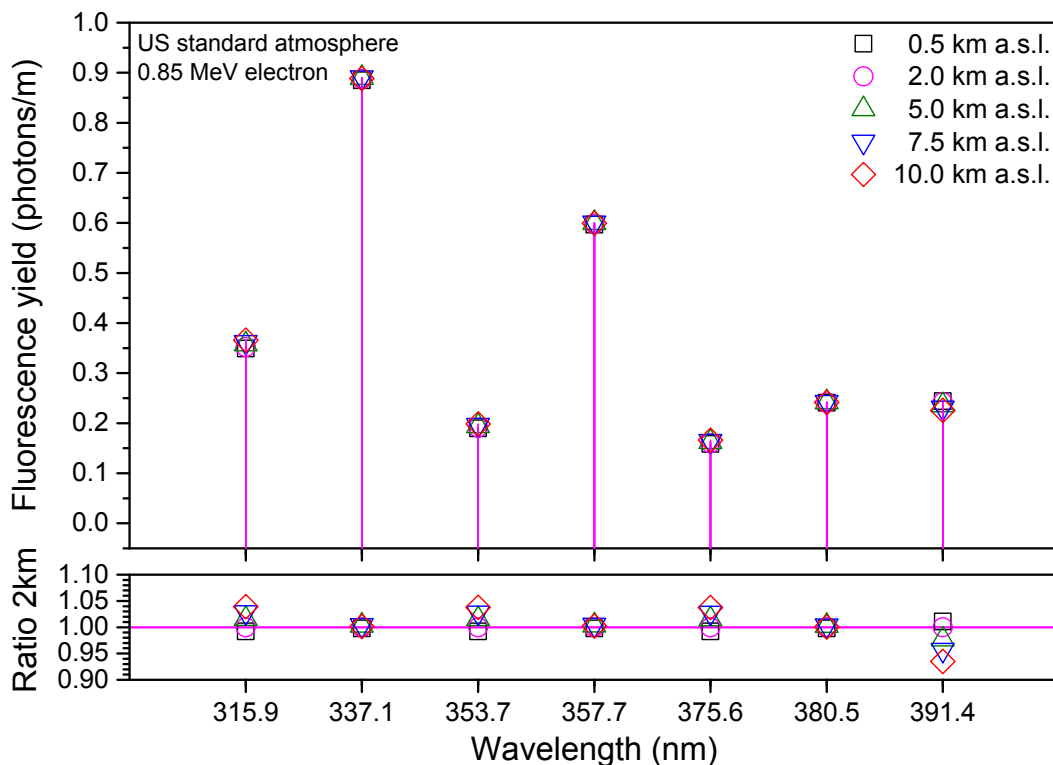
Figure 2.5: Calculated air fluorescence yield for the seven strongest contributing band systems of nitrogen relaxation for different altitudes between $0.5\,\text{km}$ to $10\,\text{km}$ above sea level. The data for this plot was updated by Bianca Keilhauer from [39]). The lower part shows the relative change versus the yield at an altitude of $2\,\text{km}$, since the fluorescence spectrum was given for this altitude in Figure 2.4.

To illustrate the different behavior of the single bands, Figure 2.5 shows the model calculations for the air fluorescence yield for the seven strongest contributing band systems of nitrogen relaxation for different altitudes between 0.5 km to 10 km above sea level. The model calculations (updated by Bianca Keilhauer from [39]) were done for a US standard atmosphere and a 0.85 MeV electron. Temperature and quenching dependencies have been neglected. It is evident that changes in the fluorescence yield within an altitude of 10 km are below the 5 % level. There are also three different band systems present that all are behaving differently with increasing altitude. The 337.1 nm, 357.1 nm, and 380.5 nm bands show no altitude dependence. The 315.9 nm, 353.7 nm, and 375.6 nm bands show a slight increase, while the 393.4 nm band shows a stronger decrease in the fluorescence yield.

To conclude, the differences for the strongest fluorescence emission systems are quite small in the range of 0 km to 10 km, however, if a calorimetric measurement of EAS is to be done with sufficiently low uncertainties, the absolute fluorescence yield has to be known and further effects have to be considered. Since the fluorescence light is composed of individual emission wavelengths that behave differently with the surrounding conditions it is essential for the fluorescence detection of EAS to have the knowledge of the spectral response of the used detector. Therefore extensive calibration efforts have to be taken, to minimize uncertainties for the reconstruction of the primary particle energy. The calibration of photodetectors is the main focus of this work and will in detail explain the calibration efforts for the JEM-EUSO mission (Chapter 4). But before we come to this, the next chapter will introduce the JEM-EUSO mission with its variety of preparatory prototype projects.

<div style="text-align: right; font-size: 3em;">3</div>

EXTREME UNIVERSE SPACE OBSERVATORY ONBOARD JAPANESE EXPERIMENT MODULE

In order to unveil the mysteries of the UHECRs, concerning their composition, sources and acceleration mechanism, a significantly higher statistic at the ultra-high energy (UHE) regime above 2×10^{19} eV of the CR flux is needed. Since the rate for CRs at an energy of 10^{20} eV is about one particle per km^2 per century, very large detector areas are needed to increase statistics. However, for land-based surface detector arrays several restriction on increasing their size or building new ones exist. This can be due to geographical, political or practical reasons.

The JEM-EUSO mission would be one solution for creating a detector area that is about 50 times bigger than the largest surface detector array of today, the Pierre Auger Observatory [9]. The idea of JEM-EUSO is to detect EAS from space with a fluorescence telescope. The JEM-EUSO collaboration consists of 349 scientist, 93 institutes from 16 countries (June 2015). The major space agencies European Space Agency (ESA), Japan Aerospace Exploration Agency (JAXA), National Aeronautics and Space Administration (NASA), and Russian Federal Space Agency (ROSCOSMOS) are also participating. In this chapter the JEM-EUSO mission is introduced. The scientific goals, the detector design and the present prototype experiments are explained. Further details on JEM-EUSO and its prototype experiments can be found in a special issue of the journal *Experimental Astronomy* [40–53].

3.1 SCIENTIFIC GOALS

The JEM-EUSO mission strives for the detection of UHECRs from space via fluorescence light, using Earth's atmosphere as a calorimeter. The main goal of the JEM-EUSO mission is to increase the exposure to CRs in the UHE regime above 5×10^{19} eV (GZK threshold) by one order of magnitude compared to current experiments. This means increased statistics for UHECRs and EECRs.

From the current CR spectrum some implications about UHECR sources can be deduced from UHECR composition, anisotropy studies and GZK effect [8, 21]. Only few known astrophysical objects are viable sources for UHECRs and they have to be within the GZK horizon. Until now no sources have been identified. If consisting of pure protons, EECRs above 8×10^{19} eV could directly point back to their sources, since their deflection due to galactic magnetic fields would be small. So the main scientific goals of JEM-EUSO are the following [54]:

- Detection and high statistics measurements of UHECRs above 5×10^{19} eV.

- Anisotropy study of UHECR arrival directions.

- Identification of sources and source regions.

- Measurement of the sources energy spectra.

An example on how JEM-EUSO could achieve these goals is described in [55]. Qualitative studies of CR source statistics have been performed as a function of source energy and composition. Because of the GZK-effect the number of CR sources above 5×10^{19} eV is expected to be highly reduced. Therefore the study concludes that the isolation of the few brightest CR sources in the sky should be possible for a CR energy range of 5×10^{19} eV to 8×10^{19} eV.

A more realistic approach including magnetic fields is given in [56]. There anisotropy studies have been performed for source candidates in the sky and different astrophysical scenarios, were UHECR source compositions, spectra, and densities have been varied. Sky maps are shown there for current Pierre Auger Observatory statistics and for expected JEM-EUSO statistics. They show significant anisotropies for all scenarios and expect them to be detected by a next-generation UHECR experiment.

(a) Exposure comparison.

(b) JEM-EUSO exposure distribution.
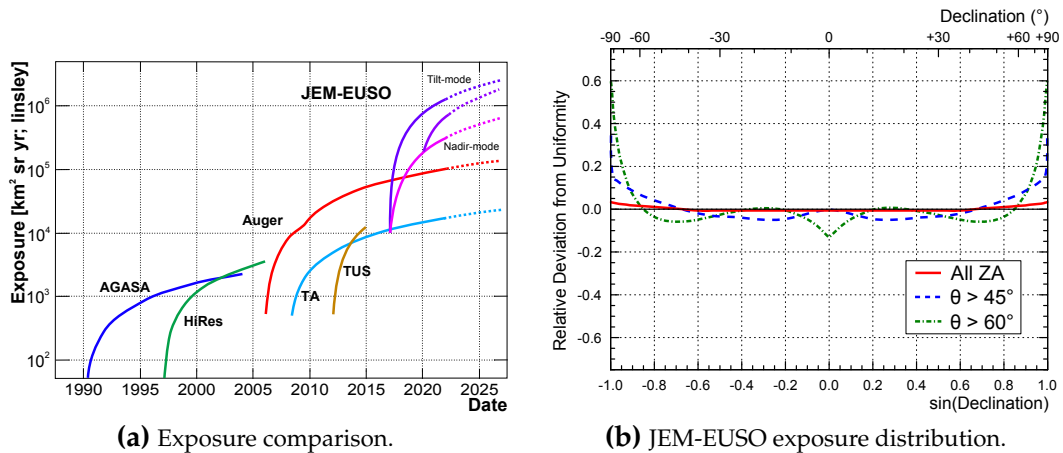
Figure 3.1: JEM-EUSO exposure. **(a)** Exposure versus time of several UHECR observatories from 1990 to 2025. Exposures from 2011 onward are estimated for the Pierre Auger Observatory, Telescope Array and JEM-EUSO. This scenario is valid for a JEM-EUSO launch in 2017. Adopted by [57] from [58]. **(b)** Relative deviation from uniformity of the expected JEM-EUSO exposure versus the declination of the celestial sky. Different zenith angles of EAS are shown. The zero line implies a uniform full sky coverage [59].

Via the study of the composition of CR conclusions can be drawn on possible source compositions. From that some astrophysical scenarios used in anisotropy studies might be validated while others might be denied. In conjunction with the arrival direction of CR source candidates (point sources or source regions) can be identified and their spectra can be further analyzed. The required statistics for the goals above are in the order of 10^3 for EECR events [60]. Since 1990 the exposures of several UHECR observatories have been increasing continuously (Figure 3.1a). However, a further increase in size of ground-based detector arrays is unlikely.

JEM-EUSO is planned to reach an exposure of an order of magnitude larger than current experiments within 5 years. With the advantage of being in an orbit around the Earth, JEM-EUSO will have an almost uniform exposure to the northern and southern hemisphere. Thus JEM-EUSO will be able to do a full sky survey for anisotropy studies (Figure 3.1b).

In addition to the main goals given before, the JEM-EUSO mission also has exploratory objectives [54]:

- Multi-messenger approach (extreme energy neutrinos and gamma-rays).

- Galactic and extra-galactic magnetic fields.

- Atmospheric phenomena.

- Meteors and meteoroids.

The multi-messenger approach in general follows the concept of collecting complementary information from different types of particles originating from astrophysical sources, like CR, gamma-rays and extreme energy neutrinos. For example, neutrinos are rarely obstructed by interstellar matter and can provide information on the physical processes of otherwise obscured source candidates. Furthermore, gamma-rays and neutrinos are not deflected by galactic and extra-galactic magnetic fields and thus point back to their sources. In conjunction with CR magnetic fields can be probed because different charged particles experience, depending on their energy, different deflection angles from magnetic fields. This results in a magnetic point spread function for incoming charged CR. If the particles characteristics and their sources are known galactic and extra-galactic magnetic fields can be calculated or at least limits can be given. Also anisotropy studies that consider magnetic fields in their analysis can provide information [56].

With measurements of the extreme energy neutrino and extreme energy gamma-ray flux, different propagation and source scenarios can be discriminated. In addition, UHE neutrinos produced inside source regions will point back to them. A high UHE gamma-ray flux is predicted by exotic dark matter theories, leading to different large scale structures in the Universe. UHE neutrinos can be identified via the positions of the first interaction point and of the shower maximum. The shower maximum of an UHE gamma-ray is strongly affected by the geomagnetic effect and the Landau-Pomeranchuk-Migdal (LPM) effect. The later leads to an early interaction in the atmosphere. JEM-EUSO will also be able to see atmospheric phenomena, such as lightning, transient luminous eventss (TLEs) and the night-glow background in the UV band. Furthermore, meteors and meteoroids can be detected via their slow UV tracks (compared to EAS).

3.2 DETECTOR DESIGN

The JEM-EUSO telescope consists of three Fresnel lenses and a focal surface made of MAPMTs. The lenses have a diameter of more than 2 m and are cut out from a polymethyl-metacrylate (PMMA) block. The first and the third lens are focusing lenses, the second lens is a diffusing lens. The optics are made with corrections

(a) JEM-EUSO observation principle.

(b) Simulated photon flux at aperture.
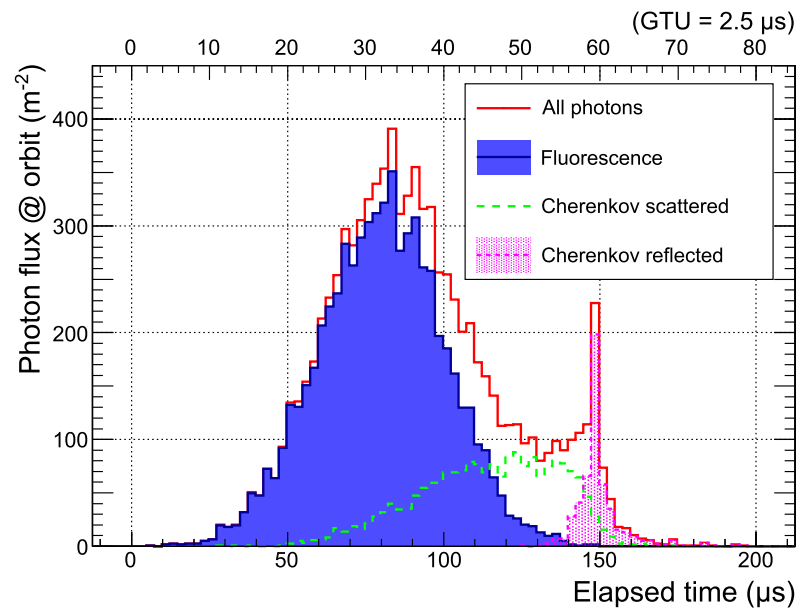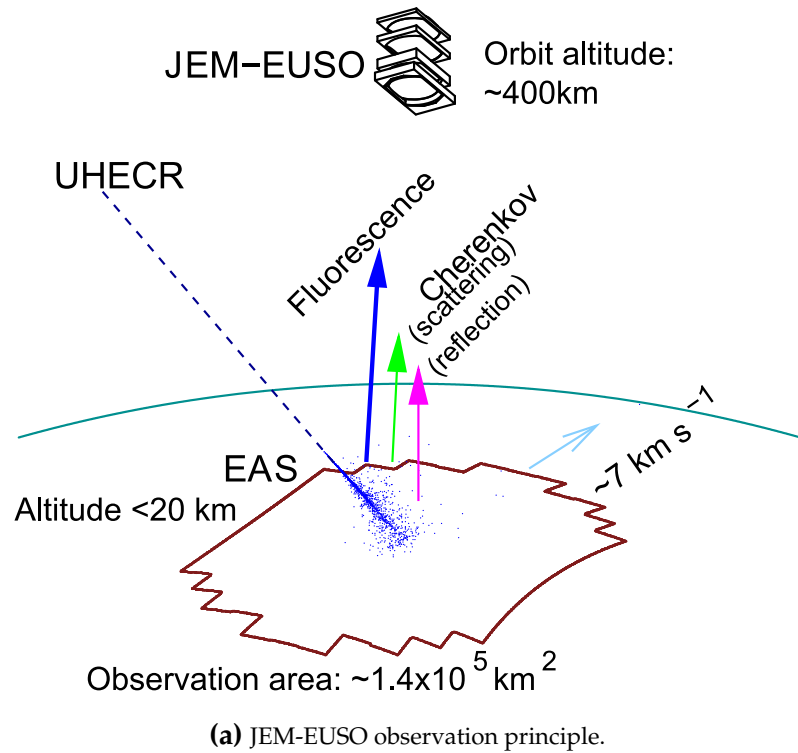
Figure 3.2: Schematic view of the JEM-EUSO mission. **(a)** JEM-EUSO in orbit at 400 km altitude and an EAS within the FOV. EAS generate fluorescence light that is emitted isotropically and Cherenkov light that is emitted in forward direction. The later is scattered and reflected before reaching the JEM-EUSO aperture. **(b)** Number of photons at the aperture of the telescope versus time for a simulated EAS with an energy of 10^{20} eV and a zenith angle of 60°. The photons arriving at different times at the aperture can be linked to different origins within the EAS [59].

for aberrations and have a focal point of roughly 2 mm in diameter at the focal surface [59]. The telescope will be attached to the ISS. With a very large field-of-view of 60° and the ISS orbit of 400 km altitude, the JEM-EUSO telescope will have an observation area on-ground of around 1.4×10^5 km^2. The detection of EAS will be done via UV light detection. The fluorescence light is isotropically emitted and the Cherenkov light is emitted in forward direction of the EAS. Since JEM-EUSO will be in a orbit around the Earth, Cherenkov light can not be seen directly but has to be either scattered in the atmosphere or reflected on clouds or the ground (Figure 3.2a).

A simulated photon flux at the JEM-EUSO aperture versus time is shown in Figure 3.2b for an EAS with an energy of 10^{20} eV and a zenith angle of 60° [59]. The first photons arriving on the aperture are the fluorescence photons that are emitted isotropically throughout the whole shower development (0 µs to 150 µs). The second component is the scattered Cherenkov light. It arrives later at the aperture, since it has a slightly longer way up (25 µs to 200 µs). The last component is the reflected Cherenkov light (125 µs to 200 µs). It is either reflected by clouds or the Earth's surface. Therefore its peak height is dependent on the abundance of clouds, the state of the atmosphere, and ground conditions [57].
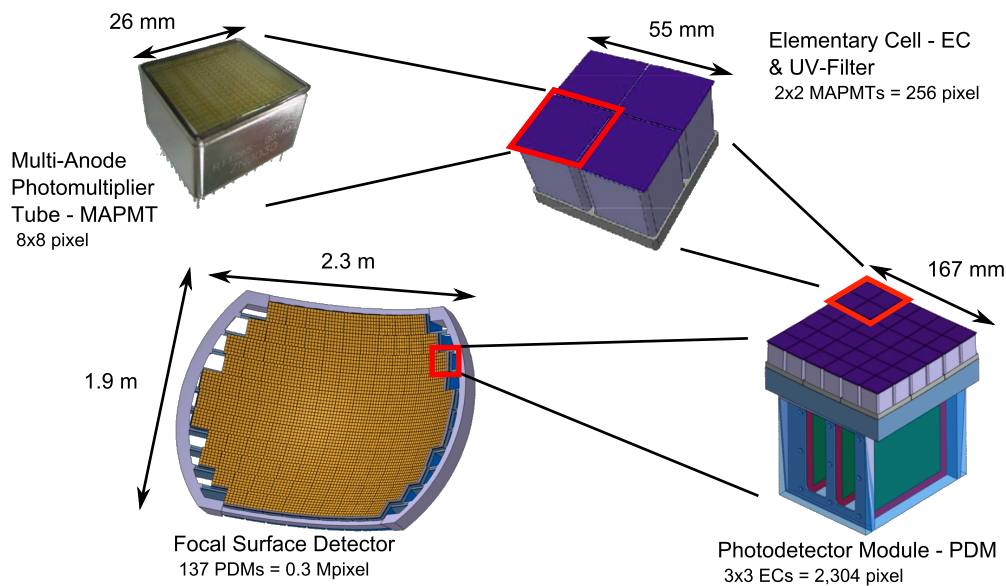
Figure 3.3: Schematic view of the components of the JEM-EUSO focal surface. The focal surface consists of 137 PDMs which are made of 3×3 ECs. Every EC consists of four MAPMTs, each of these has 8×8 pixels. Adopted from [61].

Since the atmospheric conditions have to be known at all times an EAS is recorded, JEM-EUSO will have an Atmospheric Monitoring System (AMS) installed. It consists of an infrared (IR) camera and a Light Detection and Ranging (LIDAR). With the IR camera clouds can be seen and the altitude of their top can be estimated. The LIDAR is used to get information about scattering behaviour of light in the atmosphere. Time and position of EAS events will also be recorded to use them together with meteorological data for further atmospheric information.

The focal surface of JEM-EUSO consists of roughly 5000 MAPMTs which form an area of 2.3 m $\times$ 1.9 m. The concave shape of the focal surface is the surface of a sphere with a radius of 2.5 m. Every MAPMT has 8×8 pixels and is glued with an UV transmitting band pass filter [DS62] for the range of 290 nm to 430 nm. Four MAPMTs form one EC and nine ECs form one PDM. 137 PDMs form the focal surface (Figure 3.3).

Because of the complex structure of the MAPMTs special boards for power supply and signal measurement were designed by the JEM-EUSO collaboration. The front-end readout is done by custom made electronics using 64-channel application-specific integrated circuits (ASICs) that each measure signals from one MAPMT. They are called Spatial Photomultiplier Array Counting and Integrating Chip (SPACIROC) [61, 63]. They have built-in preamplifiers for single-photon counting and charge-to-time converters to perform charge measurement for 10 to 1500 photoelectrons. Both modes work for 64-channels. To be able to use these ASICs in space, the power consumption was designed to be 1 mW per channel and radiation hardness was ensured.

After digitization of the triggered MAPMT-signals, the data of one PDM is transmitted to the PDM-board which controls the particular PDM. The first level trigger is also implemented into the PDM-boards. The data is sent to one of twenty Cluster Control Boards (CCBs), of which each is controlling a subset of PDM-boards. From there the data is sent to the JEM-EUSO CPU to be stored. The data transport from the ISS to Earth will be done via standard procedures, e. g. satellite down-link and hardware transport via spacecrafts. The mission will be supported by several ground facilities, such as mission operation control, data centers, and the Global Light System (GLS).

(a) Direct illumination.

(b) Illumination of optics and detector.
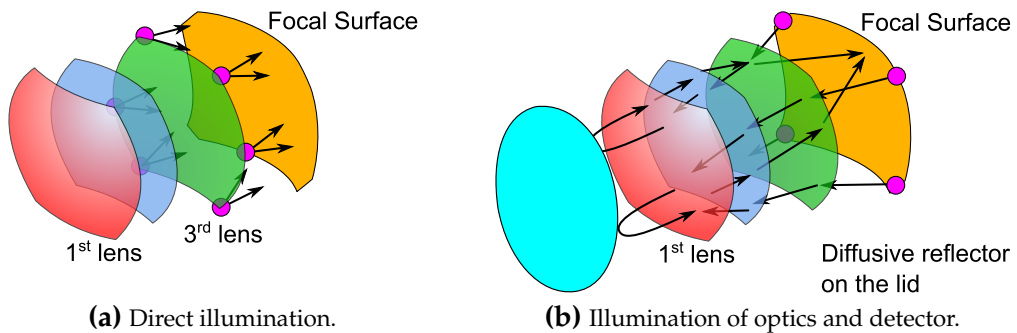
Figure 3.4: JEM-EUSO on-board calibration system. **(a)** In order to monitor the relative change in the detection efficiency, diffuse UV-light sources with controlled optical output are positioned as shown in the sketch. They are mounted along the edge of the rear lens and illuminate the focal surface directly. **(b)** Four identical light sources are positioned at the corners of the focal surface facing the rear lens. The light travels through the optics, gets reflected at the diffusive lid, goes through the optics again, and reaches the focal surface. With this the combined efficiency of the optics and the detector are measured. Both adopted from [58].

For a precise estimation of the EAS energies the detector has to be calibrated preflight in an absolute way. This will be shown in detail in Chapter 4. In order to monitor the detector performance during the whole mission time, in-flight cal-

ibration mechanisms will be implemented: the on-board calibration system and the GLS. The on-board calibration system consists of several identical diffuse light sources made of integrating spheres, pulsed light-emitting diodes (LEDs) and NIST-calibrated photodiodes, to control their optical output (National Institute of Standards and Technology (NIST) - US American measurement standards laboratory). One group of the light sources will be mounted at the edges of the rear lens of JEM-EUSO to achieve a direct illumination of the focal surface (Figure 3.4a). The other group of light sources will be placed at the corners of the focal surface to illuminate the rear lens. The light will go through the optics, be reflected on the diffusive lid, go through the optics again, and will be measured at the focal surface (Figure 3.4b). This measurement will give the combined efficiency of the optics and the detector [54, 58] The on-board calibration system will be a relative calibration to the absolute calibration that will have been done preflight on the ground. Further information can be found in Section 4.6.

The GLS for JEM-EUSO will be an on-ground network of LIDAR-stations equipped with UV-lasers and Xenon flash lamps (Xe-flashers). If a station is in the FOV of JEM-EUSO, it will send light signals of known amplitude and length, for cross-calibration and atmospheric monitoring purposes. Additionally the trigger efficiency and the reconstructed pointing direction accuracy can be monitored. The LIDAR-stations will generate tracks on the focal surface and the Xe-flashers will produce point flashes. These signals will be similar to EAS events, but are known in their characteristics.
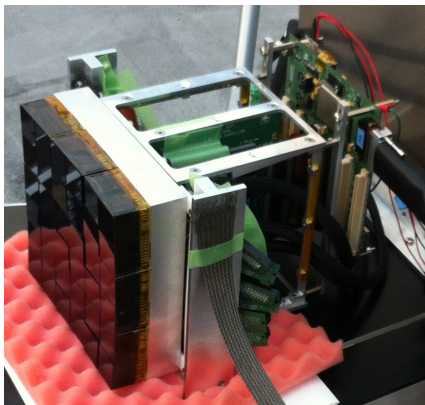
3.3 PROTOTYPES

In order to raise the technical readiness level of JEM-EUSO and to do research and development (R&D) with the apparatus, several prototype experiments have been designed: EUSO-Balloon, EUSO-TA, and Mini-EUSO.

EUSO-BALLOON is a fluorescence telescope that looks down from a balloon at 40 km altitude to observe EAS and the UV night background [64–66]. This prototype consists of one PDM with two PMMA Fresnel lenses as well as an IR camera prototype. The PDM uses the same electronics that are planned for JEM-EUSO up to the PDM-board. The IR camera is a smaller version of the one planned for JEM-EUSO. The instrument is accommodated inside a housing. The housing has crash pads and a flotation device to be save for a land and water landing (Figure 3.5b). In August 2014 the first of three planned flights was conducted from Timmins (Canada) organized by Centre national d'études spatiales (CNES). During the flight in an altitude of roughly 40 km EUSO-Balloon was measuring the night sky background, laser shoots fired from a helicopter, and light pulses coming from a Xe-flasher. It also was used for testing the trigger algorithm of JEM-EUSO. Preliminary analysis of the data indicates an average night sky background of roughly 500 photons/m^2/sr/ns and shows the technical feasibility of the instrument. A possible successor experiment will be a long flight with a super pressure balloon (SPB) organized by NASA in spring 2017.
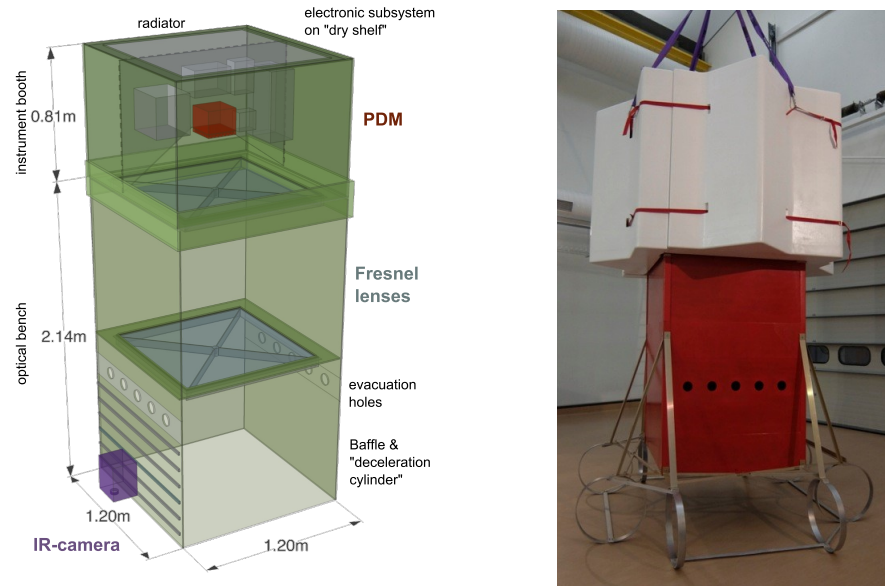
Figure 3.5: EUSO-Balloon prototype. The left side shows a sketch of the gondola. It is housing one PDM and two PMMA Fresnel lenses as well as an IR-camera prototype. The electronics are secured against water. In case of a water landing, the bottom part of the gondola functions as a deceleration cylinder and the water can get out through the evacuation holes without smashing the lenses. Adopted from [64, 65]. The right side shows the EUSO-Balloon gondola being prepared for the balloon launch. It is equipped with crash pads and pontoons for land and water landing [66].

(a) EUSO-TA PDM.
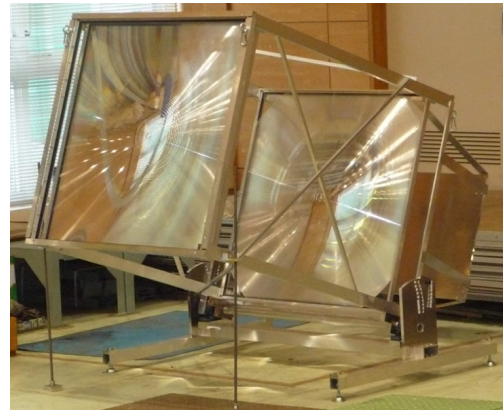
(b) EUSO-TA mechanical structure.

Figure 3.6: EUSO-TA prototype. **(a)** The EUSO-TA PDM with 36 MAPMTs and attached UV filters at an early field test in Tokyo (Japan) in November 2013. **(b)** The mechanical structure of EUSO-TA with two Fresnel lenses [67].

EUSO-TA is the second pathfinder experiment for JEM-EUSO [54, 67, 68]. It is located at the TA site in Utah (USA), in front of one of the fluorescence telescopes of TA, which is used as an EAS trigger for EUSO-TA. The pathfinder consists of one PDM (Figure 3.6a) and a mechanical structure housing two PMMA Fresnel lenses (Figure 3.6b). Since an electron light source (ELS) as well as a LIDAR is located at TA

site, this is a good environment for a prototype experiment. When measuring laser pulses or induced showers from the ELS, the time, position, and total energy of the event is known. With this EUSO-TA can be used for cross-checking the calibration, testing the trigger algorithm, and performing measurements of EAS together with TA. EUSO-TA was deployed at the TA site in March 2015. Further R&D with SiPMs instead of MAPMTs can be done.
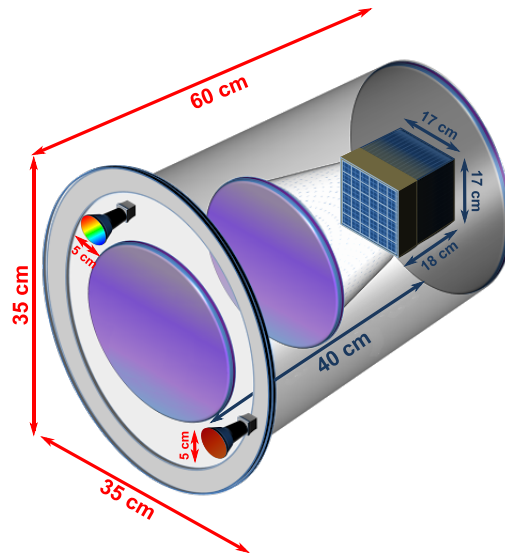
Figure 3.7: Mini-EUSO concept with two PMMA-lenses, one PDM, an optical camera, and an IR-camera. Adopted from [65].

MINI-EUSO is a 1:137 scaled prototype of JEM-EUSO, consisting of one PDM, two PMMA Fresnel lenses, one IR camera, and one camera for visible light [65, 69]. It is planned to put SiPMs on the outer rim of the PDM. The instrument will be a closed box of $60\,\mathrm{cm} \times 35\,\mathrm{cm} \times 35\,\mathrm{cm}$ and put in front of a UV transmitting window inside the Russian module of the ISS. The detection area will be as big as the one of JEM-EUSO but with only 2304 pixels. Mini-EUSO will also have two supporting cameras: an optical one and an IR-camera (Figure 3.7). The data will be saved on hard drives and transported via the Soyuz spacecraft. The start is planned for 2019.

<div style="text-align: right; font-size: 4em; color: gray;">4</div>
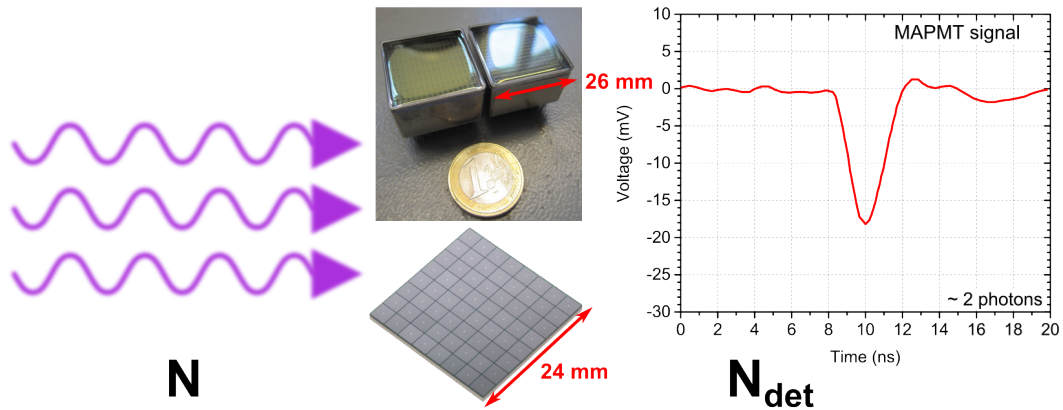
CALIBRATION OF PHOTOSENSORS

For the detection of CR via the emitted fluorescence light in EAS it is essential to calibrate the detector with paramount precision. Only by this the mass composition, the energy of the primary particle and the arrival direction can be estimated in a correct way [4, 49, 59, 70–72]. It is even more important for the space-based observation of EAS, where access to the detector is not given during the mission time. In the case of JEM-EUSO the focal surface will consist of MAPMTs (Chapter 5) [42, 50] or SiPMs (Chapter 6) [73, 74]. The focal surface is planned to have a modular structure (photo-detector module), were the detectors are supplied with a common bias voltage per elementary cell. Therefore, the detectors have to be sorted preflight, according to their photo detection efficiency, to get a focal surface with a homogeneous efficiency. Small discrepancies can be regulated via the voltage connected to the single ECs. For that the single ECs need to have a uniform PDE.

For the calibration of the used detectors and for their sorting an advanced calibration stand for single-photon detection was built at KIT within this thesis. It is named Single PhOton Calibration stand at KIT. It follows the baseline of the calibration stand built by Carl Blaksley, Gwenaëlle Lefeuvre, and Philippe Gorodetzky at Université Paris 7 - Denis Diderot [75–77]. It consists of reference light sources, detectors that should be tested, photon shielding and readout electronics. During this work, several improvements compared to the original design were developed, built and implemented.

This chapter will introduce the general idea on how to calibrate photosensors. Part of the text and figures in this chapter were published before in [54, 74, 78]. The calibration principle as well as the calibration stand at KIT, will be described in detail in Sections 4.1 and 4.2. Afterwards the capabilities of the calibration stand that was designed, built, and improved during this work, will be pointed out and possibilities for further improvements will be explored in Section 4.5. The last section will show how the experience gained with this calibration stand can be used for the inflight-calibration of JEM-EUSO (Section 4.6).

4.1 CALIBRATION PRINCIPLE

The principle thought of the calibration stand is very simple: One takes a known number of photons with a known wavelength and sends them onto the photosensor that should be calibrated. After measuring the number of detected photons by the photosensor, the efficiency can be calculated via the ratio of both numbers (Figure 4.1).

Figure 4.1: Universal calibration principle. A known number N of photons, with a set wavelength, is sent onto the photosensor that should be calibrated. The figure shows two possible photosensors: MAPMT and SiPM. The photosensor signal is measured in a controlled environment. Comparing the number of detected events N_{pe} to the number N of all sent photons gives the detection efficiency of the photosensor. The picture of the SiPM is taken from [DS79].

In practice this is a lot harder to do. First of all, every photon that is not produced by the light source has to be excluded from the measurement. This is realized with a photon shielding around the experimental set-up. To prevent the reflection of stray photons, the inside of the shielding is covered with light absorbing black flock paper. The stable and easily controllable light source consists of a 3-port integrating sphere, with two exit-ports and an entrance-port [DS80]. All ports are perpendicular to each other and the components are mounted light-tight to the ports. The LED-array is located at the entrance-port, the NIST-calibrated photodiode and the collimator are located at each exit-port (Figure 4.2).

The UV-light (≈ 376 nm) from the LED-array is diffusely reflected inside the integrating sphere and distributed uniformly over the inner surface of the sphere. The integrating sphere itself behaves as a splitter and a diffuser. The fraction of photons leaving the sphere from one port is proportional to the ratio of the area of the port itself and the sphere's area (Section 4.3.1) [76, 81]. Therefore both exit-ports emit the same number of photons N_{Sphere}. This is measured at one exit-port with a NIST-calibrated photodiode (*Photodiode* 1). Details about the photodiodes are given in Section 4.3.4. The collimator at the second exit-port is there to reduce the photon flux from the exit-port. This is necessary because the light source will illuminate MAPMTs or SiPMs and their gain is around a factor of 10^6 higher than the gain of the photodiode.

In order to characterize the light source correctly, the collimator ratio R has to be measured before and after the measurement with the photosensor. This is done by measuring the optical output of the light source by a second NIST-calibrated photodiode (*Photodiode* 2) in front of the collimator. The ratio of both photon numbers gives the collimator factor R of about 10^{-6}. Since the photodiodes measure optical
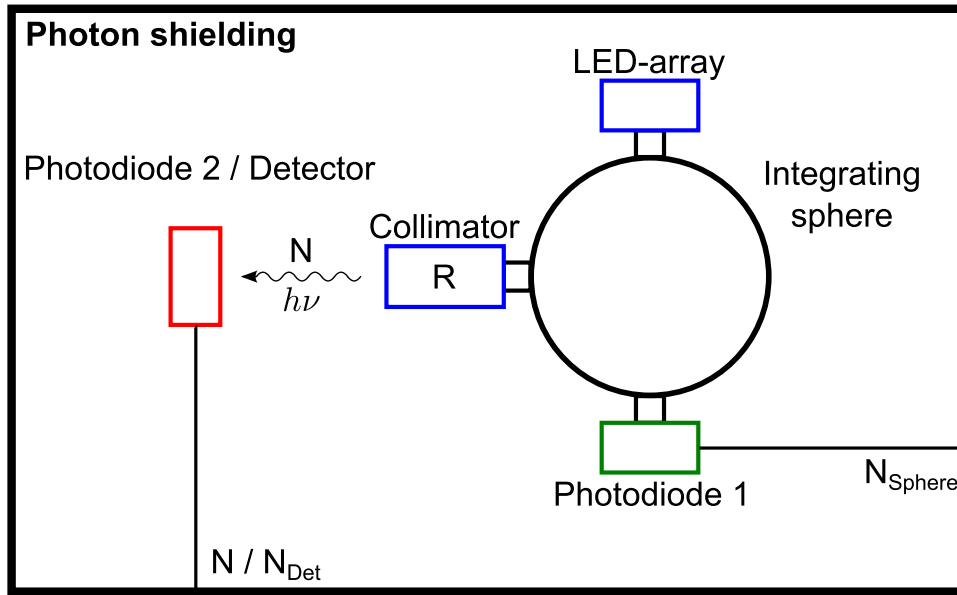
Figure 4.2: Schematic view of the calibration stand. The experimental set-up of the photon shielding, the light source, the NIST-calibrated photodiode, and the examined detector is shown. All ports on the integrating sphere are perpendicular to each other in the real set-up.

powers the ratio of both measured powers (P_{NIST1} and P_{NIST2}) can be used instead of the photon numbers:

$$R = \frac{N}{N_{Sphere}} = \frac{P_{NIST2}}{P_{NIST1}} \quad .$$

During this measurement the whole LED-array is set to continuously emit light, because of the low gain of the photodiode and the strong collimator reduction. The collimator factor R only depends on the collimator geometry and is measured very precisely with the above mentioned measurement (Section 4.3). The ratio R is also dependent on the distance of the photodiode or the detector to the exit hole of the collimator, because of the spread of the light cone exiting the collimator. This has to be taken into account for measurements.

When knowing the collimator ratio, the number of photons N that are emitted by the reference light source *per second* can be calculated via the measurement of the number of photons N_{Sphere} inside the sphere or respectively via the power measurements of P_{NIST1}. With this the number of emitted photons N *per pulse* (pulse frequency f_{pulse}) is known:

$$N = \frac{P_{NIST1} \cdot R}{E_{Photon} \cdot f_{pulse}} = \frac{P_{NIST1} \cdot R \cdot \lambda}{h \cdot c \cdot f_{pulse}} \quad . \tag{4.1}$$

Afterwards, the detector is placed in front of the collimator at the same position where the second NIST-calibrated photodiode was located before (*Photodiode 2*). For generating light one LED in the center of the array is used in pulsed mode, mean-

ing it is driven outside of normal specifications with ns-pulses of voltages up to $-24\,\text{V}$. This causes the LED to emit a small number of photons in an ultra-short light pulse within the time window of the voltage pulse. This type of operation is commonly used for different applications were low light levels or a stable output without thermal influences are needed [82–85]. While triggering the detector on every light pulse (number of triggers N_{total}), the number of photoelectrons N_{pe} that were detected by the detector are counted. The ratio gives the PDE ϵ of the detector for the wavelength of photons that were used [75]:

$$\epsilon = \frac{N_{pe}}{N \cdot N_{total}} \quad . \tag{4.2}$$

Uncertainties of the PDE originate from the determination of both photon numbers. Referring to Equation 4.1, the uncertainties of the optical power measured by the photodiode, uncertainties in the collimator ratio, uncertainties in the wavelength of the photons, and uncertainties in Planck's constant h and the speed of light c are propagated. The number of detected photoelectrons N_{pe} is dependent on the Gaussian distributions in the *single photoelectron spectra* (for MAPMTs) respectively the *finger spectra* (for SiPMs), and the uncertainties in the charge measurement by the charge-integrating analog-digital converter (QADC) that measures these charges. The total number N_{total} of triggered events is assumed to be accurate.

After data taking with the detector, the collimator ratio R is measured again with both photodiodes, to make sure that it is stable. A more detailed description on how to measure the detected photoelectron number N_{pe} and how to determine the PDE of the different detectors will follow in Chapter 5 for MAPMTs and in Chapter 6 for SiPMs.
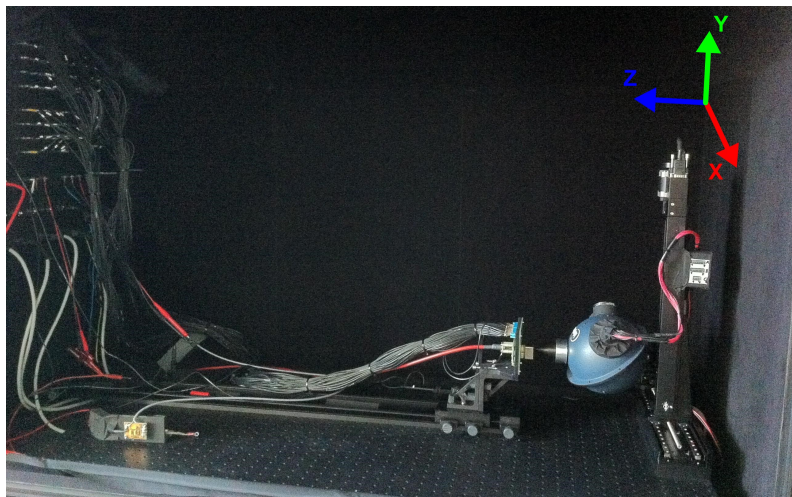
4.2 CALIBRATION STAND

The calibration stand SPOCK was designed and built during this work to be able to test and calibrate a wide range of different photosensors of all sizes. The photon shielding is a wooden box with the dimensions of $2\,\text{m} \times 1\,\text{m} \times 0.9\,\text{m}$ and a lid in the front to be able to accommodate a wide variety of different sized detectors, e. g. one whole PDM of the JEM-EUSO baseline design [61]. The inside of the shielding is covered with non-reflecting black flock paper. The lid is lifted and staying up with two pneumatic springs (Figure 4.3a). The edges of the lid and box are sealed with a UV-resistant rubber labyrinth. When the lid is closed, the two shifted profiles intertwine, sealing the box. The lid is held in place with several tension locks. An additional safety mechanism was implemented via safety pins that lock the tension locks, if an HV-cable is connected. Parts of the shielding was built together with Thomas Huber during the course of his bachelor thesis [86]. On the left side of the shielding a light-tight panel is located (Appendix B, Figure B.1). It is made of 3 mm thick aluminum and has all needed couplers for connecting signal, control, and voltage cables (Appendix C, Figures C.37 and C.38). On the inside the whole panel is coated with black rubber to make sure no gaps remain and to reduce reflection. Additionally, a black curtain was installed inside the box in front of the

panel (Appendix B, Figure B.2). Tests with old photomultiplier tubes (PMTs) and our photodiodes showed that there was a small leakage through BNC-connectors that could be fixed with attaching end-caps to these connectors.
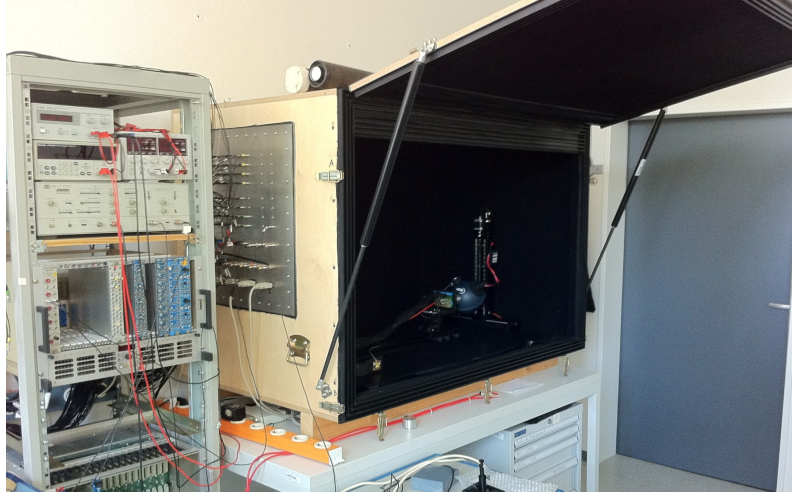
(a) Calibration stand outside.

(b) Calibration stand inside.

Figure 4.3: Photograph of the calibration set-up with open photon shielding. **(a)** The inside of the wooden box ($2\,\mathrm{m} \times 1\,\mathrm{m} \times 0.9\,\mathrm{m}$) is covered with black flock paper. The edges of the lid and the box are sealed with an UV-resistant rubber labyrinth. The side-panel as well as a part of the electronics can be seen on the left side. **(b)** All mounts are made of matt black anodized aluminum. The light source is mounted on two perpendicular linear stages (XY-plane). On the optical axis (Z-axis) the detector is mounted on an optical rail ($1000\,\mathrm{mm}$ long) perpendicular to both stages.

Inside of the photon shielding a matt black anodized optical breadboard [DS87] was installed. On that, a one meter long optical rail [DS88] was attached together with several slides [DS89] and right-angle plates [DS90] to mount the photodiode [DS91, DS92], the MAPMTs *R11265-113-M64 MOD2* (Appendix C, Figures C.30 and C.31), and the SiPMs [DS79]. This set-up makes it possible to reliably control the distance of the photodiodes and the photosensors from the light source on the

optical axis (Z-axis). On the right side of the optical rail, two computer controlled precision linear stages [DS93, DS94] were installed. They host the light source and are perpendicular to each other and to the optical rail, in order to scan the XY-plane (Figure 4.3b). With this kind of set-up single photosensors or arrays of photosensors with a sensitive area up to $295\,\mathrm{mm} \times 295\,\mathrm{mm}$ can be scanned. The set-up is also able to uniformly illuminate a whole detector area of up to $600\,\mathrm{mm} \times 600\,\mathrm{mm}$, from a distance of roughly 1 m. In that respect the calibration stand provides a maximum of versatility for photosensor calibration and testing.

4.3 REFERENCE LIGHT SOURCE

This section contains detailed information about the reference light source and test experiments that were done in order to characterize it. The components of the light source are an LED-array (Section 4.3.2), an integrating sphere (Section 4.3.3), a NIST-calibrated photodiode (Section 4.3.4), and a collimator (Section 4.3.5). A detailed list can be found in Appendix C in Table C.1.

4.3.1 *Integrating sphere theory*

The following general theoretical principles of integrating spheres are summarized from [76, 81]. They are essential to understand the properties of the reference light source. The heart of the reference light source is an integrating sphere that has one entrance-port and two exit-ports. The ports are perpendicular to each other and the area of the ports is less than 5 % of the total surface area of the sphere to maintain a high reflected flux. The inside of the sphere is made of a diffuse reflecting material, which leads to a uniform light flux on the inner surface of the sphere [81], e. g. imagine two surface elements on the inside of a sphere with radius R (Figure 4.4a). In general, the fraction of energy dF emitted by one surface element dA_1 that is then received by a second surface element dA_2 is

$$dF = \frac{\cos \theta_1 \cos \theta_2}{\pi S^2} \cdot dA_2 \quad , \tag{4.3}$$

where

θ_1 , θ_2 are measured from the surface normals of each respective surface element, and

S is the distance between both surface elements (chord).

This is an isosceles triangle (Figure 4.4a), so we have $\theta_1 = \theta_2 = \theta$ and $\alpha = \pi - 2 \cdot \theta$. The distance $S = 2 \cdot R \sin \left(\frac{\alpha}{2} \right)$ becomes $S = 2 \cdot R \cos \theta$. Putting this equation into Equation 4.3, we get for the exchange factor

$$dF = \frac{dA_2}{4\pi R^2} = \frac{dA_2}{A_S} \quad . \tag{4.4}$$

This means that a finite surface area A_2 of the sphere receives a portion of the radiant flux proportional to the ratio of its own area versus the area of the whole sphere

A_S. The important part of this result is that it is independent of the viewing angle, the size of the emitting area, and the distance to the emitting area [81].

(a) Surface elements in the sphere.

(b) Flux inside the sphere.
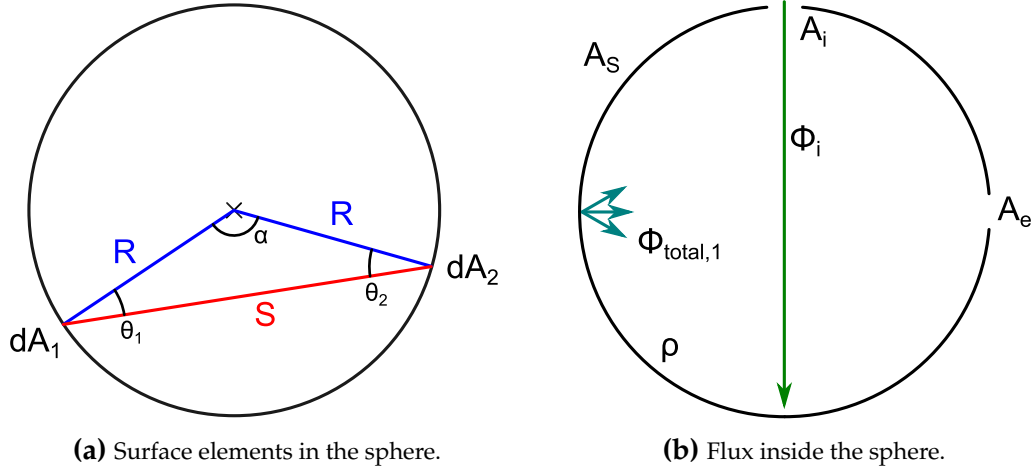
Figure 4.4: Sketches of an integrating sphere. **(a)** Geometry of the energy exchange between two surface elements inside a diffuse integrating sphere. **(b)** Illustration of geometrical and optical properties for calculating the flux inside an integrating sphere. Both pictures adopted from [81].

Figure 4.4b shows the schematics we use to calculate the flux $\Phi_{\text{total},1}$, which is incident on the internal surface of the sphere after diffusion from the first reflection. For the area fraction we take Equation 4.4 into account. We assume an incident flux that is put into the sphere. It gets diffusely reflected by the sphere material and the total surface hit by it is the effective sphere area. We get the following equation [81]

$$\Phi_{\text{total},1} = \Phi_{\text{i}} \cdot \rho \left(\frac{A_{\text{eff}}}{A_S} \right) \quad , \tag{4.5}$$

where

Φ_{i} is the incident flux,

ρ is the reflectance of the sphere material,

A_{eff} $= A_S - A_{\text{i}} - A_{\text{e}}$ is the effective surface area of the sphere,

A_S is the total surface area of the sphere, and

$\frac{A_{\text{eff}}}{A_S}$ $= F$ is the exchange factor of two areas inside the sphere.

In first approximation Equation 4.5 is the total flux inside the sphere Φ_{Sphere}. Since the flux has to be multiplied with the reflectance and the area ratio for every reflection, this is a good estimation for the flux inside the sphere. If a baffle is located inside the sphere it can be seen as an extension of the sphere's surface, however the changes to the flux introduced by a baffle are typically not significant [81]. In general the flux inside an integrating sphere is dependent on many factors, e. g. the geometry of the set-up and the coating of the sphere. For this estimation we stick

to a simple set-up without any baffle. If we assume the area of a detector device, directly attached to one port of the sphere to be A_{D1}, the flux on the device is

$$\Phi_{D1} = \Phi_i \cdot \rho \cdot \frac{A_{D1}}{A_S} \quad . \tag{4.6}$$

Note that we assume that the device is on the sphere's surface and thus the flux is only dependent on the initial flux, the reflectance, the sphere's surface area and the device area. Together with Equation 4.5, we substitute Φ_i and get

$$\Phi_{D1} = \Phi_{Sphere} \cdot \frac{A_{D1}}{A_{eff}} \quad .$$

The same holds for a second device, with an area A_{D2}. Thus, the resulting flux ratio is only a function of the projected area ratios:

$$\frac{\Phi_{D1}}{\Phi_{D2}} = \frac{A_{D1}}{A_{D2}} \quad . \tag{4.7}$$

To conclude, the flux exiting a port of the sphere (or hitting a device directly attached to one of the ports) depends only on the area of said port (or device) [76, 81]. Therefore, the flux readings from two exit ports of an integrating sphere should be the same, if the same distance to the sphere's center is maintained for both detectors. If the distance to the exit port is increased, the uniformity of the flux decreases. However, after a distance of two or three exit-port diameters (depending on the size of the detector area), uniformity is restored and an $\frac{1}{r^2}$ proportionality for the optical power is expected [81].

4.3.2 *LED-arrays*

The requirements for the light source are a well known and stable spectral output, with high reproducibility. Therefore, LEDs were used as photon generators. In order to characterize the collimator with the photodiodes a high photon flux is needed, since their gain is around one and the collimator reduces the flux with a factor of around 10^{-6} or more. On the other hand a low photon flux is needed for the single-photon generation for photosensor calibration.

Because of that LED-array A, consisting of two different types of LEDs, was built from aluminum (Figure 4.5a) to be mounted light-tight to the entrance port of the integrating sphere [86]. The array comprises $20 \times 3\,\text{mm}$ UV-LEDs *XSL-375-3E* for continuous light emission and one $5\,\text{mm}$ UV-LED *XSL-370-TB-4* for single-photon emission in the middle (Table C.2). The LEDs are distributed uniformly over the entrance port area. All LEDs of the *XSL-375-3E* type are in a parallel circuit and every LED has a resistor for current regulation ($91\,\Omega$) and a dip-switch for turning it on and off. With this several array configurations can be set, to test different light levels (Figures C.12 and C.13). The pulse mode LED of the type *XSL-370-TB-4* has a series resistor of $39.5\,\Omega$.

The main wavelength of the 3 mm UV-LEDs is $(376 \pm 6_{\text{sys}})$ nm (Figure A.2a) with an optical output of around 10 mW per LED. This corresponds to a combined optical output of around 2 mW at the first NIST-photodiode. The optical output of the 5 mm UV-LED is around 1 mW in continuous mode and has a pulsed peak wavelength of $(371 \pm 6_{\text{sys}})$ nm (Figure 4.7). This was shown via measurements with a spectrometer [DS95, DS96]. The peak wavelength in pulsed mode stay the same for both LEDs, however the peak wavelengths in continuous mode is shifted slightly to higher values for both LEDs. Details to this effect follow in Section 4.3.2.2. This LED-array is primarily used to measure the collimator ratio R of different collimators at a wavelength of $(376 \pm 6_{\text{sys}})$ nm in continuous mode.

(a) LED-array A.   **(b)** LED-array B.   **(c)** LED-array C.
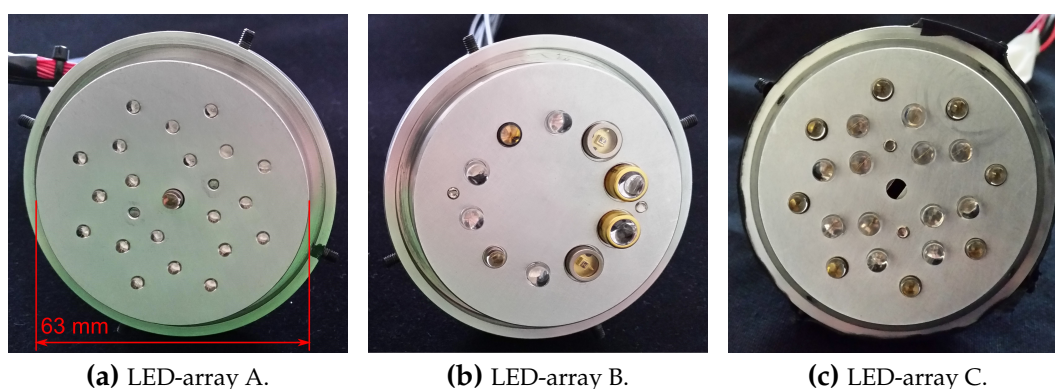
Figure 4.5: Photograph of the first three LED-arrays. All same-sized arrays (63 mm diameter) consist of aluminum and different UV-LEDs. **(a)** Twenty uniformly distributed LEDs can be switched off separately (Table C.2 and Figures C.4 and C.5). Designed and tested by Thomas Huber [86]. **(b)** LED-array for generating single photons with different wavelengths in the UV-regime (Table C.2 and Figures C.8 and C.9). Designed and tested by Nils Hampe [97]. **(c)** LED-array with high optical output for four different wavelengths: 373 nm, 380 nm, 394 nm, and 423 nm. Its structure is the same as LED-array A, but with 5 mm holes.

A second array (LED-array B) was build to be able to send single photons with different wavelengths in the UV-regime onto the photosensors (Figure 4.5b). Ten different UV-LEDs in the range of 300 nm to 420 nm were chosen (Table C.2). With these LEDs the main peaks of the fluorescence spectrum of nitrogen can be covered, as shown in Appendix A, Figure A.6. The LEDs are arranged on a circle around the middle point of the mount, to have a symmetric layout. The different elevation of the LEDs relative to the aluminum surface and their different form factors (flat windows and lenses) is no cause for concern, since the integrating sphere will smear out any geometrical information about the light source. With a rotary knob the LED to turn on can be chosen. The resistors for current regulation of every single LED were set with respect to the desired optical output, to the available voltage range, and according to the data-sheets (Table C.2). The nominal mean optical outputs of the LEDs are given in the data sheets for continuous mode. Measurements of the optical output and the spectral output of the LEDs in pulsed mode were taken in the laboratory (Figures A.4 and A.5). These measurements showed that the optical power emitted by the LEDs in continuous mode was not high enough to measure

the collimator ratio in a reliable way, since the output flux at the second photodiode was too low [97]. These measurements are shown in detail in Section 4.3.5.4.

In an attempt to get more optical power into the sphere and therefore to increase the signal at the second photodiode, a new array (LED-array C) was produced with some LEDs of the same type as used in LED-array B and a modified version of the aluminum mount of the first LED-array A. It contained several LEDs of four different kinds for the wavelengths of 373 nm, 380 nm, 394 nm, and 423 nm (Table C.2). The continuous emission of these wavelengths could be individually switched on. Except for the 423 nm LEDs, the measurements of the emitted optical power showed that the optical power transmitted by the collimator was still to low to measure the collimator ratios of the polyvinyl chloride (PVC)-collimators in a sufficiently stable way. The average optical powers were around 60 pW to 80 pW, while the fluctuations of the photodiodes were in the range of 1 pW to 2 pW. This resulted in fluctuations of the collimator ratio of 1 % to 5 % during measurements (for details see Section 4.3.5.4).
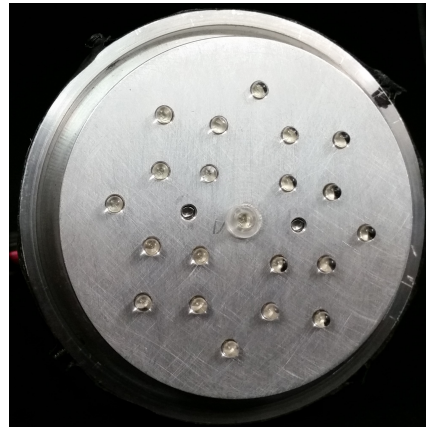
4.3.2.1 *New LED-arrays*

To get a better signal-to-noise ratio for the collimator measurements, two of the present LED-arrays were modified and two new LED-arrays were built (Figure 4.6). Every LED-array is used for one wavelength, while the middle LED is used in pulsed mode for single-photon generation and the other LEDs of the same type are used in continuous mode, to measure the collimator ratio. The different circuits for pulsed mode and continuous mode can be found in Figure C.1. Information about the used LEDs for these arrays are given in Tables C.2 to C.4. In order of the wavelength they emit, they are named:

AR1: New LED-array, built with 42+1 LEDs of type *UVLED365-110E*, i. e. there are 42 LEDs for continuous emission distributed over the array and one LED in the middle for pulsed operation. The emission wavelength is around (371 ± 6) nm (Figures A.1, C.2, and C.3).

AR2: Modification of LED-array A. The middle 5 mm UV-LED was changed to a 3 mm UV-LED, *XSL-375-3E*, the same type as the other LEDs in this array. The emission wavelength is around (376 ± 5) nm (Figures A.2a, C.4, and C.5).

AR3: New LED-array, built with 42+1 LEDs of type *VL390-5-15*. The emission wavelength is around (395 ± 7) nm (Figures A.2b and C.6).

AR4: Modification of LED-array C. For this LED-array the LEDs were changed to 12+1 LEDs of type *VL425-5-15*. The emission wavelength is around (423 ± 8) nm (Figures A.3 and C.7).

AR5: Renamed LED-array B (no modifications). This array is used for the illumination of one whole MAPMT or SiPM from a distance of roughly one meter and with a weak collimator or pinhole and pulsed light (Figures A.4, A.5, C.8, and C.9).
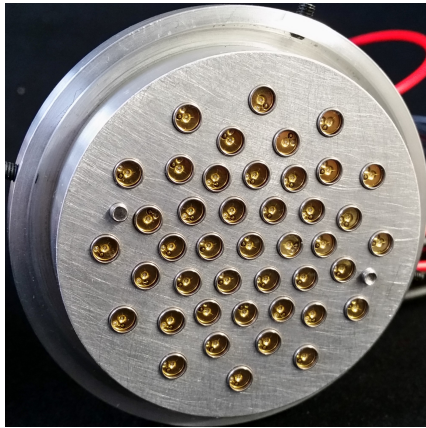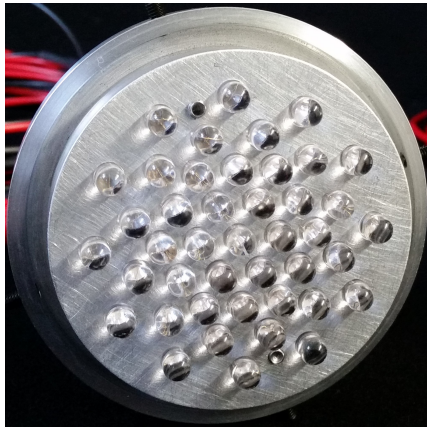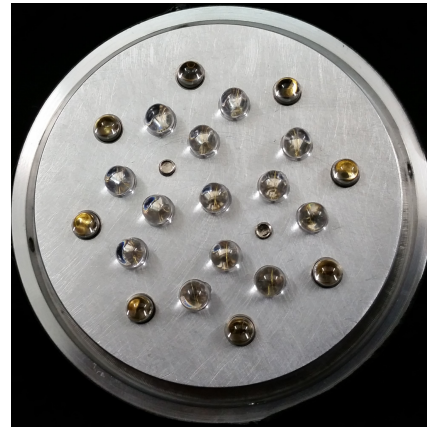
(a) LED-array AR1.

(b) LED-array AR2.

**(c)** LED-array AR3.

(d) LED-array AR4.

Figure 4.6: Photograph of the new LED-arrays AR1 to AR4. All arrays consist of aluminum and different UV-LEDs. Their dimensions are the same as the old arrays. Technical information can be found in Appendix C.1.

The LED power supply for continuous light emission is managed with a standard laboratory power source [DS98]. Pulsed operation of the LEDs is done via a pulse generator and a light diode driver (LDD) in form of a NIM-module [1]. The pulse generator *HP 8082A* sends an inverted NIM-pulse (Appendix C.3.1) with an offset of -1 V to the LDD *CERN-NP Type N4168*. The output of the LDD is a voltage square-pulse between -2 V to -24 V with the width and frequency of the input signal. The rise and fall time is around 2 ns. With this set-up voltage pulses of a very short duration (6 ns to 300 ns) and a high voltage (-2 V to -24 V) are sent to the LED that is located in the center of the array. The width was chosen to have a small integration window, since the LED emits once a bunch of photons during the pulse. The repetition rate of the pulses is around 10 Hz to 1000 Hz. The upper limit is due to limitations of the USB-connection of the Data Acquisition (DAQ) to the measurement computer.

---

1 Nuclear Instrumentation Module (NIM) - standard defining mechanical and electrical specifications of electronic modules for nuclear physics experiments (report DOE/ER-0457T).

4.3.2.2 *LED-spectra*

The spectra of all LEDs used in all LED-arrays AR1 to AR5 were measured one by one with a spectrometer *Ocean Optics S2000* and the corresponding analogue-digital converter (ADC) *Ocean Optics ADC1000-USB* [DS95, DS96] in continuous and in pulsed mode [97]. For pulsed mode the integration time had to be increased, since the optical output was decreased. Every measured spectrum shown is an averaging of at least 100 single spectra. After normalization of the measured spectra to the percent scale in respect to their peak value, they can be compared, since no normalized and calibrated optical output was used. All spectra can be found in Appendix A.1.
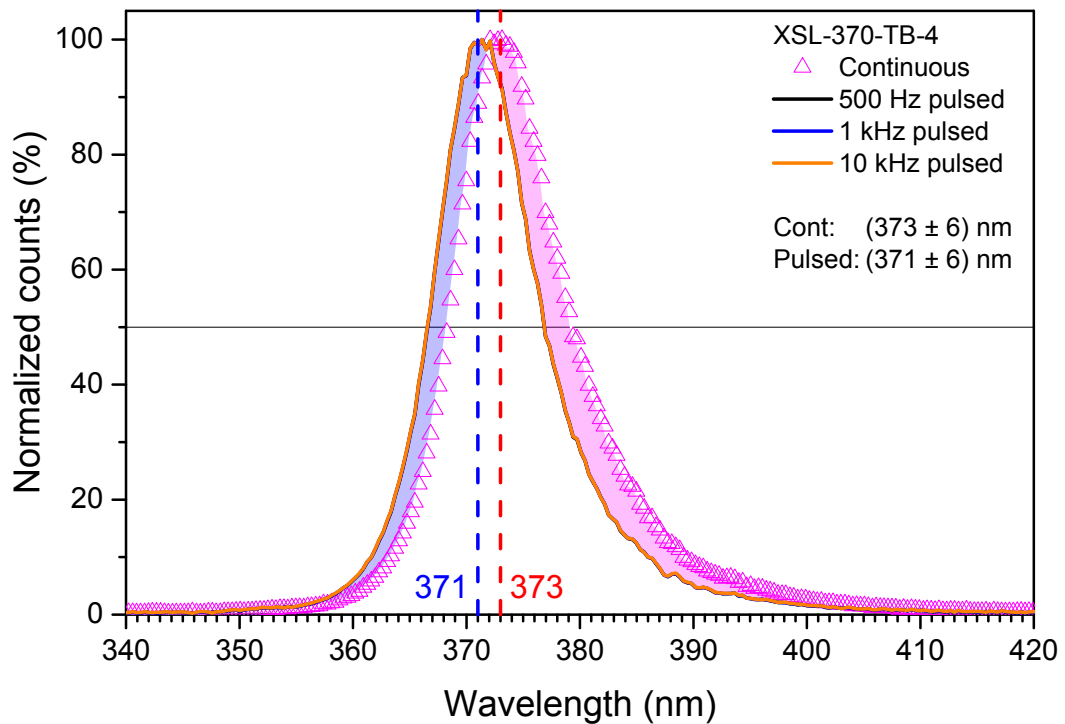
Figure 4.7: Measured continuous and pulsed spectrum of LED *XSL-370-TB-4*. Shown are the continuous and pulsed spectra for 0.5 kHz, 1 kHz, and 10 kHz. The lines of the pulsed spectra are all overlapping, therefore only the 10 kHz-line is visible. A wavelength shift from pulsed to continuous mode is clearly visible. It is illustrated by the colored areas between the 1 kHz-line and the continuous mode data points. For the area on the left, the 1 kHz-line is higher than the continuous mode data points, so the are was colored blue. On the right side the continuous mode data points are higher, so the area was colored magenta. More spectra can be found in Appendix A.1.

Figure 4.7 shows an example spectrum of one of the LEDs from LED-array AR5 for continuous and pulsed mode measured by Nils Hampe during the course of his bachelor thesis [97]. All three pulsed spectra at 0.5 kHz, 1 kHz, and 10 kHz overlap for this LED. For the continuous mode the whole spectrum is shifted by 2 nm to higher wavelengths. This shift of the peak wavelength due to thermal effects is a typical phenomenon in different LEDs [99–103]. In general LEDs are semiconductors that rely on a direct bandgap. When the bias voltage introduces electrons to the pn-junction, these electrons recombine after passing the junction. In the process,

photons are emitted at a wavelength that is characteristic of the bandgap energy of the material. Since the bandgap energy decreases with rising temperature [104, 105] the peak wavelength also changes to longer wavelengths. After the measurements in continuous mode the LED was warm to the touch. In our case the rise of temperature of the LED was because of the continuously flowing current running through the LED in continuous mode. The electronics and power source for the measurement were outside the photon shielding and thus in the climate controlled laboratory. Any strong influence on their part is unlikely. Further, the form of the spectrum stayed the same for this LED, which is illustrated by the filled areas between the pulsed (1 kHz) and continuous data points.

The same behavior can be seen for most LEDs that were examined (Figures A.4 and A.5). Only the low intensity LEDs at the low end of the UV-spectrum seem to have no shift in the peak wavelength. During the measurements there was also one LED *XSL-355-5E*, where a second peak wavelength was introduced in pulsed mode. Causes for this behavior might have been due to a misalignment of the optical fiber of the spectrometer or by a faulty LED [97].
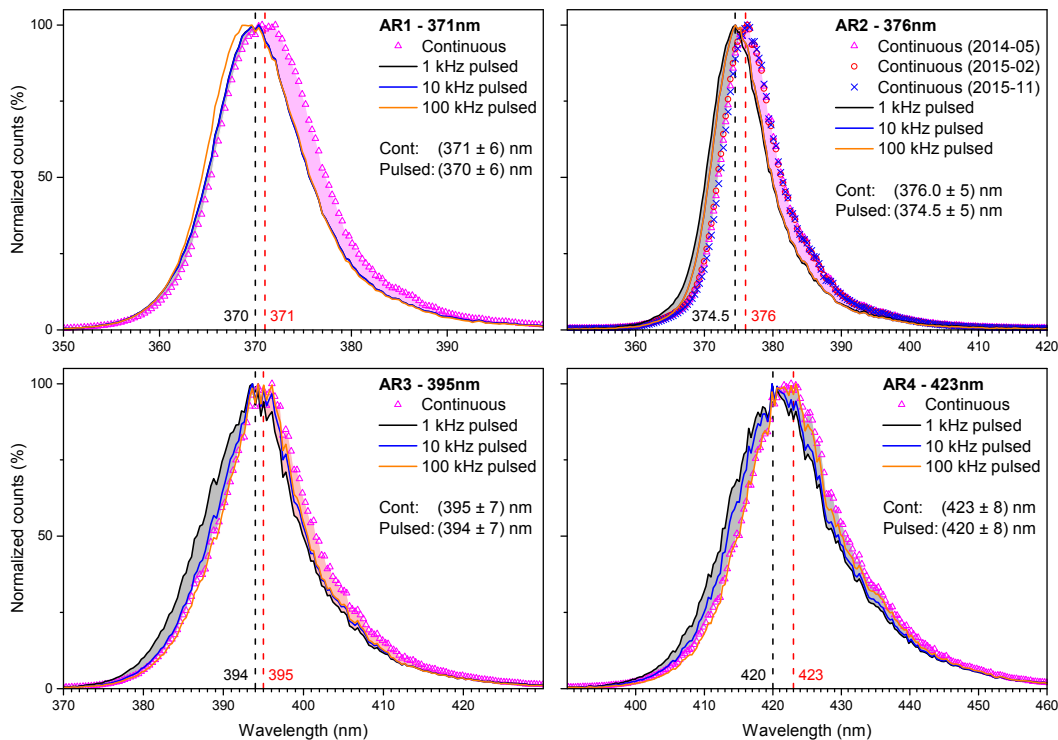
Figure 4.8: Measured continuous and pulsed spectra of LED-arrays AR1 to AR4. The aforesaid wavelength shift from pulsed to continuous mode is evident. Detailed versions can be found in Appendix A.1.

Figure 4.8 shows the measured spectra of the four LED-arrays AR1 to AR4. Here again the same behavior with a wavelength shift from lower to higher wavelengths, when going from pulsed mode to continuous mode, can be seen. The extracted peak wavelengths were taken for continuous mode and for 1 kHz, since these two modes will be used later, to measure collimator ratios and photodetectors. The wavelength spreads at half maximum height were read from the graphs for both operation

modes. If they were asymmetrical, the larger absolute value of both values for every operation mode was taken.

To conclude, both LED operation modes are similar in terms of wavelength spread (shape of the spectrum), although the main wavelength is shifted by 1 nm to 4 nm to higher wavelengths due to rising temperature of the LED junction in continuous mode. For further measurements this shift should not matter, since the uncertainty of the photodiodes in the wavelength is in the range of $\pm 6\,\%$ for 200 nm to 270 nm and in the range of $\pm 3\,\%$ for 270 nm to 950 nm [DS91]. These uncertainties are much larger than the introduced wavelength shift and are larger than the found spectral peak widths. Therefore, for all following measurements the systematic uncertainties in the wavelength will be given by the uncertainties of the photodiodes ($\pm 3\,\%$ of the measured wavelength for 270 nm to 950 nm).

4.3.3 *Integrating sphere*

The sphere used in this calibration set-up was chosen to be a *Labsphere 3P-GPS-053-SL*, a 3-port 13.5 cm diameter integrating sphere, with two 2.54 cm diameter exit-ports and a 6.35 cm diameter entrance-port [DS80]. This kind of sphere is a multipurpose integrating sphere and has the advantages of having ports of the right sizes, to be able to utilize them for our purposes, e. g. the entrance port can house a mount with many LEDs for high optical powers needed for the measurements of the collimator ratios. Between the entrance port and one of the exit ports (side port), a baffle is located, to block a direct light path to the respective exit port. To distribute light uniformly over the inner surface of the sphere, the sphere's inside is made of optical-grade *Spectralon SRM-99O* which reflects 98 % to 99 % of UV-light in the region of 300 nm to 430 nm and has a very flat reflectance over a wide range of wavelengths [106, DS107]. The 8° hemispherical spectral reflectance of Spectralon is shown in Figure C.14, i. e. the incident angle of the flux is 8° to the surface normal and the reflected flux is collected over the whole hemisphere [108]. The inset shows the UV part of the spectrum in more detail.

4.3.3.1 *Simultaneous exit–port flux*

The integrating sphere itself behaves as a splitter and a diffuser for the photons emitted by the LED-array. As shown before, the fraction of photons leaving the sphere from one port is proportional to the ratio of the port's area and the sphere's area (Equation 4.6) [76, 81]. Therefore, both equal-sized exit-ports emit the same number of photons N_{Sphere}, as seen from Equation 4.7. To check this, a simultaneous measurement of both exit-port powers was taken with two photodiodes and LED-array AR2 in continuous mode (Figures 4.9a and 4.10). The components to mount the photodiodes directly onto the ports are shown in Figures C.15 to C.17 [86]. The 3D-printed casing was added to fit the photodiodes without their filter into the aluminum mounts. The filter is an optional part, to reduce optical powers (incident on the photodiodes) that are too high and could damage the photodiodes. With this mount system the photodiodes are centered in the middle of the ports and their active detector area is fully illuminated by the flux from the exit-ports Figure 4.9b.
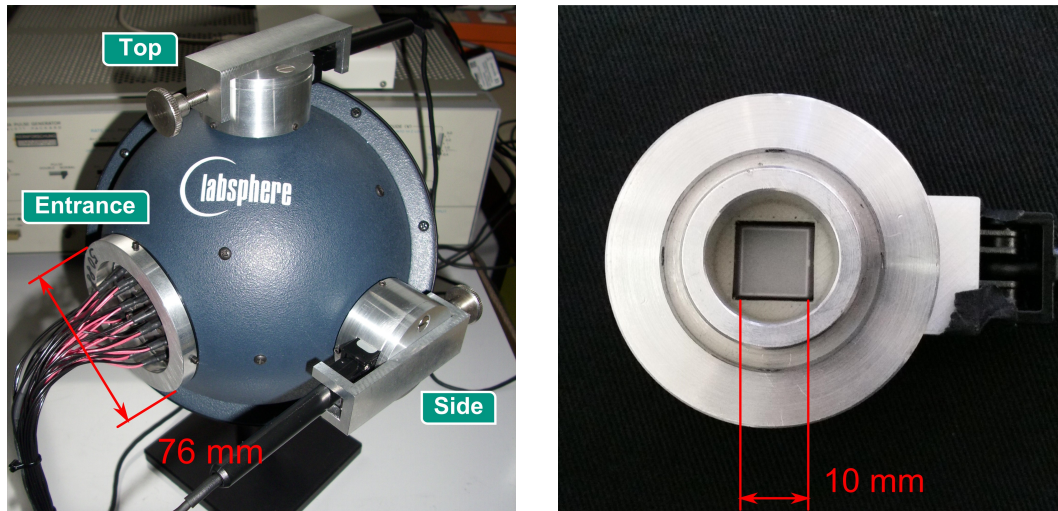
(a) Integrating sphere with attached LED-array and photodiodes.

(b) Photodiode inside mount and casing.

Figure 4.9: Photographs of the integrating sphere and one of a photodiode inside the mount. **(a)** The integrating sphere with the LED-array A (*entrance*) and two photodiodes (*top* and *side*) attached, for simultaneous exit-port flux measurements. **(b)** View onto the sensitive area (white square within the black frame) of the photodiode. The white plastic around that is the 3D-printed casing. The sensitive area is aligned to the center axis of the tube, which goes into the exit-port (Figures C.15 to C.17).

Figure 4.10 shows a sketch of the experimental set-up. Before the start of the measurements both photodiodes were set to zero, inside the photon shielding and with switched-off LEDs. Two 20 h measurements were taken with the photodiode-controller *Ophir Pulsar* [DS92] and *Ophir Starlab*, the software provided by the manufacturer of the photodiodes. The signals from the photodiodes are directly digitized by the controller and converted to optical powers by the measurement program (after providing the right wavelength to the program). The spectral responsivity of each photodiode is encoded in a micro-controller in the connector of each photodiode. The light source was in continuous mode with LED-array AR2, comprised of 20×3 mm UV-LEDs *XSL-375-3E* (Appendix C, Table C.3). A resistor of $91 \, \Omega$ is in series with this LED (Figure C.1b). The digital power source was set to 5.35 V at 400 mA, to correspond to a wavelength of 377 nm. There was no temperature measurement inside the photon shielding, however the climate control of the room was set to 24 °C. To distinguish both photodiodes, they are named after the last part of their serial numbers (*655738* and *655739*): *PD 38* and *PD 39*. For measurements, where the channel varies that each photodiode is connected to, the letters *A* and *B* are assigned to the photodiodes by the measurement program *Ophir Starlab*, e. g. Figure 4.11. The baffle is between the entrance-port and the side-port. To rule out any position dependent effects, the photodiodes were swapped together with their mounts after the first measurement.

Figure 4.11 shows the results from the simultaneous measurements of the optical powers emitted by the exit-ports. Due to the current running through the LEDs, they undergo a warming effect in continuous mode. This leads to a decrease in
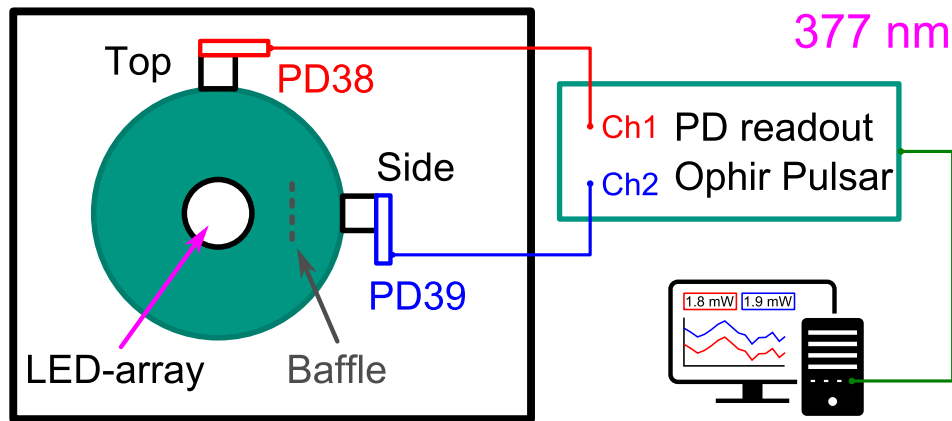
Figure 4.10: Sketch of the simultaneous exit-port flux measurement. Both photodiodes are directly mounted to the exit-ports with their respective mount and casing.

the emission power during the warm-up. This can be seen in the graphs. Therefore, the first hour of both data sets was masked for the calculation of an average power. Both plots show the optical power measured by each photodiode versus time and the 1.6 % calibration error (systematic error), given by the manufacturer for the photodiodes and their controller. The certificates of calibration can be found in Appendix C.1.3.1. Since the statistical errors are very small, they are not shown.

Figure 4.11a shows the data for *A 38* at the side and *B 39* at the top. The data from both photodiodes has the same behavior over time, except for an average offset in optical power of roughly 0.09 mW. During the initial warm up of 15 min, the emitted optical power drops by roughly 0.1 mW. After one hour the emission stabilized around 1.74 mW and 1.84 mW. After almost one hour of stable optical emission, the optical power rises during the course of 6 h to 1.78 mW and 1.87 mW. There it stays stable until the end of the measurement. This increase in optical power emission could be due to a temperature drop at nightfall that influenced the LEDs or the power supply. However, temperature was not monitored during this measurement.

Figure 4.11b shows the data for *PD A 38* at the top and *PD B 39* at the side, after swapping the positions of the photodiodes. Both photodiodes again exhibit the same behavior over time, except for the 0.09 mW offset also seen before. After the warm-up the optical power stays directly at the stable values of 1.80 mW and 1.89 mW. From the same behavior during both measurements the conclusion is drawn that the difference in measured power by the photodiodes is not dependent on the position of the photodiodes. It either comes from the photodiodes themselves, the channels used with the photodiode-controller or the mounts of the photodiodes. A second conclusion is that the light source is stable in terms of emitted optical power, after the initial warm-up phase.
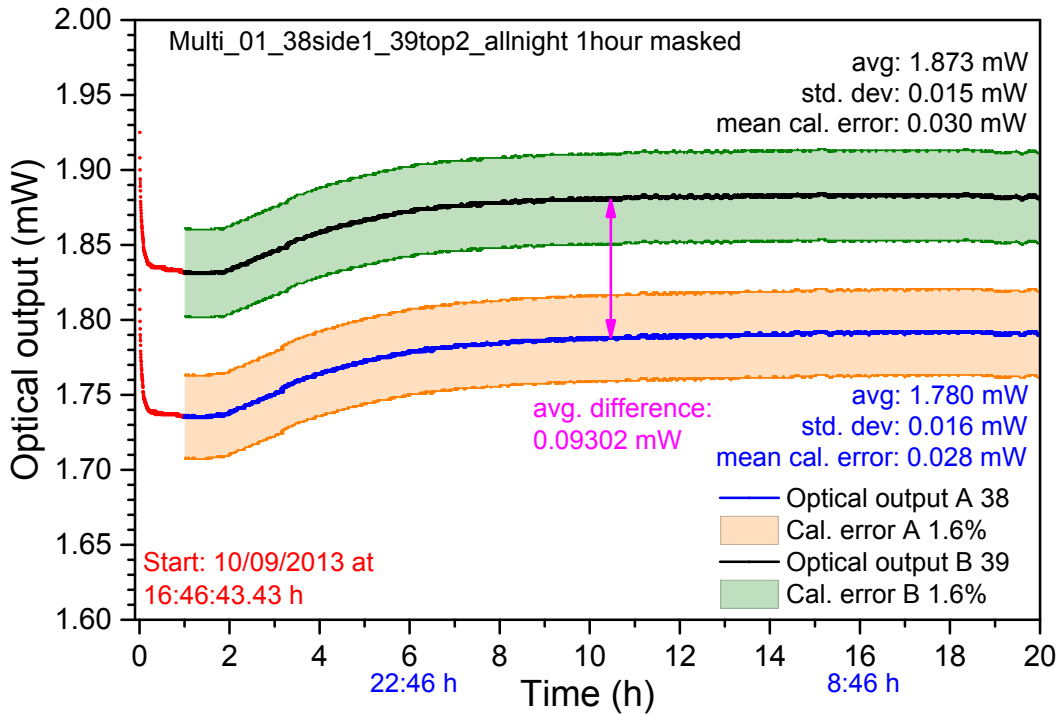
(a) Flux at both photodiodes - measurement 1.
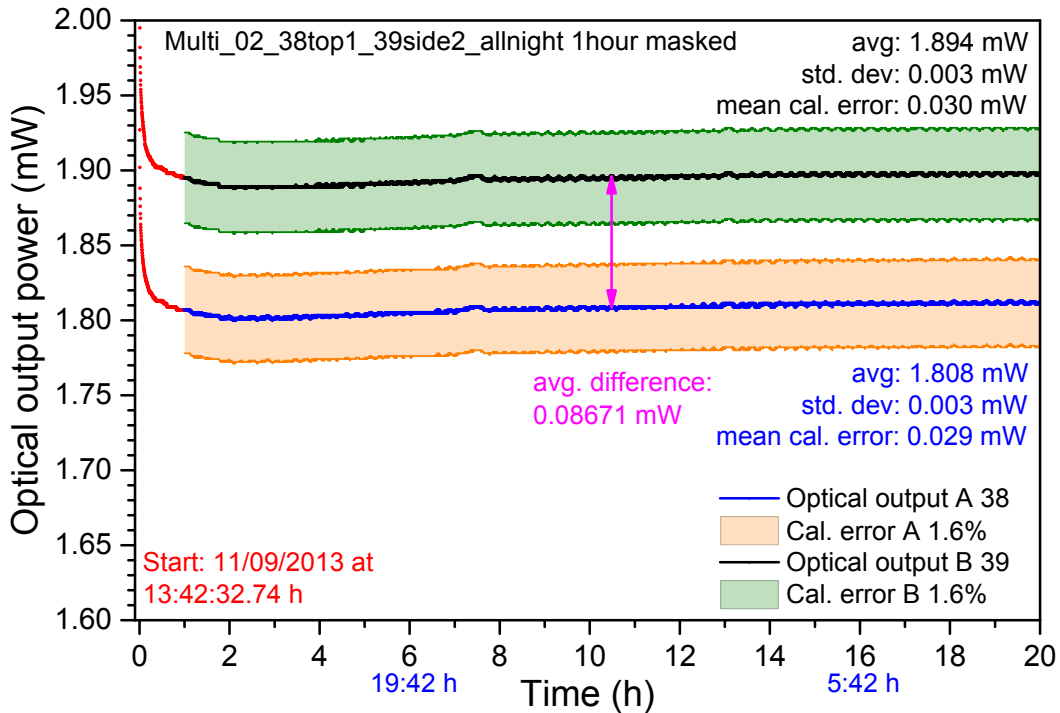
(b) Flux at both photodiodes - measurement 2.

Figure 4.11: Measurements of the optical power at each photodiode versus time. Additionally the systematic error is shown. The measurements were done in continuous mode with LED-array AR2, emitting light with 376 nm (Table C.3). **(a)** Measurement of photodiode *A 38* at the side port and photodiode *B 39* at the top port. **(b)** Measurement of photodiode *B 39* at the side port and photodiode *A 38* at the top port.

4.3.3.2 *Uncertainty calculations of optical powers*

The photodiodes measure optical powers and give mean values P for each measurement. Together with these the standard deviations σ_P are given by the measurement program:

P   mean optical power,

σ_P standard deviation of the mean optical power.

The systematic errors of the optical powers are given in the calibration certificates (Appendix C.1.3.1) for the photodiodes (1.5 % for wavelengths below 400 nm and 0.4 % for wavelengths over 400 nm) and their controller (0.1 % for all wavelengths). They amount to

$$\Delta_P = 1.6\,\% \cdot P \qquad \text{for} \quad \lambda < 400\,\text{nm} \quad \text{and} \tag{4.8}$$
$$\Delta_P = 0.5\,\% \cdot P \qquad \text{for} \quad \lambda > 400\,\text{nm} \quad .$$

4.3.3.3 *Position dependent exit–port flux*

To check if the exit-port flux is really independent of the position of the photodiodes as well as the used controller channel, the following measurement was taken. One of the photodiodes was directly attached to one exit-port with its respective mount and casing, while the other exit-port was closed with a Spectralon coated lid (Figure B.3). Before the measurement both photodiodes were set to zero within the dark environment of the photon shielding. Light was generated with LED-array AR2 in continuous mode. After an hour of warm-up, the measurements were taken for 15 min each. For every measurement either the channel or the position of each photodiode (together with its respective mount and casing) was switched. A sketch of the set-up is shown in Figure 4.12.
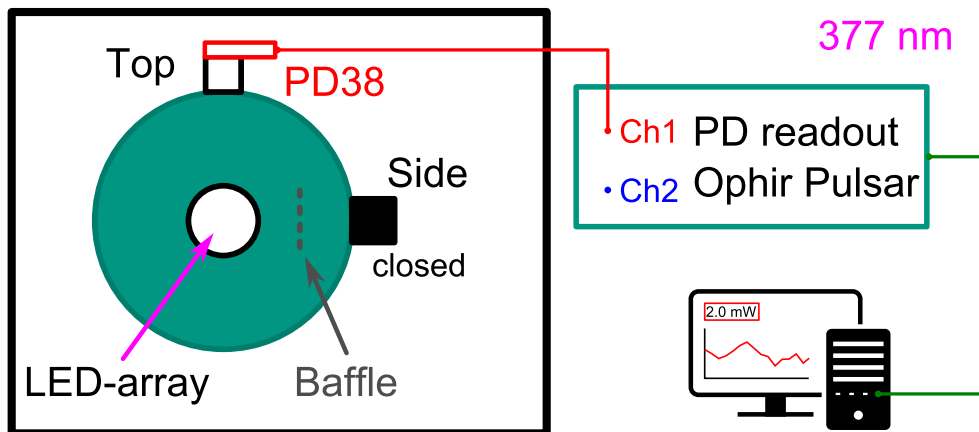
Figure 4.12: Sketch of the position dependent exit-port flux measurement with one photodiode. Both photodiodes are used at different channels (*channel 1* and *channel 2*) and different positions (*top* and *side*), one at a time. The read-out is done with the photodiode-controller and the measurement computer.

Figure 4.13 shows the visualization of the measured data. Shown is the measured optical power versus different positions and channels for each photodiode *PD38* and *PD39*. Here the full series number is used for identification, since the letters *A* and *B* from before are associated with the two channels of the photodiode-controller. For every measurement the standard deviation as well as the 1.6%-calibration error are shown. The statistical error after 15 minutes of measurement is very small with this light level and the systematic calibration error is always dominant. Photodiode *PD39* measures higher optical powers in all positions. Evidently the used channel as well as the position on the sphere have no influence on the readings. The two remaining possibilities for different readings are either that the photodiodes are calibrated differently or that the respective mounts of the photodiodes are different. Measurements examining these possibilities are shown in Sections 4.3.4.1 to 4.3.4.3.
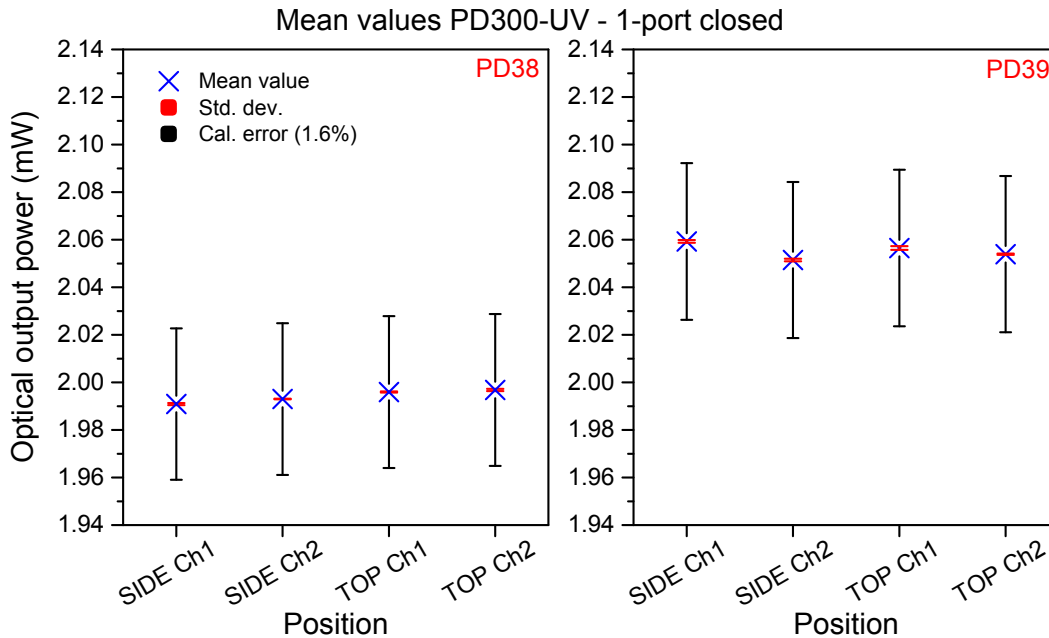
Figure 4.13: Measurements of the position dependent exit-port flux for both photo-diodes (*PD38* and *PD39*) at different channels (*channel 1* and *channel 2*) and different positions (*top* and *side*). Photodiode *PD39* measures higher optical powers in all positions.

The calibration errors of 1.6% for each photodiode are in a range, were the uncertainty in the PDE measurements Δ_ϵ are sufficiently small for calibration measurements of photodetectors. An estimation of the systematic errors, introduced by this uncertainty is as follows. The quantities that depend on the power measurement of the photodiodes are the number of sent photons N and the collimator ratio R. The wavelength uncertainty of the photodiodes can also be taken into account (Equation 4.1). The PDE is the only quantity that is influence by these measurements, since the gain is only dependent on the measured charges. As will be thoroughly explained in Section 4.3.3.5, the systematic errors in the photon number, the wave-

length, and the collimator ratio propagate in the systematic error of the PDE. The relative systematic uncertainties are as follows:

$$\Delta_P = 1.6\,\% \cdot P \quad ,$$
$$\Delta_R = \sqrt{2} \cdot 1.6\,\% \cdot R \quad , \text{ and}$$
$$\Delta_\lambda = 3\,\% \cdot \lambda \quad .$$

The relative change in the photon number is then given by:

$$\frac{\Delta_N}{N} = \sqrt{\left(\frac{\Delta_P}{P}\right)^2 + \left(\frac{\Delta_R}{R}\right)^2 + \left(\frac{\Delta_\lambda}{\lambda}\right)^2} \approx 4.1\,\% \quad .$$

For a photon number N of two photons, the absolute error would be 0.082 photons. For higher photon numbers in the range of the night sky background, as measured by EUSO-Balloon, we get: $(500 \pm 21_{sys})$ photons for photodiode-only related uncertainties. To get an estimation for the PDE, we use Equation A.12 in Appendix A.5.2. The number of detected photons is not dependent on the photodiode measurements and the wavelength, but only on the charge measurements. When only considering the photodiode measurements it follows:

$$\Delta_\epsilon = \frac{\Delta_N}{N} \cdot \epsilon = 4.1\,\% \cdot \epsilon \quad .$$

For an arbitrary chosen PDE of 31.0\,% this would yield: $(31.0 \pm 1.3_{sys})\,\%$, for photodiode-only related uncertainties. This is sufficiently small for calibration measurements of photodetectors. This systematic error can be further reduced by using the wavelength uncertainties that were measured from the LED emissions with the spectrometer (Section 4.3.2.2) and are in the range of 1.3\,% to 1.9\,%, depending on the individual wavelength (Table C.3). This results in a relative systematic uncertainty of the PDE of 3.1\,% to 3.4\,%.

4.3.3.4 *Changing optical power levels*

To test the behavior of the integrating sphere with different light levels, the following measurement was taken. The set-up was identical to the set-up shown in Figure 4.10. For this measurement the positions of the photodiodes were fixed and the whole sphere was attached to the translation stages, resulting in a 90° tilt of the light source. Because of that the *top-port* is from now on called *front-port*. Before the first measurement both photodiodes were set to zero within the dark environment of the photon shielding. For every data taking a different number of LEDs were switched on in continuous mode and before starting each measurement we waited for the warm-up phase. The configurations of the LED-array AR2 can be seen in Figures C.12 and C.13. Theoretically, no changes of the ratio with different light levels are expected, when using the sphere alone. Therefore, this measurement was done in preparation for measuring the different collimator ratios with different light levels (Section 4.3.5.2).

Figure 4.14 shows two graphs. The upper one gives the average exit-port fluxes measured with photodiode *A 39* at the side port and photodiode *B 38* at the front-port versus the different configurations of the LED-array AR2. Every data point for one configuration is the the average value of a 15 min measurement. The statistical errors are not shown in the graphs, since they are too small. The systematic errors (1.6 % calibration error) for every data point are shown in black. As seen before both photodiodes measure slightly different optical powers. As expected, with fewer LEDs switched on, both measured optical powers decline.
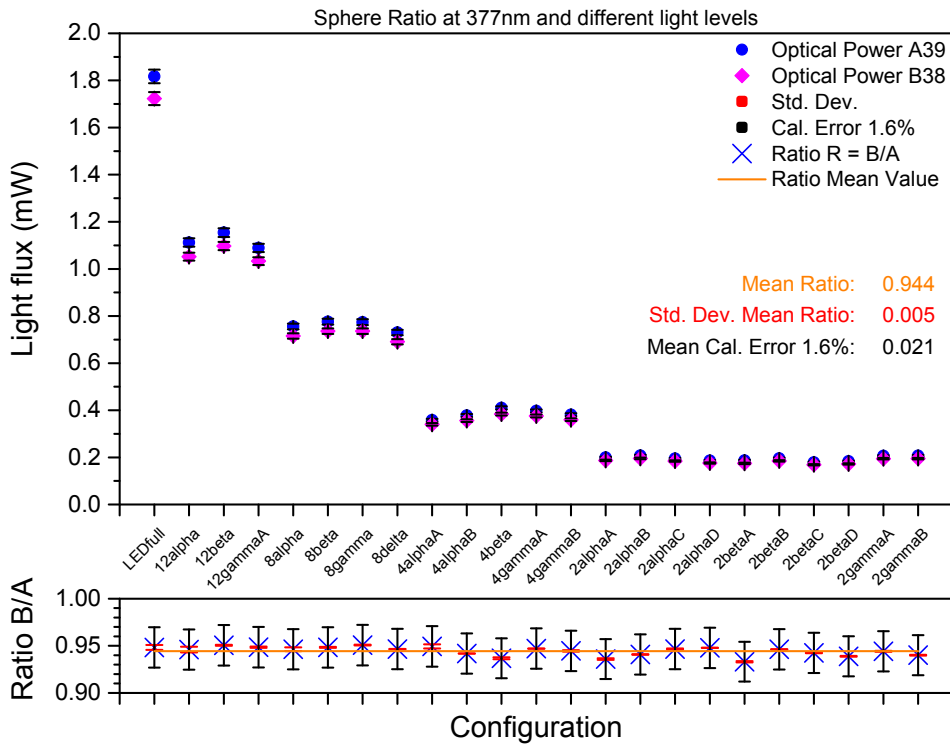
Figure 4.14: Graphs of the sphere exit-port fluxes and their ratio for different light levels. The different array configurations can be found in Figures C.12 and C.13. The number of the array configuration gives the number of LEDs switched on. For fewer LEDs the exit-port fluxes become smaller, but the ratio stays stable, as expected.

The lower graph shows the ratio $R = \frac{B\,38}{A\,39}$ for the different configurations (light levels). The single ratios for every pair of optical powers, as well as their statistical errors (red) and systematical errors (black) are shown. Both errors per data point were calculated via the variance formula (error propagation of independent variables), shown in Equations (4.9) and (4.10). As a horizontal line (orange) the overall mean ratio of both fluxes is drawn. Its numerical value R, its standard deviation σ_R, and the mean calibration error Δ_R (mean of all single calibration errors) are also given.

In conclusion the sphere is behaving as expected, although both exit-port fluxes were still off by about 6 %. With different light levels the ratio of both exit-port fluxes stays constant, if the fluxes are high enough for a good signal to noise ratio of the photodiodes. For the tested light levels, the statistical errors are negligible

for measurements of 15 minutes and longer. The systematic errors in the optical power measurements and the derived systematic errors in the collimator ratios are sufficiently small for calibration measurements, as shown in the previous section. If comparing configurations with the same number of LEDs, a slight difference in the light flux can be seen. Configurations with more central LEDs switched on produced higher fluxes than configurations with LEDs nearer to the outer part of the LED-array. Since this behavior is reflected in both exit-ports, this is not an issue. The next section will give details about the uncertainty calculations for ratios. Afterwards, details about the photodiodes will be given and we will deal with the open questions about the different light flux from both exit-ports.

4.3.3.5 *Uncertainty calculations of optical power ratios*

The photodiodes measure optical powers and give mean values P_a and P_b for each one. Together with these also the standard deviations σ_{P_a} and σ_{P_b} are given by the measurement program. The measurement program can also directly save the mean ratio $R = \frac{P_a}{P_b}$ and its standard deviation σ_R. The observable are:

P_a	P_b	mean optical powers per measurement,
σ_{P_a}	σ_{P_b}	standard deviation of the mean optical powers,
$R = \frac{P_a}{P_b}$		mean ratio of the optical powers per measurement,
σ_R		standard deviation of the mean ratio per measurement.

If the ratio R was not saved during measurement, the *statistical error* (standard deviation) of the ratio has to be calculated via the standard error propagation of independent variables [109]:

$$
\begin{aligned}
\sigma_R &= \sqrt{\left(\frac{\partial R}{\partial P_a} \cdot \sigma_{P_a}\right)^2 + \left(\frac{\partial R}{\partial P_b} \cdot \sigma_{P_b}\right)^2} \\
&= \sqrt{\left(\frac{1}{P_b} \cdot \sigma_{P_a}\right)^2 + \left(-\frac{P_a}{P_b^2} \cdot \sigma_{P_b}\right)^2} \quad .
\end{aligned}
\tag{4.9}
$$

The *systematic errors* of the optical power ratio is calculated in the same way, via the error propagation of independent variables, with the wavelength dependent calibration error (Equation 4.8). Since both relative calibration errors are the same for both photodiodes, we use:

$$
\begin{aligned}
\Delta_R &= \sqrt{\left(\frac{\partial R}{\partial P_a} \cdot \Delta_{P_a}\right)^2 + \left(\frac{\partial R}{\partial P_b} \cdot \Delta_{P_b}\right)^2} \\
&= \sqrt{\left(\frac{1}{P_b} \cdot 1.6\,\% \cdot P_a\right)^2 + \left(-\frac{P_a}{P_b^2} \cdot 1.6\,\% \cdot P_b\right)^2} \\
&= \sqrt{(-R \cdot 1.6\,\%)^2 + (R \cdot 1.6\,\%)^2} = \sqrt{2} \cdot 1.6\,\% \cdot R \quad .
\end{aligned}
\tag{4.10}
$$

If i measurements are taken with the same collimator and the single mean values for the ratio R_i or the single optical powers P_i are not strongly deviating from each other[2], i.e. differences in R_i are smaller than the individual systematic errors Δ_{R_i}, then the overall collimator ratio and its uncertainties are calculated via:

$$R = \frac{R_1 + R_2 + \cdots + R_i}{i} \quad ,$$

$$\sigma_R = \text{StdDev} (R) \quad ,$$

$$\Delta_R = \frac{\Delta_{R_1} + \Delta_{R_2} + \cdots + \Delta_{R_i}}{i} \quad . \tag{4.11}$$

4.3.4 *Photodiodes*

The previous section discussed details about the integrating sphere and measurements that were taken to characterize the behavior of said sphere. There was a discrepancy between the fluxes of two identical exit-ports. The conclusion, after switching the photodiodes, was either that the photodiodes measured different values or that the mounts of the photodiodes were different. The following section will address that issue with measurements that were taken to test the photodiodes. This is very important, since the photodiodes are the reference sensors used to estimate the light flux emitted by the integrating sphere. In order to know the number of photons emitted by the light source, one has to know the flux emitted by the integrating sphere very precisely. Therefore, the reference photodiodes have to be tested very carefully. Before every measurement the photodiodes were set to zero in the dark environment of our photon shielding. The LED-array were also kept on for a certain time before the start of the measurements to get rid of warm-up effects.

4.3.4.1 *Photodiode calibration with a NIST–photodiode*

The following measurement was taken to calibrate our reference photodiode *A 39* (in the following named *OphirPD39*) with a NIST-calibrated photodiode *OSI Optoelectronics UV-100* (named *NIST*). The cover letter of the calibration report of the *NIST* is shown in Figure C.21. The full calibration report with 9 pages is present at the Institute for Nuclear Physics (IKP) - KIT [110]. The read-out of the *NIST* is done directly via a *Keithley 6485 Picoammeter* [DS111, DS112]. The measured current can be converted into an optical power per square centimeter by the following equation:

$$P_{\text{NIST}} = I \cdot \frac{1}{R_{\text{NIST}}^{\lambda}} \cdot \frac{1}{A_{\text{NIST}}} \quad , \tag{4.12}$$

where

---

2 Otherwise refer to Appendix A.3.

P_{NIST} is the optical power per square centimeter,

I is the measured current,

R^{λ}_{NIST} is the responsivity factor at a certain wavelength λ, and

A_{NIST} is the sensitive area of the *NIST*.

For this measurement the set-up shown in Figure 4.15 was used. In a distance of more than three or four exit-port diameters (for the size of our photodiodes) the integrating sphere works as a uniform light source [81]. Therefore, two photodiodes with differently sized sensitive areas can be compared, if they are located at the same distance and on the optical axis. For larger distances the errors in distance measurements as well as tilting errors become smaller in comparison to the whole distance. The chosen distances for this calibration were between 100 cm to 200 cm in a big dark room of the research group. The overall darkness there is not as high as inside SPOCK but for a calibration of photodiodes it is sufficient. LED-array AR2 was attached to the integrating sphere to produce continuous light. Both photodiodes were set to measure a wavelength of 377 nm.
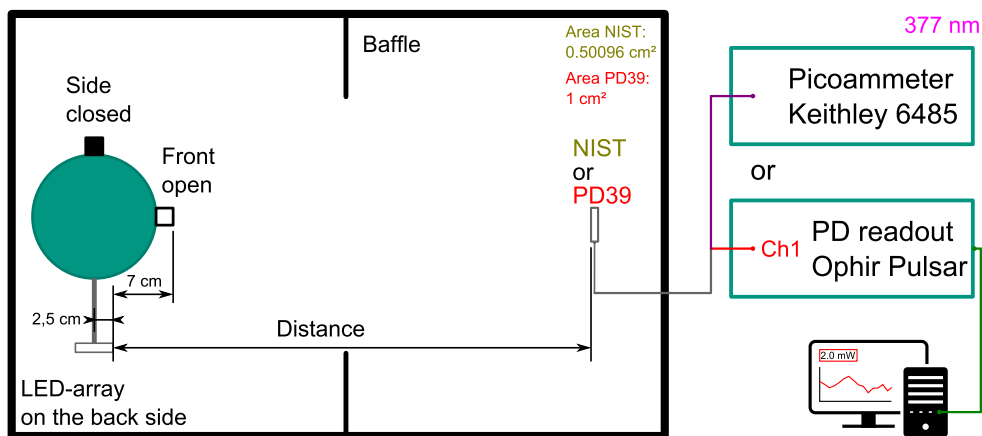
Figure 4.15: Sketch of the set-up for the calibration of the *Ophir* photodiode *A 39* with a NIST-calibrated photodiode *OSI Optoelectronics UV*-100 [DS111]. The full calibration report with 9 pages is present at the IKP - KIT [110].

With one closed port and one open port the sphere was put onto an optical rail in a darkroom and a baffle was placed between the open port and the position of the photodiodes. The baffle had an opening of roughly 20 cm to reduce scattered light during the measurement. The distance of the exit-port and the sensitive areas of both photodiodes was measured with a tape measure. This had to be done sequentially for both photodiodes, since both could not be mounted on the optical axis and at the same distance at the same time. Great care was taken to align the photodiodes orthogonal to the optical axis and to have both sensitive areas at the same distance. For different distances automated current measurements (*NIST*) and power measurements (*OphirPD39*) were taken for 10 min each.

For the optical power calculations via Equation 4.12 the sensitive area of the *NIST*-photodiode as well as the responsivity factor at 377 nm have to be known. The sensitive area A_{NIST} of the *NIST* was very well defined by an aperture of $(50.096 \pm 0.067_{sys})$ mm^2 area in front of the *NIST*. The picoammeter, the *NIST*, its

datasheet, and its calibration report were already available at the IKP - KIT [110]. The data points for the spectral power responsivity were taken from the *NIST* calibration report (Figure C.21) and plotted in Figure C.22. The missing responsivity factor at 377 nm and its systematic error were determined via an interpolation of the given values. It follows that $R_{NIST}^{377} = (0.13206 \pm 0.00120_{sys})\,A\,W^{-1}$. This systematic error is gained by interpolation from the nearest data points given and corresponds to a 0.91 % error. The systematic error in the current Δ_I is given in the datasheet of the picoammeter *Keithley* 6485 for the 200 nA range as $\Delta_I = 0.2\,\% \cdot I + 10\,pA$ [DS112]. It follows:

$$\Delta_{P_{NIST}} = \sqrt{\left(\frac{P_{NIST}}{I} \cdot \Delta_I\right)^2 + \left(-\frac{P_{NIST}}{R_{NIST}^{377}} \cdot \Delta_{R_{NIST}^{377}}\right)^2 + \left(-\frac{P_{NIST}}{A_{NIST}} \cdot \Delta_{A_{NIST}}\right)^2} \quad .$$

The optical power of the *NIST* was calculated via the mean value of the measured current (for every distance). The standard deviation σ_I of this mean current value provided the statistical error of the optical power for a certain distance via the error propagation formula. For the aperture and the responsivity factor no statistical errors were known and therefore not included. As a consequence the error propagation for the statistical error of the optical power is as follows:

$$\sigma_{P_{NIST}} = \frac{P_{NIST}}{I} \cdot \sigma_I \quad .$$

For *OphirPD39* the optical power measured did not need a correction factor, since the sensitive area is exactly $1\,cm^2$. Also the controller of that photodiode directly converts the measured current into an optical power. The mean optical power and its standard deviation are easily calculated (and in this case given by the measurement program). The calibration error of 1.6 % gives again the same systematic error for our *Ophir* photodiode (Equation 4.8).

Figure 4.16 shows the resulting mean optical powers per square centimeter of the *NIST* and the *OphirPD39* versus the distance. For simplicity the statistical and systematic errors are not shown. They are so small that their boundaries all would lie within the symbols of the data points. For three of the measurements with *OphirPD39* the standard deviations were measured to be zero and thus we suppose that fluctuations were below the resolution of the photodiode (20 pW) [DS91]. Therefore, 20 pW was applied as the statistical standard deviation of these three measurements. This should also be no problem, since the systematic errors are dominating the uncertainties. A clear decrease in optical power with larger distances is evident. Also it seems that both photodiodes have the same behavior and almost all data points lie on top of each other. The only exception seems to be the first data point were the powers are separated. To further compare both photodiodes, two fits of $y = a \cdot x^b$ (one for each photodiode) are shown. The data points were weighted with their respective systematic errors in the optical powers. Since both adjusted R-square values are very close to one, the chosen fits are correct and show that the optical power decreases with the square of the distance (minus two as exponent). That shows that this measurement was done with uniform illumination.
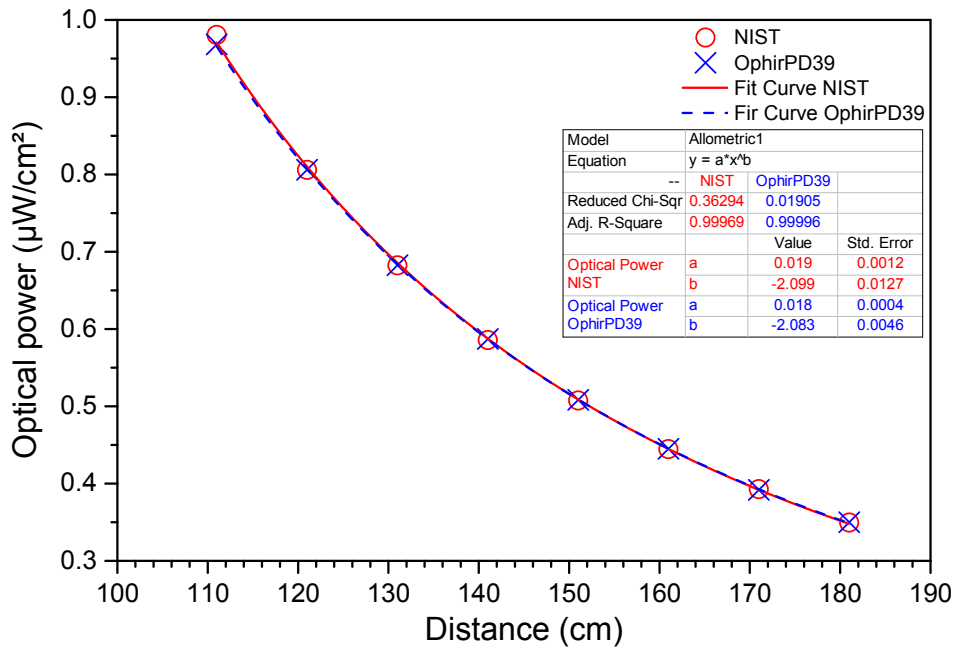
Figure 4.16: Measured optical power of the *NIST* and the *OphirPD39* versus the distance from the light source exit-port. Error bars are too small to be shown. Both sets of data are almost on top of each other, the only exception being the first pair of data at 110 cm. Each set of data points was fitted with a power law.
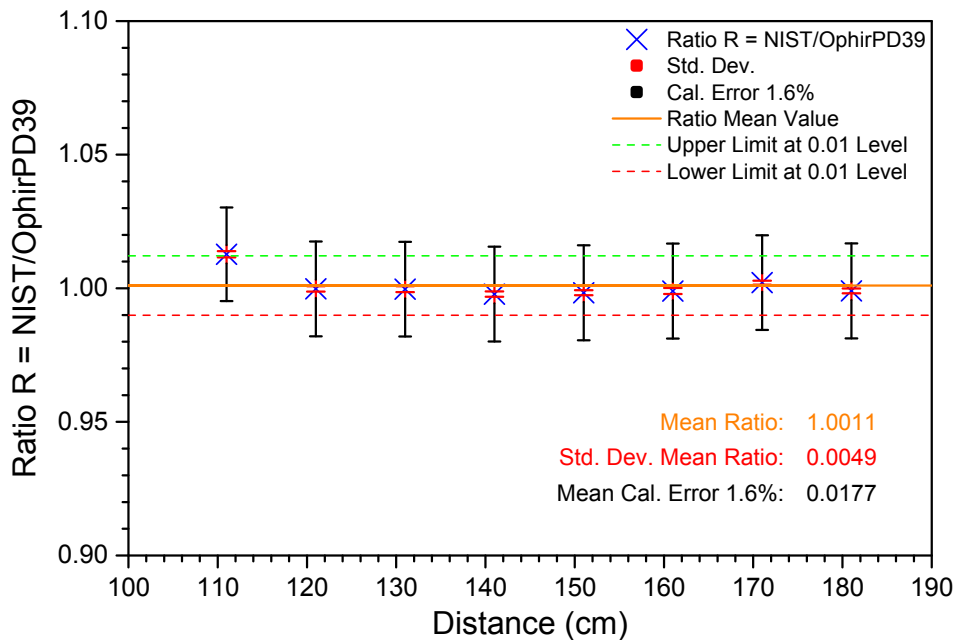
Figure 4.17: Ratio of the optical power from the *NIST* and the *OphirPD39* versus the distance. Shown are the statistical and systematic errors of each ratio as well as an overall mean ratio and the limits for a Grubbs' test for outliers at the 0.01 level. The first ratio at 110 cm is a significant outlier and not used for the mean ratio calculation.

Figure 4.17 shows the ratios of both optical powers versus the distance for a better comparison of both photodiodes. Here also the statistical and systematic errors

of the single ratios are shown. They were both calculated via the error propagation formula, similar as shown in Equations (4.9) and (4.10). The mean ratio R is shown as an orange horizontal line. It was calculated as the mean value from all ratios R_i, as shown before in Equation 4.11. The standard deviation of the mean ratio σ_R is used as its statistical error. The systematic error of the mean ratio Δ_R is calculated as the mean value of the individual systematic errors: $\Delta_R = \text{Mean}(R_i)$. This yields $1.0011 \pm 0.0049_{\text{stat}} \pm 0.0177_{\text{sys}}$ for the ratio of *NIST* and *OphirPD39* (for all data points shown in Figure 4.17). When comparing the first data point with the other data points it seems to be an outlier. Therefore, with *OriginPro 2015* a Grubbs' test for outliers at the 0.01 level was performed [113]. The upper and lower limit of that test are shown in the graph. The first data point is just outside the limits and thus is a significant outlier that should not have been taken into account for the mean ratio calculation.
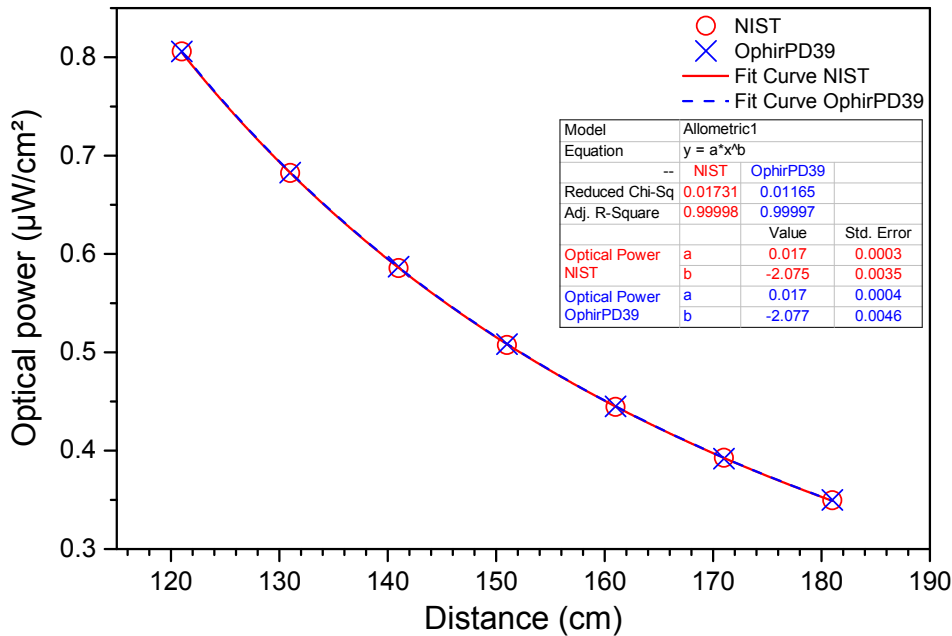
Figure 4.18: Graph of the measured optical power of the *NIST* and the *OphirPD39* versus the distance from the light source exit-port. For this graph the first pair of data at 110 cm was masked. Therefore, both sets of data are on top of each other. Each set of data points was fitted with a power law.

For comparison Figure 4.18 shows the same data as Figure 4.16, but with the outlier data being masked. Therefore, the parameters of both fits are more similar than before and reproduce the measured data better than before. The mean ratio of both optical powers became $0.9994 \pm 0.0014_{\text{stat}} \pm 0.0178_{\text{sys}}$. So it was slightly shifted to a lower value. The statistical error was reduced by a factor of 5, while the systematic error stayed the same. For these corrected data points the standard deviation of the mean ratio is only a bit bigger than the mean of the individual standard deviations (factor 1.3). *In conclusion, at 377 nm the photodiode* OphirPD39 *(PD 39) is a NIST-calibrated photodiode.*

4.3.4.2 *Photodiode cross–calibration*

With the previously seen discrepancy in optical power between our photodiodes *PD 38* and *PD 39* the question was still unanswered if they were measuring correctly or if their mounts were different. With the calibration of *PD 39* with a NIST-photodiode described in the previous section a cross-calibration of *PD 38* can be done. Thus it can be answered if both photodiodes measure the same optical powers. The principle of this measurement was the same as previously shown in Figure 4.15. This time with *PD 38* and *PD 39*. For the measurement LED-array AR2 in continuous mode was used. Since both photodiodes are identical they were each mounted with identical mounts on slides that can be freely adjusted on an optical rail. This rail is on the optical axis of the system. A third slide was used as a stopper to guarantee that both photodiodes had the same distance to the light source, resulting in the exact same position. Since the stopper was used, the absolute distance was not measured. Both photodiodes were read out via their controller which directly gives the optical powers to the measurement software. For two different positions on the optical axis data was taken for 15 min for each photodiode. The resulting values are shown in Table 4.1.

Table 4.1: Data measured during the cross-calibration of *PD 38* and *PD 39* at four wavelengths (LED-array AR1 to AR4) and at two different positions on the optical axis. The optical power, the standard deviation (statistical error), and the 1.6 % calibration error (systematic error, Equation 4.8) are given.

ARRAY	POS.	PD	OPT. POWER ($\mu W/cm^2$)	STD. DEV. ($\mu W/cm^2$)	SYS. ERROR ($\mu W/cm^2$)
AR1	1	PD 38	19.38	0.01	0.31
AR1	1	PD 39	19.36	0.01	0.31
AR1	2	PD 38	2.92	0.02	0.05
AR1	2	PD 39	2.95	0.02	0.05
AR2	1	PD 38	16.63	0.19	0.27
AR2	1	PD 39	16.67	0.18	0.27
AR2	2	PD 38	2.44	0.01	0.04
AR2	2	PD 39	2.47	0.01	0.04
AR3	1	PD 38	26.96	0.06	0.43
AR3	1	PD 39	27.05	0.06	0.43
AR3	2	PD 38	4.14	0.08	0.07
AR3	2	PD 39	4.18	0.08	0.07
AR4	1	PD 38	14.14	0.02	0.23
AR4	1	PD 39	14.16	0.02	0.23
AR4	2	PD 38	2.11	0.01	0.03
AR4	2	PD 39	2.12	0.01	0.03

From the measurement data it is evident that both photodiodes measure the same optical power at the same position and that the systematic errors are dominating the uncertainties. Therefore, we can be sure that both photodiodes are identical for the four wavelengths measured. To conclude *PD 38* and *PD 39* are NIST-calibrated

photodiodes and the differences that were measured before should be because of the different mounts or casings.

4.3.4.3 *Check of photodiode mounts and casing*

The last issue with the exit-port fluxes of the sphere and the photodiodes were whether the different power readings at different positions of the sphere are an effect of the photodiodes themselves or of the mounts (see in Section 4.3.3.3). In combination with the previous cross-calibration of both photodiodes with a NIST-photodiode, it is evident that the mounts or the casings are different. To test this the same set-up as displayed in Figure 4.12 was used. Each photodiode was placed into one of the mounts (*M 38* and *M 39*) with one of the casings (*C 38* and *C 39*) (see Figures C.15 to C.17). Here the names indicate with which photodiode the mounts and casings were used in the first time. Accordingly the mounts and casings were named and marked. Each photodiode was placed with all different combinations of mounts and casings to the front-port of the integrating sphere. The side-port was closed with a reflecting lid. The light was generated by LED-array AR2 in continuous mode at a wavelength of 377 nm. Before the measurements both photodiodes were set to zero within the photon shielding. Each measurement of 10 min was started after the warm-up phase of the LED-array.

Table 4.2: Data measured during the permutation of all mounts, casings, and photodiodes. The different configurations (photodiode, the mount, and the casing) are given for every 10 min long measurement. The optical power, the standard deviation (statistical error), and the 1.6 % calibration error (systematic error, Equation 4.8) are given.

CONFIGURATION			OPT. POWER (μW)	STD. DEV. (μW)	SYS. ERROR (μW)
PD 38	M 38	C 38	1 891	0.39	30.26
PD 39	M 38	C 38	1 897	0.60	30.36
PD 38	M 38	C 39	1 861	0.18	29.78
PD 39	M 38	C 39	1 876	0.47	30.02
PD 38	M 39	C 38	2 003	0.31	32.05
PD 39	M 39	C 38	2 018	0.31	32.29
PD 38	M 39	C 39	1 987	0.68	31.80
PD 39	M 39	C 39	2 009	4.30	32.14

Table 4.2 contains the measured data for the different configurations. As before the optical power, the standard deviation (statistical error), and the 1.6 % error (systematic error, Equation 4.8) are given. From the measured values one can identify two regions of optical powers that seem to coincide with both mounts. Both mean optical powers calculate to $P_{M38} = (1881.43 \pm 16.32_{\text{stat}} \pm 30.10_{\text{sys}})\,\mu W$ and $P_{M39} = (2004.17 \pm 12.80_{\text{stat}} \pm 32.07_{\text{sys}})\,\mu W$. The statistical error is the standard deviation of the mean optical power and the systematic error is the mean of the single calibration errors. From these the ratio of the optical powers of both mounts calculates to $0.9388 \pm 0.0115_{\text{stat}} \pm 0.0241_{\text{sys}}$. Both errors were calculated via their respective error propagation formulas with the errors above. This ratio is within its

errors in the range of the ratio measured before (Section 4.3.3.4 and Figure 4.14). Additionally, there also seems to be a slight discrepancy between both casings.

We conclude that both photodiodes were proven to measure identical optical powers if they are at the same distance from the light source and are illuminated uniformly. If they are mounted with their respective mounts and casings to the integrating sphere, there is an offset of around 6 %. This offset is due to the different height of the mounts and the casings. With this all but one part of the light source have been characterized. The last part missing is the collimator. It will be addressed in the next section.
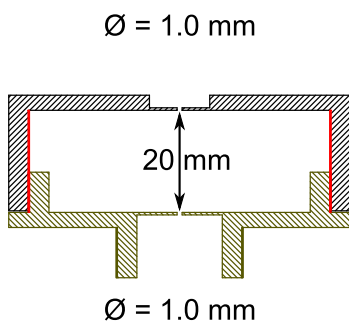
4.3.5 *Collimator*

With all the previous measurements the LED-arrays, the integrating sphere, and the photodiodes are fully characterized. Now the collimators can be measured very precisely. This section will contain the working principle of the collimator, a list of the present available collimators for SPOCK, an example calculation to estimate the collimator ratio, and all the measurements done to characterize the collimators.

The collimators used during this work consist of two pinholes that are on the optical axis of the integrating sphere's exit-port and are in a certain distance to each other. There are no other optics than these two pinholes involved. The collimators are there to reduce the flux of photons exiting the light source down to the single-photon level [76]. As shown before in Section 4.3.1 the flux from the integrating sphere only depends on the aperture size and the distance from the exit port. Therefore, the collimator does reduce the aperture of the exit port. The reduction factor introduced by the collimator can be varied with the size of both pinholes and their distance to each other. Another effect of the collimator is a smaller solid angle for the light flux.

Figure 4.19 shows an overview of all the collimator parts used during this work. Each one of them is mounted to the integrating sphere exit port with an aluminum mount (Figure C.23). There exist two groups of collimators made of different materials: aluminum and PVC. The first collimators produced were the ones made of aluminum and brass. Since both parts of the collimator are threaded one plate had to be another material to prevent cold welding of both parts. The collimator *AluB* was additionally covered with block flock paper on the inside, to reduce reflections. However, because of their size and conductivity both aluminum collimators are not suited for the operation together with high voltage (HV)-devices. With metal objects near a PMT-cathode the risk of sparks is high. Also aligning their exit-pinhole with any small detector device is challenging. The second group of collimators are made of PVC. They are not conducting and have the shape of a cone. With this the distance to any detector can be reduced to almost zero and aligning the collimator pinhole with a detector pixel down to the double size of the pinhole is possible. The following types of collimators were build during this work:
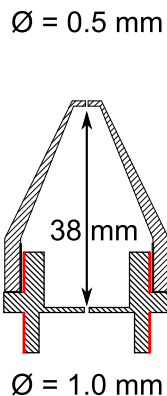
AluA: Two pinholes of 1 mm diameter each and a distance of 20 mm. To prevent cold welding when putting both plates together, the first plate is made of brass, the second one of aluminum Figures B.4, C.24, and C.25.
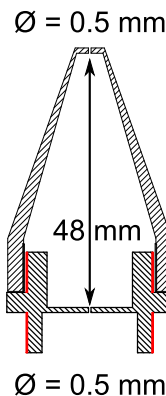
Alu-collimators
AluA & AluB

Ø = 1.0 mm

20 mm

Ø = 1.0 mm

PVC-collimators

ColA

Ø = 0.5 mm

38 mm

Ø = 1.0 mm

ColB

Ø = 0.5 mm

48 mm

Ø = 0.5 mm

ColC

Ø = 0.5 mm

38 mm

Ø = 0.5 mm

ColD

Ø = 0.5 mm

48 mm

Ø = 1.0 mm

ColE

Ø = 0.5 mm

38 mm

Ø = 5.0 mm
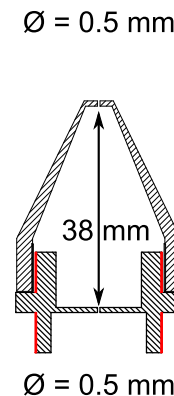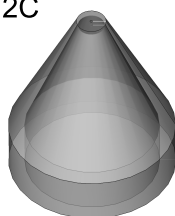
Plate 2C   Plate 2D
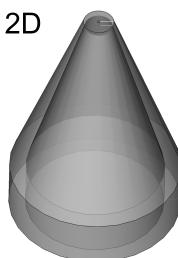
Plate 1B   Plate 1A
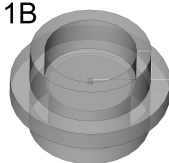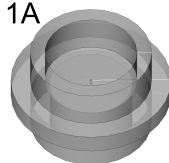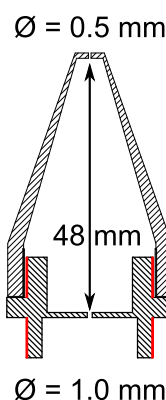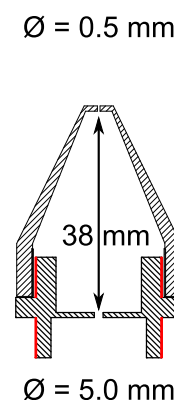
Figure 4.19: Sketch of all collimators. Alu-collimator *AluA* and *AluB* are mechanically identical. The PVC-collimators are made from black PVC. Their plates 1A, 1B, 2C, and 2D can be combined to various types with different ratios. The 5 mm-hole plate is a modification of plate 1A.

AluB: Same as *AluA* but with additional black flock paper inside to reduce reflections.

ColA: Collimator made of black PVC. Two pinholes of 1 mm and 0.5 mm diameter are in a distance of 38 mm (Figures B.5, C.27, and C.28).

ColB: Second PVC-collimator, made of two pinholes with 0.5 mm diameter and a distance of 48 mm (Figures C.26 and C.29).

ColC: Third PVC-collimator, made of two pinholes with 0.5 mm diameter and a distance of 38 mm (Figures C.26 and C.28).

ColD: Two pinholes of 1 mm and 0.5 mm diameter are in a distance of 48 mm (Figures C.27 and C.29).

ColE: A modification of *ColC*. The diameter of the pinhole of the first plate was enlarged to 5 mm. This was done to test the PVC-collimator ratio for different wavelength with a better signal-to-noise ratio.

In general the measurement of the collimator ratio requires two photodiodes and a certain light level (Section 4.1). The light level has to be high enough to be detected by one of the photodiodes after the reduction from the collimator. Therefore, multiple continuous emitting LEDs were build into the LED-arrays. The set-up is shown in Figure 4.20. *PD 39* is mounted onto the side-port of the integrating sphere. The collimator is mounted to the front-port and *PD 38* is placed with it's sensitive area directly in front of the collimator with a distance of roughly 1 mm. After closing the photon shielding, both photodiodes are set to zero. Afterwards the LED-array is switched on to initiate the warm-up phase. After a stable output of the LEDs is reached, the measurement of the collimator ratio starts by measuring both optical powers for 5 min to 10 min. The ratio is calculated via $R = \frac{P_{38}}{P_{39}}$. As shown before the statistical and systematic errors are calculated via Equations (4.9) and (4.10).
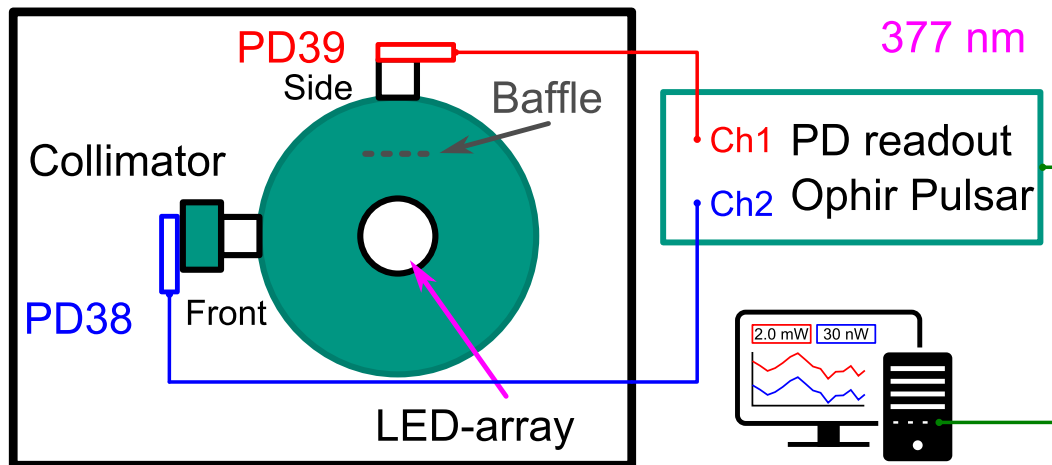

Figure 4.20: Sketch of the set-up for collimator ratio measurements.

4.3.5.1 *Example calculation for the collimator ratio*

This section contains the example calculations suggested by Philippe Gorodetzky for calculating the collimator ratio [114]. They only take geometrical effects into account. Reflections and other wavelength dependent effects are not considered. The collimator ratio is the attenuation factor applied to the photon flux that is coming out of an integrating sphere. First a sketch of the experimental set-up is given in Figure 4.21. On the right side there is an integrating sphere with radius r and two exit ports labeled *Side-port* and *Front-port*. Attached to the *Side-port* is a photodiode named *PD 39*. The respective port aperture diameters are given as d_{p1} and d_{p2}. Attached to the *Front-port* is a collimator which is characterized via its two hole diameters d_1, d_2 and the distance l between these two holes. At the exit of the collimator (*Hole 2*) is a second photodiode *PD 38*. Inside the collimator the half opening angle θ as well as the solid angle Ω are shown. The photon fluxes Φ_{p1}, Φ_1 and Φ_2

are always the fluxes after the corresponding port or hole. The efficiencies ε_1 and ε_2 are the flux transfer ratios of the respective aperture changes at *Hole* 1 and *Hole* 2 of the collimator. The resulting collimator ratio R is the product of these two.
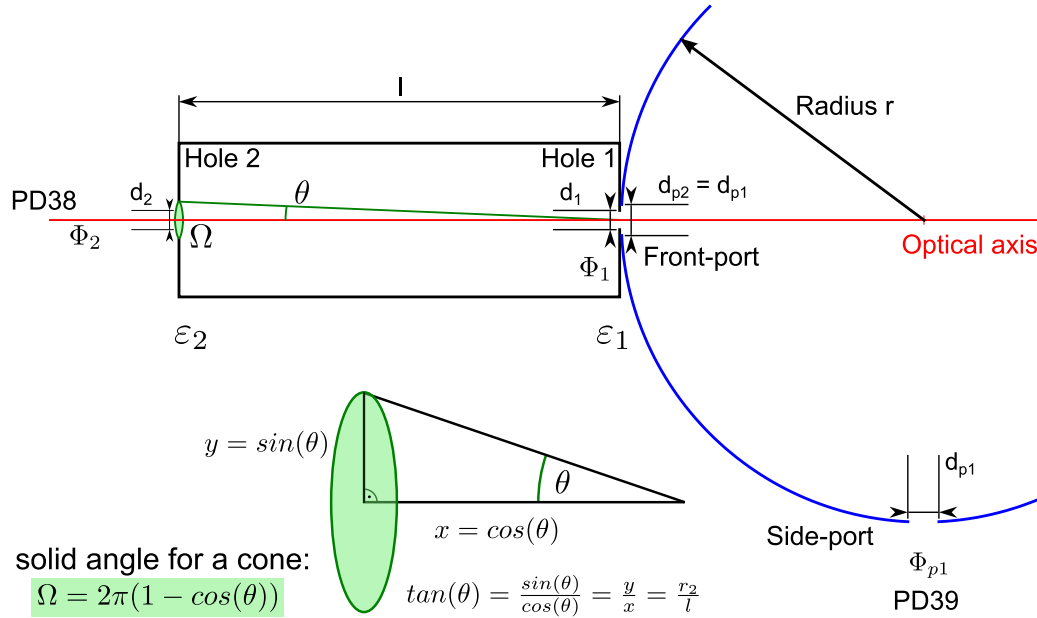
Figure 4.21: Sketch of the collimator ratio calculations with all relevant parameters (according to [114]). At the bottom a sketch of a cone with opening angle 2θ and solid angle Ω is shown.

This is a very simplistic view of the integrating sphere and the collimator. The following assumption were made to simplify the calculations. The sphere is supposed to be ideal, resulting in an uniform diffuse photon flux inside the sphere. The resulting photon flux outside any port of the sphere is therefore described with a Lambertian distribution. Changes in the flux are only dependent on changes in aperture size (if the same distance from the sphere's center is maintained). Since the *Side-port* and the *Front-port* are identical, both ports emit the same photon flux Φ_{p1}. For the following calculations any aperture structures expanding in the direction of the fluxes are neglected, e. g. in reality the sphere has a finite thickness and mounts are needed to attach the collimator and the photodiodes.

When the collimator is attached to the *Front-port*, the aperture is changed to *Hole* 1 with its respective diameter d_1. This results in a new photon flux Φ_1 after *Hole* 1. The flux transfer ratio of *Hole* 1 relative to the incident flux Φ_{p1} is given via the ratio of the aperture areas:

$$\varepsilon_1 = \frac{A_{d1}}{A_{p2}} = \frac{A_{d1}}{A_{p1}} \quad . \tag{4.13}$$

The photon flux inside the collimator can be described with a light cone with an opening angle of 2θ. Every point of the collimator entrance (*Hole* 1) can be seen from the collimator exit (*Hole* 2) with the solid angle Ω. This is further illustrated in the bottom of Figure 4.20. The y-direction corresponds to the radius r_2 of *Hole* 2.

The x-direction corresponds to the length l of the collimator. Trigonometry gives for the half opening angle:

$$\theta = \arctan\left(\frac{\sin(\theta)}{\cos(\theta)}\right) = \arctan\left(\frac{r_2}{l}\right) = \arctan\left(\frac{d_2}{2l}\right) \quad .$$

The solid angle for this cone is given via:

$$\Omega = 2\pi\left(1 - \cos(\theta)\right) \tag{4.14}$$

This is the visible area for *Hole 2* of the light that is emitted from *Hole 1* of the integrating sphere. Comparing this to the whole solid angle of 4π that would be visible without *Hole 2*, gives the flux transfer ratio:

$$\varepsilon_2 = \frac{2\pi\left(1 - \cos(\theta)\right)}{4\pi} = \frac{1 - \cos(\theta)}{2} \quad . \tag{4.15}$$

Combining the results from Equation Equation 4.13, Equation 4.14, and Equation 4.15 gives the collimator ratio R of:

$$R = \varepsilon_1 \cdot \varepsilon_2 = \frac{A_{d1}}{A_{p1}} \cdot \frac{1 - \cos(\theta)}{2} = \frac{A_{d1}}{A_{p1}} \cdot \frac{1 - \cos\left(\arctan\left(\frac{d_2}{2l}\right)\right)}{2} \quad .$$

Only the aperture areas of the collimator and its length as well as the aperture area of the exit port of the integrating sphere are in this equation. These calculations neglected scattering of light inside the collimator and therefor real collimators might have a slightly smaller ratio since more light with higher solid angles can leave the collimator.

As an example we will consider one of the aluminum collimators *AluA* on our integrating sphere. The aperture of the photodiode *PD 39* defines the area of the *Side-port* $A_{p1} = 100\,\text{mm}^2$. Both holes of the collimator have a diameter of $d_1 = d_2 = 1\,\text{mm}$ which results in $A_{d1} \approx 0.785\,40\,\text{mm}^2$. The length of the collimator is given as $l = 20\,\text{mm}$. This results in:

$$\varepsilon_1 = \frac{0.785\,40\,\text{mm}^2}{100\,\text{mm}^2} = 0.007854 \quad ,$$

$$\varepsilon_2 = \frac{1 - \cos\left(\arctan\left(\frac{1\,\text{mm}}{2 \cdot 20\,\text{mm}}\right)\right)}{2} \approx 0.0001562 \quad ,$$

$$\varepsilon \approx 1.23\,\text{E}^{-6} \quad .$$

Thus the estimated collimator ratio for the collimator *AluA* is roughly 10^{-6}. The measured collimator ratio was found to be around 2×10^{-5} for 377 nm. The difference might be, because this estimated value did not consider reflections inside the collimator. The estimated ratios of the PVC-collimators are around 10^{-8}. Table 4.3 shows the estimated ratios and the measured ratios for a wavelength of 377 nm. For collimators *ColB*, *ColC*, and *ColE* the estimated values and the measured ones are in the same order of magnitude. For the other collimators, the measured ratios are one order of magnitude bigger than the estimated ratios.

Table 4.3: Calculated and measured collimator ratios for the different collimators. The measurements were done with a wavelength of 377 nm.

COLLIMATOR	ALUA	ALUB	COLA	COLB	COLC	COLD	COLE
estimated ratio	1.2E−6	1.2E−6	8.5E−8	1.3E−8	2.1E−8	5.3E−8	2.1E−6
measured ratio	1.9E−5	1.4E−5	7.3E−7	3.2E−8	2.9E−8	2.4E−7	2.8E−6

4.3.5.2 *Collimator ratio with different light levels*

This section shows the measurement of the ratio of collimator *AluA* with different light levels. The set-up is the same as shown before in Figure 4.20. This time different light levels as in Section 4.3.3.4 are used, with different configurations of LED-array AR2. This measurement will show, if the collimator ratio is stable with different light levels. This has to be tested, since the assumption that the ratio is stable is one key feature of the light source.
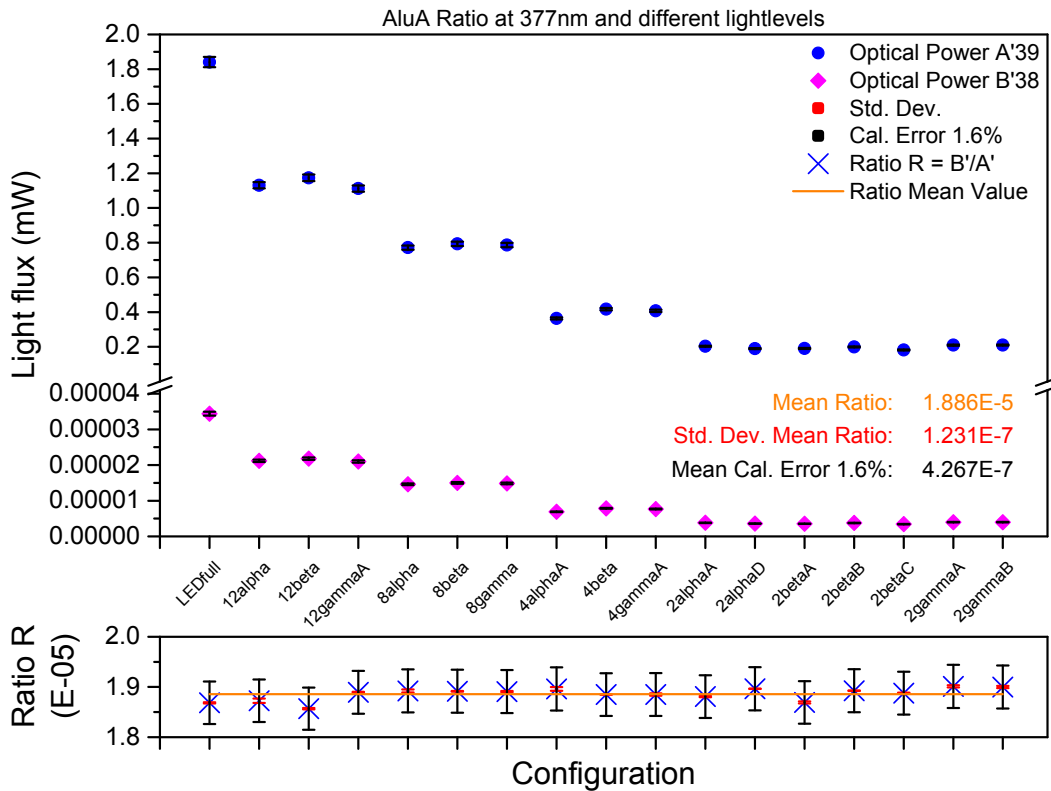
Figure 4.22: Data of the ratio measurement of collimator *AluA*. Optical power versus different array configurations, corresponding to different light levels. The lower graph shows the collimator ratio R versus the same configurations.

Figure 4.22 shows the measured data. The upper part shows the optical power versus the different light levels. These are again different configurations of LED-array AR2 shown in Figures C.12 and C.13. With lower light levels both measured optical powers decrease. Within one light level the optical powers measured seem to be stable. The lower part shows the individual ratio R_i for every data point, the corresponding standard deviation σ_{R_i} (statistical error, Equation 4.9), and the

Gauss-propagated calibration error Δ_{R_i} of 1.6 % in the ratio (systematic error, Equation 4.10). The mean ratio R of all data points is shown as a horizontal line. Its value is $(1.886 \pm 0.001_{stat} \pm 0.004_{sys})10^{-5}$. The standard deviation of the mean ratio σ_R is the statistical error. The mean of the single calibration errors is used as the systematic error as previously shown in Section 4.3.3.5. No significant outliers were detected with a Grubbs' test [113].

The formerly predicted collimator ratio of $1.23\,E^{-6}$ is not consistent with the measured collimator ratio for *AluA*. This could be due to the neglected reflections within the collimator for the example calculation. Due to reflections a bigger solid angle can be visible and more photons can exit the collimator, even at steeper angles. This can increase the collimator ratio to higher values, weakening the attenuation of the collimator.

4.3.5.3 *Collimator ratio versus distance*

Since the possibility exists that for measurements with photosensors the distance of the collimator to the photodiode can not be reproduced exactly, a distance dependent collimator ratio measurement had to be done. Since this measurement is also dependent on the size of the sensitive area of the receiving sensor, utmost care should be taken when measuring the collimator ratio during calibration runs. It should be measured at the exact same position for photodiodes and photosensors. The following measurement was again done with LED-array AR2 while in continuous mode for higher light levels with 377 nm wavelength. The collimator that was measured this time was the PVC-collimator *ColA*. The same set-up as in Figure 4.20 was used. Although data for different distances from the exit hole of the collimator to the photodiode was taken.
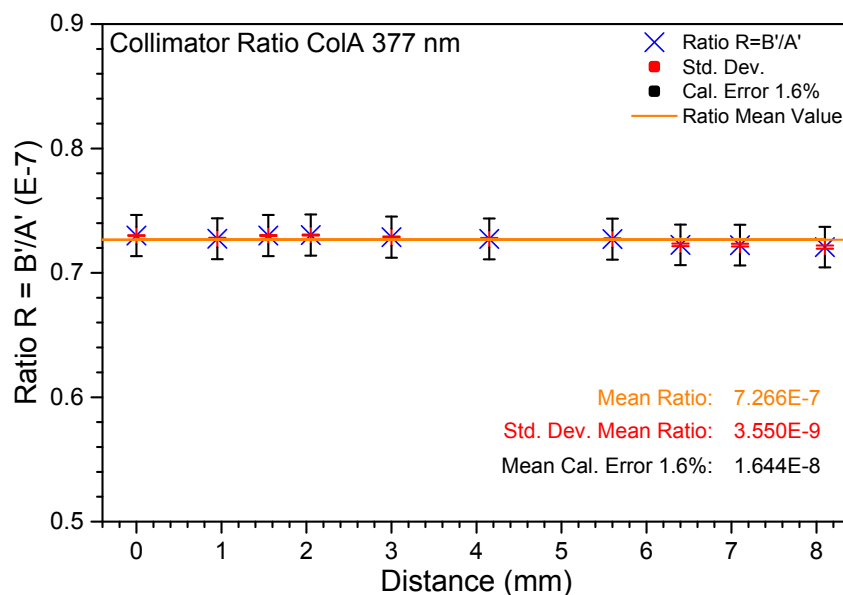
Figure 4.23: Collimator ratio of *ColA* versus distance. A stable ratio from 0 mm to 8.1 mm is present.

Figure 4.23 shows the collimator ratio R_i versus different distances from $0\,\mathrm{mm}$ to $8.1\,\mathrm{mm}$. The corresponding standard deviations σ_{R_i} and calibration errors Δ_{R_i} are shown for every ratio. Each ratio and its standard deviation was measured and directly saved by the software *Ophir Starlab*. The mean ratio R follows as $(7.266 \pm 0.036_{\mathrm{stat}} \pm 0.154_{\mathrm{sys}})10^{-7}$, with its standard deviation σ_R as the statistical error and the mean of the single calibration errors as the systematic error (refer to Section 4.3.3.5). No significant outliers were found.

Within the chosen range of $0\,\mathrm{mm}$ to $8.1\,\mathrm{mm}$ the collimator ratio seems to be stable for a target of $1\,\mathrm{cm}^2$. For smaller sensitive areas, like a single channel of an MAPMT or a SiPM, one has to be cautious that the light cone exiting the collimator does not exceed said sensitive area. Therefore, the exit-hole of the collimator should always be as near to the sensitive photosensor area as possible, without damaging the area. The collimator ratio should also always be measured very precisely at the same position as the photosensor.

4.3.5.4 *Collimator ratio versus wavelength*

Since the calibration stand also has a spectral light source (LED-array AR5), the question for a wavelength dependence of the collimator ratio is still open. Therefore, measurements with different wavelengths were taken by Nils Hampe during the course of his bachelor thesis, to investigate such a dependency [97]. The set-up used was the same as previously shown in Figure 4.20. This time different LEDs with different emission wavelengths were used in continuous mode (LED-array C, LED-array AR2 and LED-array AR5).

Figure 4.24 shows the mean values of the measured collimator ratios of three collimators (*AluB*, *ColA*, and *ColE*) versus wavelength and a zoomed-in view for *ColE*. The data shown in these graphs are all average values for the collimator ratio. For some wavelengths, several datasets were taken (Tables A.1 and A.2). For these wavelengths the *weighted mean value* $\overline{R}$ is given (Table A.3), because of the big differences between the single mean ratio values. From that weighted mean value, the statistical errors can be calculated in two ways: *internal uncertainties* and *external uncertainties* (Appendix A.3, Equations (A.1) and (A.2)). The bigger one of both is then used as the statistical uncertainty and given in the plot. The shown systematic errors are the propagated calibration errors of the photodiode power measurements. They amount to $\Delta_{\overline{R}} = \sqrt{2} \cdot 1.6\,\% \cdot \overline{R}$ for wavelengths below $400\,\mathrm{nm}$ and to $\Delta_{\overline{R}} = \sqrt{2} \cdot 0.5\,\% \cdot \overline{R}$ for wavelengths over $400\,\mathrm{nm}$. The systematic uncertainty in the wavelengths itself is in the order of $3\,\%$ and is dominated by the uncertainty of the photodiodes [DS91].

For collimator *AluB* the measurement was done once with every wavelength available, with one dataset per wavelength (Table A.1). With a collimator ratio in the range of 1×10^{-5}, this was the weakest collimator. Because of this weak attenuation, every optical output could be seen by the second photodiode in front of the collimator. However, the values for the two lowest wavelengths were very close to the detection limit of the photodiode. Therefore, fluctuations around $1\,\mathrm{pW}$ to $2\,\mathrm{pW}$ in the photodiode are stronger afflicting the collimator ratio of these two
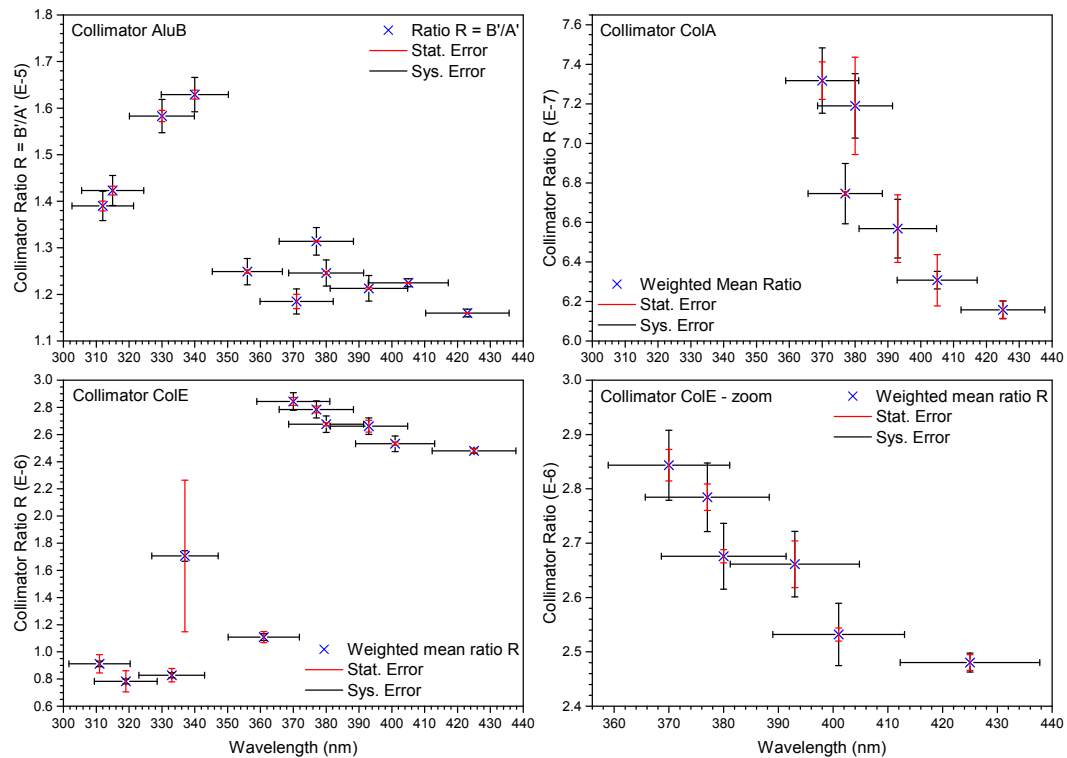
Figure 4.24: Collimator ratios of *AluA*, *ColA*, and *ColE* versus wavelength. The collimator ratio declines with increasing wavelength. Measured by Nils Hampe [97].

wavelengths. In general the collimator ratio gets smaller (stronger) with increasing wavelength for this collimator.

The plot for *ColA* comprises several datasets (Table A.2), each taken with different LED-arrays. For *ColA* wavelengths below 380 nm could not be measured with the second photodiode and LED-array AR5, since the optical powers after the collimator were to low. Here also a clear trend towards smaller (stronger) collimator ratios with higher wavelengths is seen.

Being an order of magnitude smaller in terms of collimator ratio, it was possible with *ColE* to get measurements of all possible wavelengths. The plot for *ColE* also is made from several datasets (Table A.2), taken with the same LED-arrays as before. There are two groups of data points present. One group at wavelengths below 365 nm with a collimator ratio around 1.1×10^{-6} and very large statistical errors, exceeding the systematic errors. The other group has a ratio around 2.7×10^{-6} and has clearly smaller statistical errors. The statistical errors of the first group at low wavelengths are an indicator for the quality of the measurements. For all these low wavelengths the optical power signal at the second photodiode was below 25 pW, the detection limit of the photodiode. Therefore, even small fluctuations during the measurement have a higher impact on the collimator ratio and it is doubtful, if these measurements can be used. The zoom in on the second group of data points reveals again a declining ratio with larger wavelengths. Here also the statistical errors are smaller than the systematic errors, since the optical powers at the second photodiode were sufficiently high.

In conclusion, these measurements did show that the collimator ratio has to be measured very precisely for every new dataset. Although the collimator ratio is stable for a certain wavelength, fluctuations from measurement to measurement are possible. Especially, if the optical flux that leaves the collimator is not high enough for the second photodiode for reliable detection. Therefore, the collimator ratio should always be measured with an optical power leaving the collimator that is greater than 100 pW or even higher.

4.3.6 *Summary*

In the previous sections the key components of the reference light source of SPOCK and the conducted test experiments were explained thoroughly. To recapitulate, at first the theoretical principles of integrating spheres were summarized. Afterwards, the present available LED-arrays for different wavelengths were shown with their respective emission spectra in pulsed and continuous mode. Test measurements to determine the output flux of both exit-ports of the integrating sphere were presented for different light levels. Uncertainty calculations for the measured optical power ratios were given. Afterwards, the photodiodes of SPOCK were cross-calibrated with a NIST-calibrated photodiode in a two step process. This was done to make sure that the measured power levels are accurate. After that, a theoretical estimation of the collimator ratios followed. The available collimators for SPOCK were tested for different light levels, for varying distances from the collimators exit hole, and for different wavelengths. A change of the collimator ratio with the wavelength of the light was observed.

4.4 READ-OUT ELECTRONICS

With the reference light source having been discussed in detail, the remaining parts of SPOCK are now explained. It involves the break-out-boards for the detectors, the triggering mechanism, which triggers on every light pulse, as well as signal routes through a multiplexer to the 16-channel signal detector, being a *CAEN v965* QADC. Controlling and measurements of the read-out electronics are done with a self-programmed software based on *National Instruments LabVIEW* and is running on a dedicated personal computer (PC). The read-out part for the QADC was programmed by Andreas Weindl (IKP - KIT) [115]. While the program controls the translation stages, where the light source is mounted, it can switch signal routes via the multiplexer to always have the corresponding detector pixel connected to the QADC.

Figure 4.25 shows a schematic sketch of SPOCK, with all the components used for light detector calibration measurements. The top left part with the *HP8082A* pulser [DS116], the LDD *CERN NP-4168*, and the light source were described before (Section 4.3.2.1). At the same time, as the NIM-pulse from the *HP8082A* pulser triggers the LDD, an inverted NIM-pulse is sent to a gate generator. This one generates a variable gate via a delay to the *CAEN v965* QADC [DS117, DS118]. With proper timing via the delay, which is realized via several cables with different lengths, signals
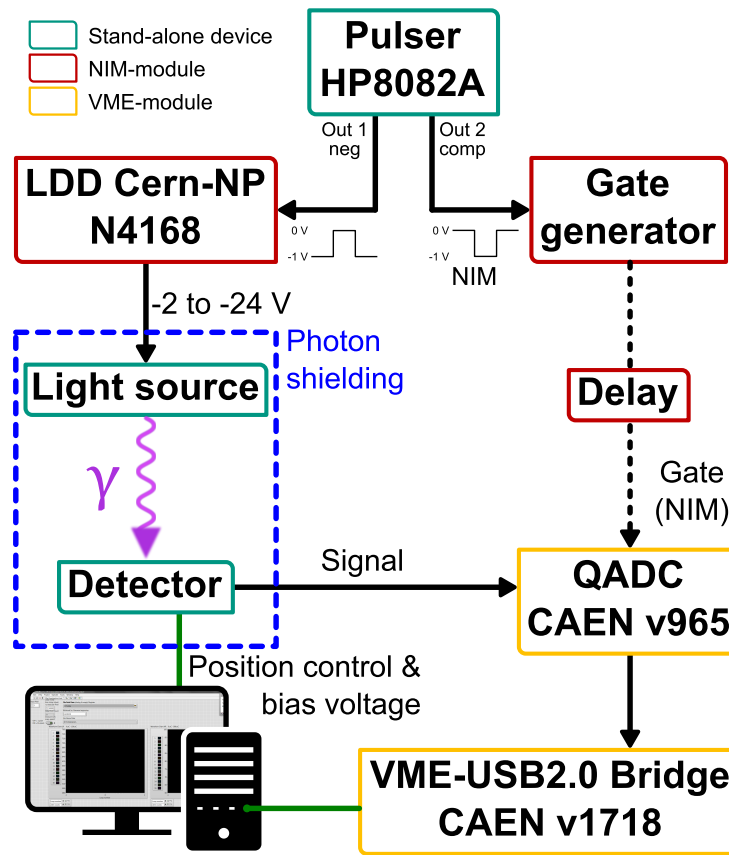
Figure 4.25: Sketch of the general measurement set-up. Specific versions for MAPMTs and SiPMs are shown in the respective chapters.

from the light detector reach the QADC during the gate time. Here it is essential, that for every trigger, the gate has to start 15 ns before the first signal arrives at the input of the QADC. The 12-bit QADC has two ranges, *low range (LR)* and *high range (HR)*. Both are recorded the whole time, if one is not above its threshold. The *LR* is for charges from 0 pC to 100 pC, corresponding to 25 fC for one QADC value, the *HR* is for charges from 0 pC to 900 pC, corresponding to 200 fC for one QADC value. Depending on the detector type, the bias voltage of the detector is either controlled via the PC or via a high voltage power source (HVPS). The digitalized data from the QADC is sent via a VMEbus[3] to a *CAEN v1718* controller [DS119, DS120] which also works as a VME-Universal Serial Bus (USB)-bridge to the measurement PC. There the data is stored as American Standard Code for Information Interchange (ASCII)-files, for further analysis.

4.4.1 *QADC calibration*

To be sure that the output signal of our detectors is measured correctly, a calibration measurement of the *CAEN v965* QADC [DS117] had to be done. A sketch of the set-

---

3 Versa Module Eurocard (VME) - computer bus standard using module cards with a fixed form factor (computer bus standard ANSI/IEEE 1014-1987).

up is shown in Figure 4.26. A pulse generator *WaveStation2012* [DS121] produced a NIM-like signal for a discriminator. Its NIM-output was used as a trigger for a gate generator and for a second pulse generator *HP8082A* [DS116]. A delay was used for proper timing of the trigger for the pulser. The gate of 130 ns was sent to the gate input of the QADC, while the output of the second pulser was sent to one of the QADC channel inputs. Both signals were also fed simultaneously to an oscilloscope *WaveRunner 610 Zi* [DS122], to measure the charge of the pulses and to be sure that the whole pulse lies inside the gate time. The gate time defines the integration time of the QADC. All measurements were done with the same gate, since the QADC-pedestal and the measured charge is dependent on the gate time. The gate also had to precede the pulse by at least 15 ns, due to the construction of the QADC.
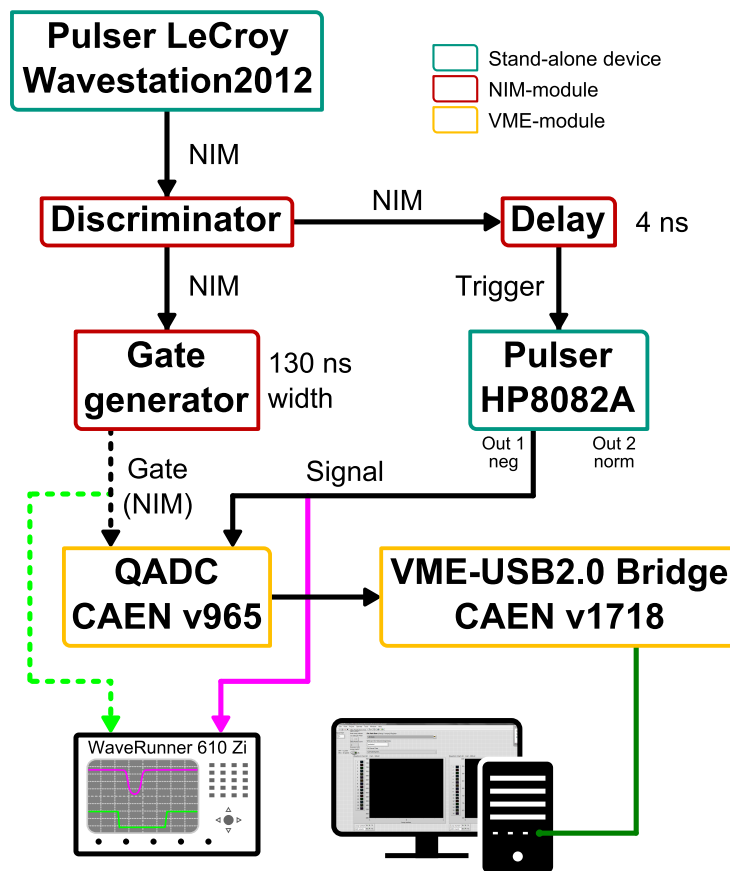
Figure 4.26: Set-up for the QADC-linearity and pedestal calibration measurements.

Every QADC channel was tested with several different pulses, ranging from around -25 pC to 850 pC, covering the whole dynamic range of the QADC. For each charge, the oscilloscope measured around 1000 waveforms that were afterwards integrated. The average of the integrations gave the charge, when taking the input impedance of 50 Ω into account $Q = \frac{U}{R_{input}} \cdot t$. The QADC measurement was done for every one of the 16 channels with 10 000 pulses, amounting to better statistics. Before and after the measurement, the QADC-pedestal was measured. For this the whole setup was still connected, but no input signal was given to the channels.

Only the gate was sent to the QADC. With this the internal offset of each channel could be measured. The measurements were done by Simon Ehnle during the course of his bachelor thesis [123].
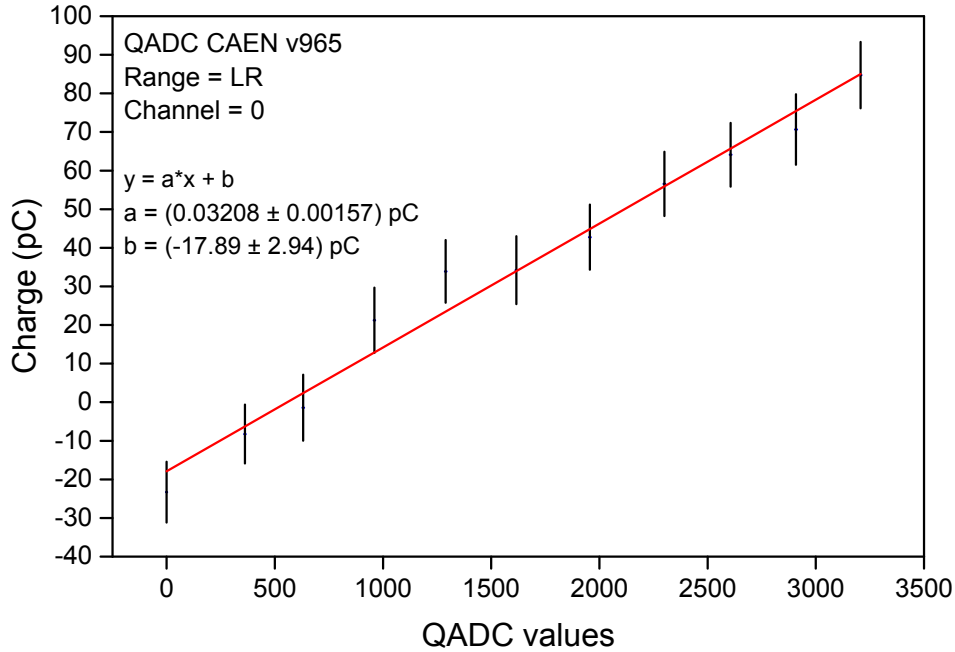
Figure 4.27: Exemplary data plot of one of the measurements of the QADC linearity for the low range (*LR*). Shown is the data after correction for the QADC-pedestal, the statistical errors of the charge and the QADC values, and a linear fit. The plots for the other channels can be found in Appendix A.4. Measured by Simon Ehnle during the course of his bachelor thesis [123].

Figure 4.27 shows exemplary the data of one measurement for the *low range* (*LR*) for one channel of the QADC. The charge Q was calculated via integrating the averaged pulses from the oscilloscope. The raw QADC values X' were directly given by the measurement software of the QADC, simultaneously for both ranges. Shown in the plot is the average charge Q versus the corresponding average QADC value X after correction for the QADC-pedestal X_{ped}. The error bars show the statistical uncertainties σ_Q and σ_X for both axes. The statistical error in the charge σ_Q is the standard deviation from the averaging of the oscilloscope. The statistical error in the QADC values σ_X is calculated via the error propagation of the uncertainties of the raw data $\sigma_{X'}$ and the pedestal $\sigma_{X_{ped}}$ (Equation 4.17). The red line is a linear fit to the data, weighted with the individual uncertainties. This seems plausible, because the manufacturer gives an integral non-linearity of 0.1 % [DS117]. The fit parameters in the plot are given with respect to the level of precision of the instrument in the range of 25 fC per QADC value (*LR*). The slope of the linear fit gives the proportionality factor k for the charge Q and the QADC value X:

$$k = \frac{Q}{X} \quad . \tag{4.16}$$

The equivalent plots for the other channels and the *high range* (*HR*) can be found in Appendix A.4.

4.4.1.1 *Uncertainty calculations for the QADC*

This section shows the uncertainty calculations for the calibration measurements of the QADCand gives the proportionality factor k for every channel, including both ranges. We start with the measured quantities, the charge Q, the QADC-pedestal X_{ped}, and the uncorrected QADC value X'. All three are measured several times and have a standard deviation σ_Q, $\sigma_{X_{ped}}$ and $\sigma_{X'}$. The corrected QADC value X follows from

$$X = X' - X_{ped} \quad .$$

The corresponding statistical error σ_X is calculated via the error propagation formula for uncorrelated variables, which gives:

$$\sigma_X = \sqrt{(1 \cdot \sigma_{X'})^2 + \left(-1 \cdot \sigma_{X_{ped}}\right)^2} \quad . \tag{4.17}$$

The statistical error in the proportionality factor σ_k follows from the standard error of the slope given in each linear fit (Table 4.4 and Appendix A.4).

For the systematic uncertainties Equation 4.16 is rewritten to

$$k = \frac{Q}{X} = \frac{U \cdot t}{R \cdot X} \quad ,$$

where

$$Q = I \cdot t = \frac{U}{R_{input}} \cdot t \quad \text{is the charge and}$$
$$X = X' - X_{ped} \qquad \text{is the corrected QADC value.}$$

With the corresponding current I, time interval t (pulse width), voltage U (pulse height), input impedance R_{input}, the measured raw data QADC value X', and the QADC-pedestal X_{ped}. The systematic uncertainties Δ_k for the proportionality factor k are calculated with the error propagation for uncorrelated variables. It follows

$$\Delta_k^2 = \left(\frac{t}{X \cdot R_{input}} \cdot \Delta_U\right)^2 + \left(\frac{U}{X \cdot R_{input}} \cdot \Delta_t\right)^2$$
$$+ \left(\frac{U \cdot t}{X^2 \cdot R_{input}} \cdot \Delta_X\right)^2 + \left(\frac{U \cdot t}{X \cdot R_{input}^2} \cdot \Delta_{R_{input}}\right)^2 \quad ,$$

where

$$\Delta_U = 1\,\% \cdot U_{max} \qquad \text{is the DC vertical gain accuracy [DS122],}$$
$$\Delta_t = 2.5 \times 10^{-6} \cdot t_{width} \quad \text{is the clock accuracy [DS122],}$$
$$\Delta_{R_{input}} = 2\,\% \cdot 50\,\Omega \qquad \text{is the uncertainty in the input impedance [DS122],}$$
$$\Delta_X = \sqrt{2} \cdot 0.1\,\% \cdot X \qquad \text{is the propagated non-linearity of the QADC, and}$$
$$\frac{\Delta_{X'}}{X'} = \frac{\Delta_{X_{ped}}}{X_{ped}} = 0.1\,\% \qquad \text{are the non-linearities of the QADC [DS117].}$$

The respective pulse heights U_{max} and pulse widths t_{width} are used for the calculation of Δ_U and Δ_t. The clock accuracy Δ_t is 1.5×10^{-6} plus an aging factor of 0.5×10^{-6} per year since the last inspection. In our case that was in September 2014. Because the second year since inspection had just started (October 2015), an uncertainty of 1.0×10^{-6} was added. The systematic uncertainty in the QADC value Δ_X has to include the propagated uncertainties $\Delta_{X'}$ and $\Delta_{X_{ped}}$, analogue to Equation 4.17. The resulting systematic uncertainties in the slope Δ_k were calculated for every channel and range (every fit) via the biggest individual systematic uncertainty in the respective fit. Table 4.4 shows all values discussed.

Table 4.4: Results of the QADC calibration measurements done by Simon Ehnle [123]. Given are the slopes k of the linear fit for both ranges (*LR* and *HR*), as well as their statistical σ_k and systematic uncertainties Δ_k. The mean relative systematic uncertainties are $\frac{\Delta_{k_{LR}}}{k_{LR}} = 3.9\,\%$ and $\frac{\Delta_{k_{HR}}}{k_{HR}} = 4.3\,\%$. The calculations were made as explained above. To translate the measured QADC values to a charge, these values are needed.

CHANNEL	k_{LR} (fC)	$\sigma_{k_{LR}}$ (fC)	$\Delta_{k_{LR}}$ (fC)	$\frac{\Delta_{k_{LR}}}{k_{LR}}$ (%)	k_{HR} (fC)	$\sigma_{k_{HR}}$ (fC)	$\Delta_{k_{HR}}$ (fC)	$\frac{\Delta_{k_{HR}}}{k_{HR}}$ (%)
0	32.08	1.57	1.24	3.87	231.84	0.95	9.89	4.27
1	32.47	1.60	1.26	3.88	234.43	0.96	10.01	4.27
2	32.44	1.59	1.26	3.88	234.03	0.96	9.98	4.26
3	33.04	1.62	1.28	3.87	239.02	0.99	10.21	4.27
4	32.96	1.62	1.28	3.88	238.36	0.99	10.16	4.26
5	32.38	1.59	1.26	3.89	233.60	0.97	10.05	4.30
6	32.11	1.57	1.25	3.89	232.38	0.97	9.95	4.28
7	32.56	1.60	1.27	3.90	234.73	0.99	10.08	4.29
8	32.12	1.58	1.25	3.89	232.12	0.98	9.94	4.28
9	33.03	1.62	1.29	3.91	238.01	1.01	10.22	4.29
10	32.10	1.58	1.24	3.86	232.10	0.98	9.91	4.27
11	33.25	1.64	1.29	3.88	239.87	1.02	10.26	4.28
12	33.15	1.63	1.28	3.86	239.83	1.02	10.24	4.27
13	32.24	1.59	1.25	3.88	233.48	1.00	9.95	4.26
14	32.97	1.63	1.27	3.85	237.89	1.02	10.10	4.25
15	32.35	1.59	1.24	3.83	233.96	1.00	9.89	4.23

4.5 CAPABILITY OF THE CALIBRATION STAND

The premise of SPOCK was that it should be a multipurpose calibration stand for photodetectors of all kinds. Therefore, its capabilities are just as wide. First of all, different kinds of detectors can be compared with the same systematics. For this, several calibration modes are possible. Detectors can be thoroughly tested in single-photon mode, measuring their PDE and their gain, with single photons. This of course is only possible with detectors that have a very low dark-count rate. SPOCK also allows for the uniform illumination of bigger detector areas and thus the simultaneous calibration of either several small detectors or of one bigger detector, as long as these detectors fit into the photon shielding. Furthermore, different wave-

lengths can be used with SPOCK, this leads to wavelength dependent measurements of the PDE. This is especially interesting, as newest SiPMs get more sensitive to the UV-regime. This is of course also important for fluorescence detection of cosmic rays, as there are several discrete wavelengths emitted during nitrogen relaxation processes within EAS. Figure 4.28 shows the expected performance of two new generation SiPMs in an overlay with a simulated nitrogen fluorescence spectrum in 4 km altitude [36, 39]. The expected PDEs are given versus the wavelength in the range of the nitrogen fluorescence. *S12642 epoxy* is a standard SiPM, coated with an epoxy layer. This layer does not allow a good transmission of UV light. The newest generation of *S13361s silicone* SiPMs is coated with a silicone layer and has a better sensitivity to UV light [DS124, 125].
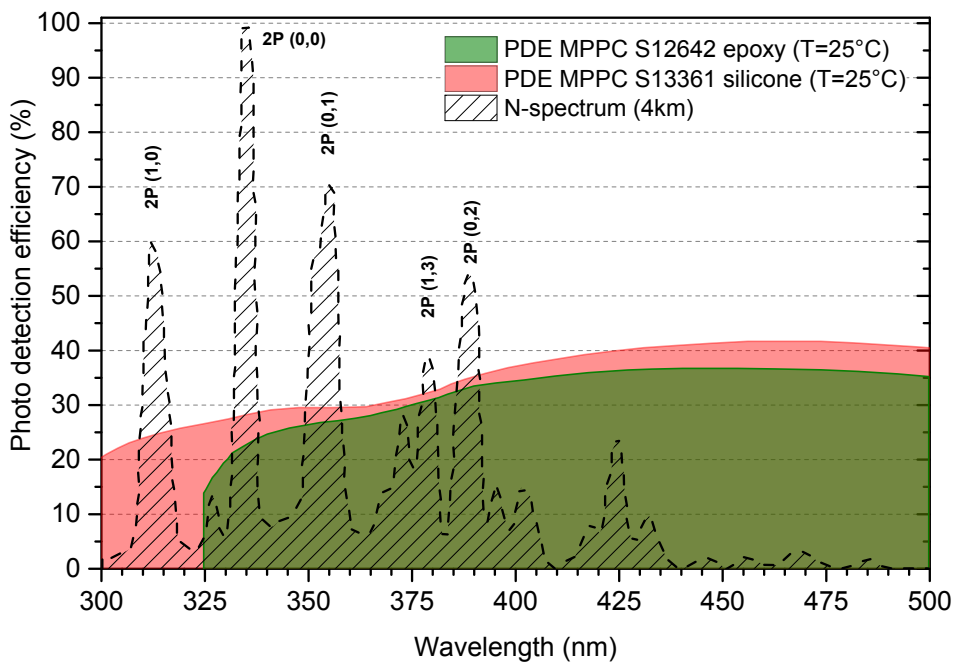
Figure 4.28: The shown nitrogen fluorescence spectrum is a model calculation for 4 km altitude [36, 39]. The expected PDEs of both SiPMs were taken from catalog graphs from Hamamatsu [DS124, 125].

Dynamic range measurements of photodetectors are also an important calibration mode. At the moment SPOCK can send between 0 to 100 photons per pulse onto a photodetector, when pulsing with 1 kHz, 6 ns pulse width and a collimator ratio of 2×10^{-5}. With a few tweaks to the collimator, as well as longer light pulses, a photon number of around 10 000 photons per pulse is feasible. When going to continuous light emission by the LEDs this number can be easily increased.

All components of the calibration stand can be modified in a fairly easy way, e. g. if new wavelengths are needed, new LED-arrays can be easily produced and calibrated by the way described above. It would also be possible to even use a wavelength tuneable laser. Ongoing work, with two master theses, is the expansion from single channel SiPMs to SiPM-arrays, as well as a photon shielded freezer for temperature controlled calibration measurements. Therefore, new connector boards for

SiPMs-arrays are built, to feed their signals to the readout electronics, and to control their operation voltage.

4.6 INFLIGHT-CALIBRATION OF JEM-EUSO

The inflight-calibration of JEM-EUSO was mentioned shortly in Section 3.2. For this relative calibration that is done after the absolute calibration with the on-ground calibration stands, like SPOCK, smaller reference light sources are needed. Research on the inflight-calibration was already published at the International Cosmic Ray Conference 2013 in Rio de Janeiro (Brasil) [54]. The following sections contain formerly published content of that contribution.

Because it is very difficult to maintain the absolute calibration during the whole mission time of JEM-EUSO, changes in the detector have to be monitored the whole time. Therefore, the on-board calibration system will be used to do a relative calibration of the detector with respect to the absolute pre-flight calibration. It is also planned to use external light sources like the Moon for further in-flight calibration.The process of calibration is the following:

1. With the on-ground calibration the MAPMTs will be characterized very precisely and sorted according to their respective PDE and gain. After that the focal surface can be built with similar MAPMTs in one PDM to achieve a uniform focal surface for the JEM-EUSO telescope. Also the optical properties of the Fresnel lens system will be measured to a sufficient precision. With this the instrument can be characterized pre-flight with an accuracy better than 5 % [54].

2. After the mission launch, the end-to-end performance of the telescope will be checked with Xe-flasher lamps on an aircraft that is flying under the ISS or with Xe-flasher stations in the field of view of JEM-EUSO.

3. Changes in the detector will be monitored by the on-board calibration system as well as the use of Xe-flasher lamps and the moon.

There will also be on-ground lasers to check the trigger efficiency and the error in the reconstruction of the arrival direction. Xe-flashers will be used in combination with the devices of the atmospheric monitoring system to measure local atmospheric conditions, e. g. absorption of photons in the atmosphere.

The on-board calibration system will be installed into the JEM-EUSO telescope to monitor changes in the PDE of the detector and in the transmission of the optics. This calibration will be relative to the absolute calibration that was done pre-flight. The on-board system will consist of several small identical diffuse light sources that will be placed at different locations inside the telescope (Figure 3.4a). The on-board light sources will be built as smaller versions of the reference light source described within this work (Section 4.3). Their size should be in the range of 2.5 cm diameter. The optical output from each source is planned to be uniform and diffuse with a maximum emitting angle from the optical axis of the source. This maximum angle is dependent on the shape and size of the pinhole that will be put on the exit-port

of the sphere. The on-board light sources will be characterized pre-flight with one of the on-ground calibration systems, e. g. SPOCK.

To measure the change in the detectors signal response, several identical diffuse light sources will be placed at the edge of the third Fresnel lens to achieve a *direct illumination* of the focal surface (Figure 3.4a). The intensity will be set to single photoelectron mode and the relative change of the PDE will be measured while the gain of the MAPMTs will be measured absolutely. The threshold level for the counting will be adjusted if a large variation in gain is found. With the *illumination through the lenses* the efficiency of the optics will be measured. Identical light sources placed at the edge of the focal surface face the rear side of the third lens (Figure 3.4b). The light will pass the optics, be reflected at the diffuse lid (sand-blasted Aluminum) and pass the optics a second time. The MAPMTs at the focal surface will detect a fraction of the emitted photons. The time variation of the performance of the optics and the detector will be obtained at the same time in this measurement. Changes in the optical system can be obtained after subtracting the degradation of the detector. Raytracing simulations by Naoto Sakaki have pointed out that the direct illumination of the focal surface produces a very uniform illumination with four light sources [54]. The calibration can still be continued if one light source fails. The indirect illumination through the optics needs further investigation, as simulation results showed that the discrimination of reflected photons from the lid and the walls of the telescope might not be possible.

Based on the experience that was gained during the development of SPOCK, there are several key points that have to be taken into account when developing these small reference light sources. First an integrating sphere with an LED and a reference photodiode are indeed very suitable for calibration purposes. The uniform illumination provided by integrating spheres are ideal to illuminate the detector surface. The wavelength of LEDs and their optical output are sufficient in terms of stability. The wavelength spread could be better but can be changed with band pass filters. Of course, a continuous spectral measurement of the PDE for the detector would be most desirable. The NIST-calibrated reference photodiode at the integrating spheres is also very stable and is necessary to monitor the optical output of the integrating sphere. Because the collimator ratio was unstable for very low light levels, it might be desirable to use a calibrated photosensor with a higher gain, directly at the detector surface, together with the photodiode at the sphere. Here, a NIST-calibrated SiPM could be used, if their temperature stability can be guaranteed. The stability of the reference light source on the ground was not an issue in the controlled laboratory environment, however space can hardly be seen as a controlled laboratory environment.

After thorough cross-calibration measurements with the reference light source of SPOCK, these compact reference light sources would need to be tested in the field. The coming pathfinder experiments, mainly EUSO-Balloon and the already existing EUSO-TA, can provide very good test environments for these kind of compact reference light sources. EUSO-TA grants access to the device itself, allowing for experimental measurements at different positions within the telescope. EUSO-Balloon on the other hand simulates a space-like environment during the flight.

Another very important point which became clear during the development of SPOCK is that the present on-ground calibration stands should define common calibration standards for the JEM-EUSO collaboration. This is important, since the sorting and the calibration of the next 100 MAPMTs for the JEM-EUSO pathfinders will be distributed over several of these facilities. With that in mind, it is only natural to cross-calibrate the different calibration stands and define target wavelengths, bias voltages, aperture sizes, and so on.

MULTI-ANODE PHOTOMULTIPLIER TUBES

In the last chapter the calibration stand SPOCK, that was developed and built during this work, was thoroughly introduced. One of its intended uses was the characterization, sorting and calibration of MAPMTs to help the collaboration to process the huge amount of photodetectors needed for JEM-EUSO.

For this work four MAPMTs *R11265-113-M64 MOD2* from an early production series of Hamamatsu were present at KIT. Two of them (SN: *ZN0854* and *ZN0884*) had an UV transmitting band pass filter *Schott BG3* [DS62] directly glued to their photocathode, as it is planned for JEM-EUSO. The other two MAPMTs (SN: *ZN0857* and *ZN0882*) had nothing attached to their photocathode. The early production models are not expected to have the best performance. Meanwhile Hamamatsu has started the automatic mass production process of 64 pixel MAPMTs, yielding a more stable product performance.

This chapter will first introduce MAPMTs and recapitulate the working principle of PMTs (Section 5.1). After that the measurements done during this work will be explained and analyzed (Section 5.2). Afterwards the results will be shown (Section 5.3) and be discussed (Section 5.4).

5.1 WORKING PRINCIPLE

The Hamamatsu MAPMTs *R11265-113-M64 MOD2*, which are intended to be used for the JEM-EUSO mission and are used for its pathfinder experiments, are an assembly of 64 very compact individual PMTs with a photosensitive area of 2.88 mm × 2.88 mm sharing one photocathode of 23.04 mm × 23.04 mm without dead space (Appendix C.2, Figures C.30 and C.31).
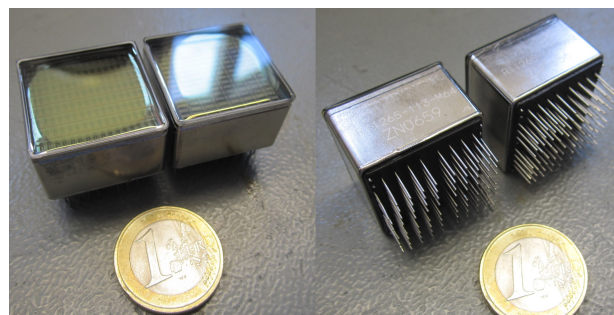
Figure 5.1: Photograph of two MAPMTs from the top (left), showing the photocathode and from the back (right), showing the connection pins for the cathode, ground, the 12 dynodes, and the 64 anodes.

The "individual PMTs" are arranged in an array of 8×8, each one having its own anode. All 64 PMTs are connected to the same high voltage, distributed via a voltage divider to the cathodes, dynodes and anodes (Figure C.32). With this kind of setup a very compact 64 pixel detector is realized (Figure 5.1). The inner structure of these devices is in general quite complicated (Figure C.33). However, the basic working principle of an MAPMT is the same as a standard PMT.

The following explanations for PMTs and the photoelectric effect are summarized from [126]. Figure 5.2 shows the sketch of the inner structure of a typical PMT [126]. It is a vacuum tube, with a photocathode, a focusing electrode, several dynodes and an anode. This well known device relies on the external photoelectric
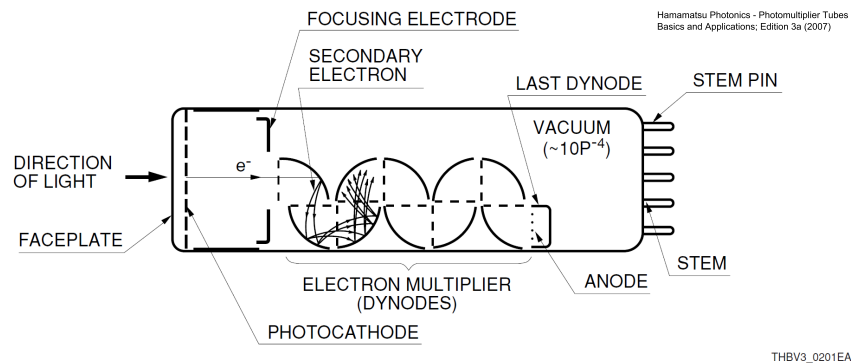
Figure 5.2: Sketch of a typical PMT showing its inner structure [126].

effect at the photocathode [126], where an incoming photon is absorbed and the excitation energy is transferred onto an electron, being able to leave the photocathode. This electron is called a photoelectron. The emitted electron is then focused by a focusing electrode and accelerated by an electric field onto the first dynode. While hitting the dynode, the photoelectron excites further electrons that can in return leave the dynode. They are then accelerated to the next dynode, and the process is repeated. At the anode, the secondary electrons are collected. With this kind of cascaded dynode chain an amplification of the initial photoelectron is realized and a measurable current pulse at the anode is the result. The multiplication factor by the dynode chain is called the *gain* of a PMT. The probability to detect a current pulse at the anode from one photon incident at the photocathode is called the PDE ϵ of the PMT.

5.1.1 *Photoelectric effect*

The photoelectric effect is a low-energy light-matter interaction resulting in the conversion of a photon into a photoelectron. Two main classifications are the external photoelectric effect and the internal photoelectric effect. The *external photoelectric effect* leads to the emission of photoelectrons from semiconductor or metal surfaces into the surrounding vacuum. This effect is used within PMTs. The *internal photoelectric effect* excites photoelectrons into the conduction band of a semiconductor material. Depending on the bias voltage on the semiconductor material (pn-junction) this can either lead to the photoconductive effect (increasing conductivity

because of unpaired electrons and holes) or the photovoltaic effect (conversion of light into electric energy). The internal photoelectric effect, or more precise, the photoconductive effect is used within SiPMs.
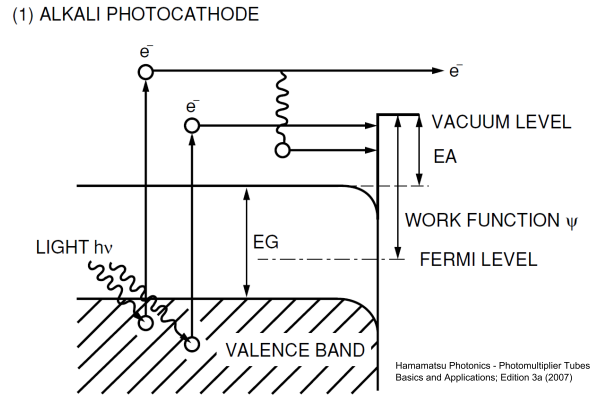
Figure 5.3: Sketch of the external photoelectric effect using the band model for an alkali photocathode [126].

Figure 5.3 shows the sketch of the external photoelectric effect using the band model for an alkali photocathode [126]. The y-axis shows the energy (of states), while the x-axis corresponds to the physical dimension of the photocathode. There are two energy bands and several energy limits in this picture: the valence band, the band gap (EG), the conduction band (upper limit not shown), the Fermi level, the work function, the electron affinity (EA), and the vacuum level. The valence band shows all occupied electron states bound to atoms of the crystal. The band gap is the energy region in the material, where no states can be occupied (this can be changed via doping). The conduction band shows empty states that can be occupied and that are not bound by atoms of the crystal. The Fermi level (or electrochemical potential) is defined as the maximum energy of the highest state occupied by electrons of a material at a given temperature. For increasing temperatures, the Fermi level increases. It can be also changed via a bias voltage. The work function is the energy difference between the vacuum level and the Fermi level. Its the minimum energy that has to be transferred to an electron occupying a state at the Fermi level, if one wants to eject that electron to the vacuum. In other words, an electron has to be elevated to an energy higher than the vacuum level, to free it from the material.

As a general example, incoming photons with the energy $E = h \cdot \nu$ can get absorbed by the photocathode [126]. The energy is transferred to electrons in the valence band and these get excited and diffuse towards the surface. The energy transfer is dependent on the wavelength of the photons, not on the intensity (number of photons). If the transferred energy E is high enough (higher than the vacuum level), the electrons get emitted into the vacuum. The emitted electrons are called photoelectrons. If the electrons lose energy during their diffusion process, and occupy a state below the vacuum level, they cannot leave the photocathode. This makes successful escapes more probable for electrons that are near to the surface. The probability for the emission of a photoelectron, when one photon is incident,

can be expressed via the ratio of both, which defines the *quantum efficiency* $\epsilon_{QE}(\nu)$ [126]. It is expressed as:

$$\epsilon_{QE}(\nu) = (1 - R) \cdot \frac{P_\nu}{k} \cdot \frac{1}{1 + \frac{1}{k \cdot L}} \cdot P_s \quad , \tag{5.1}$$

where

$\nu = \frac{c}{\lambda}$	is the frequency of the light,
R	is the reflection coefficient,
P_ν	is the probability for exciting electrons to a sufficient energy level,
k	is the full absorption coefficient of photons,
L	is the mean escape length of excited electrons, and
P_s	is the probability for the escape of electrons at the surface.

All the parameters above are dependent on the photocathode material. For the first three parameters R, P_ν, and k an appropriate material has to be chosen. The most dominating parameters for the quantum efficiency $\epsilon_{QE}(\nu)$ are the escape length L, which can be increased with the use of a pure and uniform crystal and the release probability P_s, which is dependent on the energy difference of the vacuum level and the lower conduction band level (electron affinity - EA). The quantum efficiency $\epsilon_{QE}(\nu)$ (Equation 5.1) should not be confused with the PDE ϵ of a PMT, which is the ratio of the number of detected photons and the total number of photons sent onto the PMT (Equation 4.2). It is dependent on the product of two probabilities: the quantum efficiency $\epsilon_{QE}(\nu)$ and the collection efficiency ϵ_{CE}. The collection efficiency is the probability of the photoelectron to reach the first dynode and to be multiplied. It is dependent on the internal PMT structure, that defines the electrodynamics in the PMT and on the applied voltage between the photocathode and the first dynode [76].

Figure 5.4 shows the band structure of a GaAs semiconductor photocathode [126]. To this an electropositive material Cs_2O is applied. Both materials have different band structures. Through this a depletion layer is formed and the band structure is bent down. This can make the electron affinity (EA) negative, relative to the GaAs conduction band, and thus increasing the escape probability P_s. Also the overall needed excitation energy is reduced, since the vacuum level now lies below the lower conduction band level of GaAs, resulting in an enhanced lower wavelength quantum efficiency. The mean escape length L also gets increased, since a depletion layer is formed and the mean free charged carriers are reduced, resulting in less interactions with other charge carriers. Also, if a loss of energy occurs for the diffusing electron, it might still be able to escape, because of the negative electron affinity.

Noise and false signals in an MAPMTs can occur from inter-channel crosstalk, darkcounts and afterpulses [126]. Inter-channel crosstalk can occur, when a photoelectron is focused to a wrong channel or when an electron cascade jumps from one channel to an adjacent channel. A light spread larger than the dimensions of one channel can also be a cause for crosstalk. Dark counts are caused by thermal electron excitation at the photocathode or the dynodes. Afterpulses may be caused by
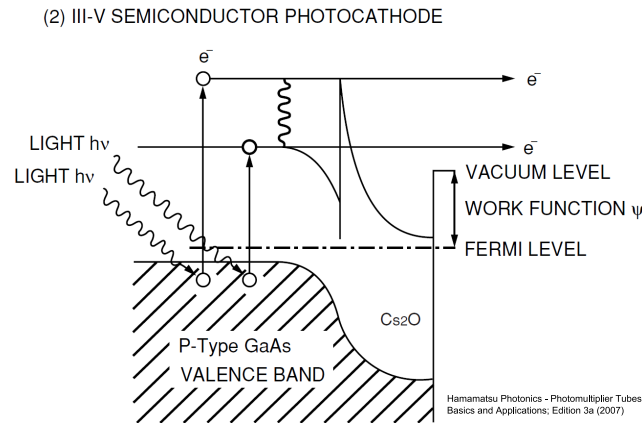
Figure 5.4: Sketch of the band model for a semiconductor photocathode. The escape length and the escape probability are enhanced by an electropositive material [126].

elastic scattering of electrons on the first dynode (very short delay to main signal) or by residual gas atoms in the vacuum that get ionized by the electron cascade and then themselves drift to the cathode (up to ms delays).

5.1.2 *The single photoelectron spectrum*

The detection of single photons is a process obeying Poisson statistics, since the obvious possible events are the detection of zero photons, one photon, two photons, three photons, and so on, per light pulse. The Poisson distribution is as a discrete probability distribution via a parameter $\lambda > 0$, that is the expected value and the variance of the distribution. The Poisson distribution gives the probability $P_\lambda(n)$ for natural numbers n, via [127]:

$$P_\lambda(n) = \frac{\lambda^n}{n!} \cdot \exp(-\lambda) \quad . \tag{5.2}$$

The parameter λ actually gives the expected number of events within a given period of observation. The Poisson distribution then gives the probability for the occurrence of a number of events n within the same period of observation, if the expected value λ is known in average. For example, the probability for two photons to be detected per light pulse, if the average value is λ_1, is given by:

$$P_2(\lambda_1) = \frac{\lambda_1^2}{2!} \cdot \exp(-\lambda_1) \quad .$$

How does this relate to our measurement? Well, when measuring the signal from an MAPMT per light pulse sent onto the MAPMT, charges are measured, that occur during a gate, given to our QADC. The gate coincides with the light pulses, as explained in the chapter before. Therefore, we get one event per gate. An event can be everything from zero photons to several ones. The measured charge per event is digitized by the QADC. For a higher number of photons, a higher number of photoelectrons is produced, which leads to higher charges and in the end to higher

QADC values. When counting the QADC values and preparing a histogram with the number of counts versus the QADC values, a single photoelectron spectrum is gained. The Gauss-distributed peaks in the resulting histogram correspond to the charges and ultimately to the number of photoelectrons. The Gauss distribution is because of fluctuations in the charge, resulting from the electron multiplying dynode chain and electronic noise in the QADC. The separation of both peaks gives the gain of the detector. The area under the one photoelectron peak gives the number of detected photons.
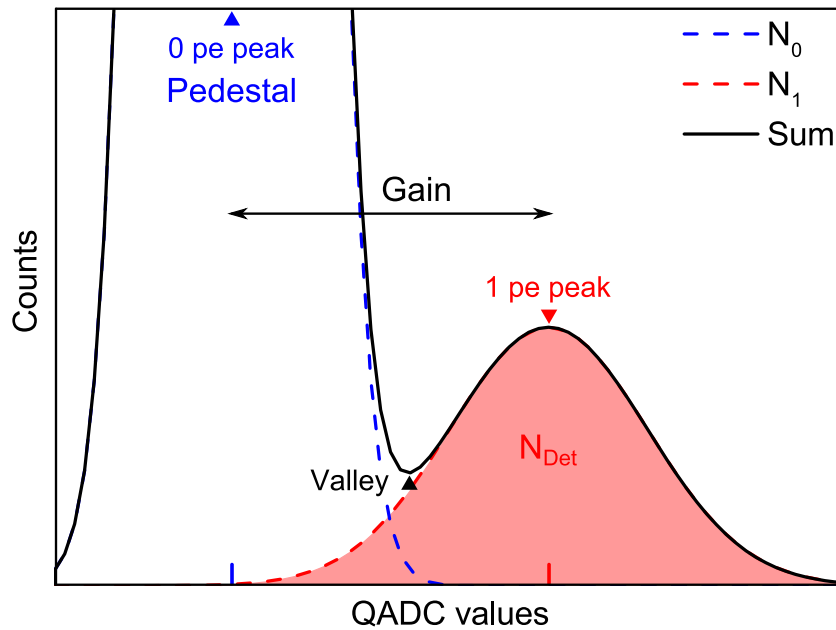
Figure 5.5: Schematic sketch of a single photoelectron spectrum with two Gauss-distributions for the *0 pe* and *1 pe* peak. The separation of both peaks gives the gain of the PMT. The area under the *1 pe* peak gives the number of detected photons (adopted from [76]).

Figure 5.5 shows a sketch of such a single photoelectron spectrum. Around the zero photoelectron peak (*0 pe peak*) are dark counts of the PMT, i. e. no signal from a photoelectron was registered at the anode of the PMT. This peak is also called the *pedestal*. At higher QADC values a one photoelectron peak (*1 pe peak*) is present. The values there correspond to one emitted photoelectron, whose signal is registered at the anode. The shown sketched spectrum does not have any higher photoelectron peaks present. In general, the resulting spectrum can be a superposition of 0 pe, 1 pe, 2 pe, 3 pe, ... peaks. If there are many peaks in the spectrum, e. g. for higher photon numbers, this kind of spectrum is also called a *finger spectrum*, because of the characteristic shape of many peaks.

5.1.3 *The 'MAPMT recipe'*

For every channel of an MAPMT, a single photoelectron spectrum is recorded, by measuring the charge pulses per light pulse sent onto the MAPMT channel. At the

same time the light level is recorded and controlled in such a way, that there are mostly *0 pe peak* and *1 pe peak* events. This is done by comparing the peak heights, since the probabilities for all events in the single photoelectron spectrum obey Poisson statistics. Using the fact that the ratio of *1 pe* and *0 pe* events can be expressed via the ratio of *2 pe* and *1 pe* events after Equation 5.2:

$$\frac{P_2(\lambda)}{P_1(\lambda)} = \frac{\lambda^2}{2!}\frac{1!}{\lambda} = \frac{\lambda}{2} = \frac{1}{2}\frac{P_1(\lambda)}{P_0(\lambda)} \quad . \tag{5.3}$$

This means, that if the ratio of *0 pe* events to *1 pe* events is higher than 50, the number of counts that belong to a *2 pe* peak (within the right end of the *1 pe* peak) will be less that 1 %. That is an acceptable level for calibration. If the ratio is not high enough, Equation 5.3 can be used as a *2 pe* event contamination estimator for the *1 pe* event number. This correction factor is used for measured spectra with a lower ratio than 50. Via this the quality of the single photoelectron spectrum can be estimated. A lower contamination with *2 pe* events means a better quality of the measurement. For this method the light level has to be in the right range. If it is too low no *1 pe* peak will be identifiable. If it is too high the *1 pe* peak will be polluted with too many *2 pe* events. For even higher light levels the pedestal will vanish from the spectrum and higher photoelectron peaks appear.

From the single photoelectron spectrum the gain G of the examined MAPMT channel can be calculated via the separation of the *0 pe* and *1 pe* peaks:

$$G = \frac{(X_1 - X_0) \cdot k}{e} \quad , \tag{5.4}$$

where

X_0 is the *pedestal* mean value in QADC values,
X_1 is the *1 pe* peak mean value in QADC values,
k is the proportionality factor for the charge and the QADC value, and
e is the charge of an electron.

From the same spectrum, the PDE ϵ is given by the ratio of the number of detected photoelectrons N_{pe} and the number N of photons sent onto the PMT *per pulse* and the total number N_{total} of events in the single photoelectron spectrum (number of triggers) [75]:

$$\epsilon = \frac{N_{pe}}{N \cdot N_{total}} \quad . \tag{5.5}$$

The number of detected photoelectrons N_{pe} is the area under the *1 pe* peak. The lower threshold for events counting as a *1 pe* event is usually set in the valley between the first two peaks or at the $\frac{1}{3}$ *pe* level [76]. In our case, a fit over the sum of two Gaussian peaks is done, yielding directly the number of detected photoelectrons N_{pe} as the area under the *1 pe* Gauss peak. If needed the Poisson correction is applied.

The number of photons *per light pulse* N sent onto the detector is given by the optical power reaching the detector divided by the energy of one photon and the pulse frequency:

$$N = \frac{P_{PD} \cdot R}{E_{photon} \cdot f_{pulse}} = \frac{P_{PD} \cdot R \cdot \lambda}{h \cdot c \cdot f_{pulse}} \quad , \tag{5.6}$$

where

P_{PD}	is the mean optical power from the photodiode,
$R = \frac{R_1 + R_2}{2}$	is the mean collimator ratio,
$E_{photon} = \frac{h \cdot c}{\lambda}$	is the energy of a sent photon,
h	is the Planck constant: $6.626\,069\,57 \times 10^{-34}\,\mathrm{J\,s}$ [128],
c	is the speed of light: $299\,792\,458\,\mathrm{m\,s^{-1}}$ [128],
λ	is the wavelength of the photons, and
f_{pulse}	is the pulse frequency of the LED.

The mean collimator ratio is calculated from the collimator ratio measured before and after the MAPMT measurement. The wavelength was determined with the spectrometer measurements shown in Section 4.3.2.2 and depends on the LED-array used (Tables C.3 and C.4). All corresponding uncertainty calculations can be found in Appendix A.5.

For measurements where some of the light from the exit of the collimator may not reach the detectors sensitive area (measurements in a distance), a correction factor R_{geom} has to be multiplied with Equation 5.6:

$$R_{geom} = \frac{A_{detector}}{A_{PD}} \quad ,$$

with the detector area $A_{detector}$ and the sensitive photodiode area $A_{PD} = 100\,\mathrm{mm^2}$.

5.2 MAPMT MEASUREMENTS

After having introduced the observables of interest in the previous section, the question is how the measurements of these observables are performed. The following introduces the general measurement scheme, the single steps of the measurements, and some of the possible parameter variations.

Figure 5.6 shows the setup for the semi-automatic measurements of an 64 channel MAPMT. The detector is put into the photon shielding and connected to a socket board (Figures B.6, C.34, and C.35), that was designed by Andreas Ebersoldt (IPE - KIT) [129]. The first pixel of the MAPMT is to the bottom left, when looking at it from the front (from the light source). The socket board distributes the HV via the voltage divider (Figures B.7 and C.32) to the MAPMT [114, 130]. The 64 anodes of the MAPMT are connected via this board to the 64 input channels of a multiplexer[1] outside of the photon shielding. The multiplexer connects one subset of 16 channels

---

1 *Keithley 2750* frame housing *Keithley 7711* multiplexer cards [DS131, DS132].
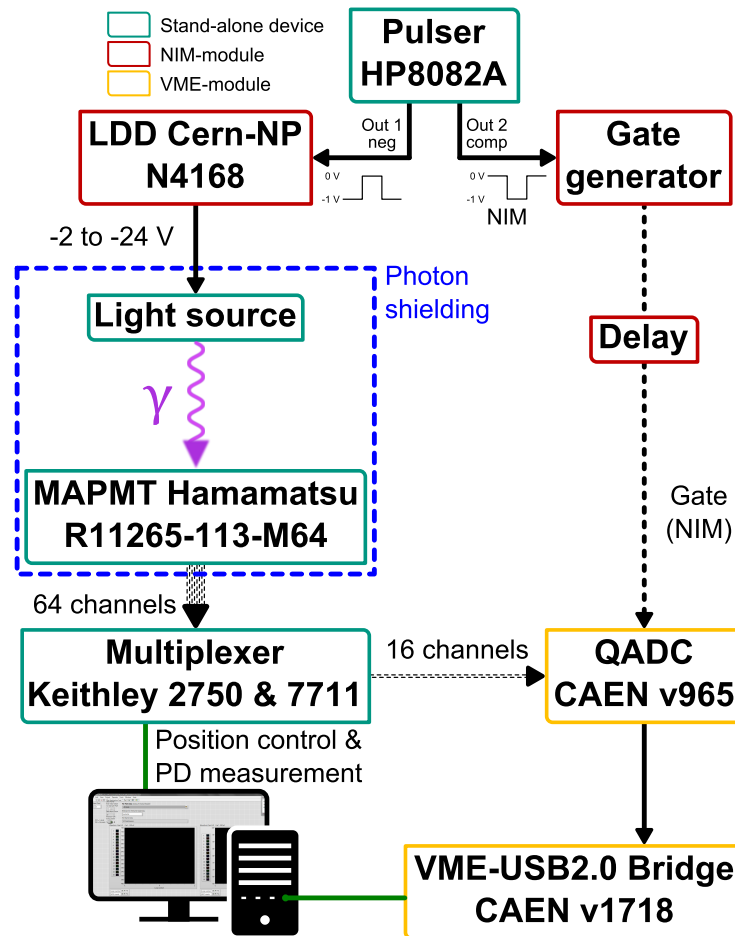
Figure 5.6: Sketch of the MAPMT measurement set-up.

of the 64 channels from the MAPMT to the 16 input channels of the QADC (see Figures B.8, B.9, and C.36). With this set-up 16 channels of the MAPMT can be measured at once. The multiplexer can be switched automatically, depending on the operation mode, to measure the signal from other channels. The switching can also be linked with the translation stages to ensure that the active channels are the ones that are illuminated. The QADC is gated in coincidence with the LDD, that produces the light pulses, which are sent onto the MAPMT. All controlling and data taking is done via the measurement PC with the self-programmed control software. The part involving the QADC read-out was programmed by Andreas Weindl [115]. The photodiodes are simultaneously read out by the PC.

Before the start of the measurement the MAPMT and the light source have to be aligned properly. This involves the lateral positioning in front of the first pixel and the distance to the exit hole of the collimator. The later should be below one millimeter and should also be the same for every pixel. As a consequence the surface of the MAPMT has to be perpendicular to the optical axis. This is controlled by checking the distances for every pixel by eye from the side, while scanning over them. Figure 5.7 shows this for one pixel.
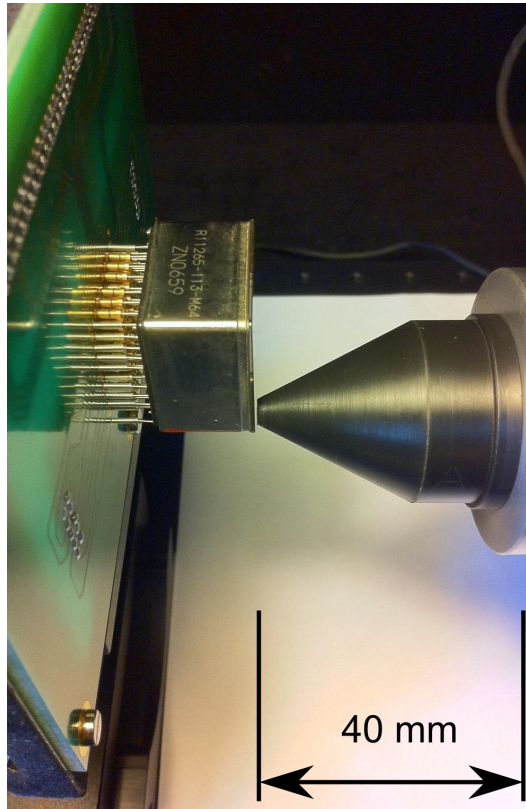
Figure 5.7: Photograph of the alignment of an MAPMT and collimator ColA. The distance as well as the first pixel are aligned here.

Afterwards the MAPMT measurements can be started. They involve the following 9 steps:

1. **Collimator ratio:** Within the closed photon shielding, the collimator ratio is measured for the desired wavelength with both photodiodes with a high light output (continuous mode). The set-up was shown before in Figure 4.20. The sensitive area of the photodiode (in front of the collimator) has to be at the same distance as the MAPMT will be later. After reaching stable conditions (after warm-up) the measurement is done for 5 min, with each data point being the average optical power per one second. After the measurement, the photodiode in front of the collimator is removed and the MAPMT is put with its surface at the same position (with the help of a slide on the optical bench). The continuous power supply is switched off and from now on pulsed light is used for the measurement steps.

2. **QADC pedestal:** The pedestal of the QADC is measured, to get the internal charge offset. While having the MAPMT connected, the light source (LDD output disconnected) and HV are turned off. For the QADC-pedestal 10 000 values are taken at the frequency f_{pulse} and gate width t_{gate}. Since the pedestal is dependent on the gate width, t_{gate} should be the same for all steps. All 16 channels of the QADC are recorded at the same time for this measurement, which takes around 35 s for 10 000 values.

3. **Dark counts:** The dark counts of the MAPMT pixels are recorded in a similar fashion as the pedestal measurement. The LDD output is disconnected (no light), the HV is switched on, and the same gate and pulse frequency is given to the QADC. For each pixel 100 000 values (triggered gates) are taken for the whole QADC at once. After 16 pixels, the multiplexer switches to the next cycle of 16 pixels (Figure C.36). Therefore 64 dark count histograms result. The measurement of 100 000 values takes around 5.5 min, resulting in a measurement time of 22 min.

4. **Timing:** The gate cable and one signal cable are disconnected from the QADC and are connected to an oscilloscope, in order to check for proper timing and adjusting the delay of the gate to the QADC. The LDD output is connected to the pulsed LED and pulsed light is used from now on. The input signal should also be 15 ns delayed from the first edge of the gate, according to the data sheet [DS117]. Of course, the light source has to be positioned in front of the respective MAPMT pixel. In some cases the light level might be too low to see a good signal on the oscilloscope. Then the light level can be adjusted by increasing the frequency by one order of magnitude or by increasing the pulse amplitude. This has to be reverted after the timing measurement. Figure 5.8 shows a screenshot of several minutes of signal taking for one channel with the same gate of 65 ns. Almost all signals are well within the gate and the delay is sufficient. If the delay is not sufficient, it can be adjusted with switches at the NIM delay module. If needed, the steps *timing* and *find pixel 1* can be swapped.

5. **Find pixel 1:** After having aligned the collimator opening and the first pixel of the MAPMT by eye, this has to be checked via the signal from the individual MAPMT pixels. Especially the middle of the first pixel and the alignment with the whole MAPMT has to be checked. This is done by going to the intersection point of four corner pixels of the MAPMT, e. g. at the corner of pixels 1, 2, 9, and 10. The collimator opening is moved in 0.5 mm steps via the remote controlled motorized linear stages in x and y direction. At the same time the signal from all four channels is shown in realtime by a LabVIEW subprogram named *pixel comparator*. If the same signal level is measured from all four pixels, the position is approximately in the middle of the four pixels. Afterwards the collimator opening has to be driven one half pixel size (1.44 mm) in the x and y direction towards the middle of the first pixel. This position is saved within the main LabVIEW control software as the home position. Afterwards the check of four pixels in each corner of the MAPMT is done for the other corners. With this method, we can be sure to be in the middle of each pixel, when scanning the whole MAPMT pixel by pixel. If needed, the steps *timing* and *find pixel 1* can be swapped.

6. **Light level finding:** For the measurement a spectrum is measured with 10 000 values (triggers) with a preset light level. The measured data is saved and shown as a histogram within the LabVIEW software, directly after the 35 s measurement. The appropriate light level can be roughly estimated via the

peak heights. As mentioned before with Equation 5.3, a good ratio of *0 pe* events to *1 pe* events would be higher than 50. The light level is adjusted at first via the pulse amplitude (potentiometer at LDD) and if that is not sufficient with the pulse width (duty cycle). Depending on the width, the gate has to be adjusted, leading to a repetition of the *timing* step.

7. **Main measurement:** The main measurement consists of the photodiode part and the MAPMT part. During the whole measurement the light level is monitored by the photodiode at the integrating sphere via the photodiodes *Starlab* software. Since the measurement can take several hours and the optical output of the light source is stable, the photodiode is set to record one average optical power value every 30 s. The MAPMT part involves different modes of operation:

   - The first possible mode is the *automatic scan of all 64 pixels* of the MAPMT with freely adjustable number of data points (triggers) per pixel. The QADC is then set to single channel mode, only recording signal from the illuminated pixel. For 100 000 values this takes around 5.5 min per pixel, leading to a measurement of 5.8 h per MAPMT.

   - The second mode is the *full illumination* of the whole MAPMT. Here we rely in the stability of the light source, since the QADC can not measure all pixels at once. The whole MAPMT is measured in four cycles with each 16 pixels (two columns) recorded at once (same as with the dark count measurement). The number of data points per pixel is again free to choose. To get a uniform illumination the collimator is replaced with a pinhole and the MAPMT is placed at a distance of around 20 cm to 100 cm to pinhole. The light source is positioned on the optical axis, which goes through the middle of the MAPMT. This method is considerably faster than the single scan of 64 pixels. For 100 000 events per pixel it takes roughly 22 min.

   - The third possible mode is a mix of both previous modes. A *cross talk measurement*, that positions the collimator in front of a given pixel and reads out the two columns containing that pixel and the adjacent one (with a number of given triggers). Here the QADC records all 16 input signals at once, corresponding to two columns of pixels. This measurement needs two cycles and thus only measures half of the pixels of an MAPMT.

8. **QADC pedestal:** After the measurement step 2 has to be repeated, to check if any changes in the QADC-pedestal occured.

9. **Collimator ratio:** At last step 1 has to be repeated, to get a second value for the collimator ratio. If it has considerably changed from the one in step 1, the validity of the measurement should be evaluated.

Figure 5.8 shows a screenshot of the timing measurement (step 4), taken with a WaveRunner 610 Zi Oscilloscope [DS122] and pixel 1 of one of the MAPMTs. The upper curve shows the signal channel that was in persistence mode (set to infinity)

for about ten minutes. The lower curve shows the gate signal, that was used as a trigger for the oscilloscope (and for the QADC). The arrows mark a range of 15 ns, that is needed as delay for the QADC. Only two signal pulses are outside of the integration gate.
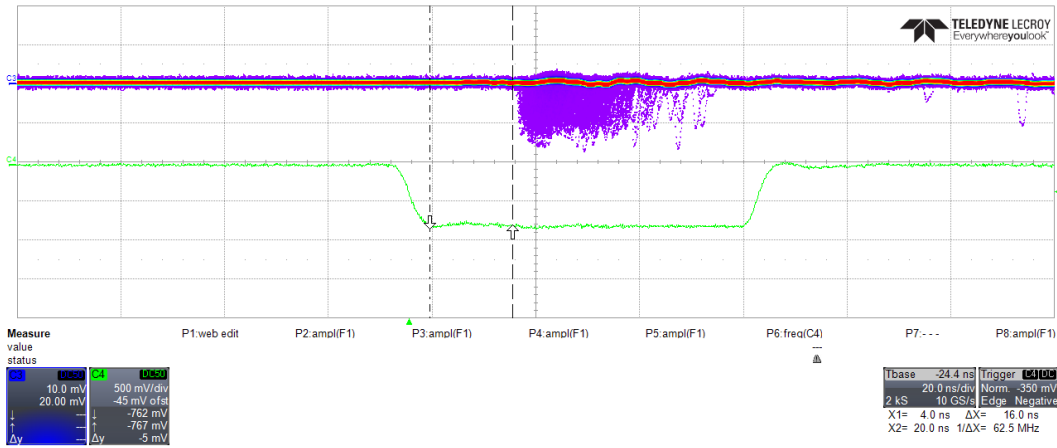
Figure 5.8: Screenshot of the timing and delay control of MAPMT signals (upper graph with persistency setting infinity) and the gate at the QADC (lower graph). The gate is open (QADC measures) while the lower level is present. The screenshot was taken with the WaveRunner 610 Zi Oscilloscope [DS122].

(a) QADC-pedestal.
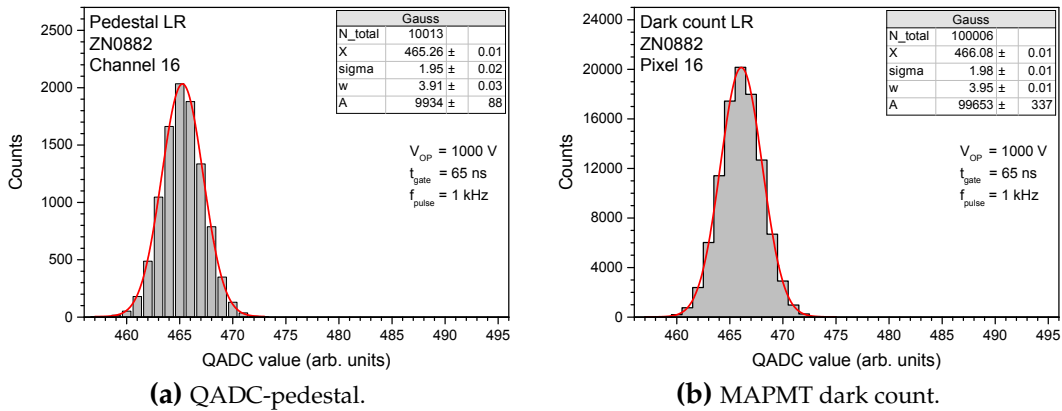
(b) MAPMT dark count.

Figure 5.9: QADC-pedestal and dark count measurement of one channel of a 64 channel MAPMT *R11265-113-M64 MOD2*. **(a)** QADC-pedestal for a 65 ns gate and 1 kHz frequency. **(b)** Dark counts for the same gate and frequency.

Figure 5.9 shows the QADC-pedestal of one QADC channel and the dark count spectrum of one of the MAPMT channels. These are recorded for every channel at every beginning of a measurement procedure. The pedestal was taken after the warm-up phase of the electronics and is stable in time. This was verified by measuring the QADC-pedestal before and after the measurement (step 2 and 8). The QADC-pedestal corresponds to an internal current of the QADC and introduces an offset to all measured values. After subtracting the QADC-pedestal value from the measured values an absolute charge value can be given. The pedestal of each QADC input channel is different. For a 65 ns gate the QADC-pedestal value ranges

from roughly 300 to 700. The dark count spectrum is given for the same gate width and the corresponding MAPMT pixel that is connected to the same QADC channel. The number of dark counts was in the range of 70 counts above a QADC threshold of 750 for a total number of roughly 6.4×10^6 data values. This shows the quality of the MAPMTs and on the other hand this demonstrated the excellent attenuation of the photon shielding.

5.2.1 Single pixel scans of MAPMTs

During this work, each of the four present MAPMTs were scanned pixel by pixel, one after another, and with four different wavelengths. Since the measurements took between six and twelve hours per MAPMT and wavelength, they were done together with Simon Ehnle, during the course of his bachelor thesis [123]. In the scope of his work, a mayor part of the data was also analyzed by a Gauss fit algorithm of the research group [133, 134]. Two of the MAPMTs (*ZN0854* and *ZN0884*) had an UV transmitting band pass filter *Schott BG3* [DS62] directly glued to their photocathode, as it is planned for JEM-EUSO. The other two MAPMTs (*ZN0857* and *ZN0882*) had nothing attached to their photocathode. For each pixel a histogram was recorded.
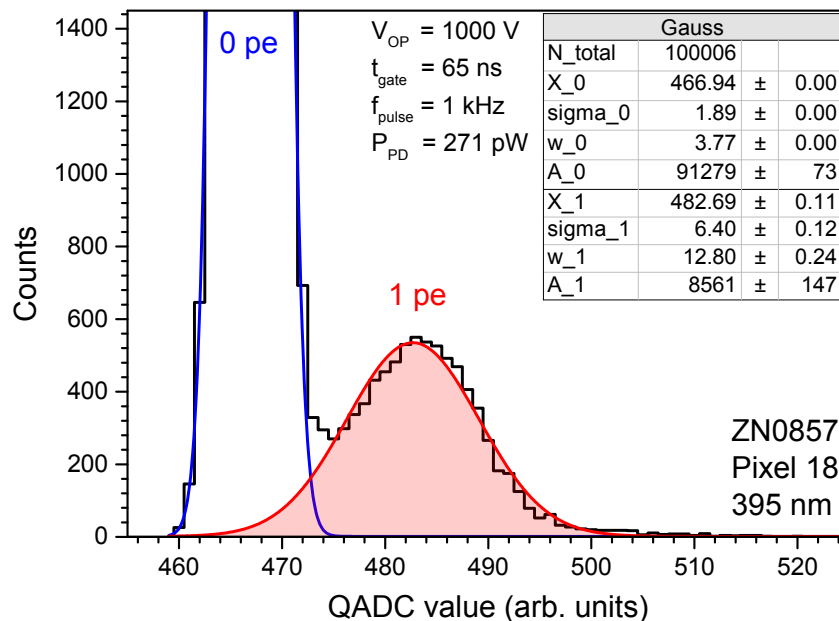
Figure 5.10: Histogram of the measured QADC values of MAPMT *ZN0857 - pixel 18* with a wavelength of 395 nm. The used collimator was *ColA* with a measured mean ratio of 616×10^{-9}. The *0 pe* and *1 pe* peaks are clearly separated. The ratio of both peaks is around 10, therefore the Poisson correction is applied and 402 events need to be subtracted from the *1 pe* peak. The total number of events exceeds the total number of events in the Gauss peaks. This is due to uncertainties in the Gauss fits.

An example can be seen in Figure 5.10. Here the peak area ratio (or the ratio of numbers of events) is in the range of ten, therefore the Poisson correction needs to be applied. 402 events are supposedly *2 pe* events and need to be subtracted from

the number of events in the *1 pe* peak (Equation 5.3). The total number of events is higher than the added number of the Gauss fits. This could be due to uncertainties in the fits and due to a not fitted *2 pe* peak.

The resulting gain, calculated from the histograms via Equation 5.4, is shown for every wavelength and every pixel of MAPMT *ZN0882* in Figure 5.11. The pixel numbers of the four corner pixels are given and the graph shows the front of the MAPMT. A change in the gain with increasing wavelength is not evident. The gain drops with increasing pixel number, resulting in an overall higher gain on the left side of the MAPMT than on the right side. However, an overall good gain uniformity is still given. This kind of data representation is useful for fast uniformity checks. However, errors during the measurement are not easily identified with this type of gain map.
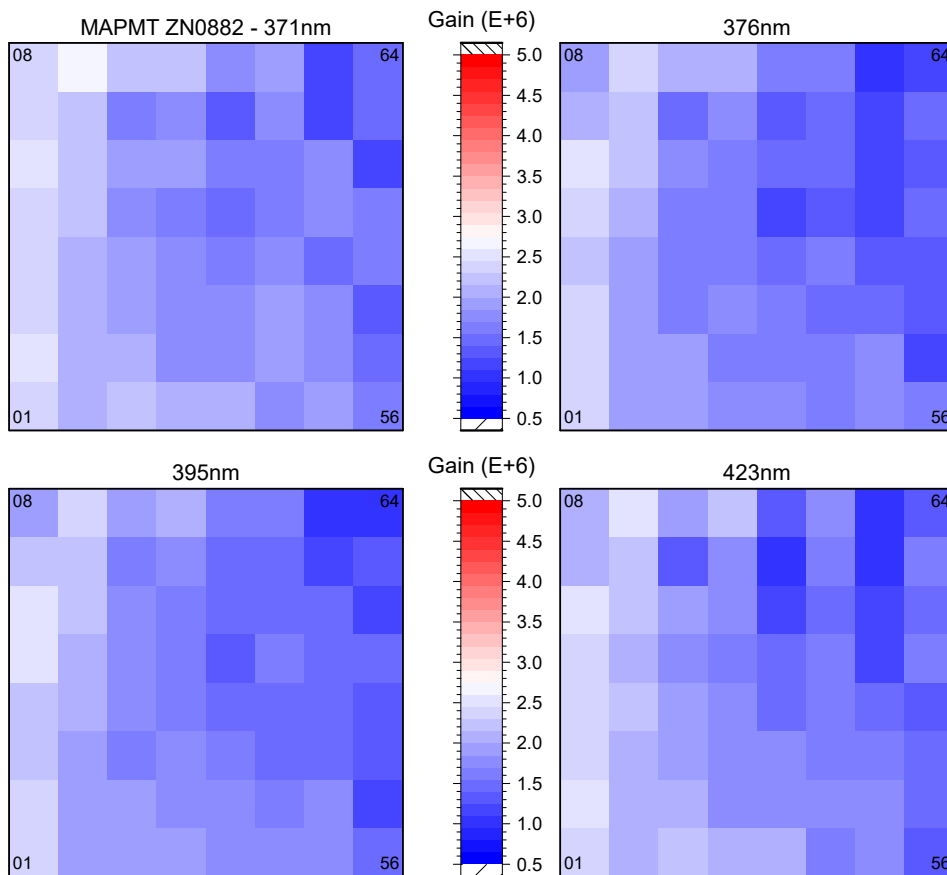
Figure 5.11: Gain maps of the single pixel scans of MAPMT *ZN0882* for different wavelengths at $-1000\,\text{V}$ bias voltage. An overall good gain uniformity is visible. The color scale for the gain (multiplication factor of the dynode chain) is given in multiples of 10^6.

In terms of PDE the same kind of heat map can be generated. The calculated PDE (via Equation 5.5) is shown for every wavelength and pixel of MAPMT *ZN0882* in Figure 5.12. For a better distinction of both kinds of maps, the color scheme was changed, however the maps still show the front view onto the MAPMT, with the corner pixel numbers given. One statistical outlier was detected, masked, and

is shown with a crossed pattern, to make clear that there is no value there. With increasing wavelength (up to 395 nm) the overall PDE increases and drops again slightly for 423 nm. The PDE is fairly uniform, except for the upper pixels in the uneven columns, where it is higher for every wavelength. This could be some effect of the inner dynode structure, having an influence on the collection efficiency and thus influencing the PDE. Another cause could be a misalignment of the collimator exit hole and the MAPMT pixels. However, this is unlikely since the alignment was checked before the measurement for every corner of the MAPMT very carefully. There should also be no big influence on the measurement, if the collimator exit hole with its 0.5 mm diameter is off from the pixel center with pixel dimensions of 2.88 mm × 2.88 mm (Figure C.31). In any case, for these pixels the associated gain maps show a slightly decreased gain. This is an indicator for a bad Gauss peak separation, leading to *0 pe* events being identified as *1 pe* events and as consequence, increasing the PDE. A check of the associated histograms confirmed, that the Gauss fit algorithm fails here.
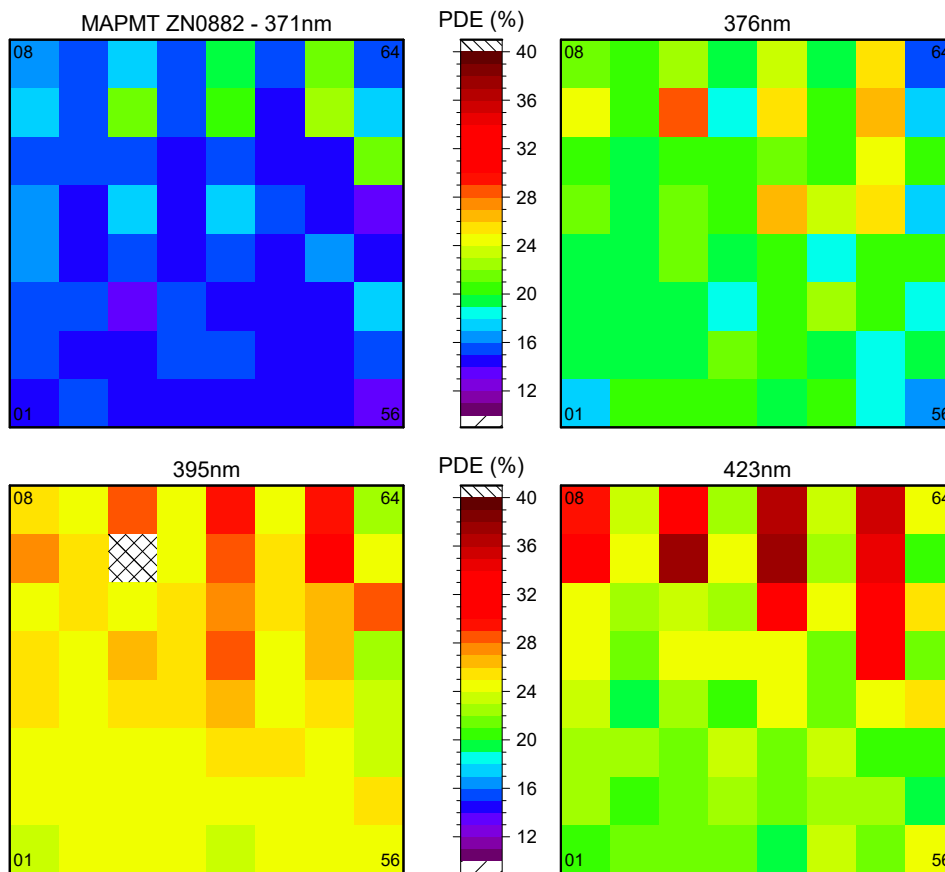
Figure 5.12: PDE maps of the single pixel scans of MAPMT *ZN0882* for different wavelengths at −1000 V bias voltage. One statistical outlier was detected, masked, and is shown with a crossed pattern. A wavelength dependence of the PDE is visible. The PDE is fairly uniform, except for some structure in the upper part of the columns.

The PDE map of an MAPMT with an attached UV-band pass filter *Schott BG3* [DS62] is shown in Figure 5.13. Although the light level was chosen carefully at

the beginning of the measurement, it was not sufficient for a good peak separation in the histograms, since the gain is very low (see Figure A.15). The uniformity in the PDE is not apparent any more. However, the overall behavior with different wavelength is still visible. Further heat maps for the gain and PDE uniformity of the other MAPMTs can be found in Appendix A.6, since they are not fundamentally different from the maps shown above.
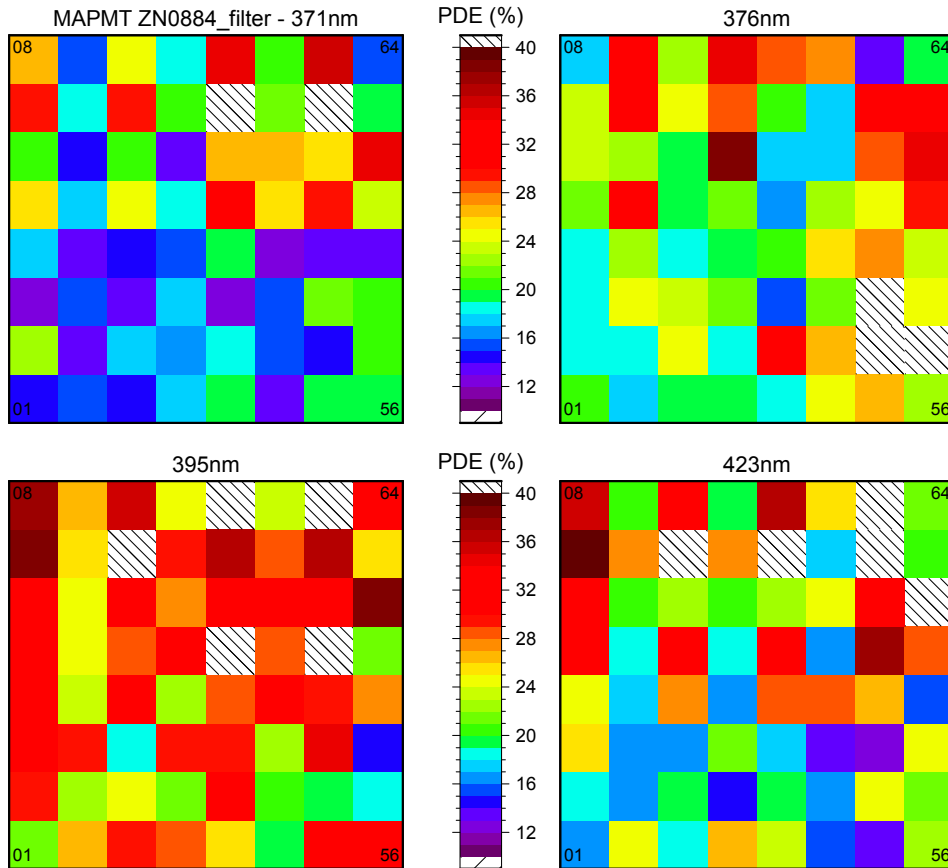
Figure 5.13: PDE maps of the single pixel scans of MAPMT *ZN0884 filter* for different wavelengths at −1000 V bias voltage. The MAPMT has a UV transmitting band pass filter *Schott BG3* [DS62] directly glued to its photocathode. Some pixels show a PDE above 40 % and are marked with a line pattern.

5.2.2 *Different gains*

In order to check how the MAPMTs behave with different operation voltages, the following measurement was taken [123]. Pixel 43 of MAPMT *ZN0882* was chosen at random and the light source was positioned in the middle of pixel 43. The measurement procedure was the same as explained above, with collimator ratio, pedestal, timing, and light level finding measurements. For the main measurement, nine spectra were taken with different voltages between −800 V to −1200 V, each spectrum with roughly 2.25 million data values. After a waiting time, allowing the

photocathode to settle down after the exposure to light, dark counts were measured for pixel 33 to 48 within the same voltage range. Afterwards the collimator ratio and the pedestal were measured again.
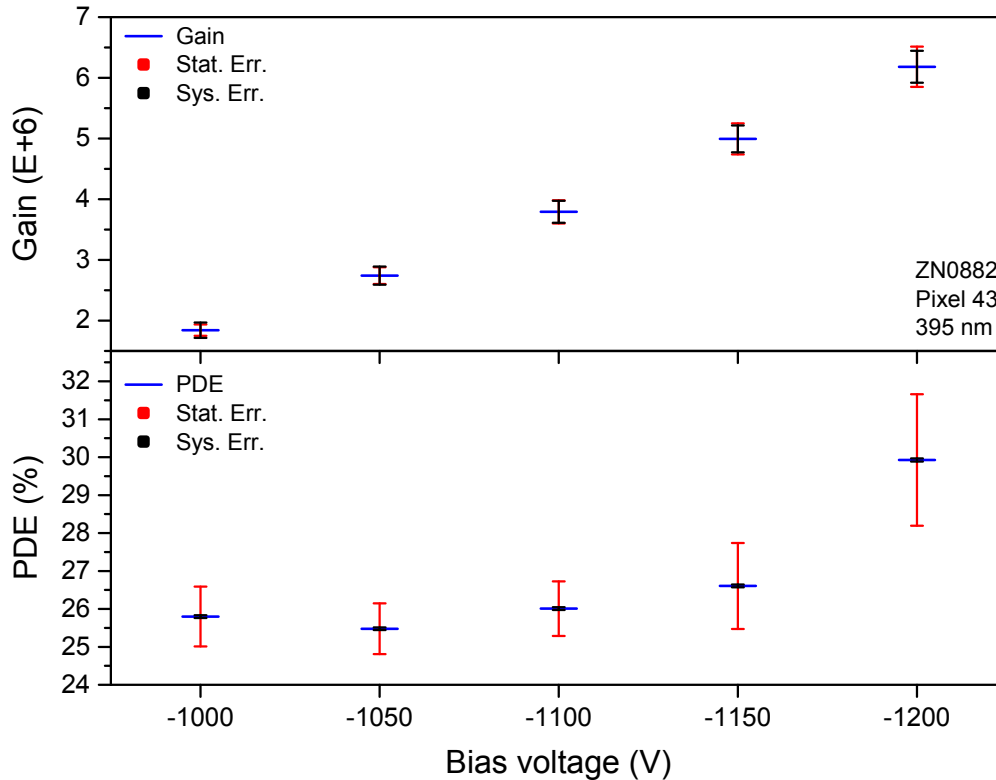
Figure 5.14: Gain and PDE versus voltage of pixel 43 of MAPMT *ZN0882* for 395 nm wavelength at different bias voltages between −800 V to −1200 V. The data was measured by Simon Ehnle during the course of his bachelor thesis [123].

Figure 5.14 shows the gain versus voltage of pixel 43 of MAPMT *ZN0882* for 395 nm wavelength at different bias voltages between −1000 V to −1200 V. Actually also spectra for voltages from −800 V to −950 V were taken, however there the gain was too low for an identification of a *1 pe* peak. For −950 V first events outside the pedestal started to appear, but a peak could not be fitted. From −1000 V onward the peak separation was increasing with increasing voltage. However for −1150 V to −1200 V the Gauss fits became more inaccurate, resulting in larger statistical uncertainties. Also random arcing occurred for voltages above −1100 V. This is not surprising, since the maximum voltage given by Hamamatsu is −1100 V Figure C.30. The gain starts out with a linear increase for the first three voltages up to −1100 V. From there the increase in the gain starts deviating slightly from the linear increase. The similar behaviour can be seen in the PDE versus the wavelength. For the first three voltages the PDE is relatively constant. As soon as random arcing occurs, the PDE is increased, as well as its statistical errors. Although a higher voltage increases the gain and thus the peak separation, it does not increase the accuracy of the measurement. Therefore the standard voltage of −1000 V for the given MAPMTs is a value suitable for calibration.

5.3 MAPMT CALIBRATION RESULTS

The expected systematic uncertainties of SPOCK are estimated for the gain and the PDE via the formulas given in Section 5.1.3. Equation 5.4 is used for the calculation of the gain via both peak positions X_0 and X_1, the proportionality factor k of the QADC and the electron charge e. Of these only the electron charge has no systematic uncertainty. The relative errors in the peak positions are given by the non-linearity of the QADC of 0.1 %. The proportionality factor k has for the *low range* a mean relative uncertainty of 3.9 % (Section 4.4.1 and Table 4.4). Since all others are independent variables we add their squared uncertainties, to get an estimation for the relative systematic uncertainties in the gain:

$$\frac{\Delta_G}{G} = \sqrt{\left(\frac{\Delta_{X_1}}{X_1}\right)^2 + \left(\frac{\Delta_{X_0}}{X_0}\right)^2 + \left(\frac{\Delta_k}{k}\right)^2}$$
$$= \sqrt{(0.1\,\%)^2 + (0.1\,\%)^2 + (3.9\,\%)^2} \approx 3.9\,\% \quad . \tag{5.7}$$

The proportionality factor k is clearly dominating the systematic uncertainty in the gain. This estimation for the mean systematic uncertainties actually slightly overestimates the systematic uncertainties, when compared to the calculated individual values from the measurements. This calculation is used for the estimation of the systematic uncertainties of mean values, e. g. for one whole MAPMT.

Via the number of detected photoelectrons from the Gauss fits N_{pe} and the number of incident photons Equation 5.6 the systematic uncertainty in the PDE is estimated (Equation 5.5). The relative systematic uncertainty of the Gauss area is approximated via the width and the height of the fitted peak (Equation A.6). The systematic error in the width is dependent on the QADC non-linearity. This yields via the quadratic sum for the number of detected photoelectrons $\frac{\Delta_{N_{pe}}}{N_{pe}} = \sqrt{2} \cdot 0.1\,\%$. The number of incident photons has four variables with systematic uncertainties: The optical power P_{PD}, the collimator ratio R, the wavelength λ, and the pulse frequency f_{pulse}. For the Planck constant h and the speed of light c, no systematic uncertainties are given. The quadratic summation over all of these independent variables yields then, as an estimation:

$$\frac{\Delta_N}{N} = \sqrt{\left(\frac{\Delta_{P_{PD}}}{P_{PD}}\right)^2 + \left(\frac{\Delta_R}{R}\right)^2 + \left(\frac{\Delta_\lambda}{\lambda}\right)^2 + \left(\frac{\Delta_{f_{pulse}}}{f_{pulse}}\right)^2}$$
$$= \sqrt{(1.6\,\%)^2 + \left(\sqrt{2} \cdot 1.6\,\%\right)^2 + (3\,\%)^2 + (10^{-5})^2} \approx 4.1\,\% \quad . \tag{5.8}$$

For $\frac{\Delta_R}{R} = \sqrt{2} \cdot 1.6\,\%$ the uncertainty estimation according to Equation A.10 was used. For the incident photon number the uncertainty in the wavelength domi-

nates. Further, the uncertainty in the number of incident photons also dominates the systematic uncertainty in the PDE. It is:

$$\frac{\Delta_\epsilon}{\epsilon} = \sqrt{\left(\frac{\Delta_{N_{pe}}}{N_{pe}}\right)^2 + \left(\frac{\Delta_N}{N}\right)^2} \approx \frac{\Delta_N}{N} \quad .$$

Since spectroscopic measurements of the used LEDs (and thus of the wavelengths) have been done (Section 4.3.2.2), the wavelength uncertainty can be reduced. For the estimation of the relative systematic uncertainty in the PDE follows as shown in Table 5.1. Detailed calculations for the systematic and statistical uncertainties in the gain and the PDE can be found in Appendix A.5.

Table 5.1: LED-arrays with the used LED types, their measured wavelength λ, the half width half maximum Δ_λ of the wavelength, the relative systematic wavelength error $\frac{\Delta_\lambda}{\lambda}$, and the relative uncertainty in the PDE $\frac{\Delta_\epsilon}{\epsilon}$ for mean PDE values. These values apply to MAPMTs and SiPMs, since the number of incident photons dominates the systematic uncertainties in the PDE.

ARRAY	LED	λ (nm)	Δ_λ (nm)	$\frac{\Delta_\lambda}{\lambda}$ (%)	$\frac{\Delta_\epsilon}{\epsilon}$ (%)
all	photodiode	all	—	3.00	4.08
AR1	UVLED365-110E	371	±6	1.62	3.20
AR2	XSL-375-3E	376	±5	1.33	3.06
AR3	VL390-5-15	395	±7	1.77	3.30
AR4	VL425-5-15	423	±8	1.89	3.36

5.3.1 *Gain*

A better representation of the data from the single pixel scans, shown as heat maps in Section 5.2.1, is to present the gain and the PDE versus the pixel number, together with the statistical and systematic uncertainties of every measurement. In addition, also the mean gain or respectively the mean PDE with its respective standard deviation can be easily shown. From the uncertainties in the graphs, the accuracy of the Gauss fits can be estimated and statistical outliers can be identified. Of course, showing the single histograms would be the most accurate method to find failed Gauss fits. Since this cannot be handled easily, we restrict ourselves for the present thesis to the following representation of the data and choose to look at histograms of "suspicious" pixels.

An example for the gain with different wavelengths versus the pixel number for MAPMT *ZN0882* is given in Figure 5.15. The gain for every pixel with its statistical and systematic errors is given. The uncertainties were calculated via the formulas given in Appendix A.5. The mean gain (dark yellow line) and its standard deviation (dark yellow dash-dot) are given as horizontal lines. The 0.01 level limits of the Grubbs outlier test are also shown (dark cyan dashed line). No statistical outlier was detected for all wavelengths for this MAPMT.
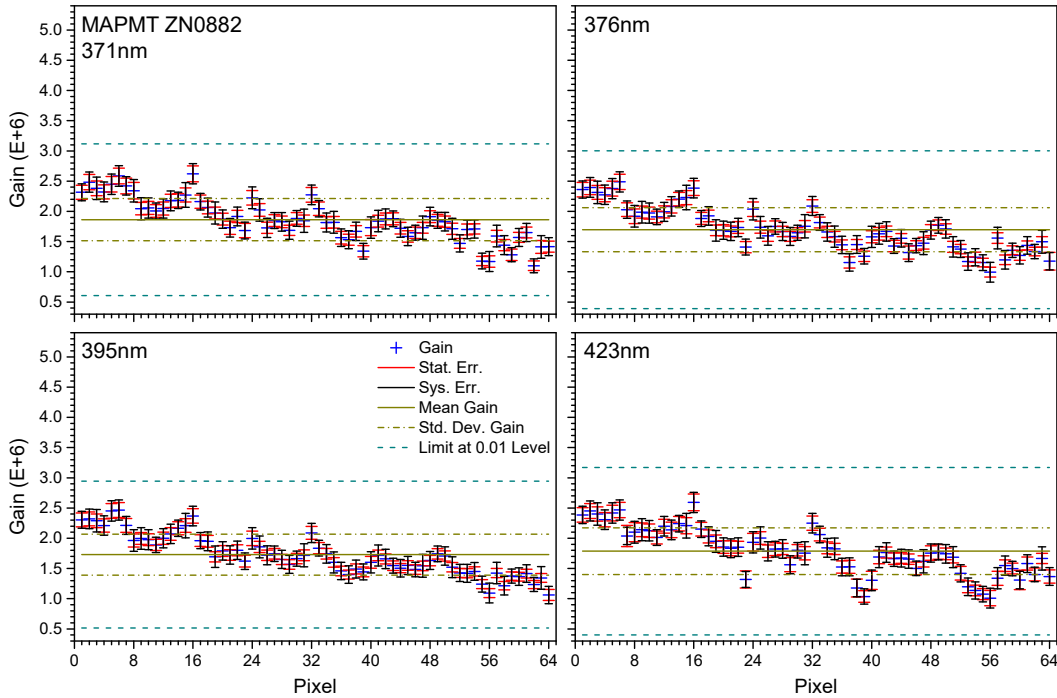
Figure 5.15: Graphs of the measured gain for different wavelengths versus the pixel number for MAPMT *ZN0882*. No statistical outlier was detected.

The gain decreases with increasing pixel number. Since the statistical and systematic errors are in a similar range for every pixel and wavelength and there are no suspicious data points apparently visible for this MAPMT, we conclude that this decreasing gain with wavelength is not a measurement error. It could stem from the inner dynode structure of the MAPMTs (it is also seen in MAPMT *ZN0857*). An effect of the voltage divider is unlikely, since its stages are connected to one whole layer of dynodes at all times. As expected, the mean gain for every wavelength stays roughly the same for all measurements, within its standard deviation and estimated systematical error (see Table 5.2).

The behavior of the gain for all MAPMTs can be seen in Appendix A, Figures A.17 and A.18. For MAPMT *ZN0854 filter* the decreasing gain with pixel number is not that apparent as in the other MAPMTs. Also for 423 nm some of the pixels were detected as outliers, and were masked for the analysis. Three data points with large statistical errors remain, but are not classified as outliers. All shown data points were included in the calculation of the mean values. For MAPMT *ZN0857* some pixels with higher gain are present for all wavelengths. Pixels showing that behavior are mainly at the edge of the MAPMT. Pixels 49 to 64 showed random arcing and were therefore not recorded. The overall reduction in gain with pixel number is also noticeable in this MAPMT. *ZN0882* and *ZN0882 filter* exhibit a similar behavior of the gain, decreasing with pixel number for all wavelengths and no outliers or suspicious values are present.

5.3.2 *PDE*

The same kind of representation is given for the PDE and it statistical and systematic errors, stemming from the single pixel scans. Figure 5.16 is shown as an example. The PDE is for all wavelengths mostly constant with the pixel number, except for some pixels, were the PDE is increased. These are the same pixels, that showed increased PDE values and lowered gain values in the heat maps. A failing Gauss fit seen there before. The statistical errors of these pixels are indeed bigger than their systematical errors. For all other pixels, the statistical errors are smaller than the systematic ones. Therefore this can be used as a requirement to check for suspicious values.

PDE graphs for all MAPMTs can be found in Appendix A, Figures A.18 and A.19. MAPMTs *ZN0857* and *ZN0882* show a very similar behavior, with some pixels having an elevated PDE, with bigger statistical uncertainties than the systematical uncertainties. Some statistical outliers were detected and masked. They are not used for the mean value calculations. For *ZN0854 filter* some data points with statistical errors over 75 % or a negative PDE were masked and are not used in the analysis. They are shown as red triangles. For both MAPMTs with attached filters all data points have statistical errors bigger than the systematic ones. This indicates bad Gauss fits for all pixels. A cause could be the weak light level and consequential a very small peak separation.
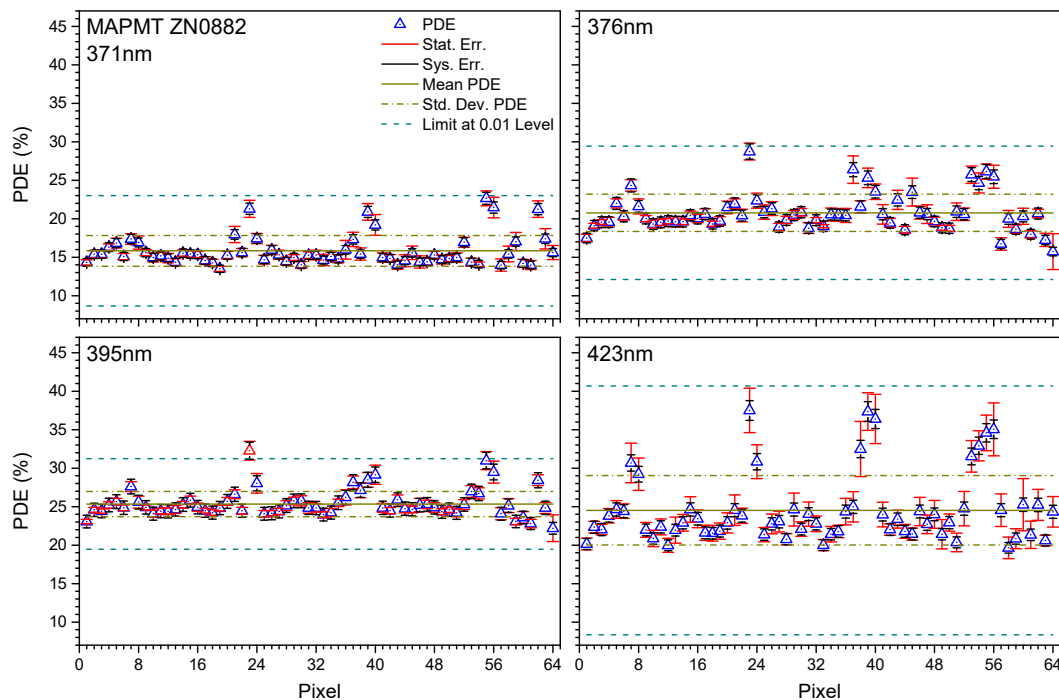
Figure 5.16: Graphs of the measured PDE for different wavelengths versus the pixel number for MAPMT *ZN0882*.

For the analysis of the spectral PDE, the mean PDE values of 64 pixels were plotted versus the respective wavelength for each MAPMT in Figure 5.17. On the left side the MAPMTs without a filter are shown, on the right side, the ones with fil-

ter. The systematic errors are shown as black error bars. For the systematic wavelength uncertainty the respective wavelength error was used (Table 5.1). For the datasheet PDE of the *Hamamatsu R11265-113-M64 MOD2* MAPMT no data was available. Therefore data for the quantum efficiency versus wavelength of a prototype from 2009 (*R11265-00-M64 MAPMT*) was provided by the manufacturer to the JEM-EUSO collaboration and then provided to the research group by Naoto Sakaki [135] via the Extreme Universe Space Observatory (EUSO) Simulation and Analysis Framework (ESAF). The PDE was estimated as a product of the quantum efficiency and a uniform collection efficiency of the MAPMT of 0.8. The estimated PDE is shown as a dashed line.
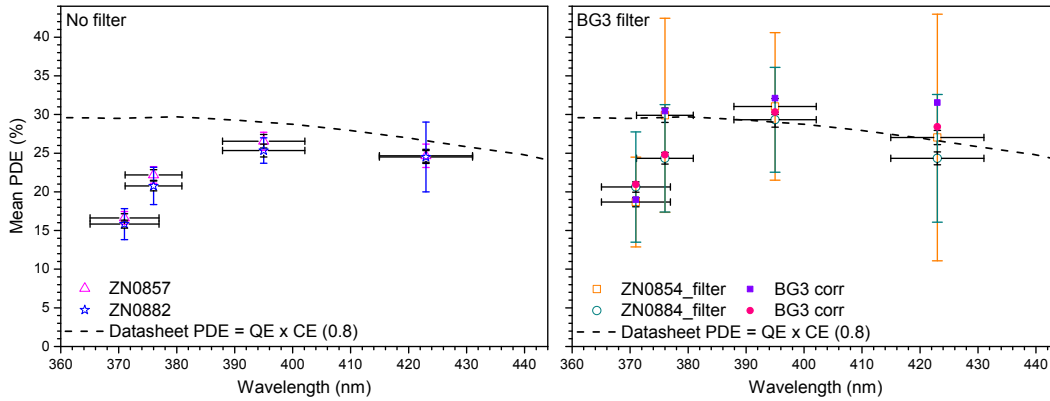
Figure 5.17: PDE that was measured and given by the manufacturer versus wavelength for all MAPMTs.

All MAPMTs show a similar behavior of the PDE with increasing wavelength: increasing for the first three wavelengths and decreasing slightly for the last wavelength. The statistical errors of the MAPMTs with filters are very large, while the ones for the MAPMTs without filter are lower than the systematic errors. However, the filter MAPMTs were measured to have a higher PDE. Further their PDE was underestimated, since the number of incident photons has to be corrected with the filter transmittance of the *BG3 filter*. A part of the photons sent onto the detector are attenuated by the filter. We get the number of photons N_x hitting the MAPMT after passing the filter, by multiplying the transmission coefficient T with the photon number N sent onto the filter. So the real number of incident photons was smaller, increasing the real PDE of the MAPMTs with filter. The corrected PDE values are shown in Figure 5.17 on the right side, exceeding the datasheet PDE. Because of the large statistical uncertainties the PDE values for the MAPMTs with filters should not be used as calibration measurements outcome. Table 5.2 shows the mean PDE values for each MAPMT, as plotted in Figure 5.17, with their respective uncertainties. An explanation for the higher PDE values of the filter MAPMTs might be again some bad Gauss fits, overestimating the number of events in the *1 pe* peak. This matter needs more investigation.

Table 5.2: For every MAPMT and wavelength the gain G_λ with its uncertainties, the mean gain G_{mean} with its uncertainties, as well as the PDE with its uncertainties, are given. The systematic uncertainties in the gain were calculated via the 3.9% relative uncertainties (Equation 5.7). The systematic uncertainties in the PDE were calculated via the wavelength dependent relative uncertainties (Table 5.1).

MAPMT	λ (nm)	G_λ (e+6)	σ_{G_λ} (e+6)	Δ_{G_λ} (e+6)	G_{mean} (e+6)	σ_G (e+6)	Δ_G (e+6)	ϵ (%)	σ_ϵ (%)	Δ_ϵ (%)
ZN0854 filter	371	0.94	0.33	0.04	0.93	0.03	0.04	18.68	5.80	0.60
	376	0.88	0.33	0.03				29.90	12.55	0.93
	395	0.90	0.31	0.03				31.68	10.78	1.02
	423	0.90	0.64	0.03				27.03	15.95	0.92
ZN0857	371	3.45	0.44	0.13	3.37	0.14	0.13	16.57	0.71	0.53
	376	3.35	0.45	0.13				22.18	1.07	0.69
	395	3.48	0.45	0.14				26.53	1.18	0.88
	423	3.18	0.40	0.12				25.21	2.29	0.84
ZN0882	371	1.86	0.35	0.07	1.77	0.07	0.07	15.83	2.00	0.51
	376	1.70	0.36	0.07				20.76	2.42	0.64
	395	1.73	0.34	0.07				25.34	1.64	0.84
	423	1.79	0.39	0.07				24.52	4.51	0.83
ZN0884 filter	371	0.82	0.27	0.03	0.83	0.02	0.03	20.62	7.13	0.66
	376	0.83	0.23	0.03				24.34	6.94	0.75
	395	0.85	0.22	0.03				29.32	6.78	0.97
	423	0.82	0.27	0.03				25.02	9.83	0.83

5.4 DISCUSSION

To summarize, SPOCK was used to take single photon measurements with four different wavelengths for four different MAPMTs. Two of which were as delivered by the manufacturer and two had a UV transmitting filter attached. Data taking was done by illumination of single pixels, scanning them one by one. The number of data points taken per pixel was at least 100 000. The measured data values were counted and histograms with discrete frequencies were made for every pixel and wavelength (Figure 5.10). The developed Gauss fit algorithm did fit the *0 pe* and *1 pe* peak for every histogram. From the peaks and their separation the gain and PDE were calculated via a python algorithm, programmed by Simon Ehnle during the course of his bachelor thesis [123]. The obtained data was plotted as heat maps and in an equivalent representation versus the single pixel numbers. The statistical errors are an indicator for the quality of the Gauss fit. This shows that the fitting algorithm for the Gauss peaks needs still some work and has room for improvement. Data analyzed with a manual Gauss fit done with *OriginLab Origin 2015* has in all cases a better precision. However, the latter is a manual process, and not feasible for all the data obtained during one measurement (64 histograms).

Figure 5.18 shows three examples of typical failed Gauss fits. The upper plot shows a *1 pe* peak fit, that is not there. In the middle plot the peak separation is bad, so that the *1 pe* peak is too much to the left and too wide, reducing the *0 pe* peak.
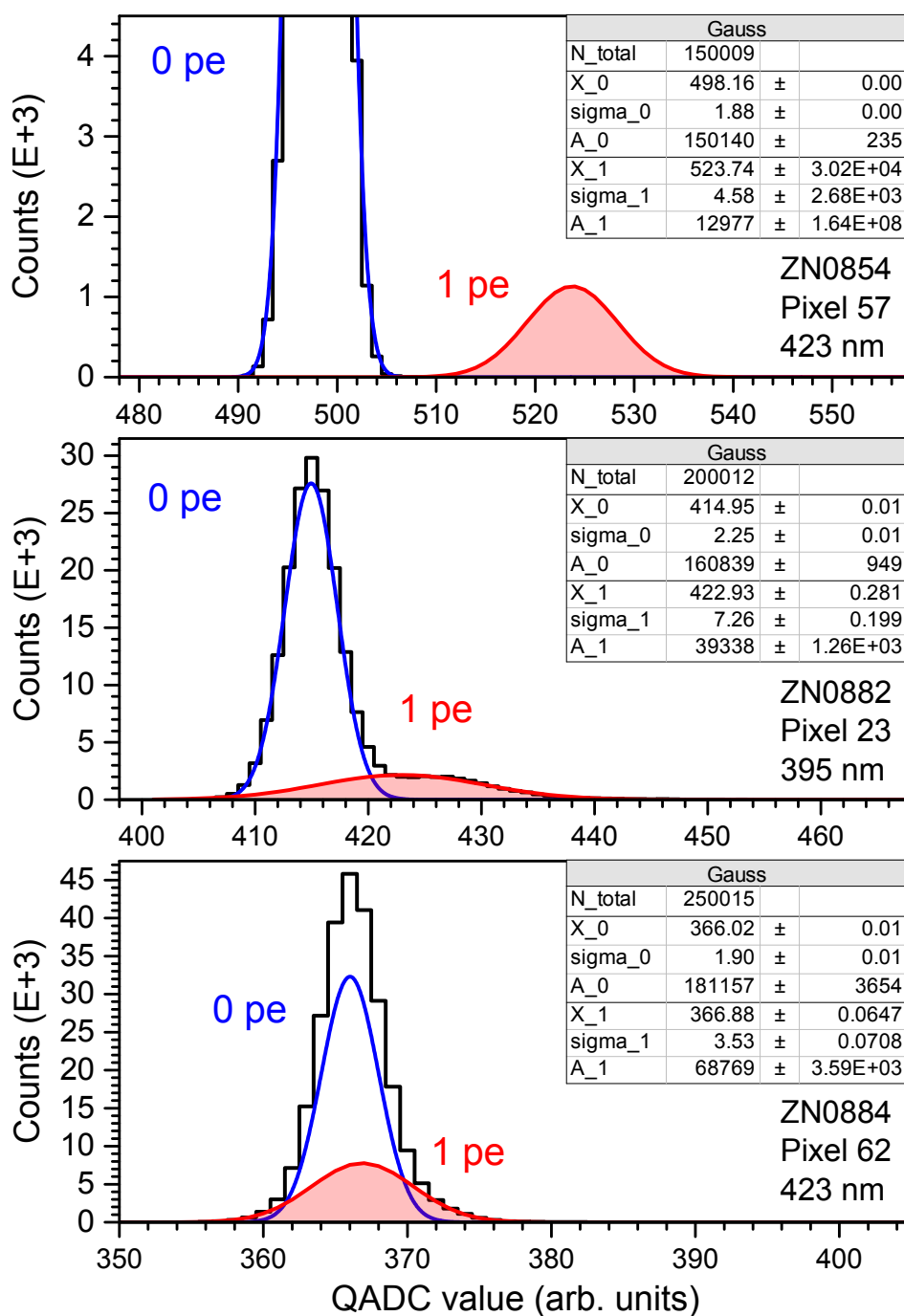
Figure 5.18: Three histograms with failed Gauss fits [123]. The upper plot shows a *1 pe* peak fit, that is not there. In the middle plot the peak separation is bad, so that the *1 pe* peak is too much to the left and too wide, reducing the *0 pe* peak. The lower plot shows almost no peak separation. As a consequence the PDE is in all cases too high. A good Gauss fit was shown in Figure 5.10.

The lower plot shows almost no peak separation. As a consequence the PDE is in all cases too high. In the upper case, all statistical errors are big, leading to an easy identification of that failed Gauss fit. The gain and the PDE might be normal

or a bit high for that one. However, the statistical errors should be large for large Gauss fit errors, since the latter dominate the statistics of the gain and the PDE. In the other cases the gain is show very small, but the PDE is calculated to be quite high. This in correspondence with high statistical errors in the Gauss fit area leads leads also to an easy identification of a bad histogram.

Histograms like these are to be responsible for the high PDE and low gain of the filter MAPMTs. As stated before, their statistical uncertainties are too high, leading to the conclusion, that filter MAPMTs cannot be calibrated with the low light level, that was used for these measurements. Further measurements should be done with higher light levels to validate if they can be calibrated after the filter was glued to their photocathode.

One of the MAPMTs, *ZN0857* without a filter, was found to be partly broken. Here pixels from 49 to 64 (Figure A.12) showed random arcing, visible as large charge spikes and far more frequent than dark counts. The rest of the pixels however had a larger gain than any other tested MAPMT.

The gain of the MAPMTs increases linearly with the voltage until a certain point, from that onward random arcing inside the dynode structure of the MAPMT can occur. The PDE is constant with the voltage until the arcing point. There random sparks are wrongly counted as *1 pe* events and therefore the PDE is overestimated for higher voltages.

As a conclusion, this chapter showed that SPOCK fulfills the requirements for the the calibration of MAPMTs without an attached filter. However, the data analysis needs a bit more work, for an automated process. The identification of good and bad data points is done via the statistical and systematic uncertainties of the single data points and via the histograms, when in doubt. The overall accuracy in terms of systematics is with 3.1 % to 4.1 % in the *relative uncertainty of the PDE* and with 3.9 % of *relative uncertainty in the gain* sufficient for an accurate calibration of MAPMTs for JEM-EUSO. One of the present calibration stands did report a relative uncertainty in the PDE of under 2 % [76]. But there the uncertainty in the wavelength (3 %) was neglected and only the uncertainty of the photodiode (1.6 %) was regarded for the estimation of the systematic uncertainty of the PDE. In our opinion the wavelength uncertainty has to be regarded for a more realistic uncertainty estimation. The measurements presented in this chapter are proof that SPOCK is usable for any future experiment which need photodetectors that are calibrated in single photon mode and have up to 64 channels per detector.

<div style="text-align: right; font-size: 3em;">6</div>

SILICON PHOTOMULTIPLIERS

Rapid advances in improving SiPMs within the last years made these relatively new photodetector devices more and more attractive for scientific experiments, where large modular detector surfaces, low power consumption, less HV, or no magnetic field sensitivity are needed [73, 136, 137]. Their properties are also interesting for technical applications that rely on the detection of fast light signals, e. g. PET-scans [138]. These interesting properties include a very short response time (several hundred ps), single photon detection capabilities, high PDE, low bias voltages around 70 V, high light damage resistance, insensitivity to magnetic fields, very compact size, low mass, and low cost. Because of the semiconductor nature of this device, however, certain disadvantages are present, like a strong temperature dependence of dark counts, the gain and the applied overvoltage as well as the presence of optical crosstalk and afterpulses. Therefore, additional temperature control has to be implemented. This can be a challenge in space-based experiments like JEM-EUSO. That is why SiPM photodetectors have to be tested in the laboratory and in the JEM-EUSO pathfinder experiments very precisely for the future use in JEM-EUSO. The advantage of the calibration stand SPOCK, that was developed during this work, is that it can directly compare the performance of MAPMTs and SiPMs with the same systematics, since the light source and the readout electronics are the same for both detector types.

   This chapter will start with a general introduction to SiPM photodetectors and the measurements taken. First the working principle of SiPMs, the physics behind, and the 'recipe' for SiPM measurements will be explained (Section 6.1). Afterwards, first measurements taken with SPOCK (Section 6.2) and their results (Section 6.3) will be shown. In the end of this chapter the results and experiences gained during this work will be discussed (Section 6.4).

6.1 WORKING PRINCIPLE

The following explanations and general theoretical principles of SiPMs are summarized from [82, 139, 140]. SiPMs or also called multi-pixel photon counters (MPPCs), are semiconductor photodetectors using the *internal photoelectric effect* (photoconductive effect) to convert light into an electrical signal (Section 5.1.1). Each channel of a SiPM is comprised of an array of identical pixels, where each pixel consists of a Geiger-mode avalanche photodiode (G-APD) and a *quenching resistor*. The G-APD and the resistor are connected in series. The pixels are connected in parallel to a bias voltage V_{bias}. The SiPM-pixels should not be confused with the MAPMT-pixels,

mentioned in the previous chapter. For an MAPMT every output channel gets the signal from one pixel (anode). For a SiPM there can be several hundreds or even thousands of pixels per output channel, with every pixel (cell) giving the same signal, when a photon hits one.

6.1.1 *Geiger-mode avalanche photodiode*

As mentioned above, a SiPM channel consists of several hundreds of pixels (or cells), that each are a G-APD and a quenching resistor. The key to understanding the working principle of SiPMs is to have a closer look at the G-APD.

Figure 6.1 shows the sketch of the pn-junction of a G-APD with the corresponding electric field and the photon flux for shorter and longer wavelengths versus the depth of the structure. The bias voltage V_{bias} is in reverse direction, resulting in the shown electrical field. The bias voltage is also a few volts higher than the breakdown voltage V_{br} of the diode. The difference of these two voltages is called the overvoltage ΔV and defines the properties of an G-APD (see Figure 6.2). When sending a photon onto a G-APD, in can penetrate to different depths (layers) of the G-APD structure, depending on the wavelength of the photon and on the absorption coefficient of the material. When a photon penetrates into the p^+-layer it can
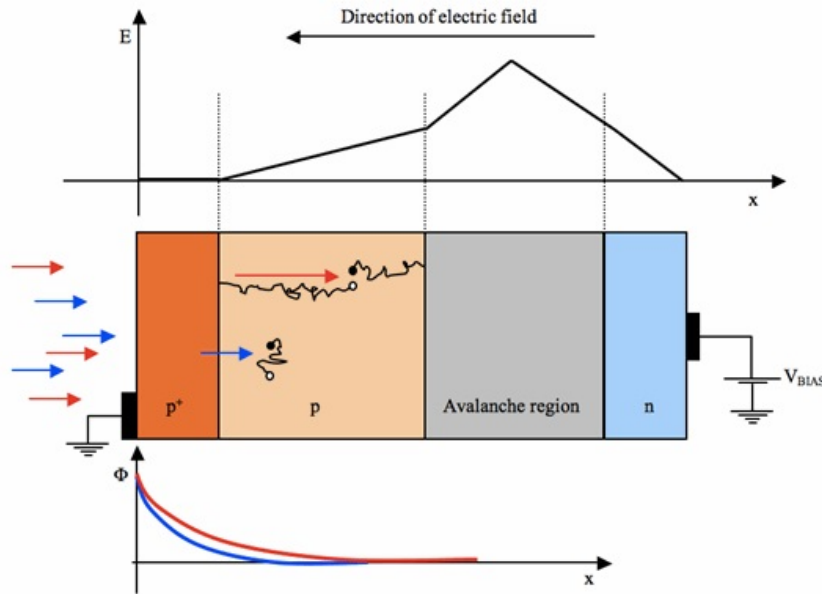
Figure 6.1: Sketch of the pn-junction of a G-APD showing the electric field and the photon flux [140].

excite an electron into the conduction band. The photon energy has to be greater than the bandgap of the layer for this. Since the photoelectron is not leaving the material, this is called the internal photoelectric effect. This can also be seen as the creation of a free electron-hole pair. The probability for the production on an electron-hole pair is given by the quantum efficiency $\eta(\lambda)$. It is defined as the ratio

of the number of photon-produced electron-hole pairs n_{e-h} and the the number of incident photons on the photosensitive area n_λ:

$$\eta(\lambda) = \frac{n_{e-h}}{n_\lambda} \quad . \tag{6.1}$$

The probability for recombination in the p^+-layer is high, since the electrical field is weak in this region. The desired semiconductor material would be one with an indirect band gap, to get mostly non-radiative recombination and longer electron-hole pair lifetimes. When a photon penetrates into the p-layer and produces an electron-hole pair, the pair is separated by the internal electrical field. These separated moving charge carriers produced by photons are also called the photocurrent. The hole is diffused into the p^+-layer and recombines. The electron is accelerated towards the avalanche region (n-layer), through the remaining p-layer, where the probability for recombination is very low, since there are no free charge carriers (depletion region). When the electron reaches the avalanche region further free charge carriers are created via impact ionization, with a certain probability [140]. This means that the total current in the junction is rising, leading to an increased voltage drop over the quenching resistor and a decreased voltage drop over the G-APD. Since the voltage drop affects the electric field, the probability for impact ionization is decreased, the avalanche reaches its maximum, and declines. The maximum is typically reached within the time of about 1 ns. After the maximum the current drops and the voltage rises again to pre-avalanche levels. This can take up to tens of nanoseconds. The signal of one G-APD resulting from that is a current pulse with a peak value that is proportional to the ratio of the overvoltage and the quenching resistor. For every G-APD within a SiPM channel, this signal height is the same. The size of the avalanche (number of free charge carriers) is typically in the range of 10^5 to 10^6, depending on the overvoltage and is called the gain. Analogue to the gain of PMTs it can be expressed as the ratio of the resulting total charge at the anode Q and the fundamental charge e. Furthermore the total current in the G-APD is the photocurrent amplified by the gain.
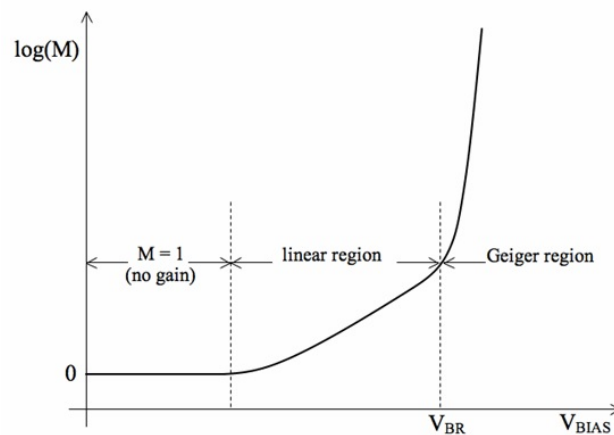
Figure 6.2: Sketch of the the working point of an APD showing the logarithmic gain versus the reverse bias voltage. There are three operation regions: the photodiode region (no gain), the linear region, and the Geiger-region [140].

The logarithmic gain over the reverse bias voltage for an avalanche photodiode is schematically shown in Figure 6.2. An avalanche photodiode can be operated in three different modes, depending on the overvoltage. The first region with a bias voltage well below the breakdown voltage, is the *no gain region*, where the avalanche photodiode is working like a normal photodiode. Here the electrical field in the avalanche region is too weak to accelerate electrons over the minimal energy threshold for impact ionization. The second region, with a higher bias voltage (up to the breackdown voltage) is the *linear region*, with a stronger electric field and thus a positive gain. The energy threshold for impact ionization is reached, but not high enough to produce an ongoing avalanche. In the linear region the avalanche stops by itself without any quenching resistor. The third region, with an applied overvoltage, is the desired operation mode region for SiPMs: the *Geiger-mode region*. Here a strong electric field is present, leading to an ongoing avalanche. Since the junction current is dependent on the gain, this means that the output signal of G-APD is very sensitive to the overvoltage. Here the quenching resistor is needed to stop the avalanche, by reducing the bias voltage at least to value of the breakdown voltage.
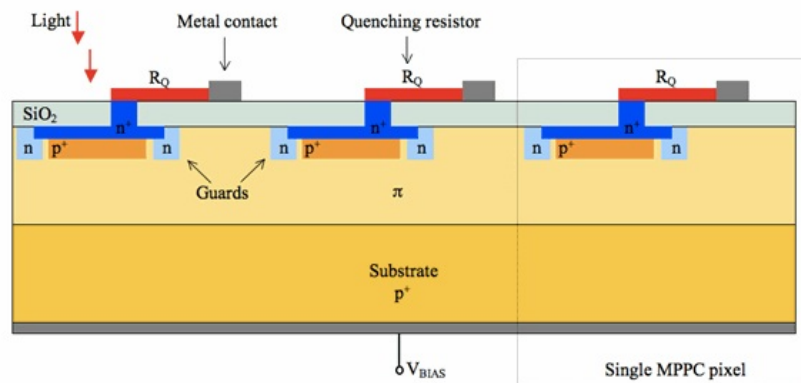
Figure 6.3: Sketch of a typical SiPM showing its inner structure of three pixels [140].

Figure 6.3 shows the typical structure of three pixels of a SiPM from the side. The metal contacts, the quenching resistors (R_Q) and the pn-junctions are clearly visible. The thickness of the whole structure is in the range of 310 µm. Photons have to pass an anti-reflection layer ($\approx$ 10 nm) and a silicon-oxide isolation layer ($\approx$ 150 nm), before passing the depletion region ($\approx$ 1 µm), formed at the boundary of the n$^+$-p$^+$-junction (a few µm). When the photon reaches the thick π-layer (300 µm thick, lightly n-doped layer), it can create an electron-hole pair. The electron is moved towards the depletion region where is can initiate an avalanche. The hole is moved towards the bottom p$^+$-layer (3 µm) where it recombines. Since photons have a material specific penetration depth, the structure and geometry of the G-APD definitely has an impact on the performance of the device, e. g. if the photons one wants to measure never reach the π-layer and produce no electron-hole pairs, then the device is not operational. This was the case for an earlier generation of SiPMs (MPPC S12642) and UV-photons below 325 nm wavelengths, where the coating on top of the SiPMs absorbed these UV-photons [125, DS141]. On the other hand, the metal contacts on top of the G-APDs are not transparent and therefore de-

crease the effective area. This is expressed via the fill factor F_g, which gives the ratio of the sensitive area and the geometrical area of a G-APD. The PDE of a G-APD can be expressed via the quantum efficiency η (Equation 6.1), the probability to generate an electron-hole pair, via the fill factor F_g, and via the probability P_a to start an avalanche in the depletion region:

$$\epsilon = \eta \cdot F_G \cdot P_a \quad . \tag{6.2}$$

In general, the performance of G-APDs is dependent on the temperature of the junction. With temperature, several parameters like the breakdown voltage and the quench resistor change. This is mainly because of the temperature dependence of the bandgap in semiconductors [104, 105]. Further more, temperature can create noise: Phonons can create electron-hole pairs, which then can trigger an avalanche and lead to signals that are indistinguishable from photon-induced signals. This kind of noise is called *dark noise* [140]. It is dependent on the overvoltage, the temperature, pixel size, and the semiconductor quality. As the name suggests, this noise is not correlated to any photons incident on the detector and therefore always present, as soon as an overvoltage is applied.

A second source of noise during the measurements can be *afterpulses*. They are secondary signal peaks after the main signal, caused by the release of trapped charge carriers after some delay. Their absolute height is normally around the *1 pe* level. If the delay of the afterpulse is longer than the recovery time of the G-APD, then the afterpulse is not distinguishable from the signal pulse. Afterpulsing increases with the overvoltage and with the pixel size [139].

Optical crosstalk within a SiPM may happen, when the charge carriers of an avalanche generate photons, that reach another pixel and cause an avalanche there. The emission of photons mainly happens due to direct and indirect recombination as well as scattering of electrons on positive ions [142]. To cause an avalanche in another pixel the emitted photons have to be absorbed in the sensitive region of the second pixel. The crossing time for a photon for a pixel of 25 µm is below 1 ps in silicon. This would lead to a *2 pe* signal for one incident photon, since the emitted photon reaches the second pixel within the relaxation time of the first pixel. However, an emitted photon is more likely to be absorbed in the same pixel it was emitted from, leading to afterpulsing in that pixel. Therefore optical crosstalk decreases with pixel size, but afterpulsing (because of emitted photons) increases. Furthermore, optical crosstalk can be prevented via optical trenches between the single pixels [143]. With an increasing overvoltage, the gain is increased and thus the emission of photons increases.

Newest generations of SiPMs use through-silicon vias (TSVs) for connecting the top layers with the bias voltage, while getting rid of the quenching resistors and the metal contacts on top of the photosensitive area [DS124]. This effectively increases the photosensitive area of the device. Other improvements have been implemented by Hamamatsu, like the use of a silicon layer (UV transmitting) instead of an epoxy layer (UV absorbing). In general the newest generation of SiPMs have been improved in every way, with less dark counts, less afterpulsing, and less crosstalk. Several single TSV SiPMs and even an 8×8 array of TSV SiPMs were

available for this work. However, no temperature dependent voltage control and read-out circuit were available in time for these newest generation SiPMs to be tested with SPOCK during the course of this work. As a consequence, for the measurements of this work an older generation ceramic packaged SiPM *Hamamatsu S12572-100C* with 900 pixels connected to one read-out channel and a sensitive area of 3 mm × 3 mm was used [DS144]. The SiPM was connected to a *Hamamatsu Evaluation Board C12332*, being used for controlling the bias voltage, measuring the temperature, and amplifying the signals from then SiPM [DS145].

6.1.2 *The finger spectrum*

As mentioned above, the signals from a pixel (G-APD) within a SiPM are current pulses, with a height depending on the overvoltage and the quenching resistor. A capacitance C_J can be assigned to the G-APD of the pixel. If an avalanche is triggered, the capacitance is unloaded. The rise time of the current pulse is typically within 1 ns. The relaxation time is in the range of tens of nanoseconds and due to the quench resistor and the capacitance of the junction [140].

Figure 6.4 shows the sketch of such a typical current pulse for one photon from one pixel on the left side. The resulting charge of the avalanche in one pixel is the integral of the pulse and amounts to $Q = C_J \cdot \Delta V$. Since the avalanche is in progress during the pulse, the pixel is blind to another photon hitting the same pixel, since there is no electrical field any more. During the relaxation time, the probability for the pixel to be ready again rises, while the voltage and the electrical field build up again. So even if two or three photons hit the same pixel at the same time, the signal emitted is still the same as shown. During the relaxation time the electrical field is built up again, this leads to an increasing probability to fire the pixel again. At full relaxation the pixel is ready again. A non relaxed pixel can also detect another photon, but the probability that a new avalanche starts during relaxation is lower. The signal from such a non-relaxed state is smaller in amplitude (smaller electric field), but it will start from the relaxation curve, leading to the same absolute signal height as the main signal. If different pixels are triggered by several photons at the
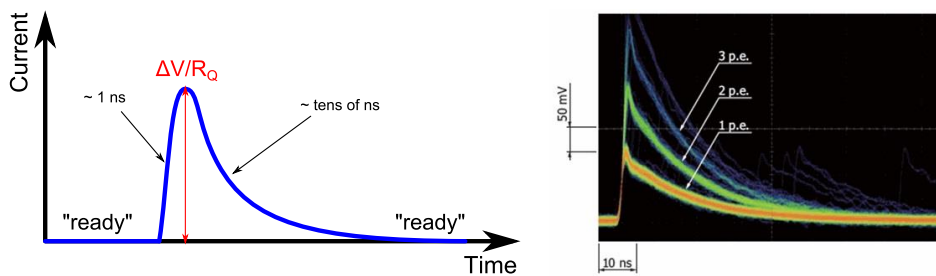
**Figure 6.4:** Sketch of a typical SiPM pixel signal and an oscilloscope screenshot of SiPM measurements. (both adopted from [140]).

same time, the charge per pixel has to be multiplied by the number of fired pixels N_{fired}. The signals are added because of the parallel circuit. This kind of behavior leads to a dynamic range of a SiPM channel that is not linearly increasing with the

number of pixels in a channel. The number of fired pixels N_{fired} is a function of the number of pixels n, the number of photons N incident on the SiPM, and the PDE ϵ (Equation 6.2) [140]:

$$N_{fired} = n \cdot \left(1 - \exp\left(-\frac{N \cdot \epsilon}{n} \right) \right) \quad . \tag{6.3}$$

On the right side of Figure 6.4 an oscilloscope measurement with an illuminated (low light level) SiPM is shown. The shown waveforms correspond to the added signals from different numbers of simultaneous fired pixels. The *1 pe* waveforms denote the signals, where only one pixel was fired. This does not mean, that only one photon did hit one pixel when such a waveform occurs. It could also have been five photons hitting the same pixel. This is due to the "digital" nature of the SiPM pixels. The *2 pe* and *3 pe* waveforms are the equivalent waveforms for two or three simultaneous fired pixels. Since the oscilloscope was set to the persistence mode, the color coding gives information about the frequency of the waveforms, with *1 pe* being the most common ones. The *1 pe* waveforms with a delay to the main signals are the aforementioned afterpulses, dark counts and crosstalk.
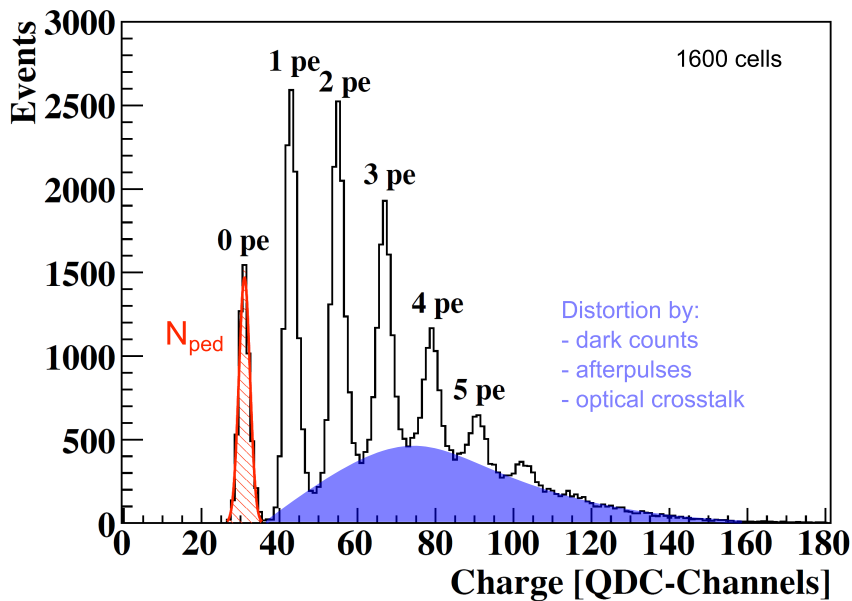
Figure 6.5: A typical finger spectrum of a SiPM. The number of counts is plotted versus the measured QADC values. Because of dark counts, afterpulses, and optical crosstalk the counts go not to zero between peaks. The gain of the SiPM can be calculated from this spectrum via the mean separation of the photoelectron peaks (adopted from [139]).

For SiPMs a histogram of the measured charged can be made, similar to the single photoelectron spectrum for MAPMTs. In the case of SiPMs it is called *finger spectrum*, because of its characteristic shape. The charges are Gauss distributed because of fluctuation in the avalanches. Figure 6.5 shows such a typical finger spectrum for a low light level (adopted from [139]). In the histogram the number of counts is plotted versus the measured QADC values. The most left peak is the pedestal (*0 pe*

peak), where no avalanche was triggered. Then the single, double, triple, ... pe peaks follow. Note that the spectrum does not go to zero counts between the peaks. This is due to a superposition of dark counts, afterpulses, and optical crosstalk with the pe peaks (shaded area).

6.1.3 *The 'SiPM recipe'*

For every channel of an SiPM, a photoelectron spectrum can be recorded, by measuring the charge pulses per light pulse sent onto the SiPM channel. At the same time the light level is recorded and controlled in such a way, that there are several peaks visible. Since there is an omnipresent noise level (dark counts, afterpulses, and optical crosstalk) due to finite temperatures, the area of the Gauss fits of the *1 pe*, *2 pe*, *3 pe*, ... peak can not be used for calculating the detected photons numbers. The pedestal however is unchanged by these sources of noise. Since the pedestal contains all events where no light was measured, it can be used to calculate the number of detected photoelectrons N_{pe}, via Poisson statistics [139].

The recorded finger spectrum comprises of m Gauss peaks X_m and therefore of $n = m - 1$ peak separations x_n. The mean value of the peak separation x is then used to calculate the SiPM gain G (Equation 6.4).

$$x = \frac{1}{n} \sum_{i=1}^{n} x_i \quad .$$

where

x	is the mean peak separation,
$x_n = X_m - X_n$	are the Gauss peak separations of adjacent peaks, and
X_m	individual Gauss peak mean values (Gauss fits).

The gain is then calculated via:

$$G = \frac{x \cdot k}{e \cdot \Lambda} \quad . \tag{6.4}$$

where

x	is the mean peak separation,
k	is the proportionality factor for the charge and the QADC value,
e	is the charge of an electron, and
Λ	is the amplification factor of an amplifier (if applicable).

The Gauss peak separations x are attained by Gauss fits (Equation A.3) with the peak values X_m and measured with the QADC. The value for the proportionality factor k is given in Table 4.4. In the case of these measurements only channel 0 of the QADC was used: $k = (32.08 \pm 1.57_{stat} \pm 1.24_{sys})$ fC. The electron charge is given as $e = 1.602\,176\,565 \times 10^{-19}$ C by the particle data group [128]. The amplification factor Λ used for SiPM measurements shown in this thesis is around 10 [DS145] and was measured to be $10.1 \pm 0.05_{sys}$. In general it can be adjusted to different values.

The PDE ϵ is given by the ratio of the number of detected photoelectrons N_{pe} and the number N of photons sent onto the SiPM (both per pulse):

$$\epsilon = \frac{N_{pe}}{N} \quad . \tag{6.5}$$

The expected number of photoelectrons shall be N_{pe}, then the Poisson equation (Equation 5.2) yields the probability to detect no photoelectron during a light pulse [139]:

$$P_{N_{pe}}(0) = \exp\left(-N_{pe}\right) \quad .$$

The same probability can be expressed via the probability of pedestal events minus the probability of thermal noise events (dark count) polluting the number of detected photoelectrons. Solving the equation for N_{pe} yields the number of *detected photons per pulse*:

$$N_{pe} = -\ln\left(\frac{N_{ped}}{N_{tot}}\right) + \ln\left(\frac{N_{ped}^{dark}}{N_{tot}^{dark}}\right) \quad , \tag{6.6}$$

where

N_{ped}	is the number of pedestal events (Gauss),
N_{tot}	is the total number of events in the spectrum (trigger),
N_{ped1}^{dark}	is the number of pedestal events in
	the first dark spectrum (Gauss),
N_{ped2}^{dark}	is the number of pedestal events in
	the second dark spectrum (Gauss),
N_{ped}^{dark}	is the mean number of pedestal events in the dark spectrum, and
N_{tot}^{dark}	is the total number of events in the dark spectrum (trigger).

Since two dark spectra were recorded, one before and after the measurement, the mean of both is taken for N_{ped}^{dark}:

$$N_{ped}^{dark} = \frac{1}{2} \cdot \left(N_{ped1}^{dark} + N_{ped2}^{dark}\right) \quad .$$

The number of photons *per light pulse* N sent onto the detector is given by the optical power reaching the detector divided by the energy of one photon and the pulse frequency:

$$N = \frac{P_{PD} \cdot R \cdot R_{geom}}{E_{photon} \cdot f_{pulse}} = \frac{P_{PD} \cdot R \cdot R_{geom} \cdot \lambda}{h \cdot c \cdot f_{pulse}} \quad , \tag{6.7}$$

where

|	
P_{PD}	is the mean optical power from the photodiode,
$R = \frac{R_1 + R_2}{2}$	is the mean collimator ratio,
$R_{geom} = \frac{A_{detector}}{A_{PD}}$	is a geometric correction factor,
$A_{detector} = 9 \, mm^2$	is the sensitive detector area [DS144],
$A_{PD} = 100 \, mm^2$	is the sensitive photodiode area [DS91].
$E_{photon} = \frac{h \cdot c}{\lambda}$	is the energy of a sent photon,
h	is the Planck constant: $6.626\,069\,57 \times 10^{-34} \, J\,s$ [128],
c	is the speed of light: $299\,792\,458 \, m\,s^{-1}$ [128],
λ	is the wavelength of the photons, and
f_{pulse}	is the pulse frequency of the LED.

The mean collimator ratio is calculated from the collimator ratio measured before and after the SiPM measurement. For measurements where some of the light from the exit of the collimator may not reach the detectors sensitive area (measurements in a distance), a correction factor R_{geom} has to be multiplied with Equation 6.7. The wavelength was determined with the spectrometer measurements shown in Section 4.3.2.2 and depends on the LED-array used (Tables C.3 and C.4). All corresponding uncertainty calculations can be found in Appendix A.7.

6.2 SIPM MEASUREMENTS

The following explains how the SiPM measurements during this work were done. The measurements with a single channel SiPM were done by Sally-Ann Sandkuhl during the course of her bachelor thesis [146]. Figure 6.6 shows the sketch of the measurement set-up for one channel SiPM measurements. The measurement set-up and procedure are similar to the one explained for MAPMTs.

For the measurements a ceramic packaged SiPM *Hamamatsu S12572-100C* with 900 pixels connected to one read-out channel and a sensitive area of $3\,mm \times 3\,mm$ was used [DS144]. The photodetector was connected to a *Hamamatsu Evaluation Board C12332*, being used for controlling the bias voltage, measuring the temperature, and amplifying the signals from the SiPM [DS145]. Because of the circuit connecting the operation voltage to the SiPM, the signal output was positive (Figure 6.7a). A fan-in/fan-out NIM-module *LeCroy LRS 428F* [DS147] needed to be used to invert the signal, for the safety of the QADC, which only should be fed with negative signals [DS117]. Via the fan-in/fan-out the inverted (now neagtive) signal, as well as the gate signal were fed to the QADC for read-out. The whole measurement was controlled by the same self-programmed *LabVIEW* software, already used for MAPMT measurements. The control of the SiPM was done via an USB-connection to the measurement computer and the software delivered by Hamamatsu for the evaluation board.

Figure 6.7b shows the Hamamatsu *MPPC evaluation board - Driver Circuit C12332* and the used single channel SiPM *MPPC S12572-100C* [DS144, DS145]. For mechanical stability the evaluation board (right side) and the SiPM connection board (left side) were attached to a wooden board. With this the SiPM could be easily positioned in front of the light source. The external power supply (± 5 V) of the board
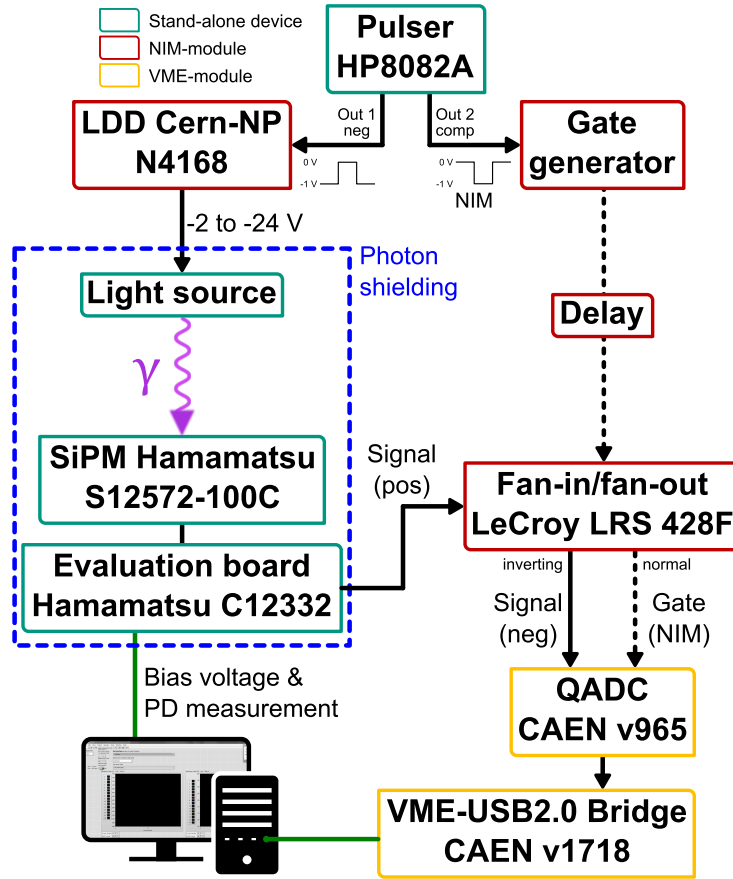
Figure 6.6: Sketch of the SiPM measurement set-up for a single channel SiPM.

was done with a standard laboratory power supply. The recommended bias voltage V_{bias} of 65.73 V was given by the manufacturer together with the SiPM, corresponding to an overvoltage of roughly 1.4 V. The breakdown voltage was not measured separately for the following measurements. The amplifier on the evaluation board was set to an amplification factor Λ of roughly 10 (default value given by Hamamatsu [DS145]), after having measured test spectra with different amplifications. The exact amplification factor was measured to be $10.1 \pm 0.05_{sys}$.

The SiPM was positioned with self-made bar spacers in front of a single pinhole with a diameter of 0.5 mm. The bar spacers made sure, that the photodiode and the SiPM were at the same distance from the pinhole. Otherwise the measurement of the pinhole ratio would not have made any sense, since it is dependent on the distance to the pinhole. Because of the spread of the light cone from the pinhole, a geometrical correction factor R_{geom} has to be taken into account for the number of incident photons. This factor scales with the area of the detector and the area of the photodiode used for the measurement of the pinhole ratio. If a collimator is used, the pinhole ratio is called collimator ratio. If the distance can be set in a way that all photons exiting the pinhole hit the sensitive area of the SiPM, then the geometrical factor is not needed.

For the following SiPM measurements the light source with 371 nm was pulsed with an 11 ns wide pulse with 1000 Hz frequency. Pulsed light was used, because

(a) SiPM-circuit - positive output.

(b) SiPM read-out evaluation board.
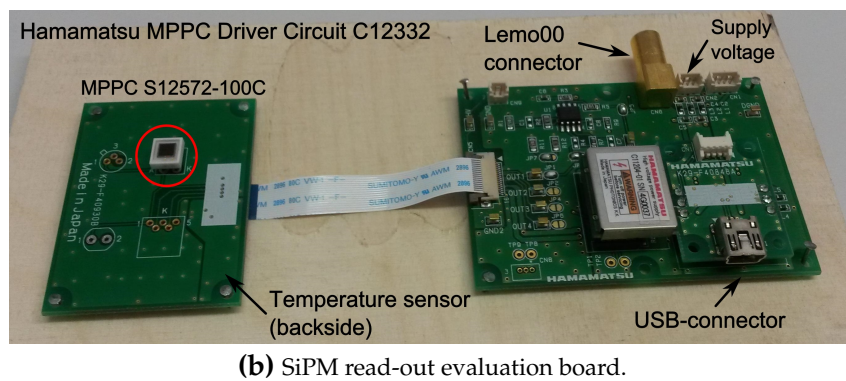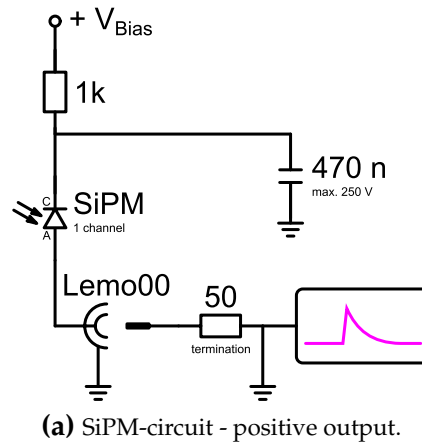
Figure 6.7: (a) Simplified sketch of the circuit for connecting the SiPM and getting a positive output signal. An amplifier can be connected to the out coming signal. Adopted from [DS144]. **(b)** Photograph of the single channel *MPPC evaluation board - Driver Circuit C12332*, used for read-out and controlling the bias voltage of the SiPM *MPPC S12572-100C* during the measurements [DS144, DS145].

a low light level within the range of single photons was wanted for calibration measurements. Of course, also continuous mode measurements could be done, but then no finger spectra would be visible. The evolution of the finger spectra with increasing light levels is shown in Figure 6.10. The gate for the QADC was set to 75 ns, making sure with the delay that the gate precedes the single signals from the SiPM by 15 ns. That was verified with an oscilloscope. The overall measurement process comprises of the same steps explained in detail for the case of MAPMTs, explained in Section 5.2. In this case, only one channel was there for read-out, so there was no need for channel finding (called pixel finding for MAPMTs) or the scan of several channels (pixels in the case of MAPMTs). The SiPM signal output was connected to channel 0 of the QADC, with a proportionality factor $k = (32.08 \pm 1.57_{stat} \pm 1.24_{sys})$ fC. The multiplexer cabling was still used, but the multiplexer had not to switch channels. In general, the multiplexer and the translation stages can be used in the same fashion as for MAPMTs also for multi-channel SiPMs.

For these measurements, first the collimator ratio was measured for 5 min and then the QADC-pedestal for channel 0 with 100 000 values (Figure 6.8a). After-

wards the SiPM was positioned in front of the pinhole, with the same distance as the photodiode before. Then a dark count spectrum of the SiPM was taken with 20 000 values (Figure 6.8b). Afterwards the measurements with light were started. Finger spectra with different light levels were measured. Afterwards the collimator ratio as well as the dark count spectrum were measured again. The resulting collimator ratio R_1 before the measurements was $(2.07 \pm 0.038_{\text{stat}} \pm 0.044_{\text{sys}})10^{-4}$, after the measurement $R_2 = (1.87 \pm 0.006_{\text{stat}} \pm 0.039_{\text{sys}})10^{-4}$, and the resulting mean collimator ratio R was then $(1.96 \pm 0.019_{\text{stat}} \pm 0.030_{\text{sys}})10^{-4}$.

(a) QADC-pedestal.
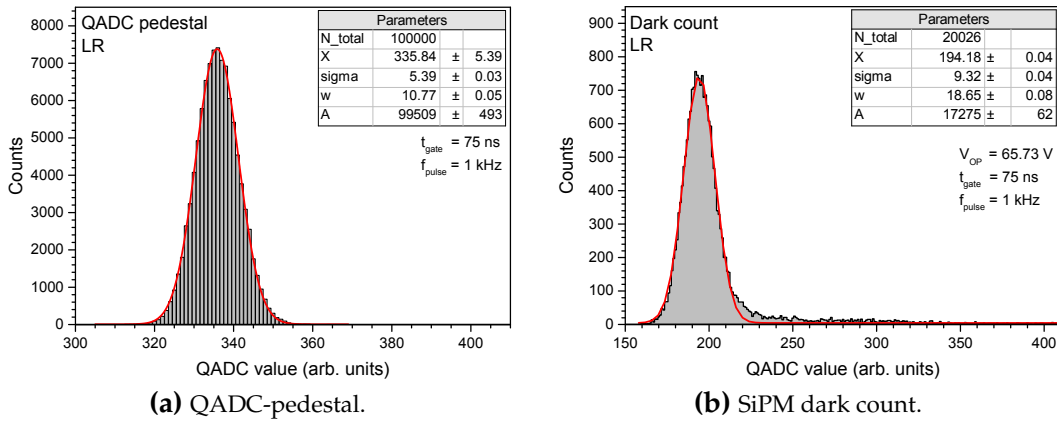
(b) SiPM dark count.

Figure 6.8: QADC-pedestal and dark count measurement of a single channel SiPM *S12572-100C*. Measured by Sally-Ann Sandkuhl during the course of her bachelor thesis [146]. **(a)** QADC-pedestal for a 75 ns gate and 1 kHz frequency. **(b)** Dark counts for the same gate and frequency. A tail on the right side of the pedestal peak is visible, exceeding the Gauss fit. This excess is due to dark counts, amounting to roughly 2800 events.

Figure 6.8 shows the QADC-pedestal and the dark count spectrum taken at the beginning of the measurement. Both spectra were fitted with a Gauss peak. Two things are evident from these spectra. First, a tail on the right side of the pedestal peak is visible, exceeding the Gauss fit. This excess is due to dark counts, amounting to roughly 2800 of the 20 026 events. Second, an offset is present between the QADC-pedestal and the SiPM dark count pedestal. This is not surprising in itself, however the QADC-pedestal is larger than the SiPM pedestal, leading to negative QADC values, and thus to a positive charge of the SiPM pedestal, when correcting for the QADC-pedestal. This might be due to the fan-in/fan-out module, which is able to set an offset value. Unfortunately, this was only discovered after the measurements, and thus an absolute scale for the charge cannot be given any more in the course of this thesis.

Figure 6.9 shows an example for one of the measured *finger spectra* with 10 013 values. The mean optical power was around 73 pW, amounting to roughly 2.4 photons per pulse, with our setup. When taking the duty cycle of the light pulse width and the pulse frequency into account, this corresponds to 547 photons per 2.5 μs (the Gate Time Unit (GTU) of the JEM-EUSO electronics). The Gauss fits were done manually with *Origin Pro 2015*. Five peaks up to the *4 pe* peak could be fitted. Further peaks are visible. More examples of finger spectra for increasing light levels
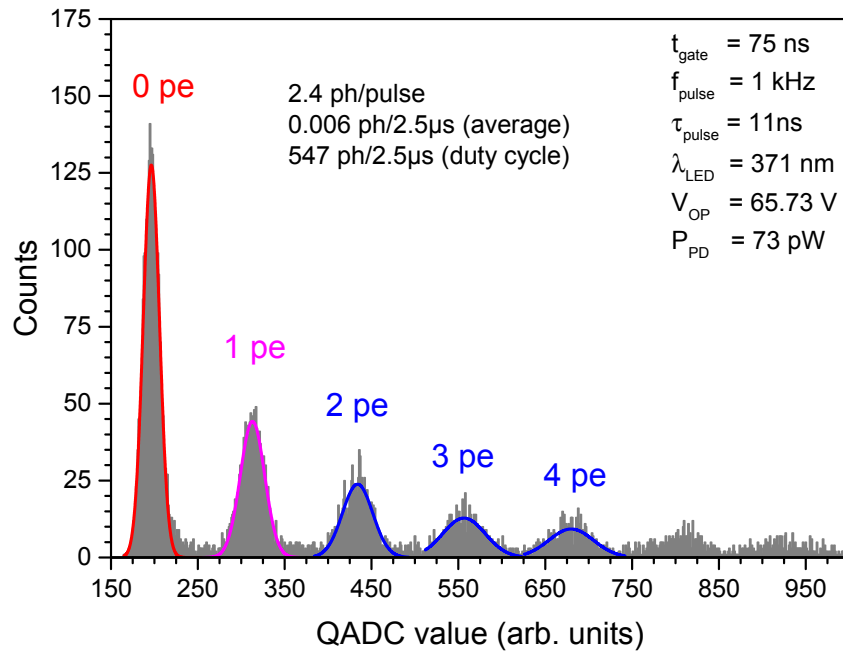
Figure 6.9: Measured finger spectrum with a mean optical power of 73 pW at 371 nm wavelength. Gauss fits for the first five peaks are shown. Measured by Sally-Ann Sand-kuhl during the course of her bachelor thesis [146].
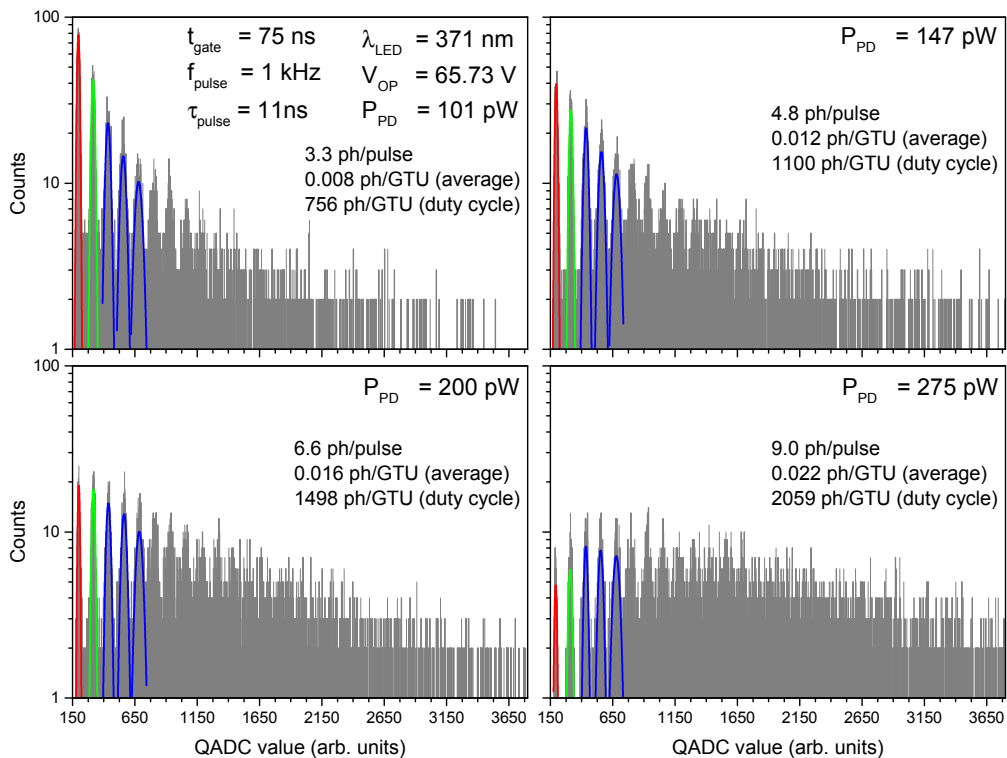
Figure 6.10: Four finger spectra for increasing light levels are shown. The number of pedestal events decreases, while the frequency of higher order peaks increases [146].

are shown in Figure 6.10. Four finger spectra with a logarithmic scale are shown. They were measured with increasing light levels, going from 3.3 to 9.0 photons per pulse. With increasing light level, the pedestal peak decreases, while the frequency of higher order peaks increases. Thus more events are seen at higher QADC values. At a certain light level the events in the pedestal become too scarce to get a good Gauss fit. This marks the upper limit for dynamic range measurements with SiPMs. Please note, that these spectra were taken with only 10 013 values. With longer measurements leading to more data points in the spectra, the upper light limit can be increased. For the measurements within this chapter the upper limit was around 13 photons per pulse.

6.3 SIPM CALIBRATION RESULTS

The following contains the results from the previously introduced measurement procedure. First, a short estimation of the systematic uncertainties is given, similar to the one done for MAPMTs (Section 5.3). The expected systematic uncertainties of SPOCK are estimated for the gain and the PDE via the formulas given in Section 6.1.3 and Appendix A.7. The gain comprises of the mean peak separation of adjacent peaks. This quantity can be rewritten as the distance of the highest order peak X_m and the pedestal peak X_0, divided by the number of peak separations n:

$$x = \frac{1}{n} \cdot (X_m - X_0) \quad .$$

The relative systematic uncertainty in the gain is obtained by the quadratic summation of the single uncertainties in both peak positions and the proportionality factor k. The electron charge has no systematic uncertainty. The systematic uncertainty in the amplification factor Λ was measured to be 0.5 % (for the set amplification factor of $10.1 \pm 0.05_{\text{sys}}$). The relative errors in the peak positions are given by the non-linearity of the QADC of 0.1 %. The proportionality factor k has for the *low range* of channel 0 a relative uncertainty of 3.9 % (Section 4.4.1 and Table 4.4):

$$\frac{\Delta_G}{G} = \sqrt{\left(\frac{\Delta_{X_m}}{X_m}\right)^2 + \left(\frac{\Delta_{X_0}}{X_0}\right)^2 + \left(\frac{\Delta_k}{k}\right)^2 + \left(\frac{\Delta_\Lambda}{\Lambda}\right)^2} \tag{6.8}$$

$$= \sqrt{(0.1\,\%)^2 + (0.1\,\%)^2 + (3.9\,\%)^2 + (0.5\,\%)^2} \approx 3.9\,\% \quad .$$

The proportionality factor k is again clearly dominating the systematic uncertainty in the gain.

The PDE is calculated via the number of detected photoelectrons and the number of incident photons. The relative systematic uncertainty in the number of incident photons is the same as for MAPMTs, with the same wavelength systematics (Equation 5.8 and Table 5.1). Yielding $\frac{\Delta_N}{N} \approx 4.1\,\%$ for a general 3 % relative wavelength uncertainty or $\frac{\Delta_N}{N} \approx 3.2\,\%$ for a 1.6 % relative wavelength uncertainty for 371 nm. The number of detected photoelectrons is comprised of two pedestal peak

Gauss fits. Each fit has a relative systematic uncertainty associated with its width $\sqrt{2} \cdot 0.1\,\%$, yielding:

$$\frac{\Delta_{N_{pe}}}{N_{pe}} = \sqrt{\left(\frac{\Delta_{N_{ped}}}{N_{ped}}\right)^2 + \left(\frac{\Delta_{N_{ped}^{dark}}}{N_{ped}^{dark}}\right)^2} \approx 0.2\,\text{percent} \quad .$$

The uncertainty in the number of incident photons dominates the systematic uncertainty in the PDE. It is:

$$\frac{\Delta_{\epsilon}}{\epsilon} = \sqrt{\left(\frac{\Delta_{N_{pe}}}{N_{pe}}\right)^2 + \left(\frac{\Delta_N}{N}\right)^2} \approx \frac{\Delta_N}{N} \quad .$$

The resulting relative systematic uncertainty in the PDE is thus: 4.1 % or respectively for a wavelength of 371 nm: 3.2 %. Detailed calculations for the systematic and statistical uncertainties in the gain and the PDE can be found in Appendix A, Appendix A.7.

These systematic uncertainties are in fact the same values as for MAPMTs (Equation 5.7 and Table 5.1). Which is not very surprising, since the PDE is dominated by the uncertainty in the number of incident photons. The gain is determined with the same kind of charge measurement, done with the same instrument as for MAPMTs. Therefore, both detector types can be calibrated with the same systematic uncertainties, which are sufficient for the calibration of both kinds of detectors.

6.3.1 *Gain*

The gain for different incident photon numbers was calculated from the finger spectra via Equation 6.4. Figure 6.11 shows the result of these calculations with the associated statistical and systematic errors. Two statistical outliers for low photon numbers were detected. They were masked and not used for the mean gain calculation. The mean gain, its standard deviation, as well as the 0.01 level of the outlier test are shown as horizontal lines. The statistical errors of the individual data points are larger than the systematic errors. This might be due to a relatively low number of data values per finger spectrum. As mentioned before, the Gauss fits were done manually by Sally-Ann Sandkuhl during the course of her bachelor thesis [146].

The mean value of the gain is in the range of $(2.40 \pm 0.12_{stat} \pm 0.01_{sys})\,10^6$. According to the datasheet the gain should be around 2.8×10^6 at 25.00 °C [DS144]. Further, a temperature coefficient of $\alpha_G = 1.2 \times 10^5\,°\text{C}^{-1}$ is given. The theoretical gain for the mean temperature T of the measurement, is calculated via:

$$G_{DS}\,(21.79\,°\text{C}) = G_{DS}\,(25\,°\text{C}) - \alpha_M \cdot (25\,°\text{C} - 21.79\,°\text{C}) = 2.42 \times 10^6 \quad .$$

The measured gain is in good agreement with the temperature corrected datasheet value. Although the used bias voltage was recommended for a temperature of 25 °C, not for the about 21 °C that were present in the laboratory, the measured gain was as given by the manufacturer. Hamamatsu is giving a bias voltage temperature coefficient of $\alpha_V = 60\,\text{mV}\,°\text{C}^{-1}$ [DS144]. That would correspond to a needed cor-
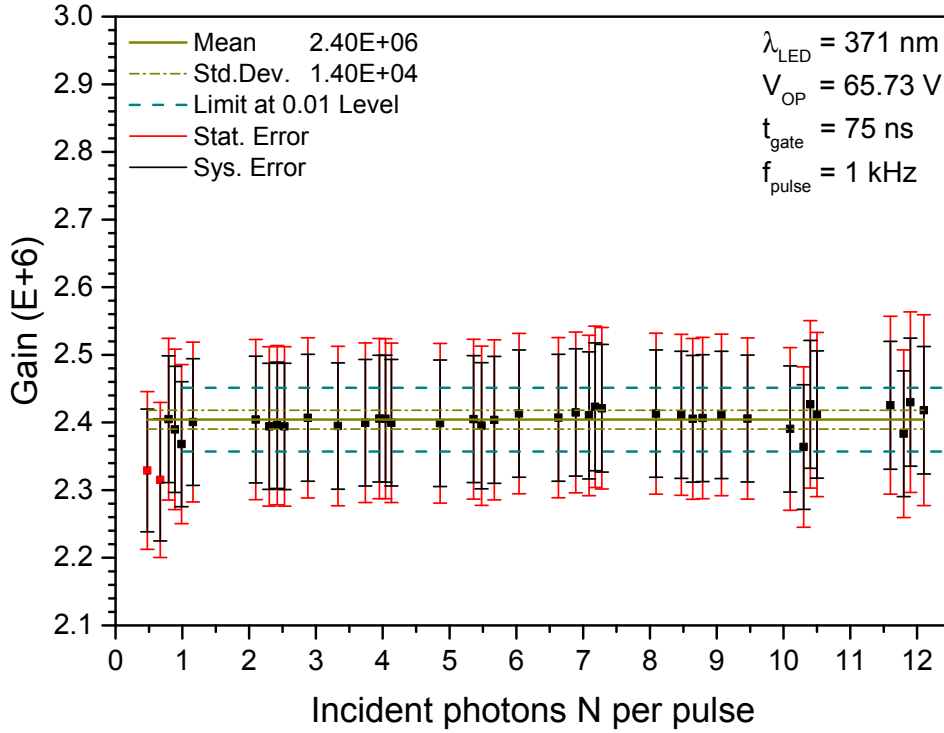
Figure 6.11: Graph of the SiPM gain and its statistical uncertainties versus the incident number of photons [146]. Two outliers were detected and masked for the analysis. The mean gain, its standard deviation, and the 0.01 confidence level of the outlier test are given as horizontal lines. The average temperature for the measurements was at 21.79 °C.

rection of around 240 mV of the operation voltage. Since the SiPM is operated in Geiger-mode, the gain is in general strongly dependent on small changes in the operation voltage (see Figure 6.2). This illustrates that a good temperature control of the SiPM or a very good adaptation of the bias voltage with changing temperatures should be implemented for a stable operation of SiPMs for varying temperatures.

6.3.2 *PDE*

The PDE of the used SiPM was now determined via a linear regression of the number of detected photoelectrons N_{pe} over the number of incident photons per pulse N. The number of photoelectrons was calculated via Equation 6.6 and the number of incident photons was calculated via Equation 6.7.

Figure 6.12 shows the number of photoelectrons N_{pe} per pulse calculated from the finger spectra versus the number of incident photons N per pulse. The slope of the linear fit gives the PDE of the SiPM. The last eight values were excluded from the fit, because of their non-linear behavior. There the pedestal events were scarce and the Gauss fit did yield large statistical errors. The slope gives a PDE of the SiPM of $(46.7 \pm 1.0_{stat} \pm 1.5_{sys})$ % with the estimated systematic uncertainty in the PDE of 3.2 %.
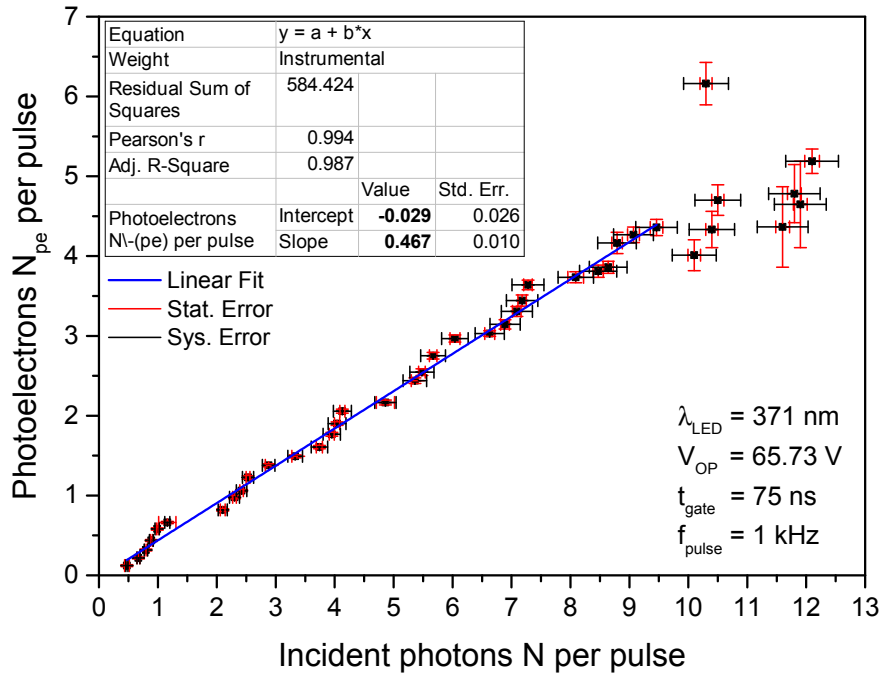
Figure 6.12: The calculated number of photoelectrons and its statistical uncertainties versus the number of incident photons (both per pulse) [146]. The slope of the linear fit gives the PDE of the SiPM. The last eight values were excluded from the fit because of their large statistical errors.
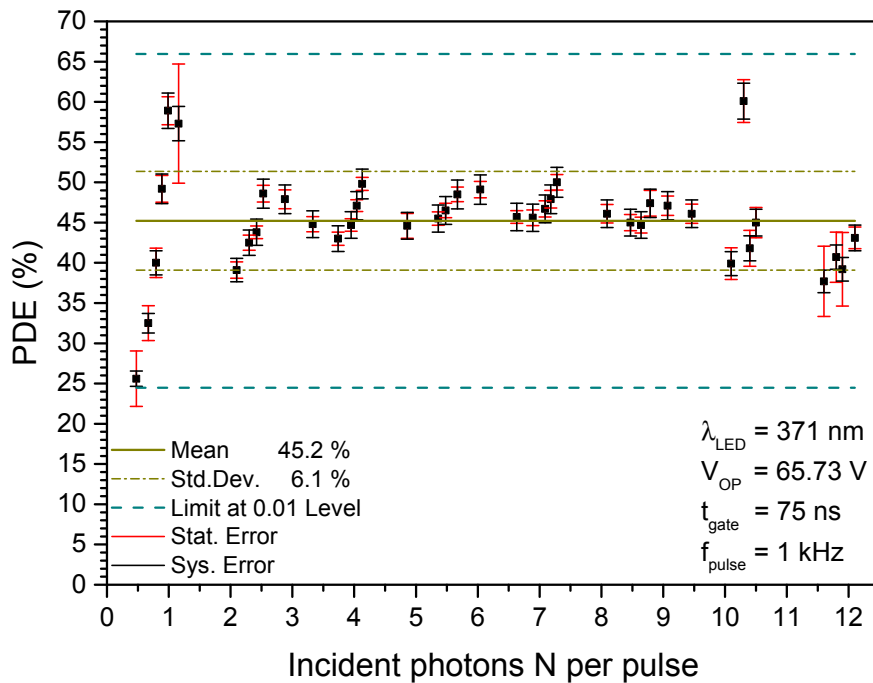
Figure 6.13: The PDE of the SiPM and its statistical uncertainties versus the incident photon number per pulse [146]. No outliers were detected. The mean PDE, its standard deviation, and the 0.01 level of the outlier test are shown as horizontal lines.

A calculation of the PDE for individual numbers of incident photons was also done. Figure 6.13 shows the individual PDE values of every finger spectrum versus the incident photon number N per pulse. Every value is shown with its respective statistical and systematic error. No statistical outliers were detected. The mean PDE, its standard deviation and the 0.01 level limits of the outlier test are shown as horizontal lines. Between 2 to 10 photons per pulse, the individual values have very low statistical errors. Outside of that region the Gauss peak separation was either not very good or the pedestal peak got too small for a good fit. However, all values were taken into account for the mean value calculation. The resulting mean PDE from this method yields $(45.2 \pm 6.1_{\mathrm{stat}} \pm 1.4_{\mathrm{sys}})\,\%$, with the same estimated PDE uncertainty as before.

Both shown methods result in a PDE of around 45 % to 46 %. This means, that of 100 incident photons, 45 are detected as photoelectrons. The datasheet gives a peak PDE of 35 % for a wavelength of 450 nm, for a temperature of 25° and an over voltage of 1.4 V. Further, Hamamatsu notes that the given PDE does not include crosstalk and afterpulses [DS144]. Although the calculations of the PDE via the probability to not detect any photon, try to compensate for noise phenomena like crosstalk and afterpulsing, some events might still be in the number of photoelectrons and thus be counted as signal. Another possibility for the increased PDE might be again the not temperature-corrected bias voltage, which does not increase the "real" PDE, but instead increases noise phenomena that are then wrongly interpreted as photoelectron signals.

6.3.3 *Number of fired pixels*

For dynamic range measurements the number of fired pixels per incident number of photons is used. Because of the timing characteristics of the G-APDs even a few photons might be only detected as one photoelectron. An ideal SiPM without any noise and recovery time would detect every incoming photon:

$$N_{\text{fired ideal}} = N \quad .$$

An empirical relation of the number of fired cells for a SiPM with a finite number n of pixels was given with Equation 6.3. From this, the theoretical relation for the used SiPM with its PDE from the *datasheet* $\epsilon = 35\,\%$ and no noise is calculated via:

$$N_{\text{fired datasheet}} = 900 \cdot \left(1 - \exp\left(-\frac{N \cdot 35\,\%}{900}\right)\right) \quad .$$

The number of fired cells can also be calculated from the *measured data*, via the ratio of the mean charge and the total charge coming out of the SiPM. The total charge is calculated via the product of the gain and the electron charge. The mean charge can be estimated via the median of the QADC values X_{med} of each finger spectrum times the proportionality factor. Simplifying this ratio gives:

$$N_{\text{fired raw}} = \frac{X_{\mathrm{med}}}{x} \quad ,$$

with the mean peak separation x. For an absolute charge, the QADC-pedestal X_{Qped} has to be subtracted from the whole spectrum or from the median QADC value.

$$N_{\text{fired corrected}} = \frac{X_{\text{med}} - X_{\text{Qped}}}{x} \quad .$$

For our setup, the QADC-pedestal was higher than the median QADC values for low light level, yielding for low light levels (up to 3 photons per pulse) a negative number of fired cells. This was due to the offset introduced by the fan-in/fan-out module.
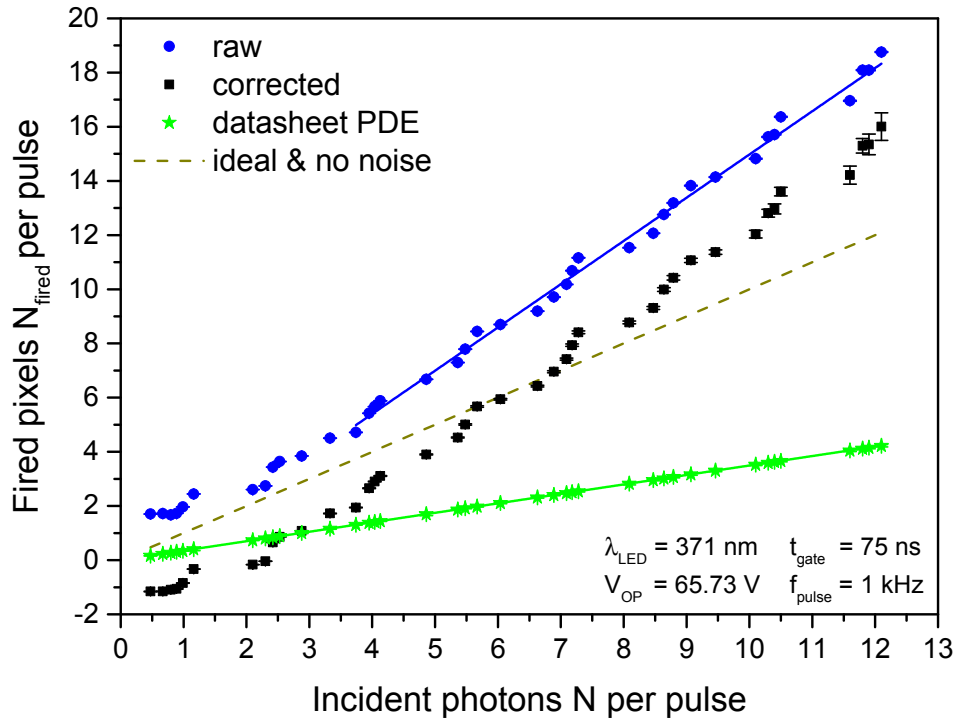
Figure 6.14: Graph of the number of fired pixels and its statistical uncertainties versus the incident photon number [146]. The measured raw data, its QADC-pedestal-corrected values, the ideal SiPM line, and the expectation for a SiPM with the datasheet PDE and 900 pixels are shown.

Figure 6.14 shows the number of fired pixels versus the incident photon number for the measured raw data, for the QADC-pedestal-corrected data, for an ideal SiPM without noise, and for the theoretical behavior of a SiPM with 900 pixels without noise. The theoretical behavior of a real SiPM goes linear with the number of incident photons in this region of photon numbers. The dashed line with slope one represents an ideal SiPM without any noise phenomena and perfect distribution of photons (or zero recovery time). Here every incident photon would fire one cell, regardless of the interaction points of the photons with the SiPM. Since the number of fired cells is calculated via the mean charge of all fired cells, the raw data (blue dots) has to be corrected by the pedestal. This was done for the black squares. Values below 2.5 incident photons are negative, because of the used inverter and its unknown offset towards positive voltages. A negative number of fired pixels

is unphysical. Therefore the raw data was examined a bit more in detail. Until an incident photon number of four, the number of fired cells increases exponentially. After that the increase is linear, as shown by the fit line. As an indication from the corrected data, the transition to more fired cells per incident photon than one is around 6 to 7 photons. At all times the raw data is larger than the ideal line, and the theoretical behavior, showing that there are lots of noise phenomena measured, e. g. dark counts, crosstalk and afterpulsing. This noise amounts to more fired pixels than theoretically expected.

6.4 DISCUSSION

During this work and the bachelor thesis of Sally-Ann Sandkuhl [146], the first calibration measurement of SiPMs with SPOCK was done in single photon mode and higher light levels. Finger spectra could be measured for different light levels. In addition, the gain and the PDE of the used SiPM could be determined with relative systematic uncertainties of 3.9 % in the gain and 3.2 % in the PDE. In comparison to the datasheet, the values were too high, which might have been due to the miss of the experimental determination of breakdown voltage and with this the setting of the temperature depending operation voltage. Future SiPM calibration measurements will have to include this step into the measurement process. Also noise phenomena like dark counts, crosstalk, and afterpulsing are suspected to be partly identified as signal, and thus increasing the measured PDE.

The estimated systematic uncertainties are the same ones as for MAPMTs (Equation 5.7 and Table 5.1). Which is not surprising, since the PDE is dominated by the uncertainty in the number of incident photons. The gain is determined with the same kind of charge measurement, done with the same instrument as for MAPMTs. Therefore, both detector types can be calibrated with the same systematic uncertainties, which are sufficient for the calibration of both kinds of detectors. Overall, the systematic uncertainties of SPOCK are comparable to previous calibration stands.

(a) SiPM-circuit - positive output.

(b) SiPM-circuit - negative output.
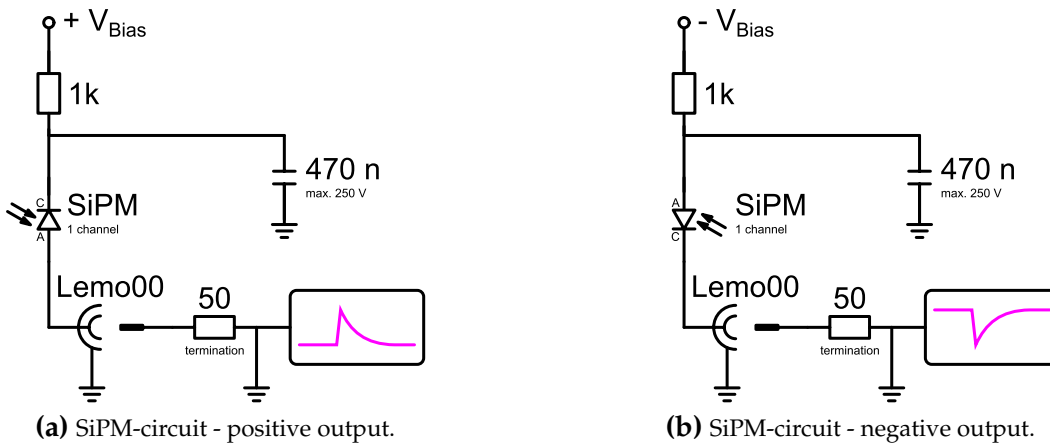
Figure 6.15: Sketch of the simplified circuits for connecting the SiPM and getting a positive or a negative output signal. No amplifiers are shown. Adopted from a discussion within the research group [130, 134, 148].

A clear improvement of the statistics of SiPM calibration measurements is needed and easily achieved by expanding the measurement time, e. g. using 1×10^6 data values for a finger spectrum. Future SiPM measurements should also use the ability of SPOCK to be able to generate different wavelengths. Therefore one can expect spectral PDE plots from SPOCK. One major improvement would be the use of a different SiPM circuit, to get rid of the fan-in/fan-out module, which introduced an unwanted charge offset. This is easily achieved by inverting the bias voltage and adapting the components of the circuit (Figure 6.15b). As a comparison both possible circuit layouts are shown in Figure 6.15.

During this work some experience was gained for adapting SPOCK to the use of SiPMs. One of the first tasks initiated by this experience was the development of an own SiPM read-out and control board by the research group, using an inverted circuit for negative output signal. Further work in the research group is ongoing into the expansion of SPOCK to multi-channel SiPM-arrays of the newest generation, that could be used as an alternative to MAPMTs. Furthermore, temperature measurements with several sensors on these SiPM-arrays are mandatory and also a work in progress by the research group.

CONCLUSION

The main goals of this work were to build, test, and improve a multipurpose calibration stand for photodetectors of all kinds. Important here is to be able to test these different detectors with the same reference light source and the same read-out electronics. At the same time the same systematics are applied to all tested detectors that might be viable options for future experiments, where single photon counting is important. This leads to a very robust comparison of the characteristics of different detector types. For that purpose, SPOCK (Single PhOton Calibration stand at KIT), a single photon calibration stand for photodetectors was designed. This involved the building of a photon shielding, ensuring a very dark environment with no photons present that are not directly coming from the light source. Therefore, reflecting surfaces were reduced as much as possible and the large opening lid was sealed with a rubber labyrinth. All needed mechanical parts, for attaching photodiodes and LED-arrays to the light source were designed and built in the course of this work. Light-tight connections for HV, control signal, and detector signal were used for the photon shielding and tested. Additional safety mechanisms like a light-tight curtain inside the photon shielding and a lock, preventing an opening of the photon shielding when HV is applied to the detector, were implemented to the calibration stand. Further improvements to the calibration stand involved a modular design of the light source, making it easily modifiable for different wavelengths and variable output power, ranging from single photons to ten thousands of photons, available for detector calibration and dynamic range measurements. Also a computer controlled positioning system for the light source was built into the system, to enable the scan of photosensitive surfaces up to $295 \times 295\,\mathrm{mm}^2$. The optical output of the light source was proven to be stable in time and wavelength for both pulsed and continuous mode. Especially for SiPMs a temperature sensor was added to the calibration stand. With the feedback from the temperature control, the bias voltage supplied to the SiPM can be regulated in dependency of the temperature, to ensure a stable gain and an overall stable performance of the SiPM. The whole slow control, software, and data acquisition of the calibration stand was planned and implemented during this work.

All components were checked thoroughly with the highest precision available, which involved the cross-calibration of the photodiodes with a NIST-calibrated photodiode, the measurement of the spectra of all LEDs in continuous mode and different pulsed modes, and the behavior of the collimators with different light levels, wavelengths, and distances to the exit hole of the collimators. Because of the gain of the photodiodes around one, the light level needs to be high, when measuring the collimator ratio, with an attenuation around 10^{-6}. This is achieved with

continuous light. For the generation of single photons, a much lower light level is needed and pulsed light is used. Further, the read-out electronics and their support equipment were tested with utmost precision. The linearity of the QADC was tested with defined pulses from a pulse generator for every channel. From that the proportionality factor of the charge and the measured QADC value were obtained for every QADC input channel.

The mayor part of the control and measurement software for SPOCK was programmed in *National Instruments LabVIEW* during this work. This involved the control of the translation stages, the multiplexer, and the graphical user interface for the calibration stand. Subcomponents controlling the read-out of the QADC were programmed within the research group and were implemented into the main software during this work. Further more, some quick data analysis tools within the framework of the control and measurement program were added. Also measurement procedures were defined for different photosensors. This involved different movement patterns of the light source and switching of the multiplexer depending or not on the illuminated channel of the photodetector. Further, analysis tools for the measured data were also programmed during this work and within the research group.

The behavior of the multiplexer and the different movement patterns of the light source are used for different calibration modes, like single-photon mode, measuring the PDE and the gain of photosensors with single photons. SPOCK also allows for the uniform illumination of larger detector areas for a simultaneous calibration of either several small detectors or of one bigger detector. At the moment a maximum number of 64 channels can be read out, either sequentially or in bunches of 16 channels at once, due to the multiplexer and the QADC. A third calibration mode involves the measurement of the dynamic range of photodetectors. All these can be done with different wavelength, examining the wavelength dependency of the PDE of different photodetectors. This makes a direct comparison of different detector types possible.

Gain and PDE measurements were done during this work for two kinds of photodetectors, MAPMTs and SiPMs. Both photodetector types required a slightly different measurement procedure, because of their different working principle. In the case of MAPMTs they were done for different wavelengths and supply voltages. In the case of SiPMs further investigation is needed to get more precise data, especially longer measurements with more data are needed for better statistics. However, both types of photodetectors could be characterized with satisfactory results.

For MAPMTs the measured gain was around 1×10^6, which is in the range given by the manufacturer. The mean relative systematic uncertainty of SPOCK was estimated as 3.9 % for the gain. That comes mainly from the systematic uncertainty of the proportionality factor of the QADC. The mean relative statistical uncertainties of the gain for the measurements done during this work were in the range of 5 % to 10 %. This can be due to too few data points per MAPMT pixel, resulting in bad Gauss fits. The gain is also sensitive to the separation between the pedestal and the *1 pe* peak, which were not clearly separated in some of the measurements. The mean PDE of the MAPMTs was measured between 15.8 % to 26.5 %, depending on the MAPMT and the wavelength. The relative mean systematic uncertainty in the PDE

was estimated to 4.1 %, mainly dominated by the photodiodes 3 % uncertainty in the wavelength. When using the wavelength uncertainties in the LED-arrays (measured with the spectrometer), the wavelength uncertainty can be reduced to 1.3 % to 1.9 % (depending on the used LED). This yields a mean systematic uncertainty in the PDE of 3.1 % to 3.4 %. This is sufficient for calibration measurements.

For SiPMs the measured mean gain was around 2×10^6 with a standard deviation of one order of magnitude lower, being in good agreement with the temperature corrected datasheet value. However, the relative mean systematic gain uncertainty was around 3.9 %, also dominated by the systematic uncertainty of the QADC proportionality factor. The mean statistical uncertainties were 5.0 %. One cause for the better statistical uncertainties than MAPMTs might be the better quality of the Gauss fits, since they were fitted individually to each finger spectrum. The mean PDE value of $(45 \pm 6_{\text{stat}})$ % was higher than the one given in the data sheet (35 %). This is believed to be due to dark counts, crosstalk and afterpulsing. The systematic uncertainties were dominated again by the wavelength uncertainty of the photodiode. The resulting maximum mean relative systematic uncertainty for the PDE is 4.1 %. The mean relative statistical uncertainty was calculated from the measured values to be 3.8 % of the respective PDE values. This is also sufficient for calibration measurements.

The systematic uncertainties of SPOCK are at a sufficient level for calibration measurements and also are comparable to the uncertainties of previous calibration stands. But now they are applicable also to different sensors, larger focal surfaces and different wavelengths.

Overall SPOCK is ready for the characterization and sorting of the coming MAPMTs (in the order of several hundreds) for the next phase of the JEM-EUSO pathfinder experiments, providing the ideal test and calibration environment with stable laboratory conditions. Further more new technologies, like SiPMs, can be tested with SPOCK too. As a multipurpose calibration stand it can be used for different experiments involving photosensors or the need for single photons.

Part

APPENDIX

A

MEASUREMENTS

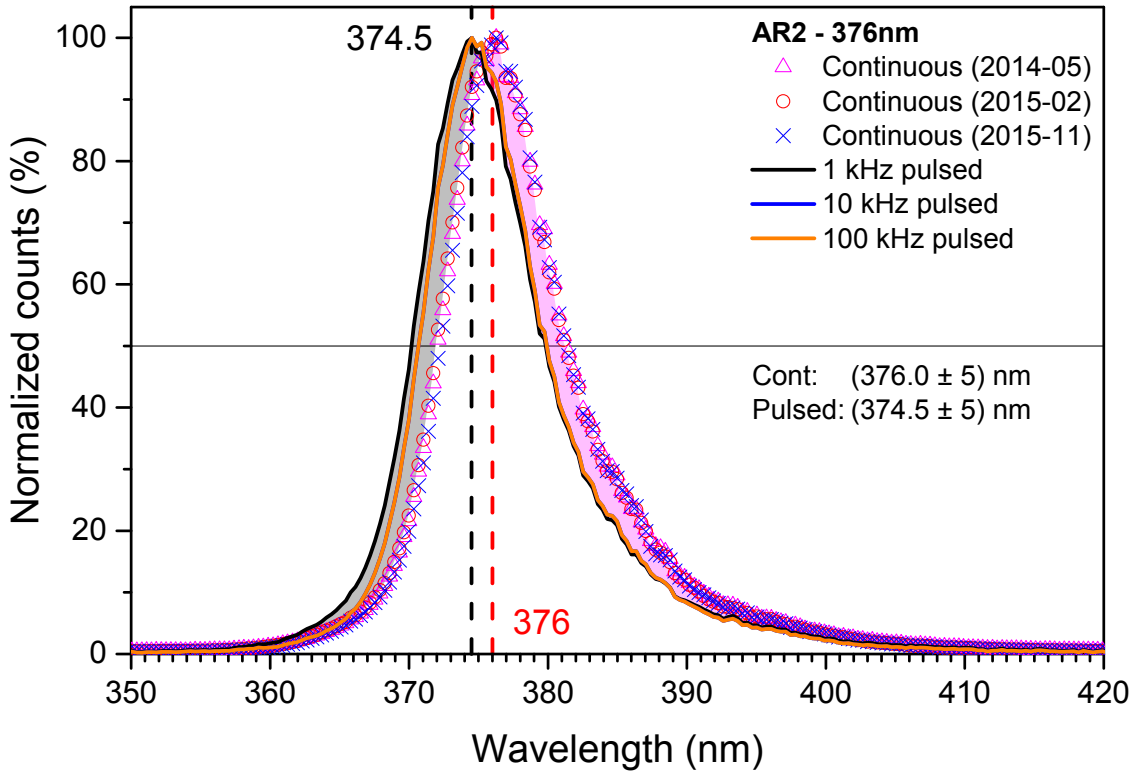## A.1 LED-ARRAY SPECTRA
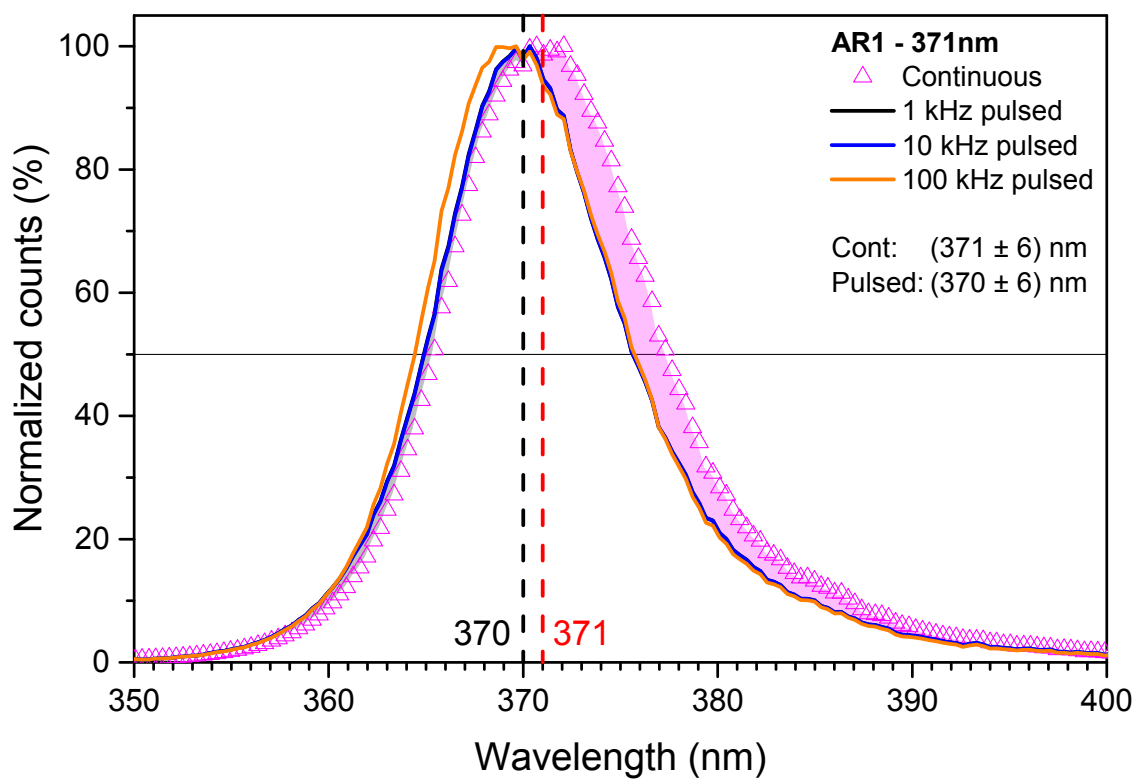
Figure A.1: Measured continuous and pulsed spectra of LED-array AR1. LEDs of the type *UVLED365-110E* are used for this array (Table C.3).

(a) Spectra of LED-array AR2 - LED *XSL-375-3E*.

(b) Spectra of LED-array AR3 - LED *VL390-5-15*.

Figure A.2: Measured continuous and pulsed spectra of LED-array AR2 and AR3. More information can be found in (Table C.3).
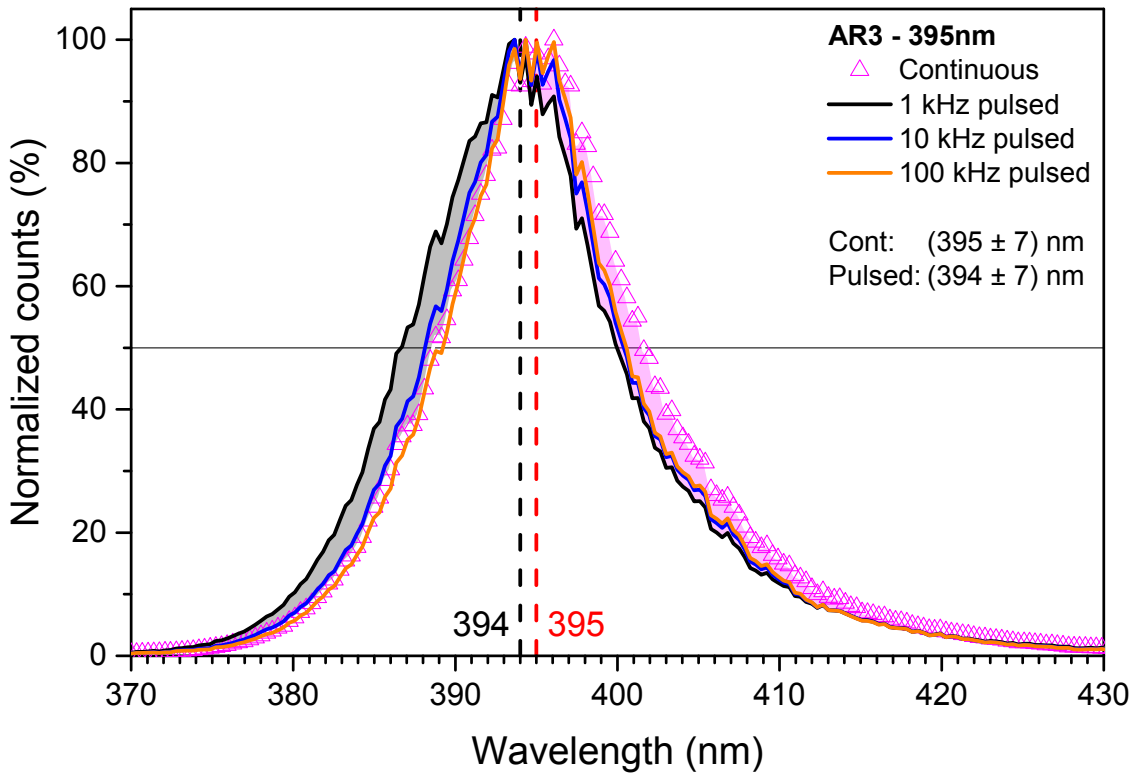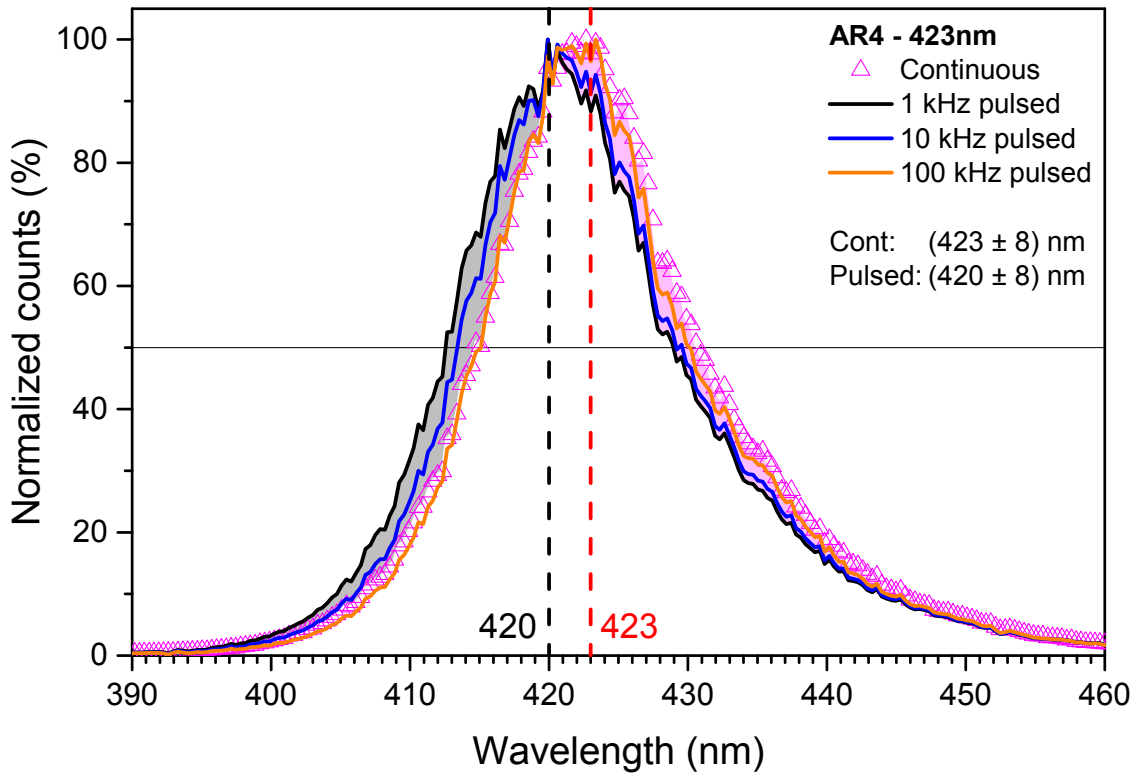
Figure A.3: Measured continuous and pulsed spectra of LED-array AR4. LEDs of the type *VL425-5-15* are used for this array (Table C.3).
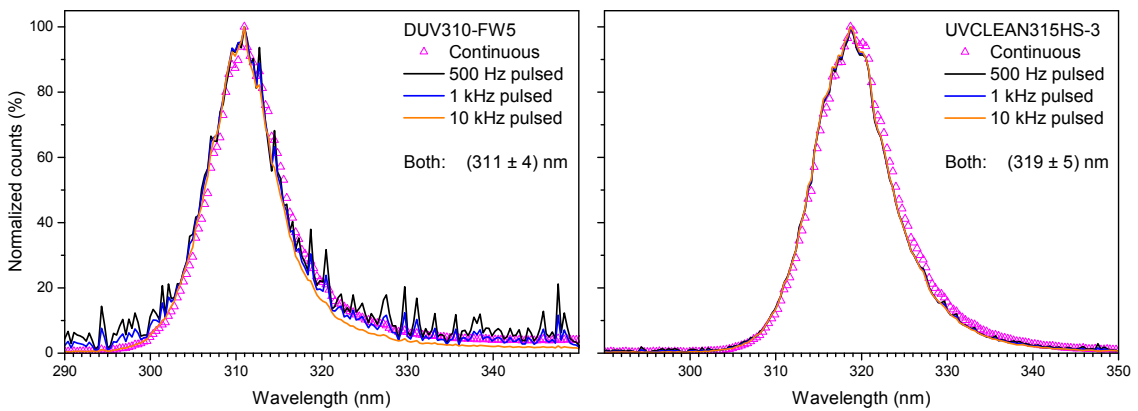
Figure A.4: Measured continuous and pulsed spectra of the first six LEDs of LED-array AR5. Measured by N. Hampe [97].
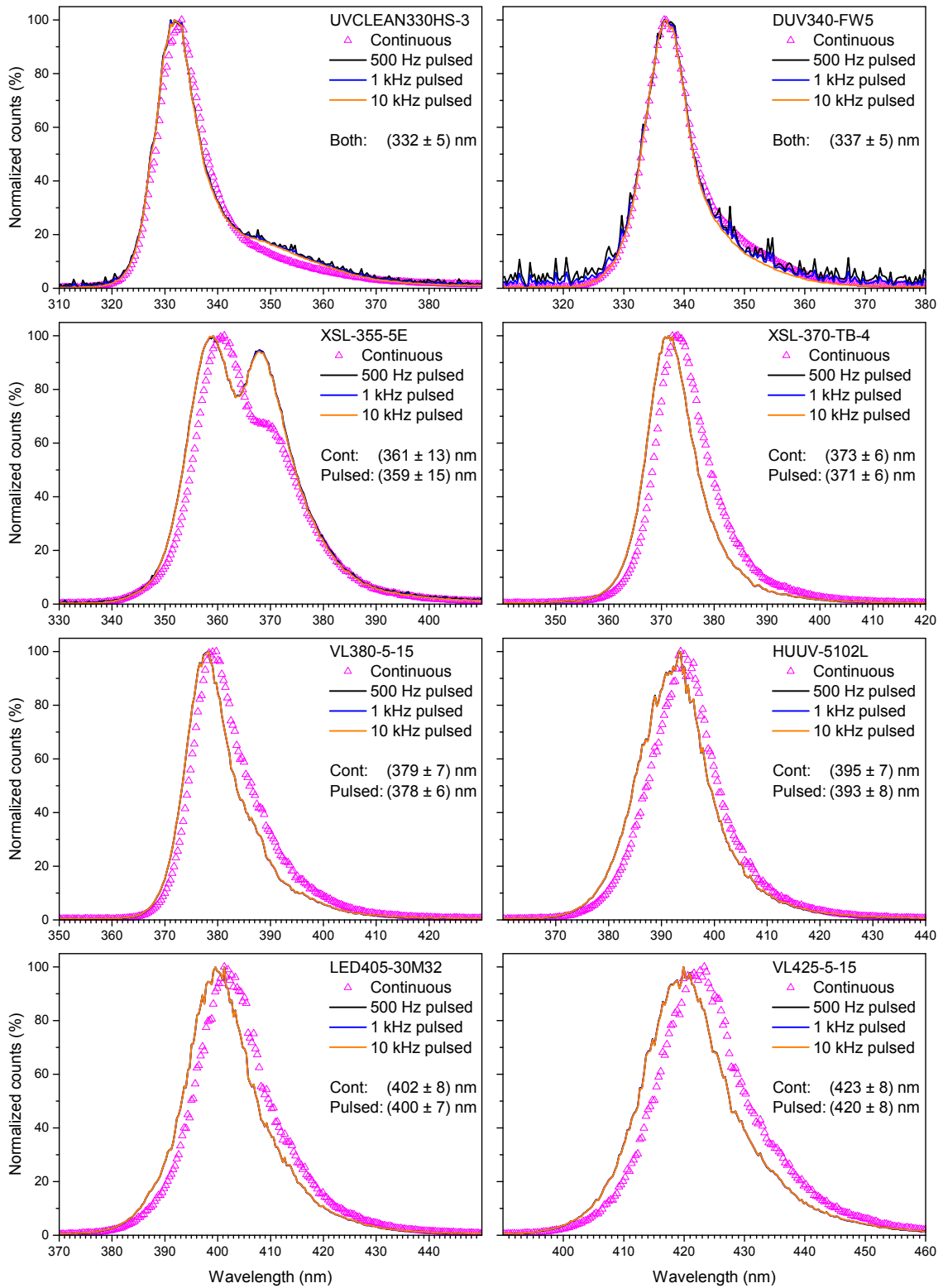
Figure A.5: Measured continuous and pulsed spectra of the last four LEDs of LED-array AR5. Measured by N. Hampe [97].
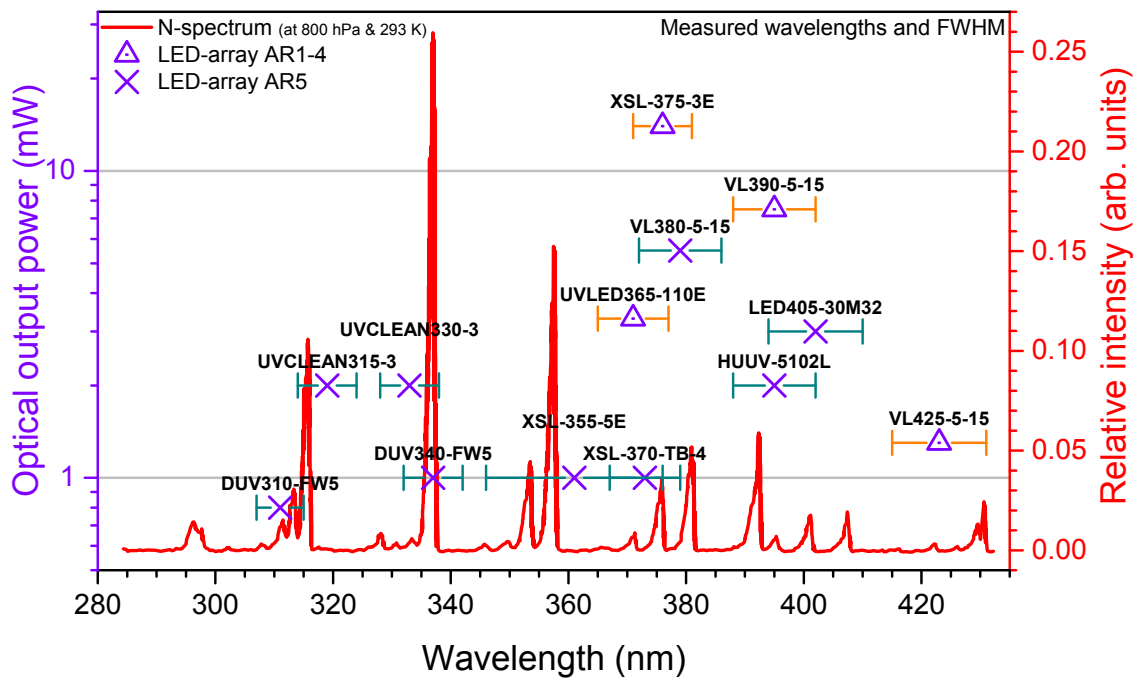
Figure A.6: Overlay of the nominal UV-LED optical outputs with the measured peak wavelengths and their wavelength deviations (for continuous mode) together with the fluorescence spectrum of nitrogen in 2 km altitude (N-spectrum adopted from [36]).

A.2 COLLIMATOR RATIO VERSUS WAVELENGTH

Table A.1: Overview of the datasets taken for the collimator ratio versus wavelength by Nils Hampe [97]. The blue[†] values indicate measurements, where the photodiode in front of the collimator measured an optical power smaller than 100 pW, which is the lower threshold for a good signal-to-noise ratio of the photodiode.

| **Collimator AluB**		AR5		Array C		AR2	
λ	Δ_λ	R	σ_R	R	σ_R	R	σ_R
(nm)	(nm)	(10^{-5})	(10^{-5})	(10^{-5})	(10^{-5})	(10^{-5})	(10^{-5})
425	13	1.160	0.001				
405	12	1.225	0.001				
393	12	1.213	0.002				
380	11	1.246	0.004				
377	11					1.314	0.001
371	11	1.185	0.015				
356	11	1.249	0.004				
340	10	1.629	0.010				
330	10	1.583	0.012				
315	9	1.423	0.009				
312	9	1.390[†]	0.011[†]				

Table A.2: Overview of the datasets taken for the collimator ratio versus different wavelengths by Nils Hampe [97]. The blue† values indicate measurements, where the photodiode in front of the collimator measured an optical power smaller than 100 pW, which is below the lower threshold for a good signal-to-noise ratio of the photodiode. The red* values indicate the same for optical powers smaller than 50 pW.

Collimator ColA		AR5		Array C		AR2	
λ	Δ_λ	R	σ_R	R	σ_R	R	σ_R
(nm)	(nm)	(10^{-7})	(10^{-7})	(10^{-7})	(10^{-7})	(10^{-7})	(10^{-7})
425	13	6.520	0.047	6.280	0.014		
		6.063†	0.138†	6.215	0.026		
				6.104	0.008		
405	12	6.191†	0.108†				
		6.452†	0.120†				
393	12	7.409*	0.233*	6.727†	0.178†		
		6.365*	0.465*	6.424†	0.087†		
380	11			7.245	0.039		
				6.086	0.176		
377	11					6.752	0.005
						6.729	0.008
370	11			7.318*	0.095*		

Collimator ColE		AR5		Array C		AR2	
λ	Δ_λ	R	σ_R	R	σ_R	R	σ_R
(nm)	(nm)	(10^{-6})	(10^{-6})	(10^{-6})	(10^{-6})	(10^{-6})	(10^{-6})
425	13	2.421	0.014	2.488	0.007		
				2.487	0.007		
401	12	2.532	0.012				
393	12	2.628	0.017	2.707	0.009		
				2.563	0.014		
380	11	2.710	0.015	2.676	0.007		
				2.654	0.012		
377	11					2.797	0.003
						2.737	0.007
370	11	1.872*	0.157*	2.829	0.008		
				2.868	0.009		
361	11	1.109*	0.041*				
337	10	1.708*	0.558*				
333	10	0.828*	0.049*				
319	10	0.783*	0.077*				
311	9	0.912*	0.067*				

A.3 COLLIMATOR RATIO VERSUS WAVELENGTH - UNCERTAINTY CALCULATIONS

The mean collimator ratio R is a ratio of mean optical powers P_a and P_b, that are measured during a measurement by the photodiodes. The standard deviations of said mean powers σ_{P_a} and σ_{P_b} are given by the measurement program. The measurement program can also directly save the mean ratio $R = \frac{P_a}{P_b}$ and its standard deviation σ_R. The following observables result:

P_a P_b mean optical powers,

σ_{P_a} σ_{P_b} standard deviation of the mean optical powers,

$R = \frac{P_a}{P_b}$ mean ratio of the optical powers,

σ_R standard deviation of the mean ratio.

If the mean ratio R is not given by the measurement program, it can be calculated, via Equation 4.9:

$$\sigma_R = \sqrt{\left(\frac{\partial R}{\partial P_a} \cdot \sigma_{P_a}\right)^2 + \left(\frac{\partial R}{\partial P_b} \cdot \sigma_{P_b}\right)^2} = \sqrt{\left(-\frac{P_a}{P_b^2} \cdot \sigma_{P_a}\right)^2 + \left(\frac{1}{P_b} \cdot \sigma_{P_b}\right)^2} \quad .$$

For several measurements of the collimator ratio, with *differences in the individual mean collimator ratios* R_i *larger than the individual systematical errors* Δ_{R_i}, the overall *weighted mean ratio* $\overline{R}$ is used:

$$\overline{R} = \frac{\sum_{i=1}^{n} \sigma_{R_i}^{-2} R_i}{\sum_{i=1}^{n} \sigma_{R_i}^{-2}} \quad .$$

where

$\overline{R}$ is the weighted mean ratio,

R_i are the mean collimator ratios, and

σ_{R_i} are the standard deviations of the individual mean collimator ratios.

From that weighted mean value, the statistical errors can be calculated via:

$$\sigma_{int} = \sqrt{\frac{1}{\sum_{i=1}^{n} \sigma_{R_i}^{-2}}} \quad . \tag{A.1}$$

This yields the weighted mean ratio as a maximum likelihood estimator, if the single ratios R_i are independent and no systematic errors are apparent. Here only internal uncertainties have been taken into account.

Corrections for errors that were not taken into account, like systematic errors or other external circumstances, can be made via:

$$\sigma_{\text{ext}} = \sqrt{\frac{\sum_{i=1}^{n} \sigma_{R_i}^{-2} \left(R_i - \overline{R}\right)^2}{(n-1) \sum_{i=1}^{n} \sigma_{R_i}^{-2}}} \quad . \tag{A.2}$$

The bigger one of both uncertainties is then used as the statistical uncertainty and given in the plot.

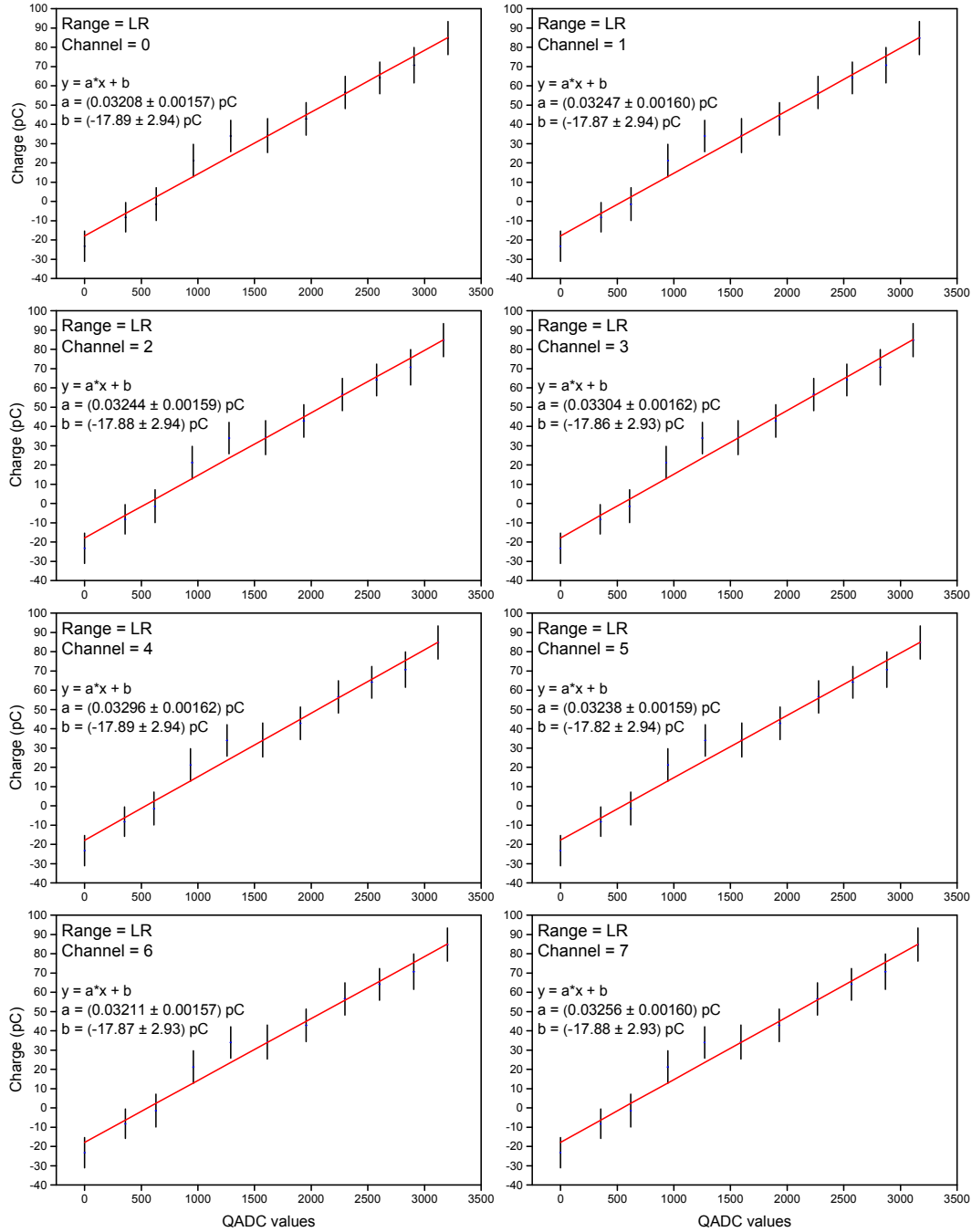The systematic uncertainties in the weighted mean collimator ratio $\Delta_{\overline{R}} = \sqrt{2} \cdot \Delta_P \cdot \overline{R}$ are calculated via the standard error propagation formula for uncorrelated variables (analogue to Equation 4.10). As seen before in Equation 4.8, the wavelength dependent systematic error is given by:

$$\Delta_P = 1.6\% \cdot P \qquad \text{for} \quad \lambda < 400\,\text{nm} \quad \text{and}$$
$$\Delta_P = 0.5\% \cdot P \qquad \text{for} \quad \lambda > 400\,\text{nm} \quad .$$

Table A.3: Overview of the uncertainties for the collimator ratio versus wavelength measurements for *ColA* and *ColE*. This data was used for the graphs shown in Section 4.3.5.4.

Collimator ColA	λ (nm)	Δ_λ (nm)	$\overline{R}$ (10^{-7})	$\sigma_{\overline{R},\text{int}}$ (10^{-7})	$\sigma_{\overline{R},\text{ext}}$ (10^{-7})	$\Delta_{\overline{R}}$ (10^{-7})
	425	13	6.158	0.007	0.045	0.044
	405	12	6.308	0.080	0.130	0.045
	393	12	6.569	0.073	0.171	0.149
	380	11	7.190	0.038	0.246	0.163
	377	11	6.746	0.004	0.010 1	0.153
	370	11	7.318	0.095		0.166

Collimator ColE	λ (nm)	Δ_λ (nm)	$\overline{R}$ (10^{-6})	$\sigma_{\overline{R},\text{int}}$ (10^{-6})	$\sigma_{\overline{R},\text{ext}}$ (10^{-6})	$\Delta_{\overline{R}}$ (10^{-6})
	425	13	2.480	0.005	0.015	0.018
	401	12	2.532	0.012		0.057
	393	12	2.661	0.007	0.043	0.060
	380	11	2.676	0.006	0.012	0.061
	377	11	2.785	0.003	0.024	0.063
	370	11	2.843	0.006	0.029	0.064
	361	11	1.109	0.041		0.025
	337	10	1.706	0.558		0.039
	333	10	0.828	0.049		0.019
	319	10	0.783	0.077		0.018
	311	9	0.912	0.067		0.021

A.4 QADC-LINEARITY

Figure A.7: Measurements of the QADC-linearity for the low range (*LR*) and channels 0 to 7. Measured by Simon Ehnle in the course of his bachelor thesis [123].
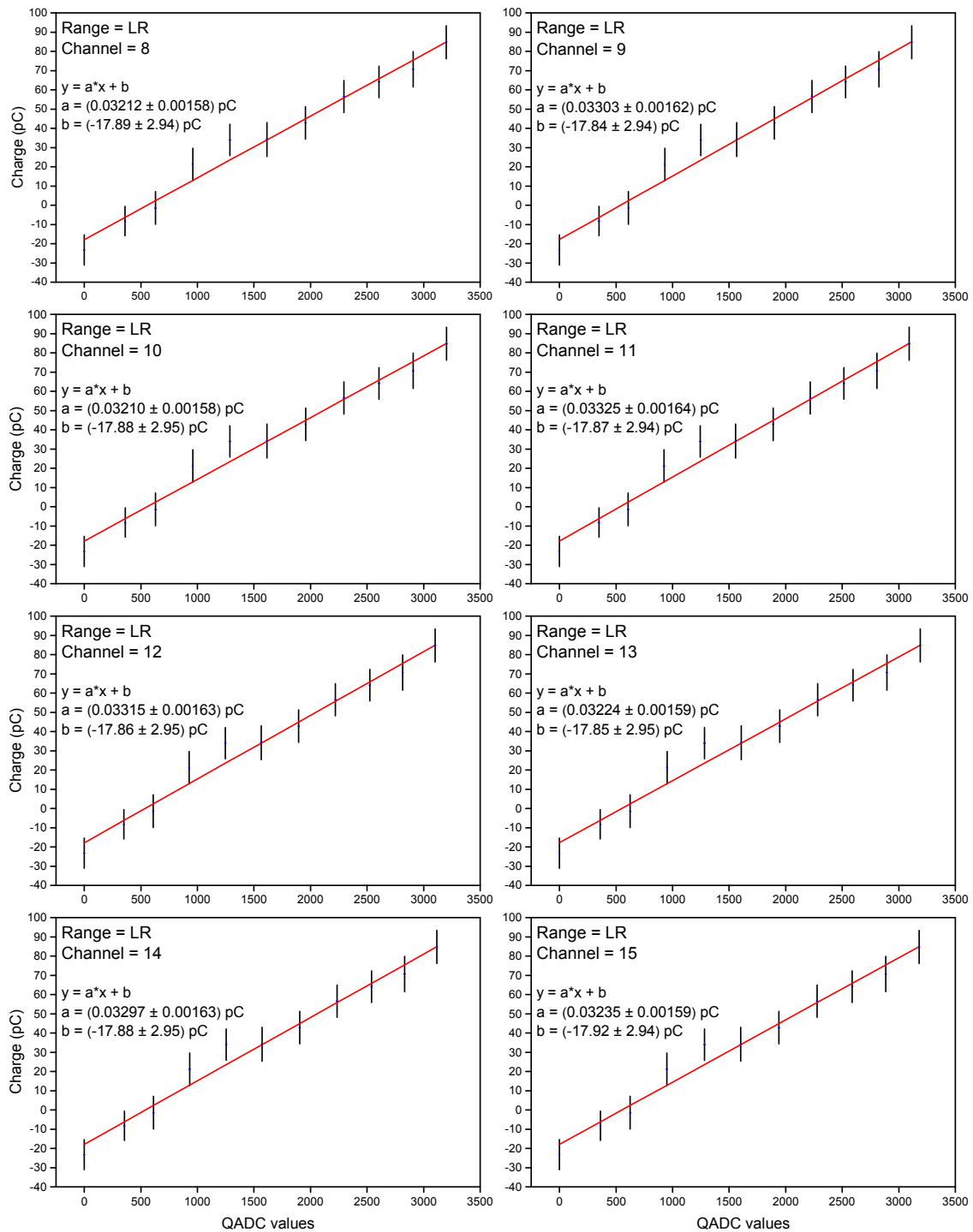
Figure A.8: Measurements of the QADC-linearity for the low range (*LR*) and channels 8 to 15. Measured by Simon Ehnle in the course of his bachelor thesis [123].
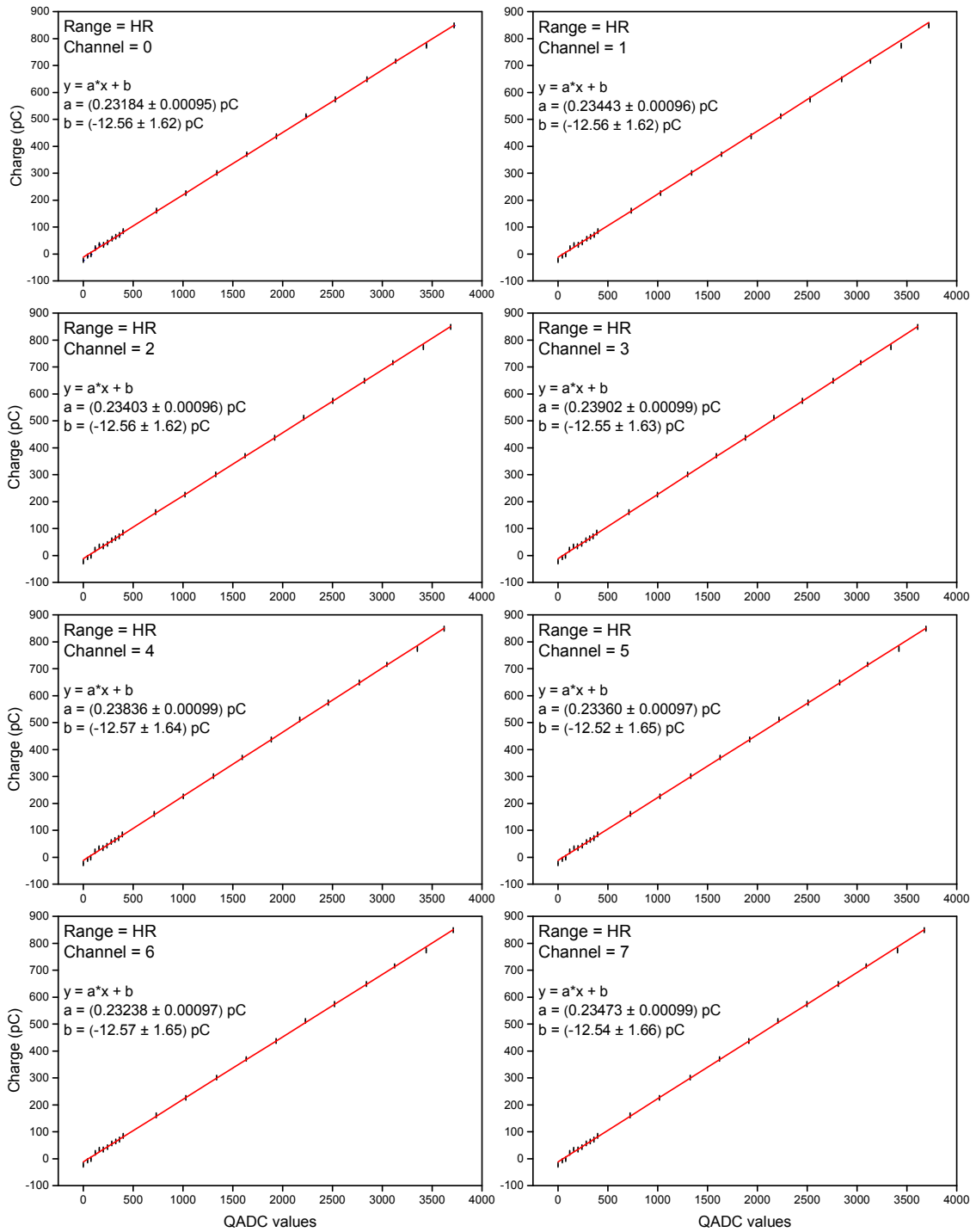
Figure A.9: Measurements of the QADC-linearity for the high range (*HR*) and channels 0 to 7. Measured by Simon Ehnle in the course of his bachelor thesis [123].
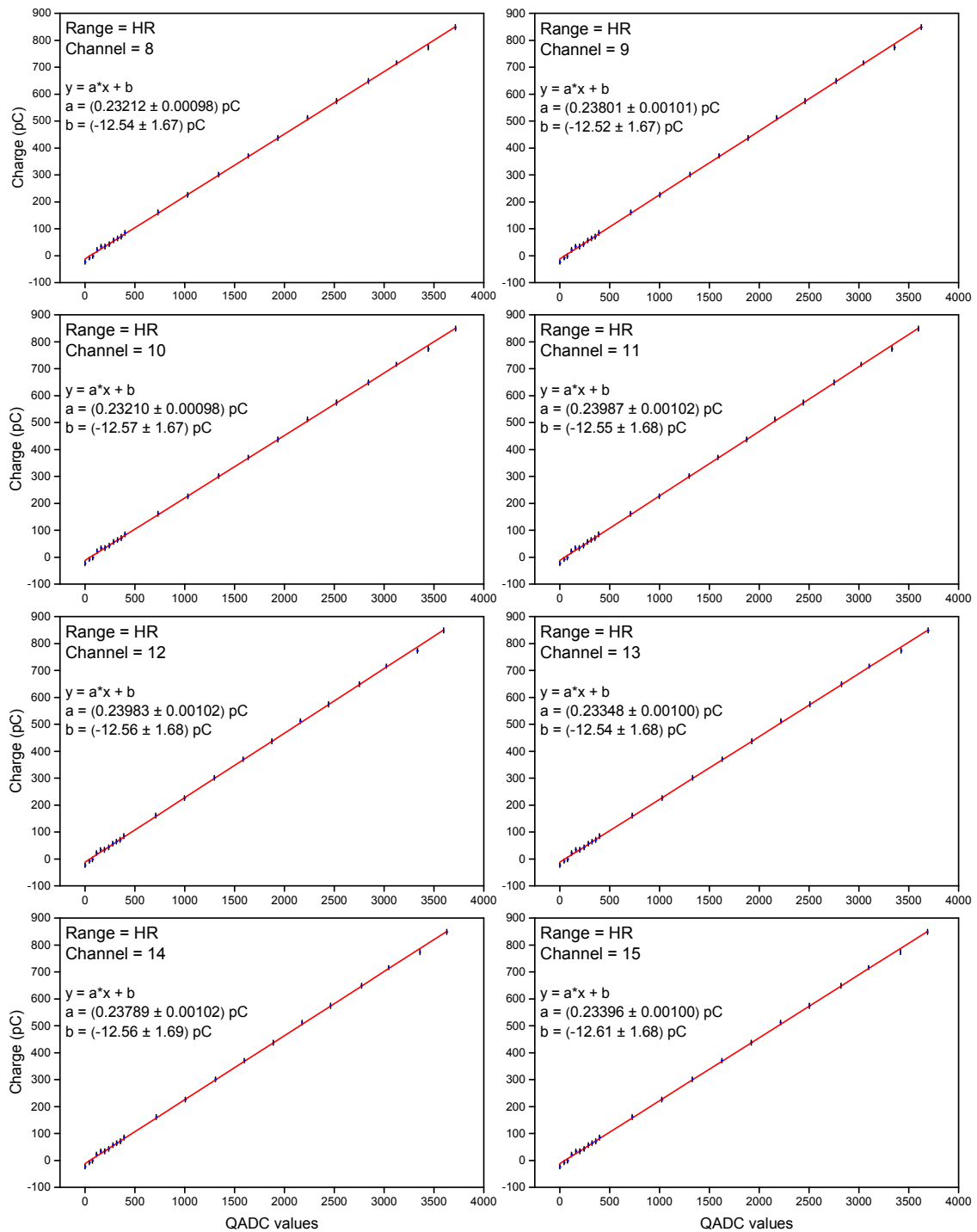
Figure A.10: Measurements of the QADC-linearity for the high range (*HR*) and channels 8 to 15. Measured by Simon Ehnle in the course of his bachelor thesis [123].

A.5 UNCERTAINTY CALCULATIONS FOR MAPMTS

Since all above mentioned measurements with MAPMTs are analyzed with the '*MAPMT algorithm*' described in Section 5.1.3, the corresponding uncertainty calculations are given at this point. At first the uncertainty calculations are given for the gain G. Afterwards the uncertainty calculations are given for the PDE ϵ.

A.5.1 Uncertainty calculations - gain

Observables for the gain were already given in Equation 5.4:

$$G = \frac{(X_1 - X_0) \cdot k}{e} \quad .$$

where

$\quad\quad X_0 \quad$ is the *pedestal* mean value in QADC values,
$\quad\quad X_1 \quad$ is the *1 pe* peak mean value in QADC values,
$\quad\quad k \quad$ is the proportionality factor for the charge and the QADC value, and
$\quad\quad e \quad$ is the charge of an electron $1.602\,176\,565 \times 10^{-19}$ C.

The Gauss peak mean values X_m are attained by Gauss fits (Equation A.3) and measured with the QADC. The proportionality factor k for the charge and the QADC value was precisely measured for every channel and range (Section 4.4.1). The values for k are given in Table 4.4. The electron charge is given as $e = 1.602\,176\,565 \times 10^{-19}$ C by the particle data group [128].

STATISTICAL UNCERTAINTIES: The *statistical uncertainties* in the gain G are the single systematic uncertainties propagated via the standard error propagation formula for independent variables:

$$
\sigma_G^2 = \left(\frac{\partial G}{\partial X_1} \cdot \sigma_{X_1} \right)^2 + \left(\frac{\partial G}{\partial X_0} \cdot \sigma_{X_0} \right)^2 + \left(\frac{\partial G}{\partial k} \cdot \sigma_k \right)^2 + \left(\frac{\partial G}{\partial e} \cdot \sigma_e \right)^2
$$
$$
= \left(\frac{k}{e} \cdot \sigma_{X_1} \right)^2 + \left(\frac{-k}{e} \cdot \sigma_{X_0} \right)^2 + \left(\frac{X_1 - X_0}{e} \cdot \sigma_k \right)^2 + \left(\frac{(X_0 - X_1) \cdot k}{e^2} \cdot \sigma_e \right)^2 ,
$$

where

$\quad\quad \sigma_{X_0} \quad$ is the standard error of the *pedestal* Gauss peak fit,
$\quad\quad \sigma_{X_1} \quad$ is the standard error of the *1 pe* Gauss peak fit,
$\quad\quad \sigma_k \quad$ is the standard deviation of the proportionality factor (Table 4.4), and
$\quad\quad \sigma_e \quad$ is $0.000\,000\,035 \times 10^{-19}$ C [128].

SYSTEMATIC UNCERTAINTIES: The *systematic uncertainties* in the gain G are also propagated via the Gauss error propagation formula. The systematic uncertainties in both Gauss peak centers is their respective value times 0.1 %. Since there is no systematic error for the electron charge given, it follows:

$$
\begin{aligned}
\Delta_G^2 &= \left(\frac{\partial G}{\partial X_1} \cdot \Delta_{X_1} \right)^2 + \left(\frac{\partial G}{\partial X_0} \cdot \Delta_{X_0} \right)^2 + \left(\frac{\partial G}{\partial k} \cdot \Delta_k \right)^2 \\
&= \left(\frac{k}{e} \cdot \Delta_{X_1} \right)^2 + \left(\frac{-k}{e} \cdot \Delta_{X_0} \right)^2 + \left(\frac{X_1 - X_0}{e} \cdot \Delta_k \right)^2 \quad,
\end{aligned}
$$

where

$\frac{\Delta_{X_0}}{X_0} = \frac{\Delta_{X_1}}{X_1} = \frac{\Delta_x}{x} = 0.1\,\%$ are the non-linearities of the QADC and

Δ_k is the systematic error of the proportionality factor (Table 4.4).

A.5.2 Uncertainty calculations - PDE

For the uncertainty calculations of the PDE the number of detected photoelectrons N_{pe} as well as the number of sent photons N onto the detector is needed. Therefore, the Gauss fitting function that is used for the Gauss peaks needs to be defined:

$$
y(x) = \frac{A}{w\sqrt{\frac{\pi}{2}}} \cdot e^{-2 \cdot \left(\frac{x - x_c}{w} \right)^2} \quad, \tag{A.3}
$$

where

A	is the area under the curve,
$w = 2\sigma$	is double the standard deviation,
x_c	is the center of the peak (mean value), and
y_c	is the peak height.

A good estimation for the area and thus for the number of events within a peak is the height times the width of the peak times a correction factor:

$$
A = y_c \cdot w \cdot \sqrt{\frac{\pi}{2}} \quad. \tag{A.4}
$$

The area A_m directly is the number of events N_m for the respective peak m. This means, the *statistical uncertainty* for the number of events in a Gauss peak, result from the respec-

tive fit. For the *1 pe* peak, this gives the number of events $N_{pe} = A_1$, as well as their statistical uncertainty $\sigma_{N_{pe}} = \sigma_{A_1}$, which is the standard error of the area. In general:

$$N_m, \quad \sigma_{N_m} \qquad \text{result from the area of the respective Gauss peak fit.} \tag{A.5}$$

A Poisson correction factor is applied to N_1 for spectra measured with a lower ratio of ratio of *0 pe* events to *1 pe* events than 50. The ratio of *1 pe* and *0 pe* events can be expressed via the ratio of *2 pe* and *1 pe* events after Equation 5.2:

$$\frac{P_2(\lambda)}{P_1(\lambda)} = \frac{\lambda^2}{2!}\frac{1!}{\lambda} = \frac{\lambda}{2} = \frac{1}{2}\frac{P_1(\lambda)}{P_0(\lambda)} \quad .$$

This means, that if the ratio of *0 pe* events to *1 pe* events is higher than 50, the number of counts that belong to a *2 pe* peak will be less that 1 %. If the wanted ratio of 50 is not achieved, the *2 pe* event estimation is subtracted from the *1 pe* event number stemming from the Gauss fit.

For measurements where some of the light from the exit of the collimator may not reach the detectors sensitive area (e. g. full illumination), a correction factor R_{geom} has to be multiplied with Equation 5.6:

$$R_{geom} = \frac{A_{detector}}{A_{PD}} \quad ,$$

with the detector area $A_{detector}$ and the sensitive photodiode area $A_{PD} = 100\,\text{mm}^2$.

SYSTEMATIC UNCERTAINTIES: The *systematic uncertainties* in the number of events per peak, is estimated via Equation A.4. The systematic error in the area Δ_A can be expressed via the error in the width Δ_w. Since the width is a difference of two QADC values, we use the quadratic sum of the errors in the QADC value and get $\Delta_w = \sqrt{2} \cdot 0.1\,\% \cdot w$. The height is not considered here, because the counting of the trigger signals is believed to be accurate. Since there are no further systematic errors, it follows:

$$\Delta_A = \frac{\partial A}{\partial w} \cdot \Delta_w = y_c \cdot \sqrt{\frac{\pi}{2}} \cdot \Delta_w = \frac{A}{w} \cdot \sqrt{2} \cdot 0.1\,\% \cdot w \tag{A.6}$$
$$= \sqrt{2} \cdot 0.1\,\% \cdot A \quad .$$

Corresponding to that, we set $A_m = N_m$ and get for the systematic error in the number of events in peak i:

$$\Delta_{N_m} = \sqrt{2} \cdot 0.1\,\% \cdot N_m \quad . \tag{A.7}$$

The number of photons per light pulse N sent onto the detector is given by the optical power reaching the detector divided by the energy of one photon and the pulse frequency:

$$N = \frac{P_{PD} \cdot R}{E_{photon} \cdot f_{pulse}} = \frac{P_{PD} \cdot R \cdot \lambda}{h \cdot c \cdot f_{pulse}} \quad,$$

where

P_{PD}	is the mean optical power from the photodiode,
$R = \frac{R_1 + R_2}{2}$	is the mean collimator ratio,
$E_{photon} = \frac{h \cdot c}{\lambda}$	is the energy of a sent photon,
h	is the Planck constant: $6.626\,069\,57 \times 10^{-34}$ J s [128],
c	is the speed of light: $299\,792\,458$ m s^{-1} [128],
λ	is the wavelength of the photons, and
f_{pulse}	is the pulse frequency of the LED.

The mean collimator ratio is calculated from the collimator ratio measurement before and after the measurement. The wavelength was determined with the spectrometer measurements shown in Section 4.3.2.2 and depends on the LED-array used (Tables C.3 and C.4).

STATISTICAL UNCERTAINTIES: The *statistical uncertainties* are propagated with the Gauss error propagation formula. There are no statistical errors for the wavelength and the pulse frequency. They were only measured once. The speed of light is given as 'exact' by the particle data group [128]. It follows:

$$\sigma_N^2 = \left(\frac{\partial N}{\partial P_{PD}} \cdot \sigma_{P_{PD}} \right)^2 + \left(\frac{\partial N}{\partial R} \cdot \sigma_R \right)^2 + \left(\frac{\partial N}{\partial h} \cdot \sigma_h \right)^2 \tag{A.8}$$

$$= \left(\frac{R \cdot \lambda}{h \cdot c \cdot f_{pulse}} \cdot \sigma_{P_{PD}} \right)^2 + \left(\frac{P_{PD} \cdot \lambda}{h \cdot c \cdot f_{pulse}} \cdot \sigma_R \right)^2 + \left(-\frac{P_{PD} \cdot R \cdot \lambda}{h^2 \cdot c \cdot f_{pulse}} \cdot \sigma_h \right)^2 \quad,$$

where

$\sigma_{P_{PD}}$	is the standard deviation of the power measurement,
σ_R	is the standard deviation of the mean ratio, and
σ_h	is $0.000\,000\,29 \times 10^{-34}$ J s [128].

SYSTEMATIC UNCERTAINTIES: The *systematic uncertainties* are again calculated via the propagation of uncorrelated variables[1]. Except for the speed of light [128] and the Planck constant [128], every observable has a systematic error. It follows:

$$\Delta_N^2 = \left(\frac{R \cdot \lambda}{h \cdot c \cdot f_{pulse}} \cdot \Delta_{P_{PD}} \right)^2 + \left(\frac{P_{PD} \cdot \lambda}{h \cdot c \cdot f_{pulse}} \cdot \Delta_R \right)^2$$
$$+ \left(\frac{P_{PD} \cdot R}{h \cdot c \cdot f_{pulse}} \cdot \Delta_\lambda \right)^2 + \left(-\frac{P_{PD} \cdot R \cdot \lambda}{h \cdot c \cdot f_{pulse}^2} \cdot \Delta_{f_{pulse}} \right)^2 \quad , \tag{A.9}$$

where

$$\Delta_{P_{PD}} = 1.6\,\% \cdot P_{PD} \qquad \text{is the error of the photodiode [DS91, DS92],}$$
$$\Delta_R^2 = \tfrac{1}{4} \cdot \left(\Delta_{R_1}^2 + \Delta_{R_2}^2 \right) \qquad \text{is the systematic error of the mean ratio,}$$
$$\tfrac{\Delta_{R_1}}{R_1} = \tfrac{\Delta_{R_2}}{R_2} = \sqrt{2} \cdot 1.6\,\% \qquad \text{are the systematic errors of the single ratios,}$$
$$\tfrac{\Delta_\lambda}{\lambda} \qquad \text{is the uncertainty in the wavelength (Table 5.1), and}$$
$$\Delta_{f_{pulse}} = 1 \times 10^{-5} \cdot f_{pulse} \qquad \text{is the frequency error of the oscilloscope [DS149].}$$

For a basic uncertainty estimation, it can be approximated that

$$\Delta_R^2 = \frac{1}{4} \cdot \left(\Delta_{R_1}^2 + \Delta_{R_2}^2 \right) \approx \frac{1}{4} \cdot \left(\Delta_{R_1} + \Delta_{R_2} \right)^2 \quad .$$

With $\quad \frac{\Delta_{R_1}}{R_1} = \frac{\Delta_{R_2}}{R_2} = a \quad$ it follows:

$$\Delta_R^2 = \frac{1}{4} \cdot \left(a \cdot (R_1 + R_2) \right)^2 \tag{A.10}$$
$$= a^2 \cdot \frac{(R_1 + R_2)^2}{4} = a^2 \cdot R^2 \quad .$$

Substitution of $a = \sqrt{2} \cdot 1.6\,\%$ yields: $\frac{\Delta_R}{R} = \sqrt{2} \cdot 1.6\,\% \quad$. However, this is an overestimation of the systematic uncertainty and the real uncertainty should be smaller.

For the frequency measurement the oscilloscope *WaveJet 324A* [DS149] was used. The frequency error $\Delta_{f_{pulse}}$ is derived from the timing accuracy $\frac{\Delta_t}{t} = 1 \times 10^{-5}$. With $f = \frac{1}{t}$ the resulting error in the frequency is:

$$\Delta_{f_{pulse}} = \left| -\frac{1}{t^2} \cdot \Delta_t \right| = \frac{1}{t^2} \cdot \Delta_t = f_{pulse} \cdot \frac{\Delta_t}{t} \quad . \tag{A.11}$$

---

1 For sufficiently small differences between the single mean ratio R_i from each other, i.e. differences in R_i are smaller than the individual systematic errors Δ_{R_i}. Else see Appendix A.3

PDE: Now the PDE can be calculated via Equation 5.5. As a reminder, the PDE formula is given again:

$$\epsilon = \frac{N_{pe}}{N \cdot N_{total}} \quad ,$$

with the number of incident photons N per pulse and the total number N_{total} of events in the single photoelectron spectrum (number of triggers). The error propagation formula yields:

$$\sigma_\epsilon = \sqrt{\left(\frac{\partial \epsilon}{\partial N_{pe}} \cdot \sigma_{N_{pe}}\right)^2 + \left(\frac{\partial \epsilon}{\partial N} \cdot \sigma_N\right)^2} \tag{A.12}$$

$$= \sqrt{\left(\frac{1}{N} \cdot \sigma_{N_{pe}}\right)^2 + \left(-\frac{N_{pe}}{N^2} \cdot \sigma_N\right)^2} \quad ,$$

$$\Delta_\epsilon = \sqrt{\left(\frac{1}{N} \cdot \Delta_{N_{pe}}\right)^2 + \left(-\frac{N_{pe}}{N^2} \cdot \Delta_N\right)^2} \quad ,$$

where

N_{pe}	is the area under *1 pe peak* (Gauss fit) (Equation A.5),
$\sigma_{N_{pe}}$	is the standard error of the area (Gauss fit) (Equation A.5),
$\Delta_{N_{pe}}$	is the systematic error of the area (Equation A.7),
N	is the number of photons sent on the detector per pulse (Equation 5.6),
σ_N	is the statistical error in the photon number (Equation A.8), and
Δ_N	is the systematic error in the photon number (Equation A.9).

The total number N_{total} of triggered events is assumed to be accurate.

A.6 MAPMT PLOTS

For this work four MAPMTs *R11265-113-M64 MOD2* from an early production series of Hamamatsu were present at KIT. Two of them (SN: *ZN0854* and *ZN0884*) had an UV transmitting band pass filter *Schott BG3* [DS62] directly glued to their photocathode. The other two MAPMTs (SN: *ZN0857* and *ZN0882*) had nothing attached to their photocathode. The discussion of example plots is given in Section 5.2.1.
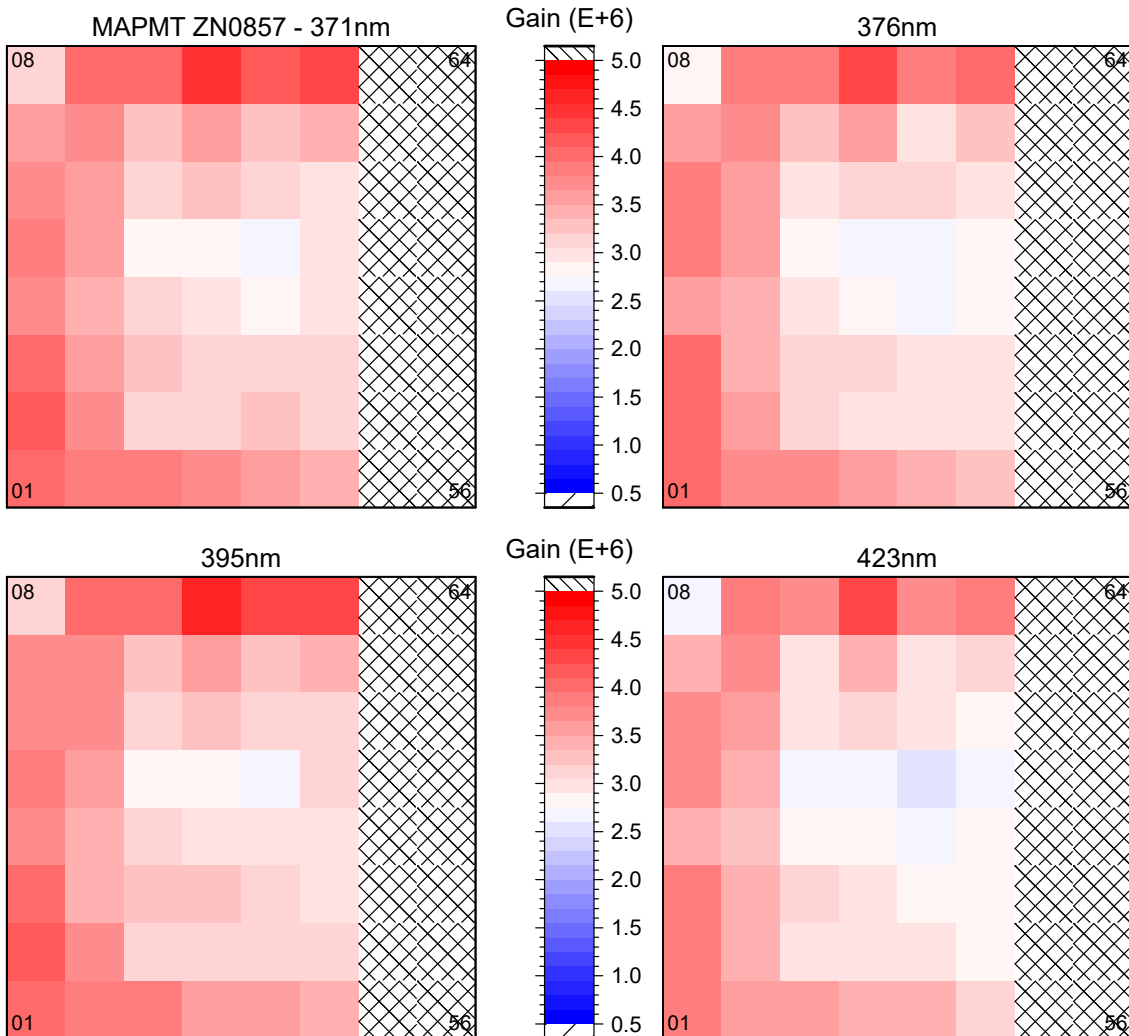
Figure A.11: Gain maps of the single pixel scans of MAPMT *ZN0857* for different wavelengths at −1000 V bias voltage. This MAPMT had lots of strong dark count signals in pixels 49 to 64, most likely due to arcing inside the dynode structure. Therefore these pixels were not measured further and are marked with a cross pattern. This only occurred with this one MAPMT.
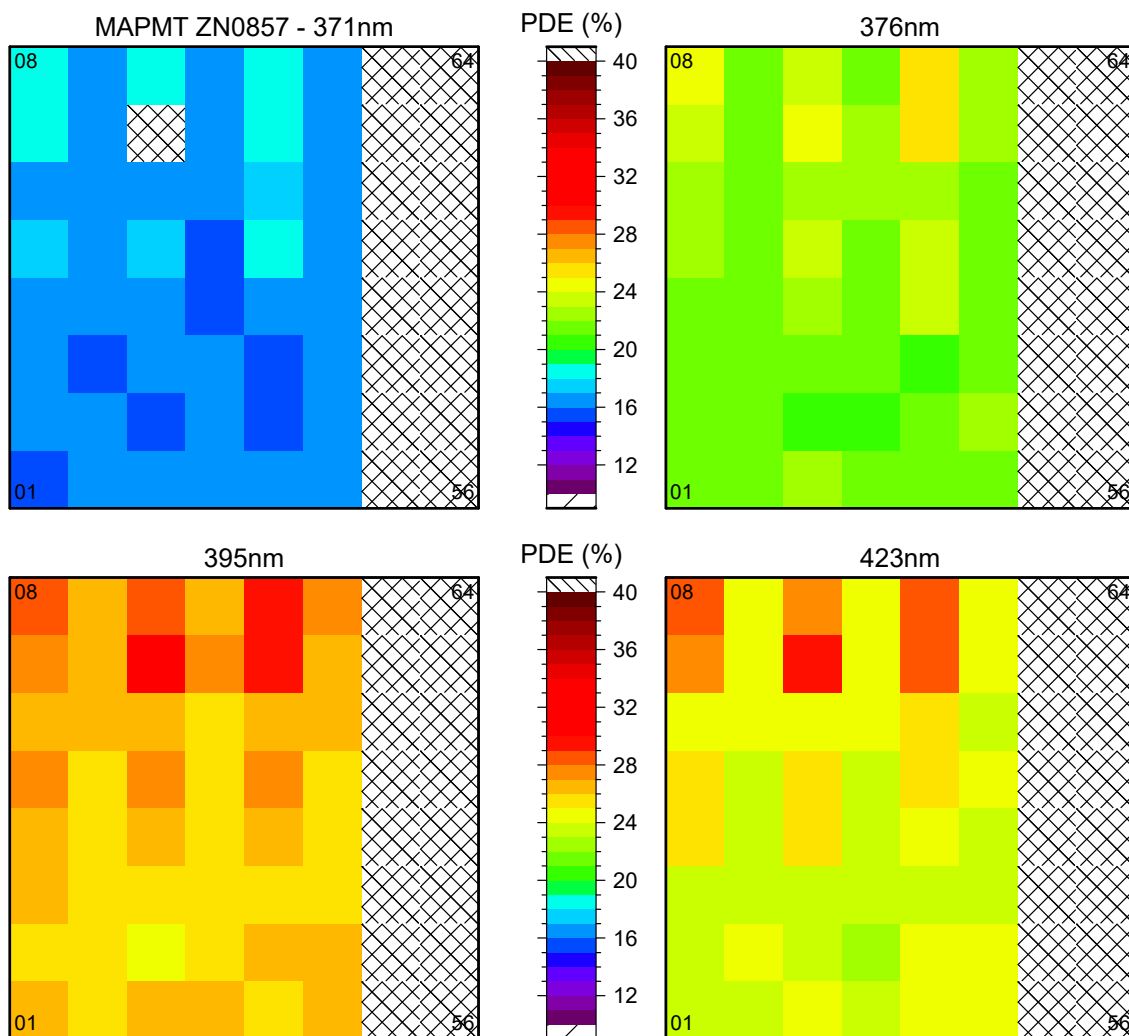
Figure A.12: PDE maps of the single pixel scans of MAPMT *ZN0857* for different wavelengths at -1000 V bias voltage. This MAPMT had lots of strong dark count signals 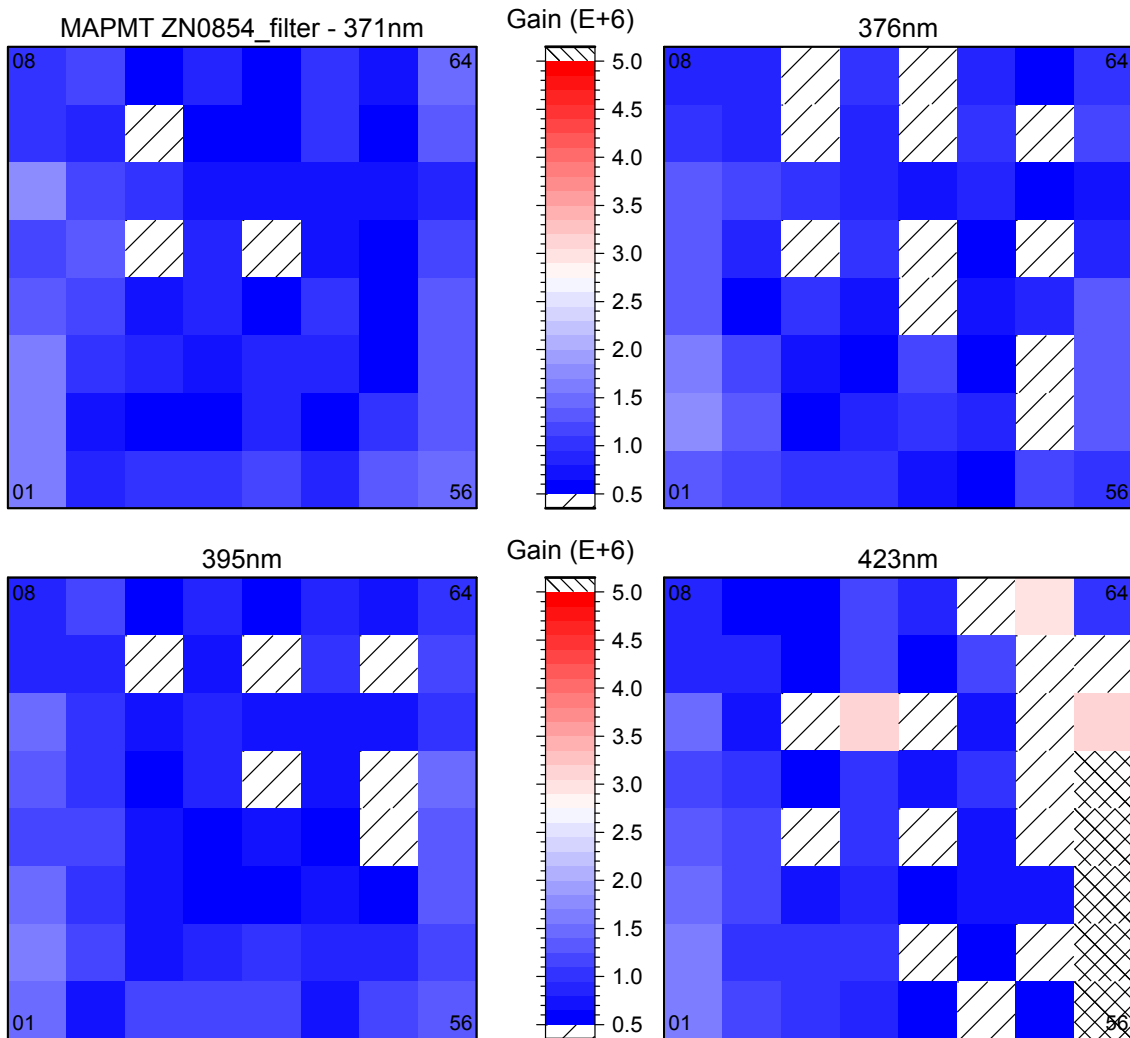in pixels 49 to 64, most likely due to arcing inside the dynode structure. Therefore these pixels were not measured further and are marked with a cross pattern. This only occurred with this one MAPMT.

Figure A.13: Gain maps of the single pixel scans of MAPMT *ZN0854 filter* for different wavelengths at $-1000\,\mathrm{V}$ bias voltage. The MAPMT has a UV transmitting band pass filter *Schott BG3* [DS62] directly glued to its photocathode. Some of the gain values are below 0.5×10^6 and are therefore marked with a low density line pattern. Five outliers were detected for a wavelength of 423 nm and were masked. They are marked with a cross pattern.

Figure A.14: PDE maps of the single pixel scans of MAPMT *ZN0854 filter* for different wavelengths at −1000 V bias voltage. The MAPMT has a UV transmitting band pass filter *Schott BG3* [DS62] directly glued to its photocathode. Some of the PDE values are below 10 % and are therefore marked with a low density line pattern. PDE values higher than 40 % are marked with a high density line pattern. Statistical outliers are marked with a cross pattern.
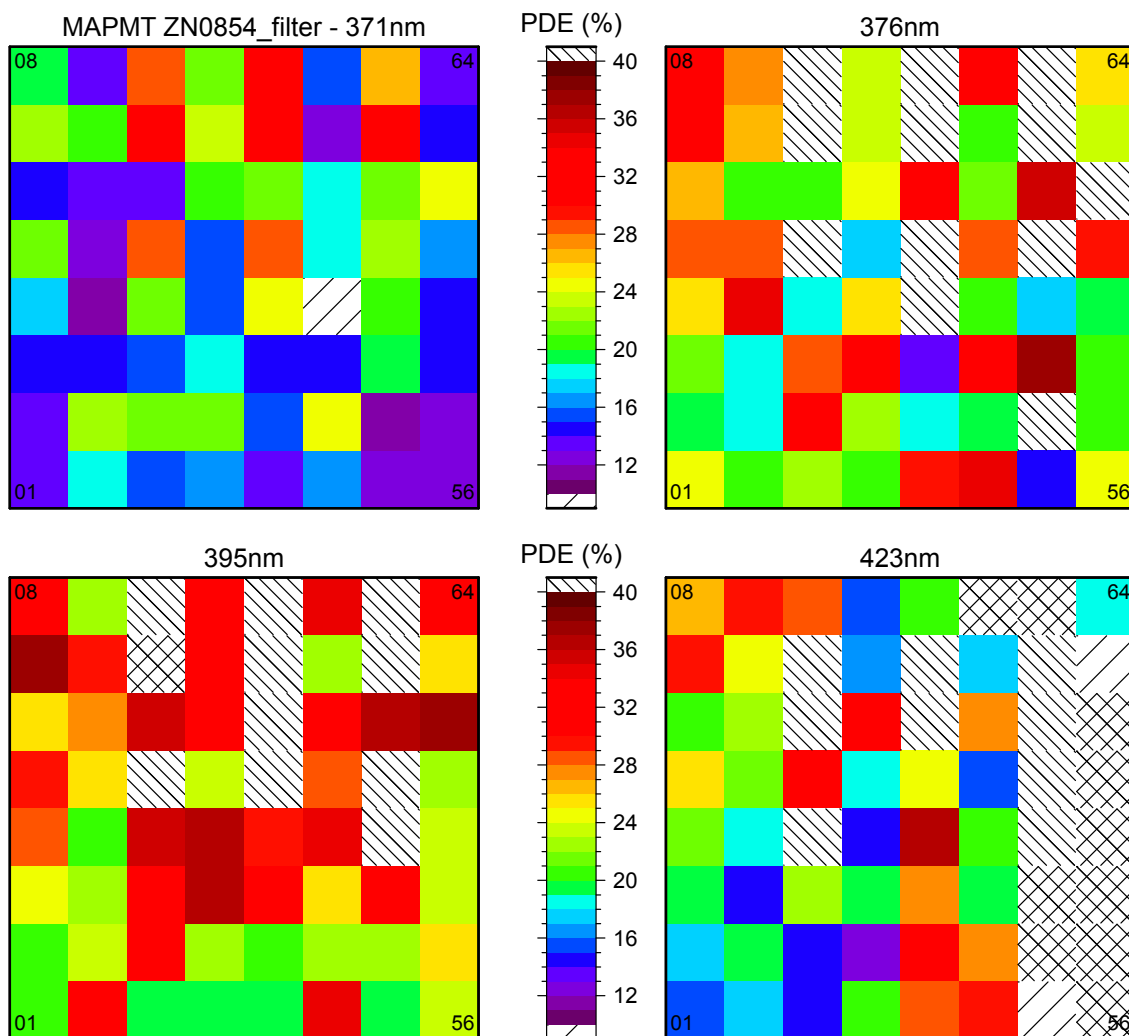
Figure A.15: Gain maps of the single pixel scans of MAPMT *ZN0884 filter* for different wavelengths at −1000 V bias voltage. The MAPMT has a UV transmitting band pass filter *Schott BG3* [DS62] directly glued to its photocathode. Some of the gain values are below 0.5×10^6 and are therefore marked with a low density line pattern.
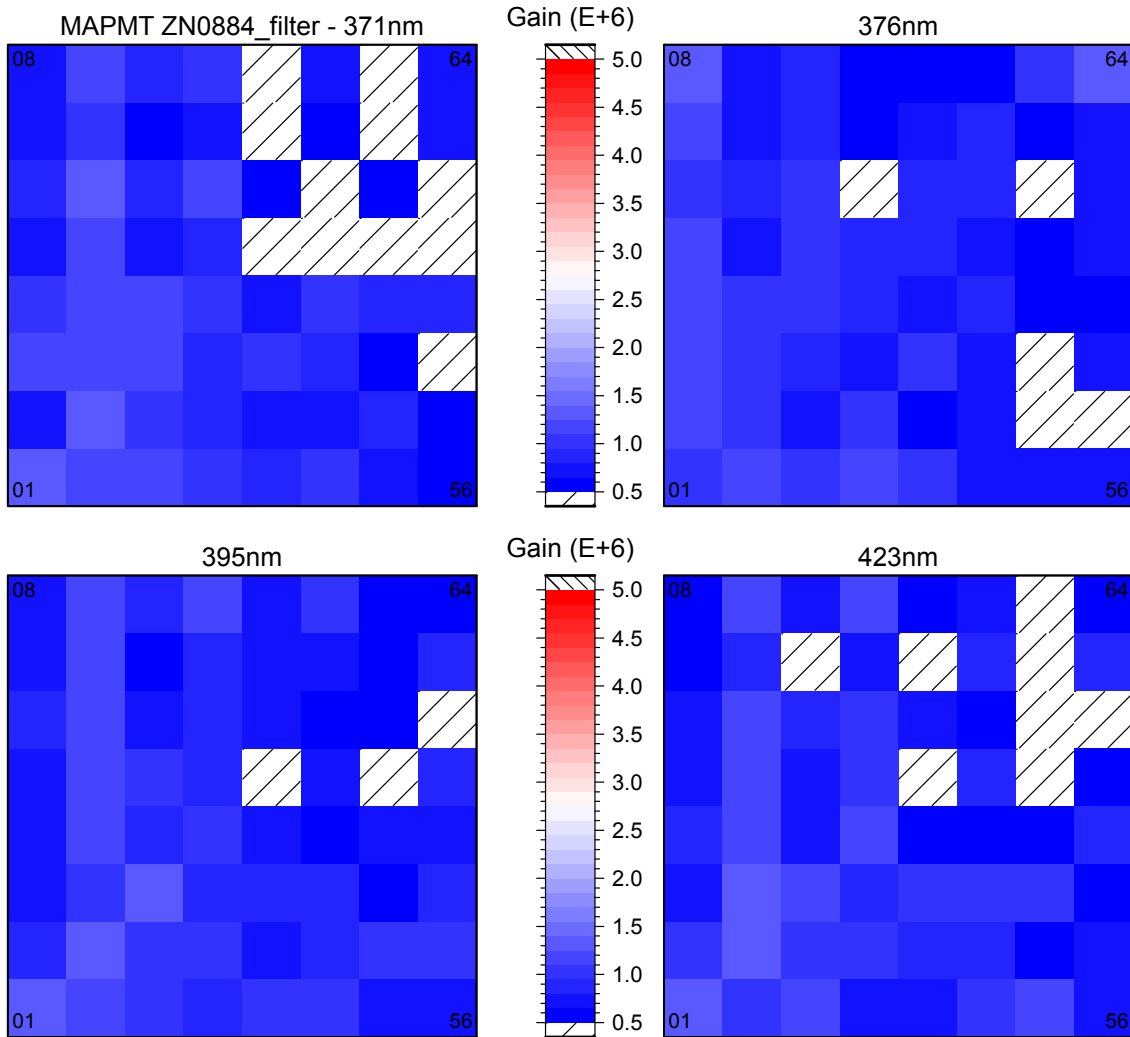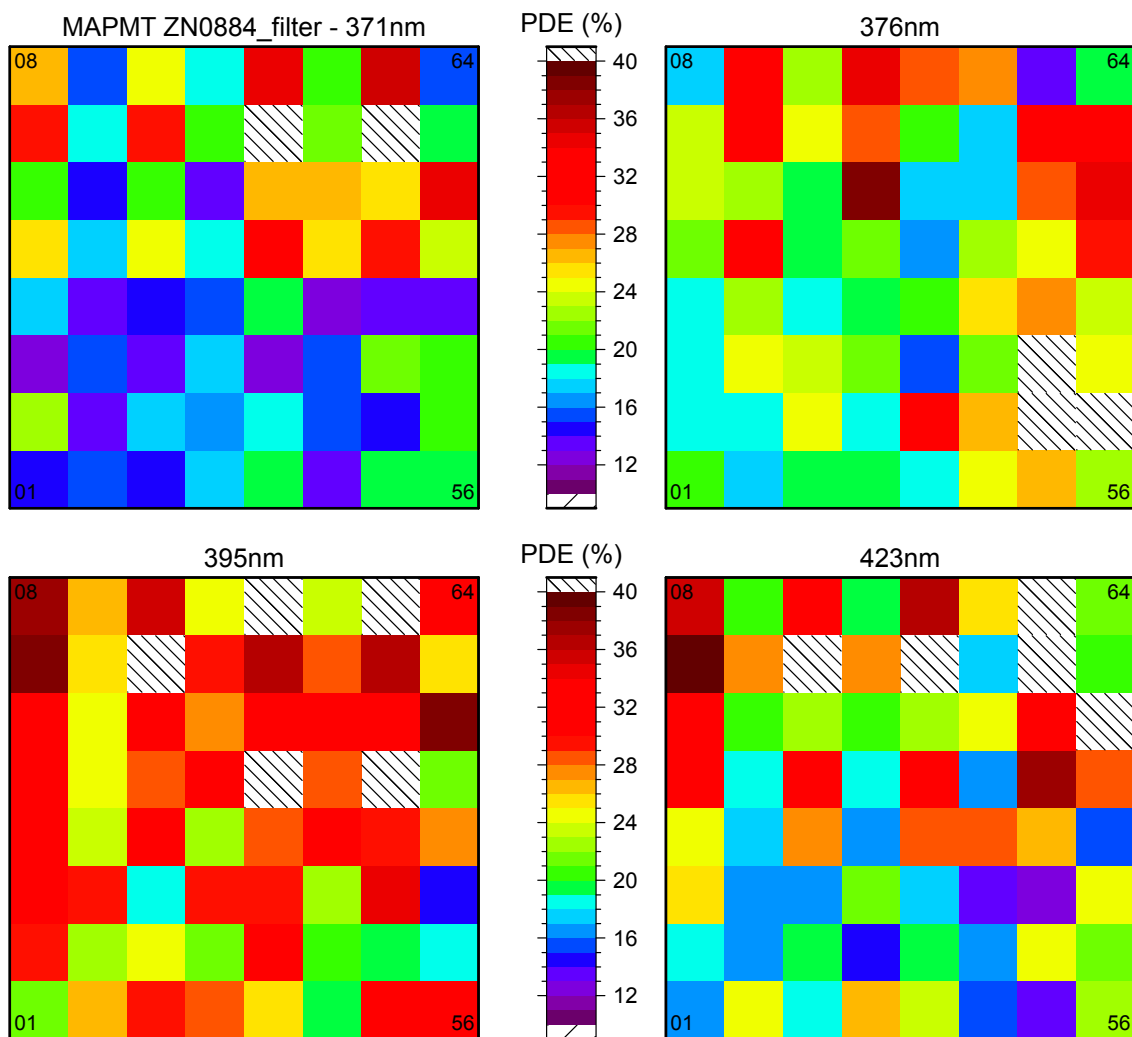
Figure A.16: PDE maps of the single pixel scans of MAPMT *ZN0884 filter* for different wavelengths at −1000 V bias voltage. The MAPMT has a UV transmitting band pass filter *Schott BG3* [DS62] directly glued to its photocathode. PDE values higher than 40 % are marked with a high density line pattern.
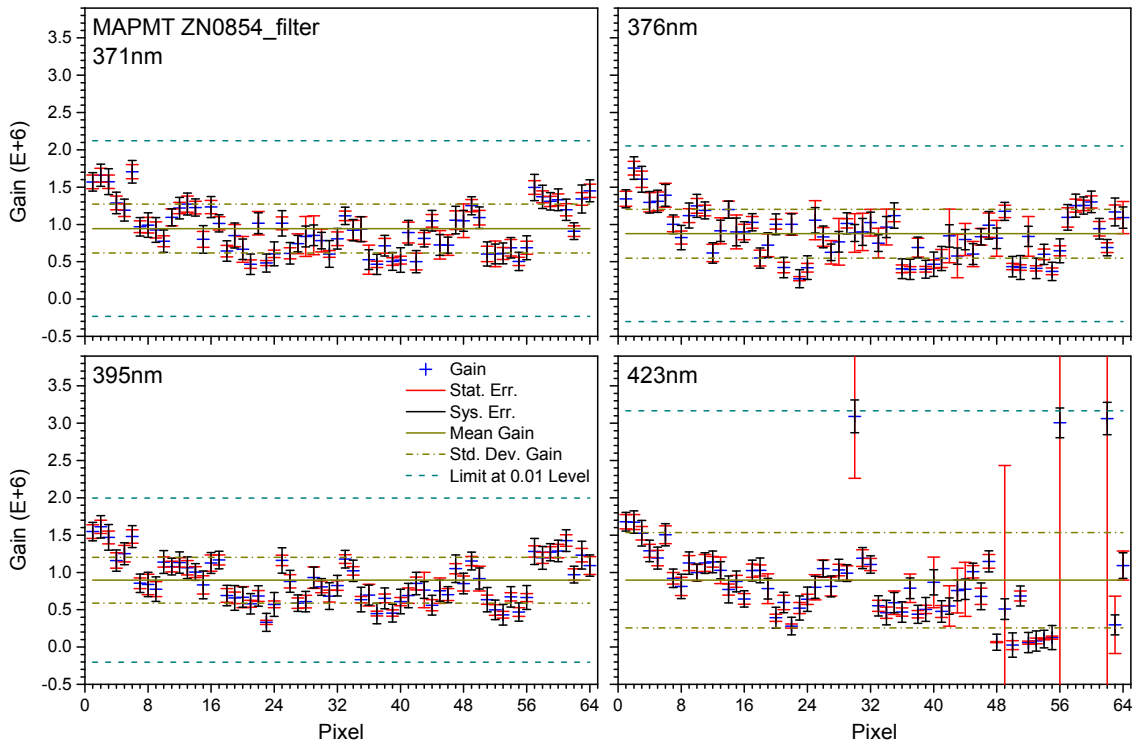
(a) MAPMT *ZN0854 filter* - gain versus pixel.
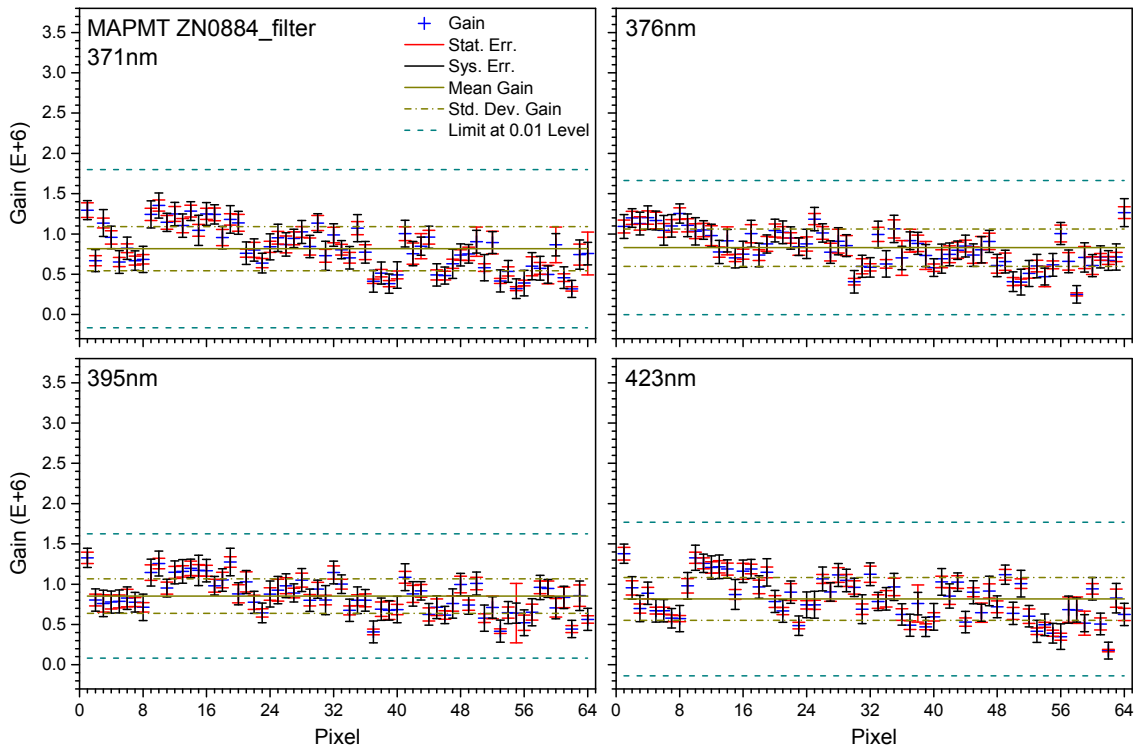
(b) MAPMT *ZN0884 filter* - gain versus pixel.

Figure A.17: Gain versus pixel of MAPMTs *ZN0854 filter* and *ZN0884 filter* for different wavelengths at $-1000\,$V bias voltage.
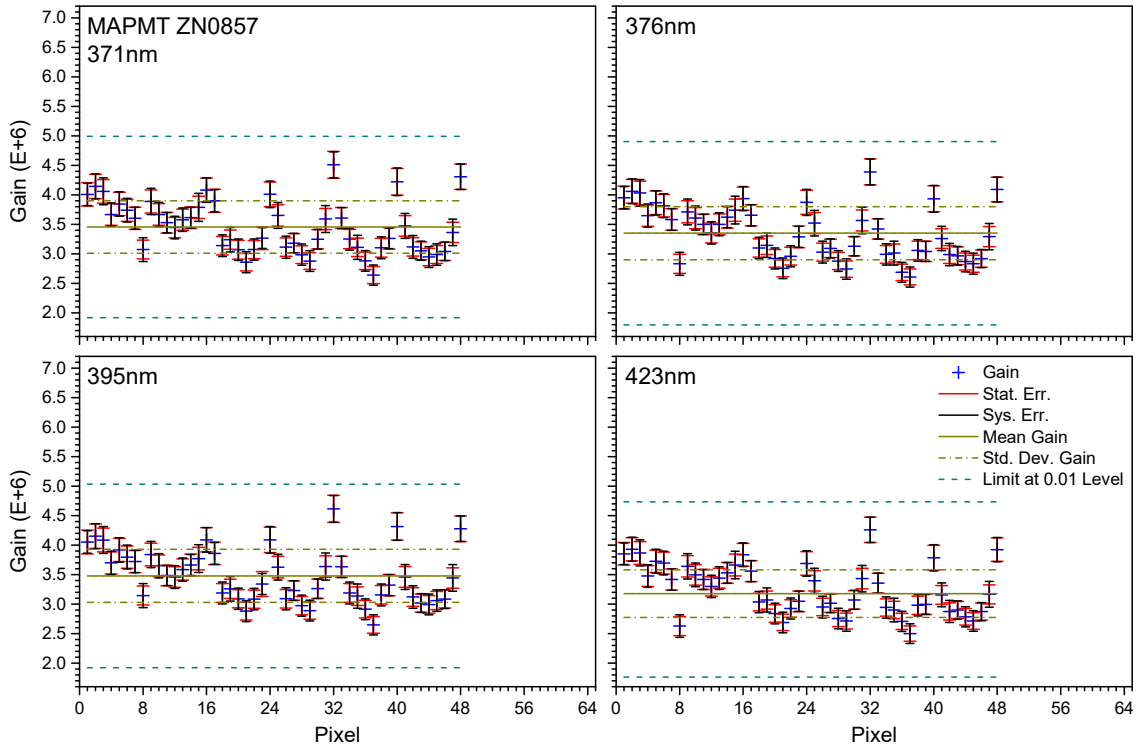
(a) MAPMT *ZN0857* - gain versus pixel.

(b) MAPMT *ZN0882* - gain versus pixel.

Figure A.18: Gain versus pixel of MAPMTs *ZN0857* and *ZN0882* for different wavelengths at −1000 V bias voltage.

(a) MAPMT *ZN0854 filter* - PDE versus pixel.

(b) MAPMT *ZN0884 filter* - PDE versus pixel.

Figure A.19: PDE versus pixel of MAPMTs *ZN0854 filter* and *ZN0884 filter* for different wavelengths at −1000 V bias voltage.
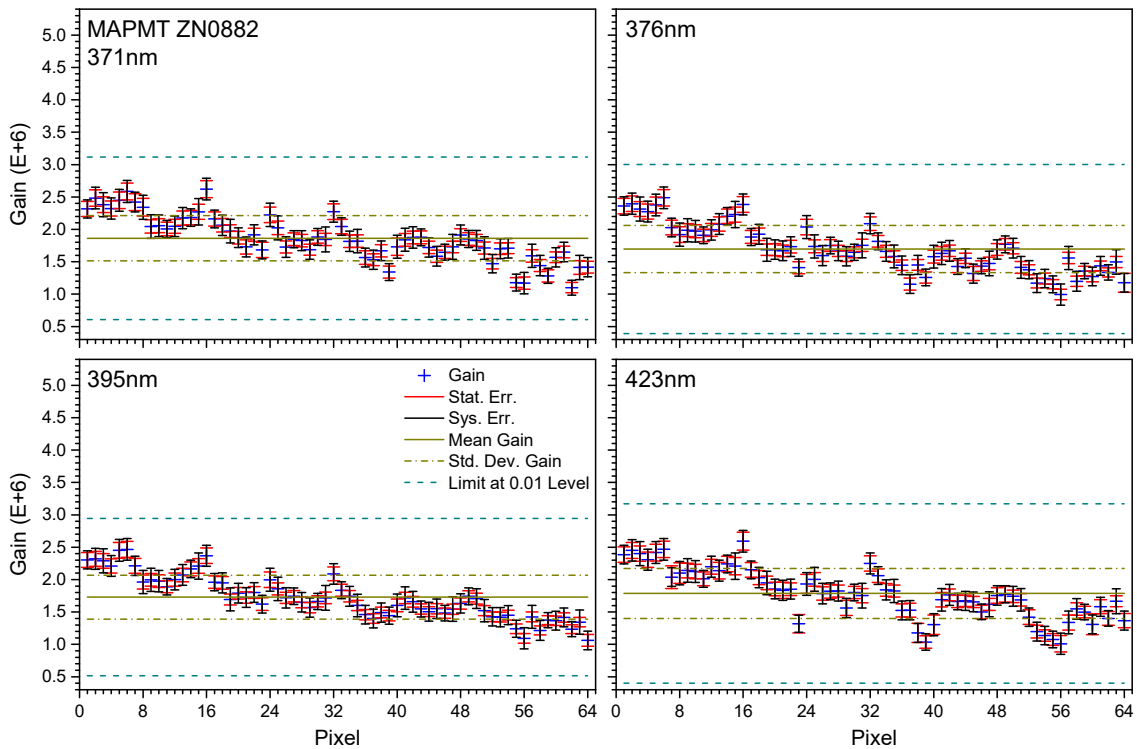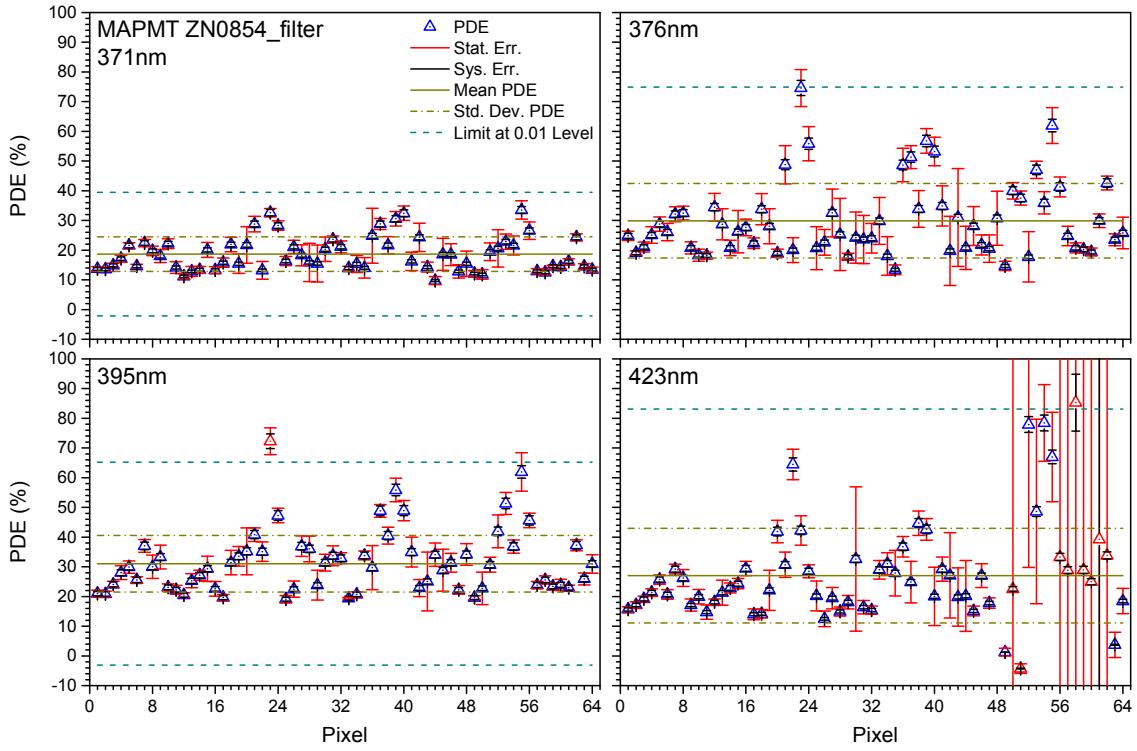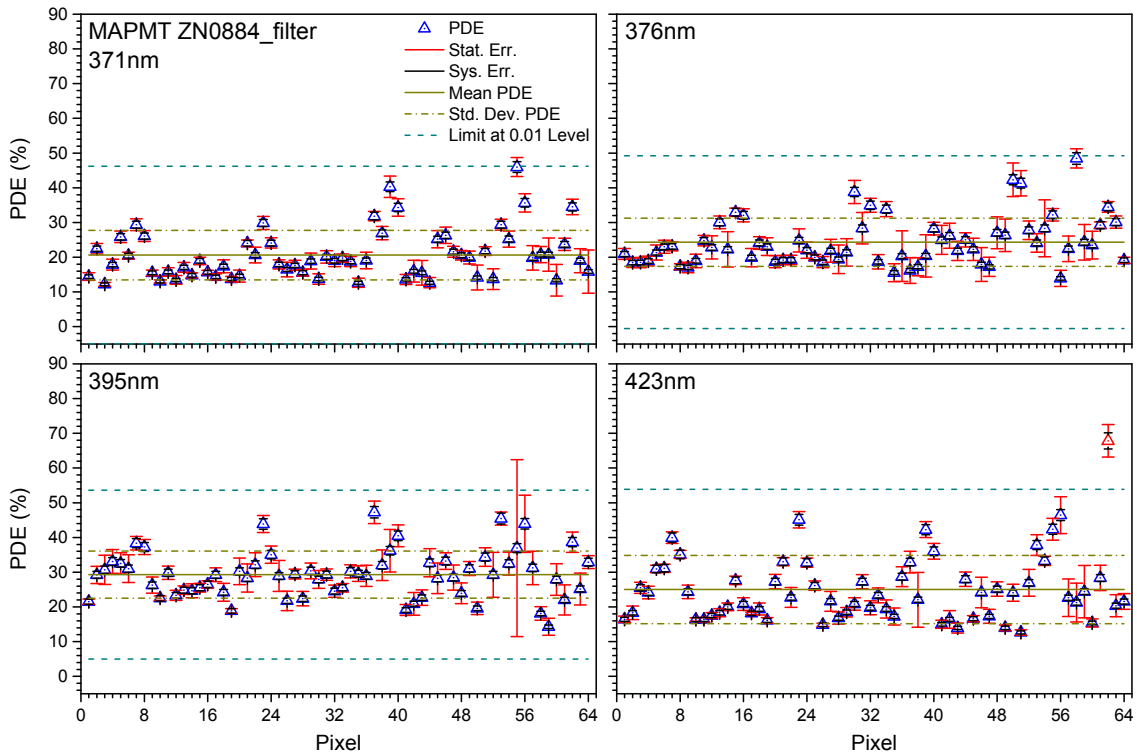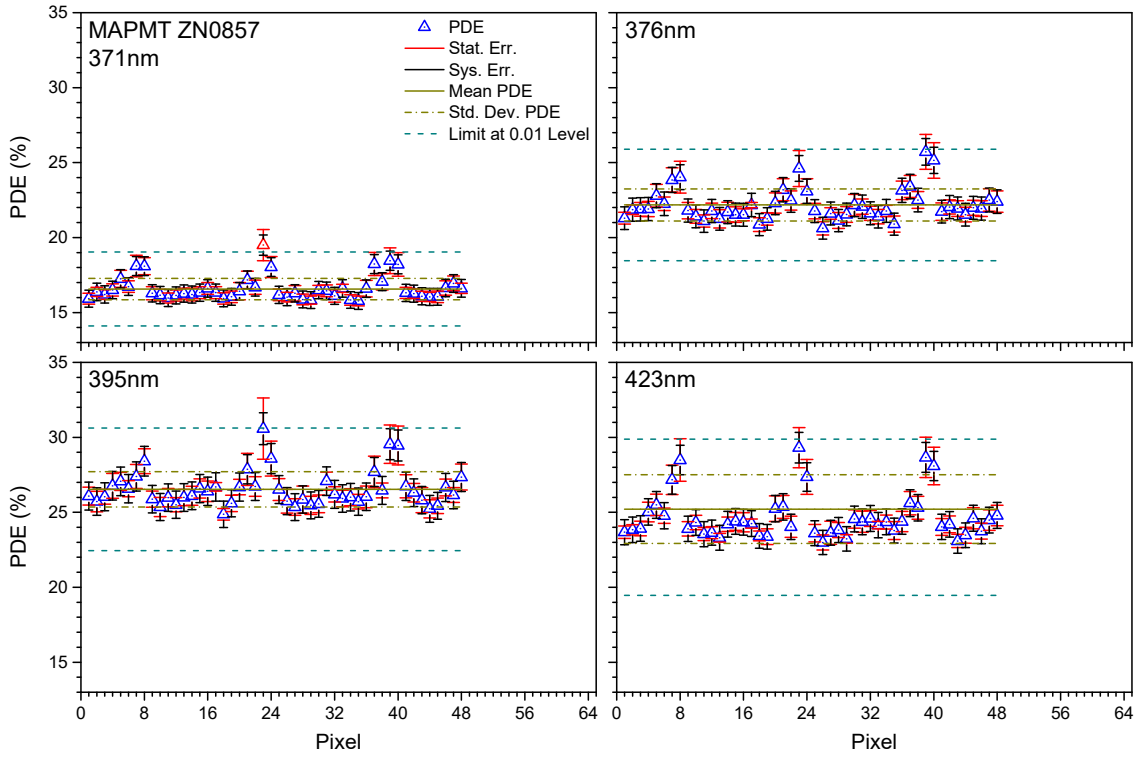
(a) MAPMT *ZN0857* - PDE versus pixel.
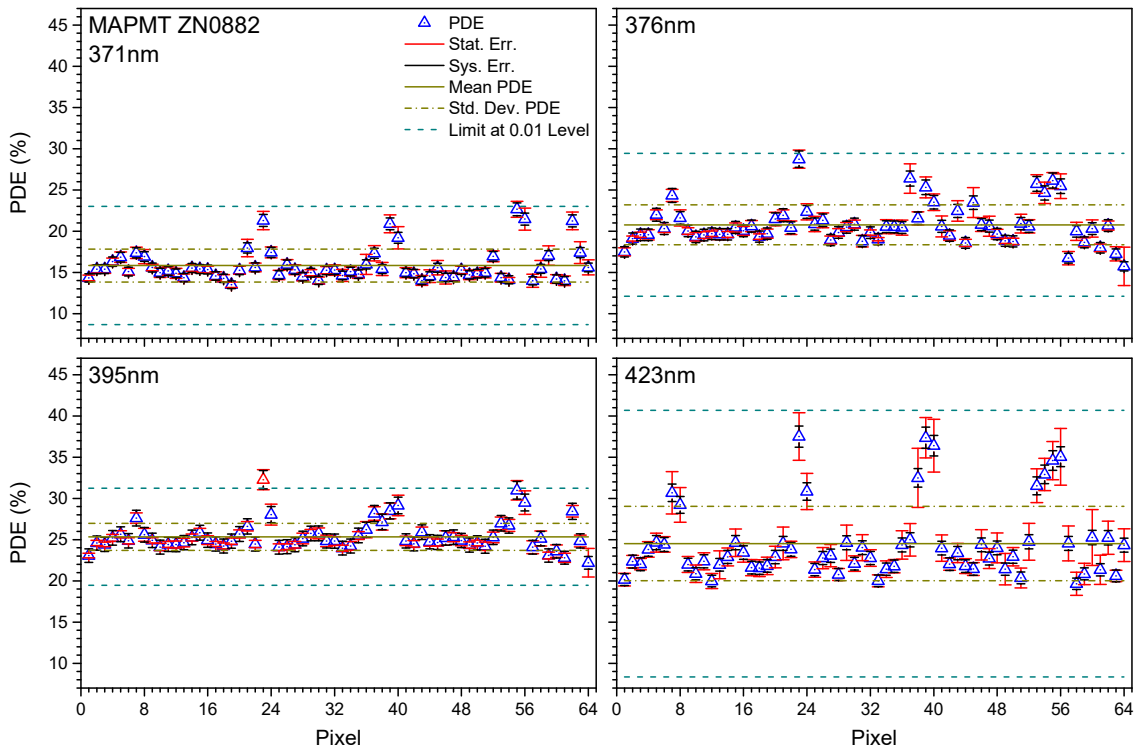
(b) MAPMT *ZN0882* - PDE versus pixel.

Figure A.20: PDE versus pixel of MAPMTs *ZN0857* and *ZN0882* for different wavelengths at −1000 V bias voltage.

A.7 UNCERTAINTY CALCULATIONS FOR SIPMS

Since all measurements with SiPMs are analyzed with the same algorithm, that was described in Section 6.1.3, the corresponding uncertainty calculations are given at this point. First the uncertainty calculations are given for the gain G. They are similar to the gain calculations done for MAPMTs, but use a mean value for the peak separation, since there are several peaks in a finger spectrum. Afterwards the uncertainty calculations are given for the PDE ϵ. Which relies on Poisson statistics, to define the number of detected photons via the number of not detected photons.

A.7.1 Uncertainty calculations - gain

The recorded finger spectrum comprises of m Gauss peaks X_m and therefore of $n = m - 1$ peak separations x_n. The mean value of the peak separation x is then used to calculate the SiPM gain G (Equation 6.4).

$$x = \frac{1}{n} \sum_{i=1}^{m} x_i \quad .$$

(A.13)

where

x	is the mean peak separation,
$x_m = X_m - X_n$	are the Gauss peak separations of adjacent peaks, and
X_m	individual Gauss peak mean values (Gauss fits).

The gain is then calculated via:

$$G = \frac{x \cdot k}{e \cdot \Lambda} \quad .$$

where

x	is the mean peak separation,
k	is the proportionality factor for the charge and the QADC value,
e	is the charge of an electron, and
Λ	is the amplification factor of an amplifier (if applicable).

The Gauss peak separations x are attained by Gauss fits (Equation A.3) with the peak values X_m and measured with the QADC. The value for the proportionality factor k is given in Table 4.4. In the case of these measurements only channel 0 of the QADC was used: $k = (32.08 \pm 1.57_{\mathrm{stat}} \pm 1.24_{\mathrm{sys}})$ fC. The electron charge is given as $e = 1.602\,176\,565 \times 10^{-19}$ C by the particle data group [128]. The amplification factor Λ used for SiPM measurements shown in this thesis is $10.1 \pm 0.05_{\mathrm{sys}}$.

STATISTICAL UNCERTAINTIES: The *statistical uncertainties* in the gain G are the single systematic uncertainties propagated via the standard error propagation formula for independent variables. There is no statistical uncertainty given for the amplification factor. It follows:

$$
\begin{aligned}
\sigma_G^2 &= \left(\frac{\partial G}{\partial x} \cdot \sigma_x \right)^2 + \left(\frac{\partial G}{\partial k} \cdot \sigma_k \right)^2 + \left(\frac{\partial G}{\partial e} \cdot \sigma_e \right)^2 \\
&= \left(\frac{k}{e \cdot \Lambda} \cdot \sigma_x \right)^2 + \left(\frac{x}{e \cdot \Lambda} \cdot \sigma_k \right)^2 + \left(\frac{x}{e^2 \cdot \Lambda} \cdot \sigma_e \right)^2 \quad ,
\end{aligned}
$$

where

σ_x is the standard deviation of the mean peak separation,
σ_k is 1.57 fC (Table 4.4), and
σ_e is $0.000\,000\,035 \times 10^{-19}$ C [128].

SYSTEMATIC UNCERTAINTIES: The *systematic uncertainties* in the gain G are also propagated via the Gauss error propagation formula. We substitute the mean peak separation with the highest peak X_m and the pedestal peak X_0, since $x = \frac{1}{n} \cdot (X_m - X_0)$ is equivalent to Equation A.13. It follows:

$$
G = \frac{(X_m - X_0) \cdot k}{n \cdot e \cdot \Lambda} \quad .
$$

Since there is no systematic error for the electron charge given, and we do not make any mistake in counting the number of peaks fitted, it follows:

$$
\begin{aligned}
\Delta_G^2 &= \left(\frac{\partial G}{\partial X_m} \cdot \Delta_{X_m} \right)^2 + \left(\frac{\partial G}{\partial X_0} \cdot \Delta_{X_0} \right)^2 + \left(\frac{\partial G}{\partial k} \cdot \Delta_k \right)^2 + \left(\frac{\partial G}{\partial \Lambda} \cdot \Delta_\Lambda \right)^2 \\
&= \left(\frac{k}{e \cdot \Lambda} \cdot \Delta_{X_m} \right)^2 + \left(-\frac{k}{e \cdot \Lambda} \cdot \Delta_{X_0} \right)^2 + \left(\frac{x}{e \cdot \Lambda} \cdot \Delta_k \right)^2 + \left(-\frac{x \cdot k}{e \cdot \Lambda^2} \cdot \Delta_\Lambda \right)^2 \quad ,
\end{aligned}
$$

where

$\frac{\Delta_{X_m}}{X_m} = \frac{\Delta_{X_0}}{X_0} = 0.1\,\%$ are the non-linearities of the QADC,
$\frac{\Delta_k}{k} = 3.9\,\%$ with $\Delta_k = 1.24$ fC (Table 4.4), and
$\frac{\Delta_\Lambda}{\Lambda} = 0.5\,\%$ for an amplification factor of $10.1 \pm 0.05_{sys}$.

Thus, yielding an overall systematic uncertainty for the gain of SiPMs of roughly 3.9 % (Equation 6.8). Alternatively, the systematic errors in the peak separations $\Delta_{x_n} = \sqrt{2} \cdot 0.1\,\% \cdot x_n$ can be used. They were calculated via the propagated systematics of the QADC non-linearity for each Gauss fit mean value $\Delta_{X_m} = 0.1\,\% \cdot X_m$, yielding the same result.

A.7.2 Uncertainty calculations - PDE

For the uncertainty calculations of the PDE the number of detected photoelectrons N_{pe} as well as the number of sent photons N onto the detector is needed. The number of detected photoelectrons N_{pe} is calculated via Poisson statistics from the probability to detect no events, i.e. via the pedestal events of the illuminated finger spectrum and the dark count spectrum (Equation 6.6). The Gauss fitting function (Equation A.3) was already shown in Appendix A.5.2. The area A_i directly yields the number of events N_i for the respective peak. The number of detected photons per pulse is calculated as was shown in Equation 6.6:

$$N_{pe} = -\ln\left(\frac{N_{ped}}{N_{tot}}\right) + \ln\left(\frac{N_{ped}^{dark}}{N_{tot}^{dark}}\right) \quad , \tag{A.14}$$

where

N_{ped} is the number of pedestal events (Gauss),

N_{tot} is the total number of events in the spectrum (trigger),

N_{ped}^{dark} is the number of pedestal events in

the dark spectrum (Gauss), and

N_{tot}^{dark} is the total number of events in the dark spectrum (trigger).

STATISTICAL UNCERTAINTIES: The *statistical uncertainty* of the number of detected photons follows via error propagation:

$$\sigma_{N_{pe}}^2 = \left(\frac{\partial N_{pe}}{\partial N_{ped}} \cdot \sigma_{N_{ped}}\right)^2 + \left(\frac{\partial N_{pe}}{\partial N_{ped}^{dark}} \cdot \sigma_{N_{ped}^{dark}}\right)^2 \quad . \tag{A.15}$$

The number of total events in the illuminated and the dark spectrum is controlled by the measurement program and assumed to be accurate, therefore it was used that $\sigma_{N_{tot}} = \sigma_{N_{tot}^{dark}} = 0$. The other statistical uncertainties follow from the Gauss peak fits of the pedestals of the respective spectrum (analogue to Equation A.5).

$\sigma_{N_{tot}} = \sigma_{N_{tot}^{dark}} = 0$ total events in the spectra (trigger),

$\sigma_{N_{ped}}$ is the standard error of the pedestal area (Gauss), and

$\sigma_{N_{ped}^{dark}}$ is the standard error of the dark pedestal area (Gauss).

SYSTEMATIC UNCERTAINTIES: The *systematic uncertainty* of the number of detected photons follows via error propagation:

$$\Delta^2_{N_{pe}} = \left(\frac{\partial N_{pe}}{\partial N_{ped}} \cdot \Delta_{N_{ped}} \right)^2 + \left(\frac{\partial N_{pe}}{\partial N_{ped}^{dark}} \cdot \Delta_{N_{ped}^{dark}} \right)^2 \quad . \tag{A.16}$$

Again the number of total events in the illuminated and the dark spectrum is assumed to be accurate, therefore $\Delta_{N_{tot}} = \Delta_{N_{tot}^{dark}} = 0$. The other systematic uncertainties in the number of events per peak, is estimated via Equation A.4. Analogue to Equations (A.6) and (A.7) follows:

$$\Delta_{N_{tot}} = \Delta_{N_{tot}^{dark}} = 0 \qquad \text{total events in the spectra (trigger),}$$
$$\Delta_{N_{ped}} = \sqrt{2} \cdot 0.1\,\% \cdot N_{ped} \qquad \text{is the propagated QADC non-linearity, and}$$
$$\Delta_{N_{ped}^{dark}} = \sqrt{2} \cdot 0.1\,\% \cdot N_{ped}^{dark} \qquad \text{is the propagated QADC non-linearity.}$$

The number of photons per light pulse N sent onto the detector is given by the optical power reaching the detector divided by the energy of one photon and the pulse frequency:

$$N = \frac{P_{PD} \cdot R \cdot R_{geom}}{E_{photon} \cdot f_{pulse}} = \frac{P_{PD} \cdot R \cdot R_{geom} \cdot \lambda}{h \cdot c \cdot f_{pulse}} \quad , \tag{A.17}$$

where

P_{PD}	is the mean optical power from the photodiode,
$R = \frac{R_1 + R_2}{2}$	is the mean collimator ratio,
$R_{geom} = \frac{A_{detector}}{A_{PD}}$	is a geometric correction factor,
$A_{detector} = 9\,mm^2$	is the sensitive detector area [DS144],
$A_{PD} = 100\,mm^2$	is the sensitive photodiode area [DS91].
$E_{photon} = \frac{h \cdot c}{\lambda}$	is the energy of a sent photon,
h	is the Planck constant: $6.626\,069\,57 \times 10^{-34}\,J\,s$ [128],
c	is the speed of light: $299\,792\,458\,m\,s^{-1}$ [128],
λ	is the wavelength of the photons, and
f_{pulse}	is the pulse frequency of the LED.

The mean collimator ratio is calculated from the collimator ratio measured before and after the SiPM measurement. For measurements where some of the light from the exit of the collimator may not reach the detectors sensitive area (measurements in a distance), a correction factor R_{geom} has to be multiplied with Equation 6.7. The wavelength was determined with the spectrometer measurements shown in Section 4.3.2.2 and depends on the LED-array used (Tables C.3 and C.4).

STATISTICAL UNCERTAINTIES: The *statistical uncertainties* are propagated with the Gauss error propagation formula. There are no statistical errors for the geometrical correction, the wavelength, and the pulse frequency. The speed of light is given as 'exact' by the particle data group [128]. It follows:

$$
\begin{aligned}
\sigma_N^2 &= \left(\frac{\partial N}{\partial P_{PD}} \cdot \sigma_{P_{PD}} \right)^2 + \left(\frac{\partial N}{\partial R} \cdot \sigma_R \right)^2 + \left(\frac{\partial N}{\partial h} \cdot \sigma_h \right)^2 \\
&= \left(\frac{R \cdot R_{geom} \cdot \lambda}{h \cdot c \cdot f_{pulse}} \cdot \sigma_{P_{PD}} \right)^2 + \left(\frac{P_{PD} \cdot R_{geom} \cdot \lambda}{h \cdot c \cdot f_{pulse}} \cdot \sigma_R \right)^2 \\
&\quad + \left(-\frac{P_{PD} \cdot R \cdot R_{geom} \cdot \lambda}{h^2 \cdot c \cdot f_{pulse}} \cdot \sigma_h \right)^2 \quad ,
\end{aligned}
$$

(A.18)

where

$\sigma_{P_{PD}}$ is the standard deviation of the power measurement,

σ_R is the standard deviation of the mean ratio, and

σ_h is $0.000\,000\,29 \times 10^{-34}$ J s [128].

SYSTEMATIC UNCERTAINTIES: The *systematic uncertainties* are again calculated via the propagation of uncorrelated variables[2]. Except for the speed of light [128], the Planck constant [128], and the geometrical correction factor, every observable has a systematic error. It follows:

$$
\begin{aligned}
\Delta_N^2 &= \left(\frac{R \cdot R_{geom} \cdot \lambda}{h \cdot c \cdot f_{pulse}} \cdot \Delta_{P_{PD}} \right)^2 + \left(\frac{P_{PD} \cdot R_{geom} \cdot \lambda}{h \cdot c \cdot f_{pulse}} \cdot \Delta_R \right)^2 \\
&\quad + \left(\frac{P_{PD} \cdot R \cdot R_{geom}}{h \cdot c \cdot f_{pulse}} \cdot \Delta_\lambda \right)^2 + \left(-\frac{P_{PD} \cdot R \cdot R_{geom} \cdot \lambda}{h \cdot c \cdot f_{pulse}^2} \cdot \Delta_{f_{pulse}} \right)^2 \quad ,
\end{aligned}
$$

(A.19)

where

$\Delta_{P_{PD}} = 1.6\,\% \cdot P_{PD}$ is the error of the photodiode [DS91, DS92],

$\Delta_R^2 = \frac{1}{4} \cdot \left(\Delta_{R_1}^2 + \Delta_{R_2}^2 \right)$ is the systematic error of the mean ratio,

$\frac{\Delta_{R_1}}{R_1} = \frac{\Delta_{R_2}}{R_2} = \sqrt{2} \cdot 1.6\,\%$ are the systematic errors of the single ratios,

$\Delta_\lambda = b\,\% \cdot \lambda$ is the uncertainty in the wavelength (Table 5.1), and

$\Delta_{f_{pulse}} = 1 \times 10^{-5} \cdot f_{pulse}$ is the frequency error of the oscilloscope [DS149].

---

2 For sufficiently small differences between the single mean ratio R_i from each other, i. e. differences in R_i are smaller than the individual systematic errors Δ_{R_i}. Else see Appendix A.3

For the frequency measurement the oscilloscope *WaveJet 324A* [DS149] was used. The same formula as given in Equation A.11 was applied. For a basic uncertainty estimation, it can be approximated that $\frac{\Delta_R}{R} = \sqrt{2} \cdot 1.6\,\%$, as shown in Equation A.10.

PDE : Now the PDE can be calculated via Equation 6.5. As a reminder, the PDE formula is given again:

$$\epsilon = \frac{N_{pe}}{N} \quad .$$

The error propagation formula yields:

$$\sigma_\epsilon = \sqrt{\left(\frac{1}{N} \cdot \sigma_{N_{pe}}\right)^2 + \left(-\frac{N_{pe}}{N^2} \cdot \sigma_N\right)^2} \quad ,$$

$$\Delta_\epsilon = \sqrt{\left(\frac{1}{N} \cdot \Delta_{N_{pe}}\right)^2 + \left(-\frac{N_{pe}}{N^2} \cdot \Delta_N\right)^2} \quad ,$$

where

N_{pe}	is the number of detected photons (Equation A.14),
$\sigma_{N_{pe}}$	is the standard error of the number of detected photons (Equation A.15),
$\Delta_{N_{pe}}$	is the systematic error of the number of detected photons (Equation A.16),
N	is the number of photons sent on the detector per pulse (Equation A.17),
σ_N	is the statistical error in the photon number (Equation A.18), and
Δ_N	is the systematic error in the photon number (Equation A.19).

B

PICTURES
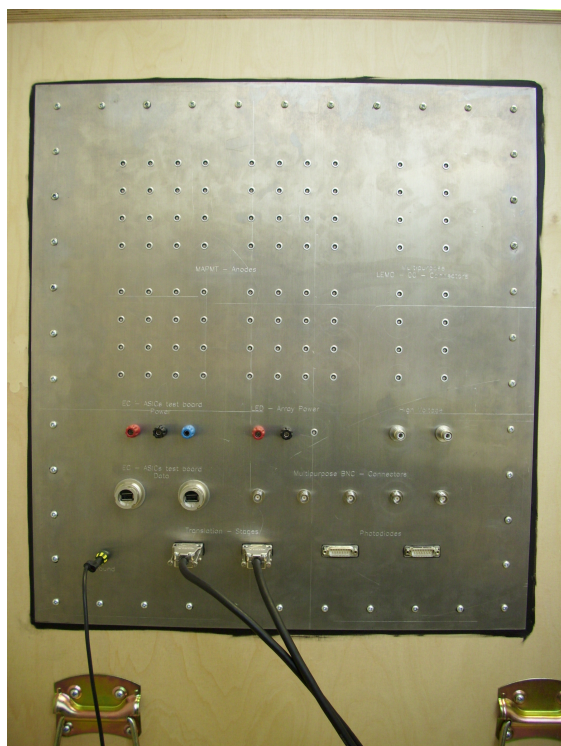
(a) Clean side panel outside.

(b) Side panel outside.

Figure B.1: Side panel of the photon shielding. **(a)** Outside view of the side panel. **(b)** Outside view of the side panel with connected cables.
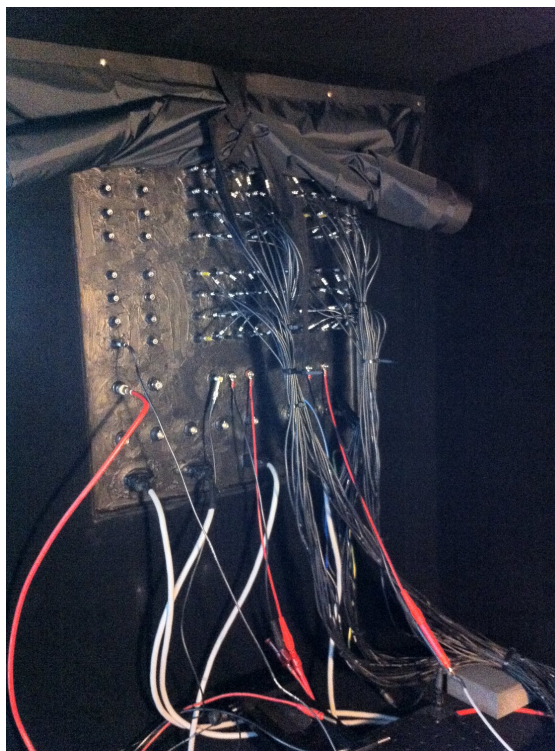
Figure B.2: Inside view of the side panel.

Figure B.3: Photograph of the set-up for the position dependent flux measurements. Here LED-array AR2 (*entrance*) and a photodiode (*top*), with its respective mount, are attached to the sphere. The second exit port (*side*) is closed with a lid coated with Spectralon.

(a) Alu-collimator front.

(b) Alu-collimator back.
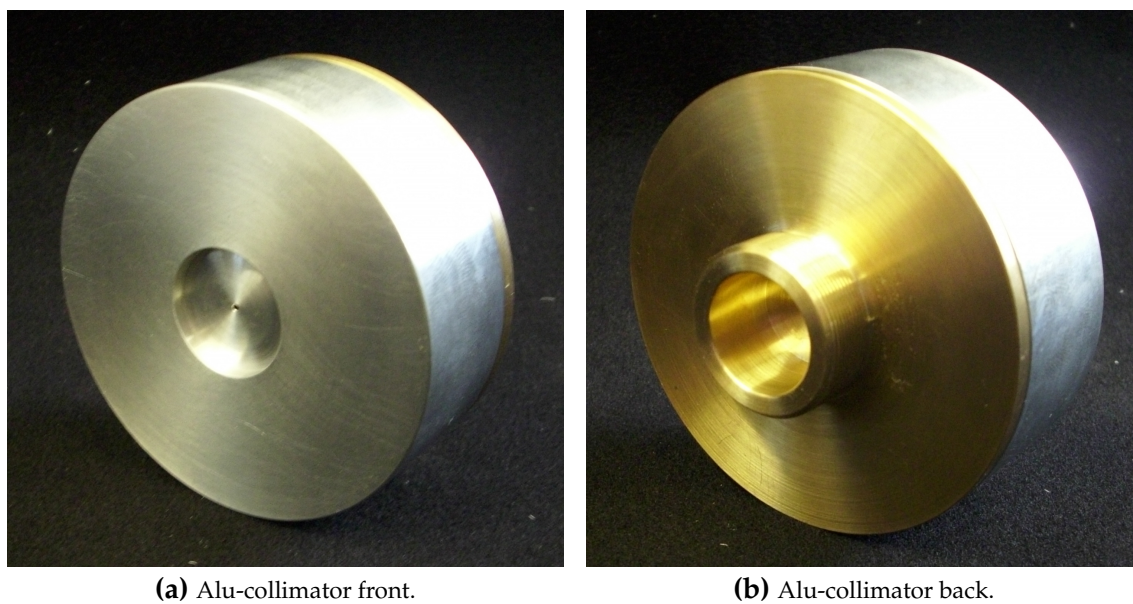
Figure B.4: Photographs of the alu-collimator. **(a)** Front view of the alu-collimator with the 1 mm pin hole in the aluminum plate. **(b)** Back view of the alu-collimator with the M25 fine thread and the 1 mm pin hole in the brass plate.

Figure B.5: Photograph of the PVC-collimator *ColA* mounted on the integrating sphere.
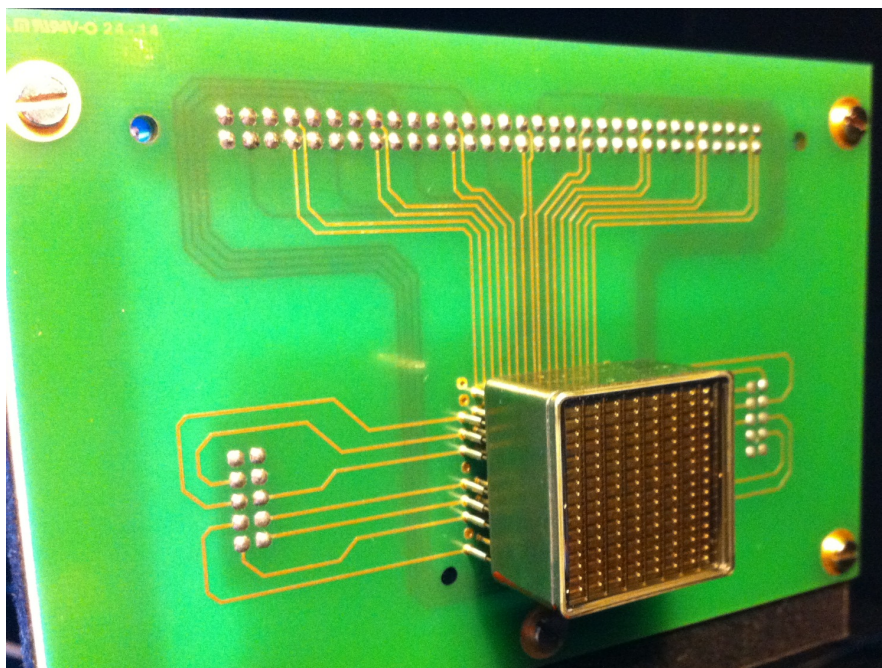
Figure B.6: Photograph of the front of the MAPMT socket board, designed by Andreas Ebersoldt (IPE - KIT) [129].
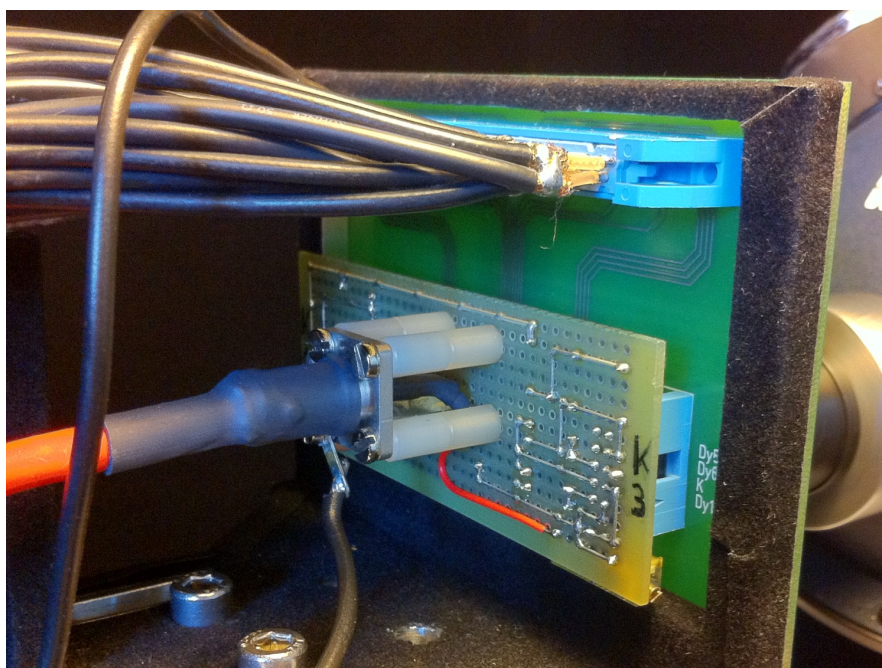
Figure B.7: Photograph of the back of the MAPMT socket board, showing the voltage divider. Designed by Philippe Gorodetzky (APC - Paris) and built by Bernd Hoffmann (IKP - KIT) [114, 130].

Figure B.8: View of the back side of the two *Keithley 2750 frames* with each four *Keithley 7711 multiplexer cards*.
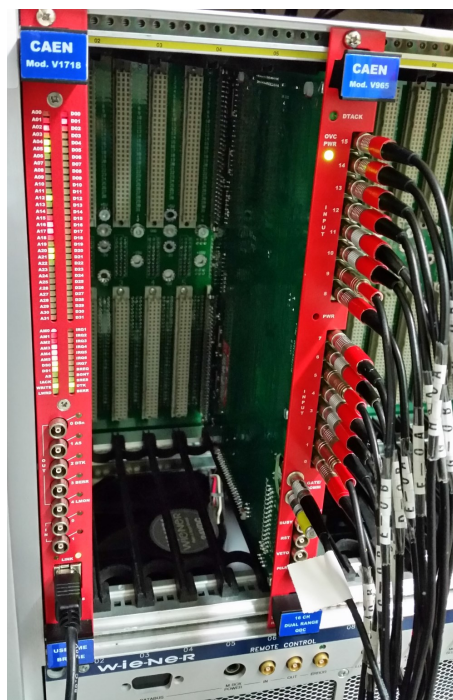
Figure B.9: View of the inputs to the *CAEN V965* QADC.

C

TECHNICAL INFORMATION

This appendix chapter holds various technical information on the components used during the course of this thesis.

C.1 REFERENCE LIGHT SOURCE

Table C.1: Components of the reference light source.

PART	TYPE	DATASHEET
LED-array AR1	Aluminum	Figures C.2 and C.3
LED-array AR2	Aluminum	Figures C.4 and C.5
LED-array AR3	Aluminum	Figure C.6
LED-array AR4	Aluminum	Figure C.7
LED-array AR5	Aluminum	Figures C.8 and C.9
Integrating sphere	Labsphere 3P-GPS-053-SL	[DS80]
NIST-calibrated photodiode PD 38	Ophir PD300-UV SN: 655738	[DS91]
NIST-calibrated photodiode PD 39	Ophir PD300-UV SN: 655739	[DS91]
Photodiode controller	Ophir Pulsar 2	[DS92]
Photodiode mount	Aluminum	Figures C.15 and C.16
Photodiode casing	3D-print	Figure C.17
Collimator mount	Aluminum	Figure C.23
Alu-collimator AluA	Aluminum	Figures C.24 and C.25
Alu-collimator AluB	Aluminum, black flock paper	Figures C.24 and C.25
PVC-collimator ColA	PVC	Figures C.27 and C.28
PVC-collimator ColB	PVC	Figures C.26 and C.29
PVC-collimator ColC	PVC	Figures C.26 and C.28
PVC-collimator ColD	PVC	Figures C.27 and C.29
PVC-collimator ColE	PVC	Figure C.28

C.1.1 *LED-arrays*

Table C.2: LEDs that are used for the various LED-arrays with the *nominal values* from the datasheets. Given are type of the LED, the mean wavelength λ, the half width half maximum of the spectrum σ_λ, the mean optical output P_{opt}, the maximal forward current I_F, the maximal pulsed forward current I_{FP}, and the mean bias voltage U_{bias}. All values are given for the ambient conditions specified in the datasheets. Both UVCLEAN-LEDs came each with a calibration sheet, shown in Figures C.10 and C.11.

TYPE	λ (nm)	σ_λ (nm)	P_{opt} (mW)	I_F (mA)	I_{FP} (mA)	U_{bias} (V)	DATASHEET
DUV310-FW5	310	± 4.5	0.8	40	200	6.5	[DS150]
UVCLEAN315FW-3	315	± 6.0	2.0	80	80	5.5	[DS151]
UVCLEAN330FW-3	330	± 6.0	2.0	80	80	5.5	[DS151]
DUV340-FW5	340	± 4.5	1.0	40	200	4.0	[DS150]
XSL-355-5E	357	± 7.5	1.0	25	100	3.6	[DS152]
UVLED365-110E	365	± 7.5	3.3	25	80	3.6	[DS153]
XSL-370-TB-4	373	± 6.0	1.0	25	100	3.6	[DS154]
XSL-375-3E	378	± 7.5	14.0	25	100	3.6	[DS155]
VL380-5-15	380	± 5.0	5.5	30	100	3.7	[DS156]
VL390-5-15	390	± 5.0	7.5	30	100	3.7	[DS157]
HUUV-5102L	395	± 10.0	2.0	—	120	3.4	[DS158]
LED405-30M32	405	± 7.5	0.8	30	100	3.8	[DS159]
VL425-5-15	425	± 5.0	13.0	20	100	3.7	[DS160]

Table C.3: LED-arrays with the used LED types, their measured wavelength λ, the half width half maximum Δ_λ of the wavelength, the relative systematic wavelength error $\frac{\Delta_\lambda}{\lambda}$, the series resistor R of every LED, the continuous forward current I_{cont}, the continuous bias voltage U_{bias}, and the total continuous forward current I_{total} (the whole array). Also given are the series resistor R_P for pulsed mode, that was calculated via the maximal forward current I_{FP} and 12 V (median voltage available from the LDD). The circuits are given in Figure C.1.

ARRAY	LED	λ (nm)	Δ_λ (nm)	$\frac{\Delta_\lambda}{\lambda}$ (%)	R_P (Ω)	I_{FP} (mA)	R (Ω)	I_{cont} (mA)	U_{bias} (V)	I_{total} (mA)
AR1	UVLED365-110E	371	±6	1.62	33	80	68	20	5.00	840
AR2	XSL-375-3E	376	±5	1.33	81	100	91	20	5.35	400
AR3	VL390-5-15	395	±7	1.77	33	100	62	20	5.00	840
AR4	VL425-5-15	423	±8	1.89	33	100	110	20	6.00	240

Table C.4: LED-array *AR5* with the used LED types, their measured wavelength λ, the *forward voltage* U_{FT}, and the *total forward current* I_{FT} of every LED for continuous mode. Also given are the *series resistor* R_P (calculated from I_{FP} and 12 V) and the *maximal forward current* I_{FP} for pulsed mode. Here, only the circuit for pulsed mode is used (Figure C.1a). Therefore, the series resistor R is not given in the table, since it is identical to the series resistor R_P. For continuous mode, the signal pin of the Lemo00 connector has to be connected to the negative output of the power source and the housing has to be connected to the positive one.

NUMBER	LED	λ (nm)	U_{FT} (mV)	I_{FT} (mA)	R_P (Ω)	I_{FP} (mA)
1	VL425-5-15	423	4.74	20	62	100
2	LED405-30M32	401	5.20	30	62	100
3	HUUV-5102L	394	4.42	20	56	120
4	VL380-5-15	380	5.88	30	68	100
5	XSL-370-TB-4	373	5.35	25	64	100
6	XSL-355-5E	361	5.23	25	64	100
7	DUV340-FW5	337	5.65	40	30	200
8	UVCLEAN330FW-3	333	8.20	40	83	80
9	UVCLEAN315FW-3	319	9.60	40	112	80
10	DUV310-FW5	311	7.66	40	15	200

(a) Pulsed mode circuit.

(b) Continuous mode circuit.
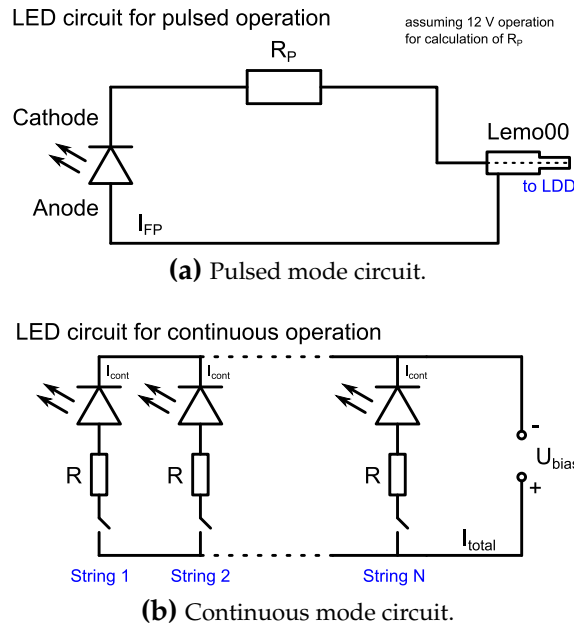
Figure C.1: Electrical circuits for all LED-arrays. Specific values can be found in Tables C.3 and C.4. **(a)** A resistor R_p is in series with the pulsed LED for current control. The cathode of the LED is connected to the casing of a *Lemo00* connector, while the anode is connected to the signal. The *Lemo00* connector can be connected to the output of the LDD. **(b)** Every one of the N LEDs has a resistor R in series. For LED-array AR2 there is also a dip-switch in series. The continuous voltage U_{bias} is connected via standard banana connectors.

Hole table			
Number	X	Y	Type
1	-23,00	0,00	M3x0.5 - 6H
2	23,00	0,00	
3	-6,21	-23,18	
4	6,21	-23,18	
5	0,00	-18,00	
6	-16,97	-16,97	
7	16,97	-16,97	
8	-9,00	-15,59	
9	9,00	-15,59	
10	-3,43	-12,80	
11	3,11	-11,59	
12	9,37	-9,37	
13	-15,59	-9,00	
14	15,59	-9,00	
15	-8,49	-8,49	
16	-1,81	-6,76	
17	-23,18	-6,21	
18	23,18	-6,21	
19	4,95	-4,95	
20	-12,80	-3,43	
21	11,59	-3,11	
22	-6,76	-1,81	
23	-18,00	0,00	⌴ Ø5,40
24	0,00	0,00	⌴ ▽0,40
25	18,00	0,00	Ø4,70 PASS
26	6,76	1,81	
27	-11,59	3,11	
28	12,80	3,43	
29	-4,95	4,95	
30	-23,18	6,21	
31	23,18	6,21	
32	1,81	6,76	
33	8,49	8,49	
34	-15,59	9,00	
35	15,59	9,00	
36	-9,37	9,37	
37	-3,11	11,59	
38	3,43	12,80	
39	-9,00	15,59	
40	9,00	15,59	
41	-16,97	16,97	
42	16,97	16,97	
43	0,00	18,00	
44	-6,21	23,18	
45	6,21	23,18	

Designed by	Modified by	Material		Date			
Thomas Huber	Michael Karus	Aluminium 6061		07.10.2015			
Mount for LED-array 1				Mount for LED-array 1			
UVLED365-110E							
Doktorarbeit/Documents/CAD-Projekte/LED-arrays/AR1-365nm/AR1mount_365nm_UVLED365-110E_sketch.idw				mount_AR1		Version v1.0	Page 1 / 1

Figure C.2: Top, cut and projected view of the mount of LED-array *AR1* with a hole table. The 43 LEDs are attached to the mount with a corresponding lid. This design is a modification of the original design that was done by Thomas Huber (see Figure C.4).

Hole table			
Number	X	Y	Type
1	-6,21	-23,18	
2	6,21	-23,18	
3	0,00	-18,00	
4	-16,97	-16,97	
5	16,97	-16,97	
6	-9,00	-15,59	
7	9,00	-15,59	
8	-3,43	-12,80	
9	3,11	-11,59	
10	9,37	-9,37	
11	-15,59	-9,00	
12	15,59	-9,00	
13	-8,49	-8,49	
14	-1,81	-6,76	
15	-23,18	-6,21	
16	23,18	-6,21	
17	4,95	-4,95	
18	-12,80	-3,43	
19	11,59	-3,11	
20	-6,76	-1,81	
21	-18,00	0,00	
22	0,00	0,00	Ø4,00 PASS
23	18,00	0,00	
24	6,76	1,81	
25	-11,59	3,11	
26	12,80	3,43	
27	-4,95	4,95	
28	-23,18	6,21	
29	23,18	6,21	
30	1,81	6,76	
31	8,49	8,49	
32	-15,59	9,00	
33	15,59	9,00	
34	-9,37	9,37	
35	-3,11	11,59	
36	3,43	12,80	
37	-9,00	15,59	
38	9,00	15,59	
39	-16,97	16,97	
40	16,97	16,97	
41	0,00	18,00	
42	-6,21	23,18	
43	6,21	23,18	
44	-23,00	0,00	Ø3,40 PASS
45	23,00	0,00	
46	0,00	-24,00	M4x0.7 - 6H
47	0,00	24,00	

A-A (2 : 1)

3,50

55,00

Designed by		Modified by		Material		Date	
Thomas Huber		Michael Karus		Aluminium 6061		07.10.2015	

Lid for LED-array 1 & 3	Lid for LED-array 1 & 3		
UVLED365-110E & VL390-5-15		Version	Page
Doktorarbeit/Documents/CAD-Projekte/LED-arrays/AR1-365nm/AR1+3lid_365nm-UVLED365_390nm-VL390_sketch.idw	lid_AR1+3	v1.0	1 / 1

Figure C.3: Top, cut and projected view of the lid of LED-array *AR1* and *AR3* with the corresponding hole table. This design is a modification of the original design that was done by Thomas Huber (see Figure C.5).
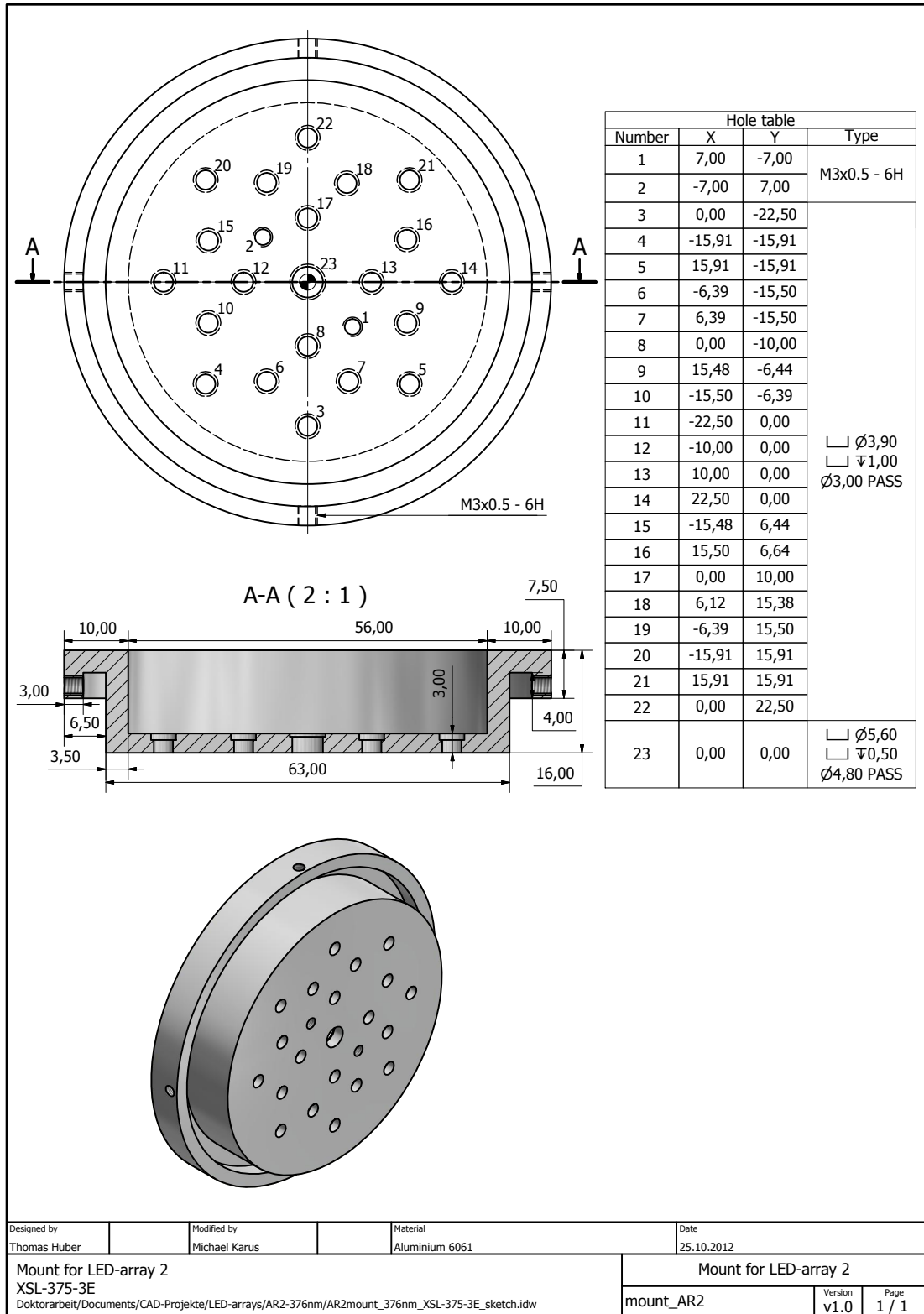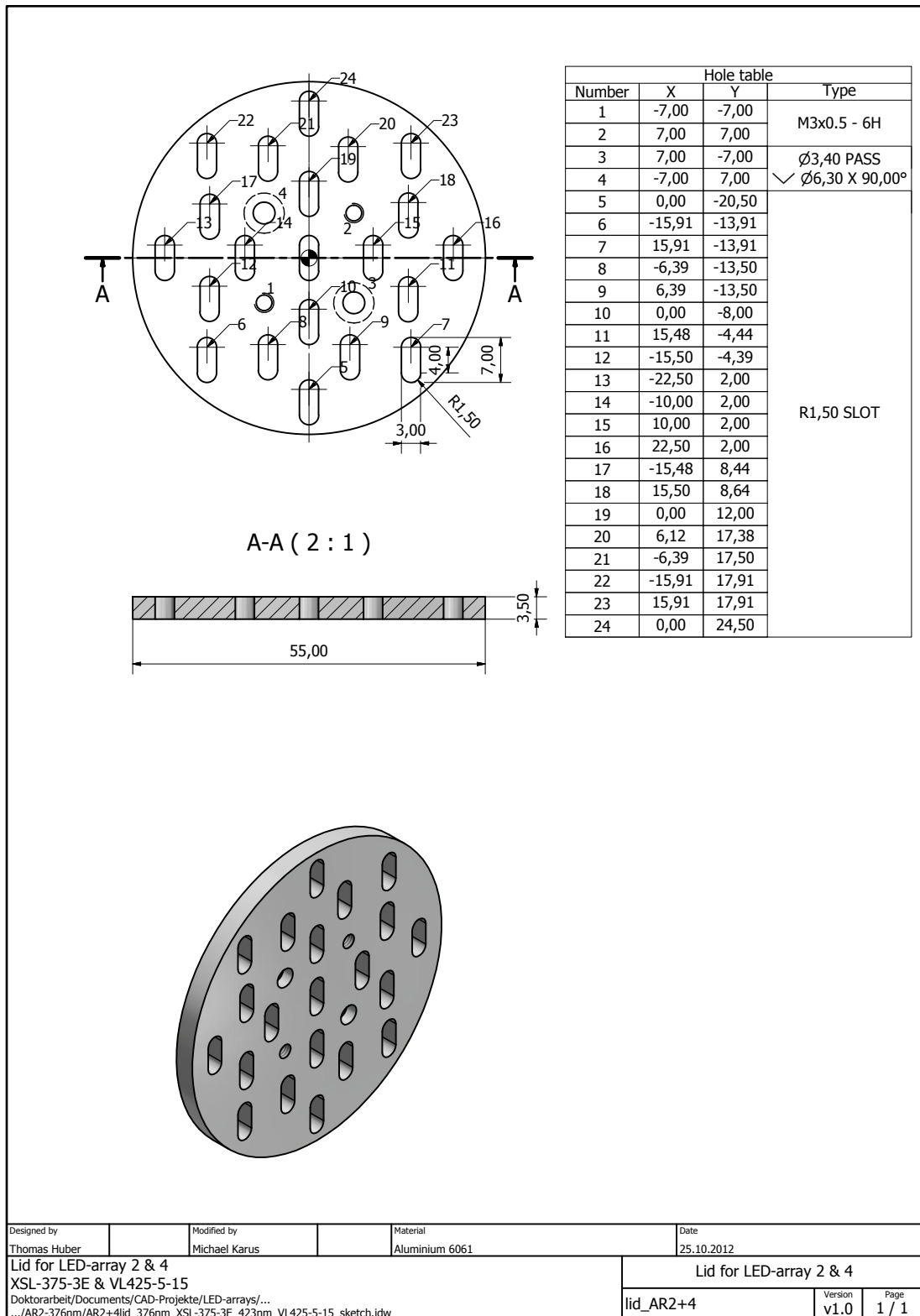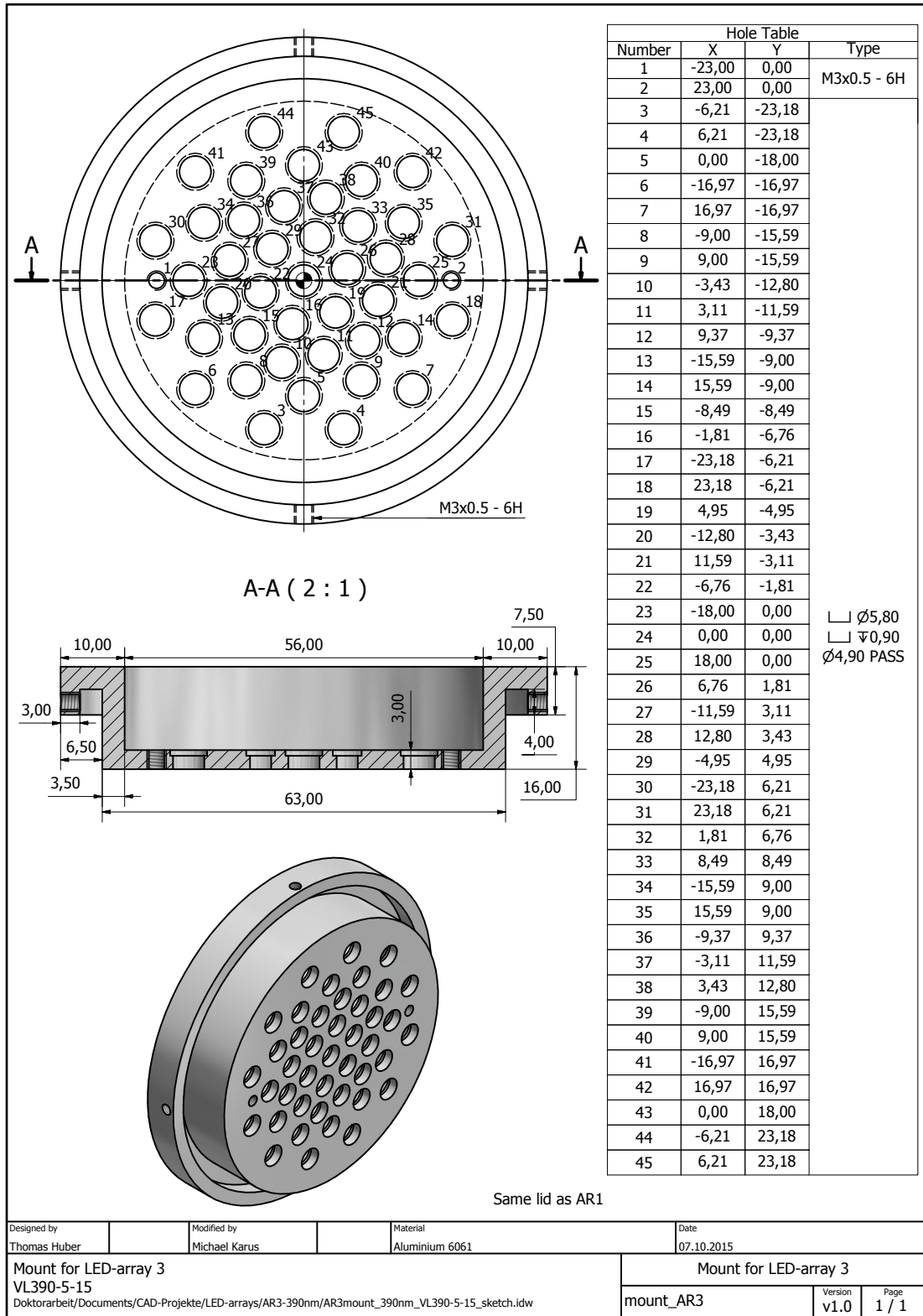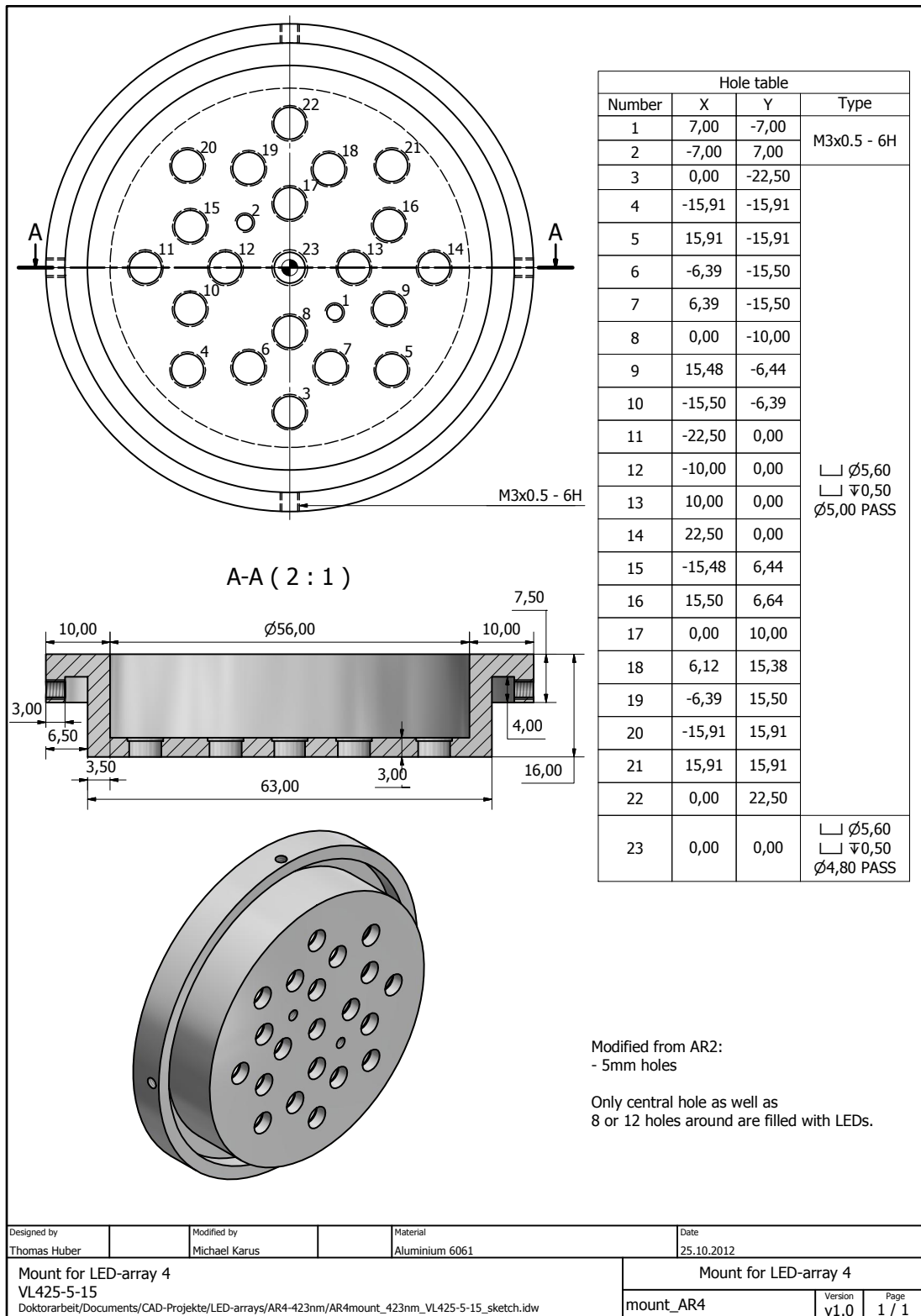
Figure C.4: Top, cut and projected view of the mount of LED-array *AR2* with a hole table. The 21 LEDs are attached to the mount with a corresponding lid. This is the original design that was done by Thomas Huber in the course of his bachelor thesis [86].
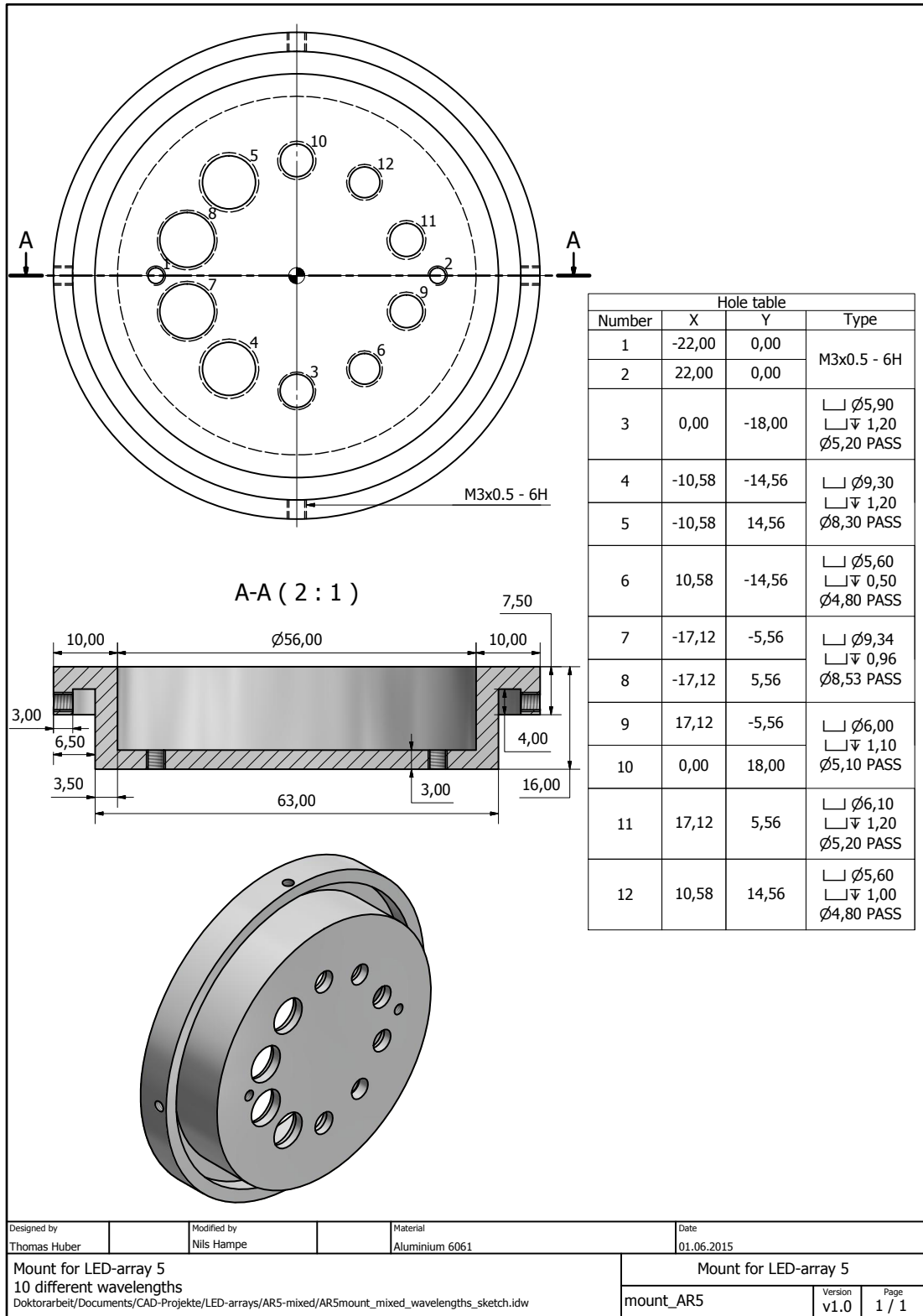
Hole table			
Number	X	Y	Type
1	-7,00	-7,00	M3x0.5 - 6H
2	7,00	7,00	
3	7,00	-7,00	Ø3,40 PASS
4	-7,00	7,00	⌵ Ø6,30 X 90,00°
5	0,00	-20,50	
6	-15,91	-13,91	
7	15,91	-13,91	
8	-6,39	-13,50	
9	6,39	-13,50	
10	0,00	-8,00	
11	15,48	-4,44	
12	-15,50	-4,39	
13	-22,50	2,00	
14	-10,00	2,00	
15	10,00	2,00	R1,50 SLOT
16	22,50	2,00	
17	-15,48	8,44	
18	15,50	8,64	
19	0,00	12,00	
20	6,12	17,38	
21	-6,39	17,50	
22	-15,91	17,91	
23	15,91	17,91	
24	0,00	24,50	

A-A (2 : 1)

Designed by		Modified by		Material		Date	
Thomas Huber		Michael Karus		Aluminium 6061		25.10.2012	

Lid for LED-array 2 & 4
XSL-375-3E & VL425-5-15

Lid for LED-array 2 & 4

Doktorarbeit/Documents/CAD-Projekte/LED-arrays/...
.../AR2-376nm/AR2+4lid_376nm_XSL-375-3E_423nm_VL425-5-15_sketch.idw

lid_AR2+4 | Version v1.0 | Page 1 / 1

Figure C.5: Top, cut and projected view of the lid of LED-array *AR2* and *AR4* with the corresponding hole table. This is the original design that was done by Thomas Huber in the course of his bachelor thesis [86].

Hole Table			
Number	X	Y	Type
1	-23,00	0,00	M3x0.5 - 6H
2	23,00	0,00	
3	-6,21	-23,18	
4	6,21	-23,18	
5	0,00	-18,00	
6	-16,97	-16,97	
7	16,97	-16,97	
8	-9,00	-15,59	
9	9,00	-15,59	
10	-3,43	-12,80	
11	3,11	-11,59	
12	9,37	-9,37	
13	-15,59	-9,00	
14	15,59	-9,00	
15	-8,49	-8,49	
16	-1,81	-6,76	
17	-23,18	-6,21	
18	23,18	-6,21	
19	4,95	-4,95	
20	-12,80	-3,43	
21	11,59	-3,11	
22	-6,76	-1,81	
23	-18,00	0,00	⌴ ⌀5,80
24	0,00	0,00	⌴ ⌵0,90
25	18,00	0,00	⌀4,90 PASS
26	6,76	1,81	
27	-11,59	3,11	
28	12,80	3,43	
29	-4,95	4,95	
30	-23,18	6,21	
31	23,18	6,21	
32	1,81	6,76	
33	8,49	8,49	
34	-15,59	9,00	
35	15,59	9,00	
36	-9,37	9,37	
37	-3,11	11,59	
38	3,43	12,80	
39	-9,00	15,59	
40	9,00	15,59	
41	-16,97	16,97	
42	16,97	16,97	
43	0,00	18,00	
44	-6,21	23,18	
45	6,21	23,18	

Same lid as AR1

Designed by	Modified by	Material	Date		
Thomas Huber	Michael Karus	Aluminium 6061	07.10.2015		
Mount for LED-array 3			Mount for LED-array 3		
VL390-5-15					
Doktorarbeit/Documents/CAD-Projekte/LED-arrays/AR3-390nm/AR3mount_390nm_VL390-5-15_sketch.idw			mount_AR3	v1.0	1 / 1

Figure C.6: Top, cut and projected view of the mount of LED-array *AR3* with a hole table. The 43 LEDs are attached to the mount with the same lid as LED-array *AR1*. This design is a modification of the original design that was done by Thomas Huber (see Figure C.4).

Hole table			
Number	X	Y	Type
1	7,00	-7,00	M3x0.5 - 6H
2	-7,00	7,00	
3	0,00	-22,50	
4	-15,91	-15,91	
5	15,91	-15,91	
6	-6,39	-15,50	
7	6,39	-15,50	
8	0,00	-10,00	
9	15,48	-6,44	
10	-15,50	-6,39	
11	-22,50	0,00	
12	-10,00	0,00	⌴ Ø5,60
13	10,00	0,00	⌴ ▽0,50 Ø5,00 PASS
14	22,50	0,00	
15	-15,48	6,44	
16	15,50	6,64	
17	0,00	10,00	
18	6,12	15,38	
19	-6,39	15,50	
20	-15,91	15,91	
21	15,91	15,91	
22	0,00	22,50	
23	0,00	0,00	⌴ Ø5,60 ⌴ ▽0,50 Ø4,80 PASS

A-A (2 : 1)

M3x0.5 - 6H

Modified from AR2:
- 5mm holes

Only central hole as well as
8 or 12 holes around are filled with LEDs.

Designed by		Modified by		Material		Date
Thomas Huber		Michael Karus		Aluminium 6061		25.10.2012

Mount for LED-array 4		Mount for LED-array 4		
VL425-5-15			Version	Page
Doktorarbeit/Documents/CAD-Projekte/LED-arrays/AR4-423nm/AR4mount_423nm_VL425-5-15_sketch.idw	mount_AR4		v1.0	1 / 1

Figure C.7: Top, cut and projected view of the mount of LED-array *AR4* with a hole table. The 3 mm holes were bored to 5 mm holes and 13 LEDs were attached to the mount with the same lid as LED-array *AR2*. This design is a modification of the original design that was done by Thomas Huber (see Figure C.4).

Hole table			
Number	X	Y	Type
1	-22,00	0,00	M3x0.5 - 6H
2	22,00	0,00	
3	0,00	-18,00	⌴ Ø5,90 ⌴▽ 1,20 Ø5,20 PASS
4	-10,58	-14,56	⌴ Ø9,30 ⌴▽ 1,20 Ø8,30 PASS
5	-10,58	14,56	
6	10,58	-14,56	⌴ Ø5,60 ⌴▽ 0,50 Ø4,80 PASS
7	-17,12	-5,56	⌴ Ø9,34 ⌴▽ 0,96 Ø8,53 PASS
8	-17,12	5,56	
9	17,12	-5,56	⌴ Ø6,00 ⌴▽ 1,10 Ø5,10 PASS
10	0,00	18,00	
11	17,12	5,56	⌴ Ø6,10 ⌴▽ 1,20 Ø5,20 PASS
12	10,58	14,56	⌴ Ø5,60 ⌴▽ 1,00 Ø4,80 PASS

Designed by		Modified by		Material		Date	
Thomas Huber		Nils Hampe		Aluminium 6061		01.06.2015	

Mount for LED-array 5
10 different wavelengths
Doktorarbeit/Documents/CAD-Projekte/LED-arrays/AR5-mixed/AR5mount_mixed_wavelengths_sketch.idw

Mount for LED-array 5

mount_AR5 — Version v1.0 — Page 1 / 1

Figure C.8: Top, cut and projected view of the mount of LED-array *AR5* with a hole table. The 10 different LEDs are attached to the mount with a corresponding lid. This design was done by Nils Hampe and is a modification of the original design that was done by Thomas Huber (see Figure C.4) [86, 97].

Hole table			
Number	X	Y	Type
1	-7,00	0,00	M3x0.5 - 6H
2	7,00	0,00	
3	0,00	-22,00	Ø3,00 PASS ⌵ Ø4,00 X 90,00°
4	0,00	22,00	
5	-6,18	-19,02	R1,50 SLOT
6	6,18	-19,02	
7	-4,94	-15,22	
8	4,94	-15,22	
9	-16,18	-11,76	
10	16,18	-11,76	
11	-12,94	-9,40	
12	12,94	-9,40	
13	-20,00	0,00	
14	-16,00	0,00	
15	16,00	0,00	
16	20,00	0,00	
17	-11,73	8,52	R2,00 SLOT
18	11,73	8,52	
19	-17,39	12,64	
20	17,39	12,64	
21	-5,46	13,48	R2,50 SLOT
22	3,51	14,11	
23	-8,08	19,97	
24	5,20	20,91	

A-A (2 : 1)

Designed by	Modified by	Material	Date
Thomas Huber	Nils Hampe	Aluminium 6061	01.06.2015

Lid for LED-array 5
10 different wavelengths
Doktorarbeit/Documents/CAD-Projekte/LED-arrays/AR5-mixed/AR5lid_mixed_wavelengths_sketch.idw

Lid for LED-array 5

lid_AR5 — Version v1.0 — Page 1 / 1

Figure C.9: Top, cut and projected view of the lid of LED-array *AR5* with the corresponding hole table. This design was done by Nils Hampe and is a modification of the original design that was done by Thomas Huber (see Figure C.5) [86, 97].

QC Inspection Report

SETi — SENSOR ELECTRONIC TECHNOLOGY, INC.

Customer	KIT			Date	5/27/2015	PO #	713/20578008/I KP/GFB
Part #	UVCLEAN	315	TO39	HS		Box #	0
Tested	CWG					Item #	1

#	Voltage*, V	Current, mA	Power*, W	Peak Wave*, nm	HB, nm	PSV*, W / nm		Date / Time
A6	4.881484	20.00	4.99E-04	318.9	9.8	3.91E-05		5/27/15 14:52
	5.204351	39.99	1.05E-03	318.9	9.8	8.16E-05		5/27/15 14:52
	5.415519	60.00	1.59E-03	318.9	9.9	1.23E-04		5/27/15 14:52
	5.572162	79.99	2.11E-03	318.9	10.0	1.62E-04		5/27/15 14:52
5								
6								
7								
8								
9								
10								
11								
12								
13								
14								
15								
16								
17								
18								
19								
20								
21								
22								
23								
24								
25								
26								
27								
28								
29								
30								
MIN	4.881484	20.00	4.99E-04	318.9	9.8	3.91E-05		
MAX	5.572162	79.99	2.11E-03	318.9	10.0	1.62E-04		
AVG	5.268379	50.00	1.31E-03	318.9	9.9	1.01E-04		

TESTED BY	CWG	*Peak wavelength measurement tolerance is +/- 2 nm
QC INSPECTOR	FJ	*Optical power output measurement tolerance is +/- 10% *Forward voltage measurement tolerance is +/- 2%

Rev 1
022113

Figure C.10: Calibration sheet of *UVCLEAN315FW-3* that was included in the delivery.

	SETi SENSOR ELECTRONIC TECHNOLOGY, INC.			**QC Inspection Report**						
	Customer	KIT			Date	5/27/2015	PO #	713/20578008/I KP/GFB		
	Part #	UVCLEAN	330	TO39	HS		Box #	0		
	Tested	CWG					Item #	2		
#	Voltage*, V	Current, mA	Power*, W	Peak Wave*, nm	HB, nm	PSV*, W / nm		Date / Time		
C42	4.550826	20.00	2.10E-04	332.1	9.9	1.44E-05		5/27/15 14:54		
	5.008599	39.99	6.35E-04	332.7	9.9	4.52E-05		5/27/15 14:54		
	5.305518	60.00	1.11E-03	332.7	9.9	8.02E-05		5/27/15 14:54		
	5.537867	79.99	1.60E-03	332.7	9.9	1.16E-04		5/27/15 14:55		
5										
6										
7										
8										
9										
10										
11										
12										
13										
14										
15										
16										
17										
18										
19										
20										
21										
22										
23										
24										
25										
26										
27										
28										
29										
30										
MIN	4.550826	20.00	2.10E-04	332.1	9.9	1.44E-05				
MAX	5.537867	79.99	1.60E-03	332.7	9.9	1.16E-04				
AVG	5.1007025	50.00	8.89E-04	332.5	9.9	6.40E-05				
TESTED BY			CWG	*Peak wavelength measurement tolerance is +/- 2 nm *Optical power output measurement tolerance is +/- 10% *Forward voltage measurement tolerance is +/- 2%						
QC INSPECTOR			FJ							

Rev 1
022113

Figure C.11: Calibration sheet of *UVCLEAN330FW-3* that was included in the delivery.

5,35 V   PD-A SIDE 39   PD-B FRONT 38   20 min
377 nm
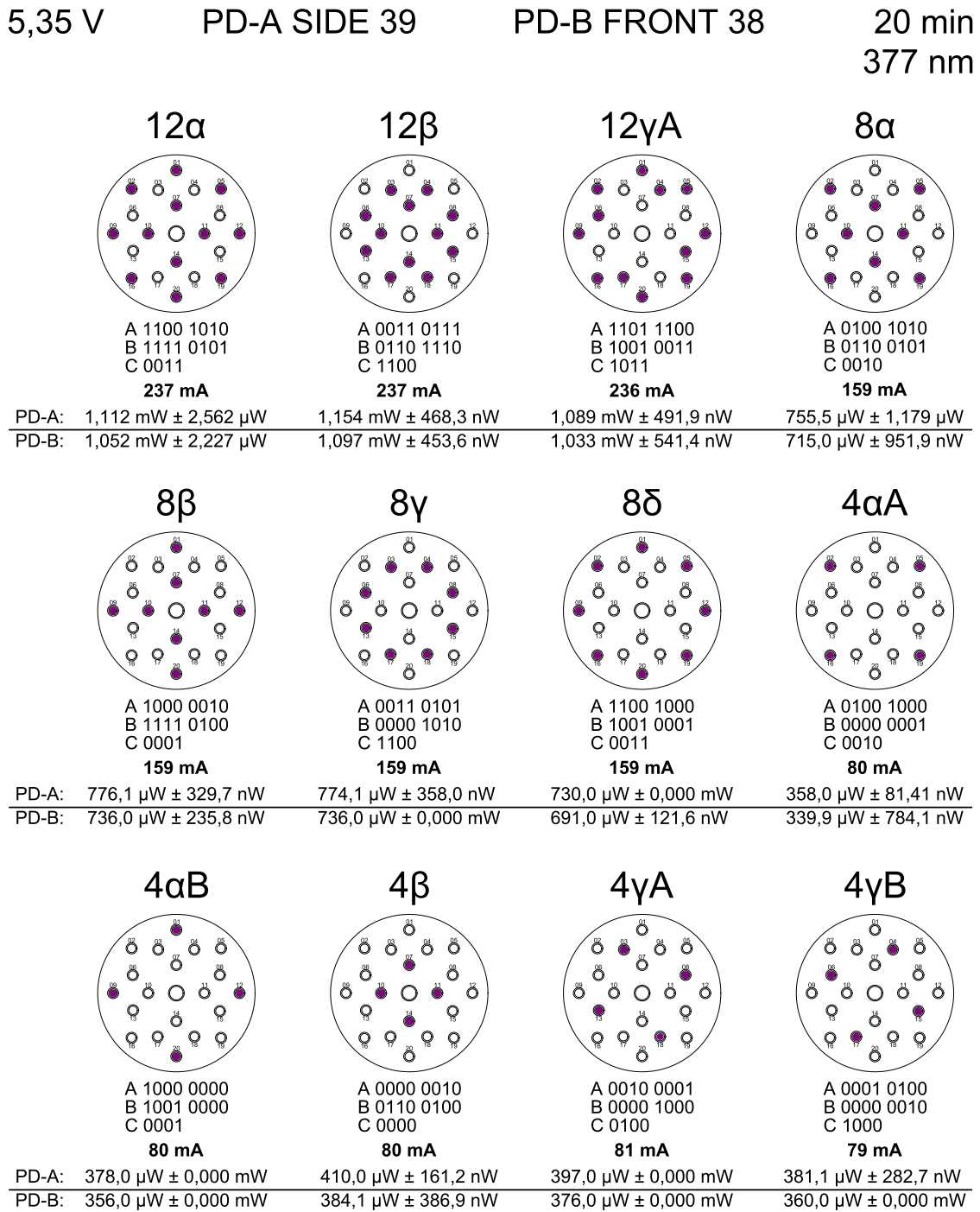
Figure C.12: LED-array AR2 configuration for different light levels, with 12 to 4 LEDs. The binary code below the sketches of the array shows the dip switch positions for switching the LEDs on and off. Below that are the measured currents as well as the measured optical powers given.

5,35 V   PD-A SIDE 39   PD-B FRONT 38   20 min
377 nm

2αA

A 0001 0000
B 0000 0000
C 1000
40 mA

2αB

A 0010 0000
B 0000 0000
C 0100
41 mA

2αC

A 0000 0001
B 0000 1000
C 0000
41 mA

2αD

A 0000 0100
B 0000 0010
C 0000
39 mA

	2αA	2αB	2αC	2αD
PD-A:	199,9 µW ± 131,1 nW	207,9 µW ± 72,3 nW	194,8 µW ± 79,65 nW	185,9 µW ± 0,000 mW
PD-B:	187,1 µW ± 99,67 nW	195,6 µW ± 7,056 nW	184,4 µW ± 86,4 nW	176,2 µW ± 32,02 nW

2βA

A 1000 0000
B 0000 0000
C 0001
40 mA

2βB

A 0000 0000
B 1001 0000
C 0000
40 mA

2βC

A 0100 0000
B 0000 0000
C 0010
40 mA

2βD

A 0000 1000
B 0000 0001
C 0000
40 mA

	2βA	2βB	2βC	2βD
PD-A:	187,0 µW ± 94,92 nW	195,6 µW ± 10,74 nW	179,0 µW ± 13,50 nW	183,3 µW ± 53,52 nW
PD-B:	174,5 µW ± 98,59 nW	185,1 µW ± 0,000 mW	168,7 µW ± 58,40 nW	172,1 µW ± 68,52 nW

2γA

A 0000 0010
B 0000 0100
C 0000
41 mA

2γB

A 0000 0000
B 0110 0000
C 0000
39 mA

	2γA	2γB
PD-A:	206,1 µW ± 73,59 nW	207,1 µW ± 65,63 nW
PD-B:	194,6 µW ± 81,53 nW	194,7 µW ± 63,03 nW

Figure C.13: LED-array AR2 configuration for different light levels, with 12 to 4 LEDs. The binary code below the sketches of the array shows the dip switch positions for switching the LEDs on and off. Below that are the measured currents as well as the measured optical powers given.

C.1.2 *Integrating sphere*
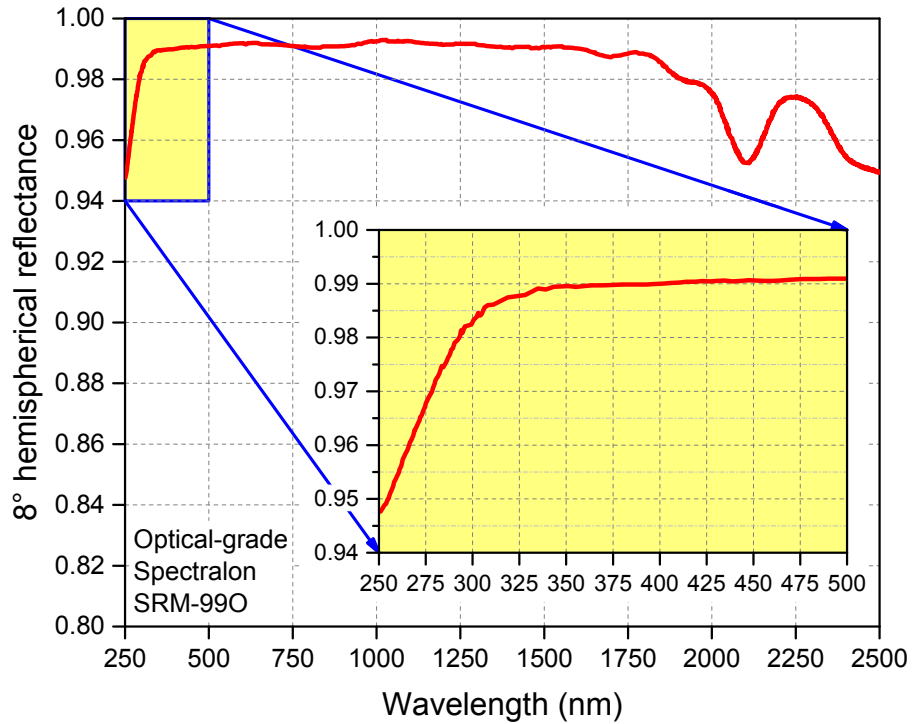
Figure C.14: 8° hemispherical reflectance of Spectralon SRM-99O versus a wide wavelength range of 250 nm to 2500 nm. The incident angle of the flux is 8° to the surface normal and the reflected flux is collected over the whole hemisphere [108]. Above 300 nm a flat reflectance distribution around 99 % up to 1500 nm is present. The inset shows the reflectance for the wavelength range of 250 nm to 500 nm. Adopted from [106].

C.1.3 *Photodiodes, mounts and casing*
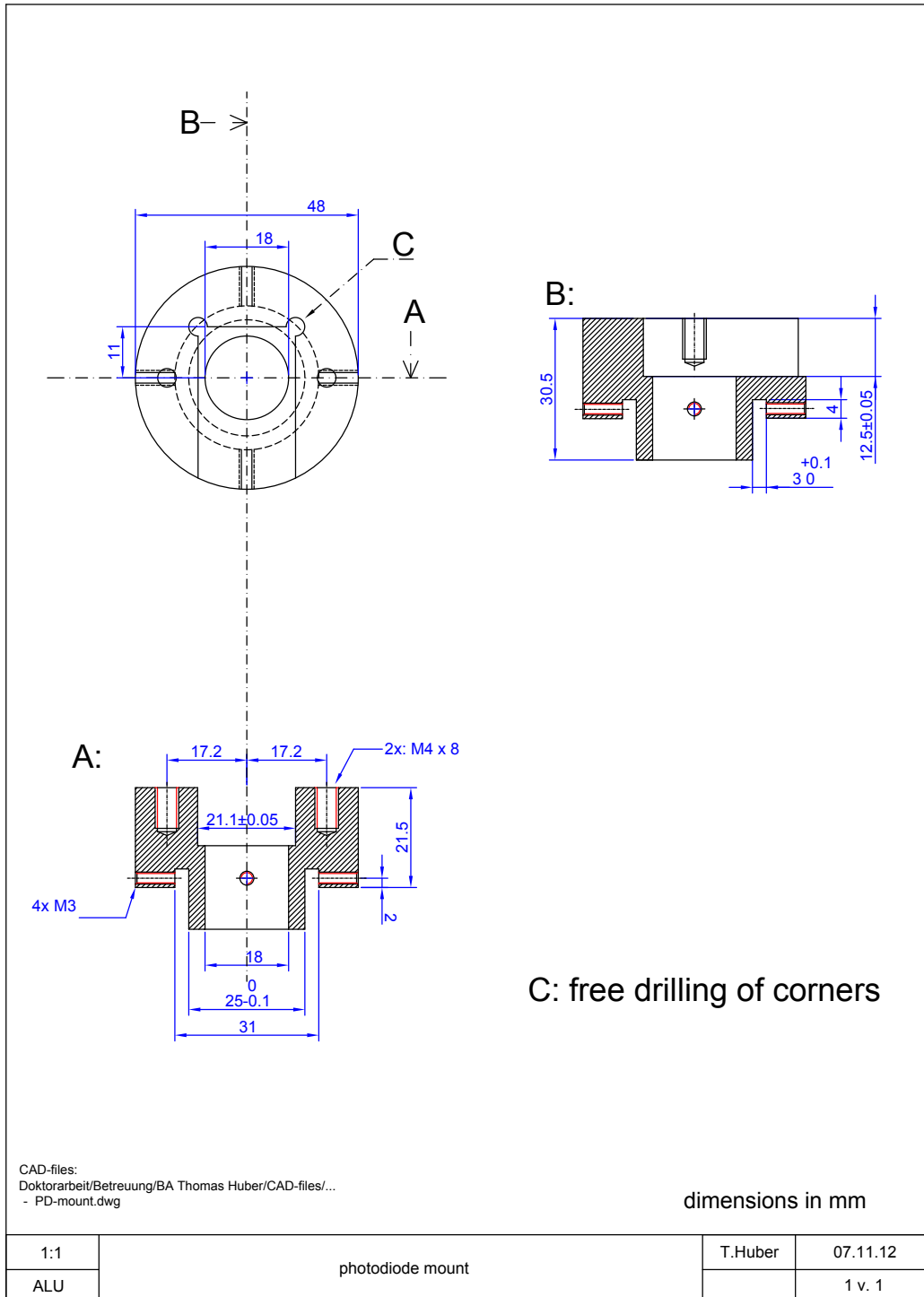
Figure C.15: Mount of the photodiodes Ophir PD300-UV with threads for four headless screws (designed by Thomas Huber) [86].
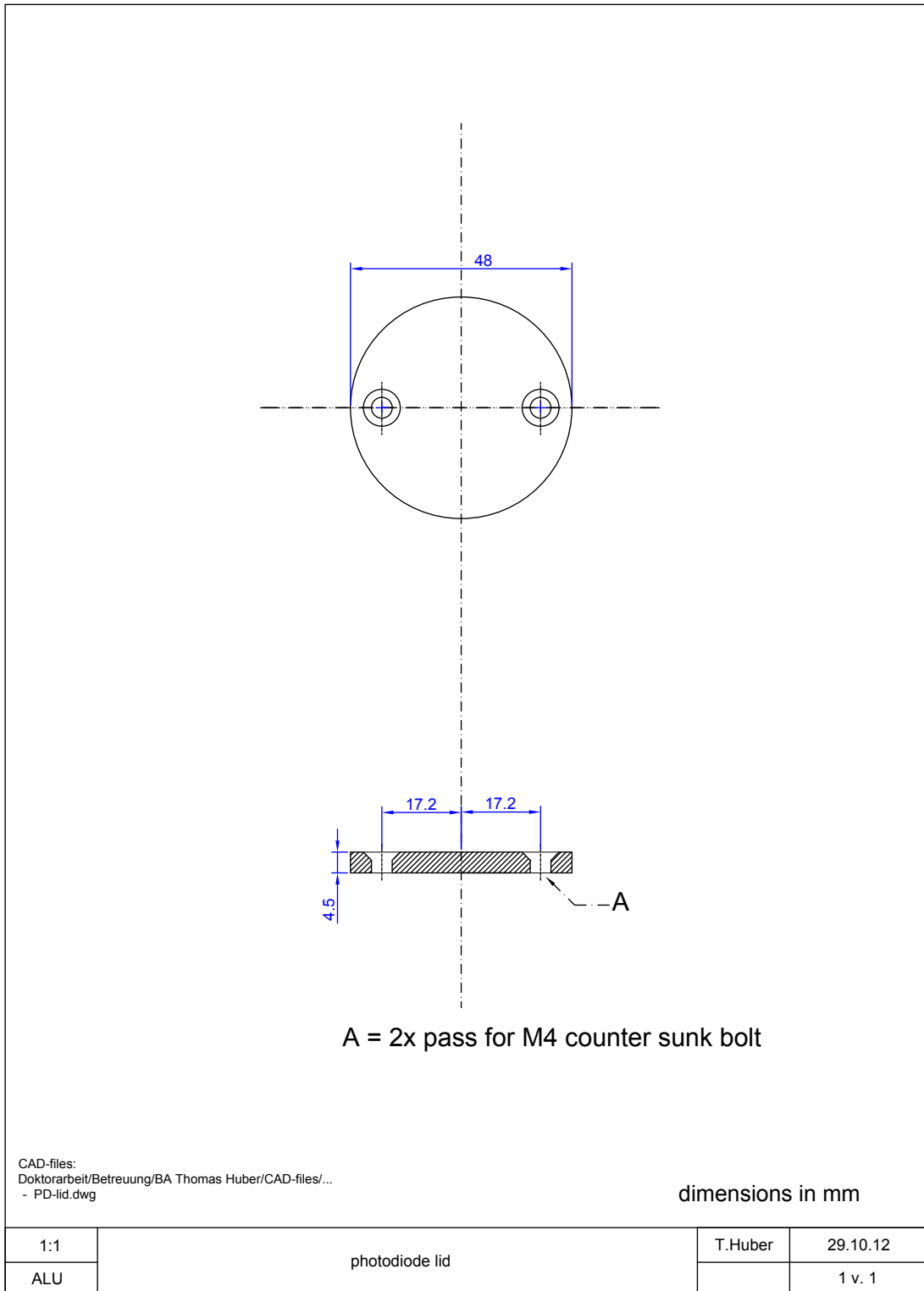
Figure C.16: Lid for the photodiode mount with two passes for M4 counter sunk bolts (designed by Thomas Huber) [86].
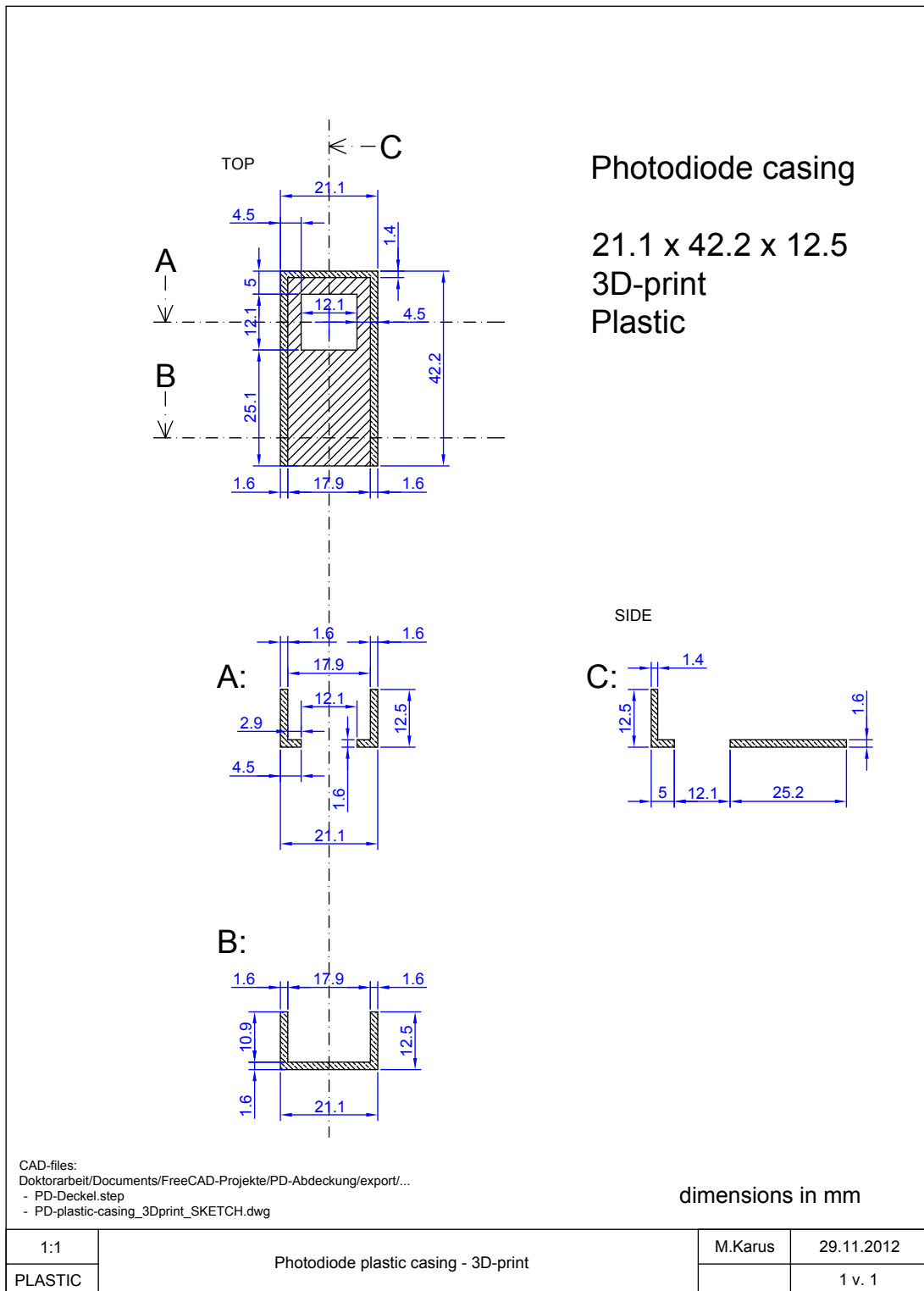
Figure C.17: Plastic casing for the photodiode to fit into the photodiode mount without any filter.

C.1.3.1 Calibration certificates

Certificate Of Calibration

OPHIR OPTRONICS HEREBY CERTIFIES THAT THIS INSTRUMENT MEETS ALL CURRENT PUBLISHED SPECIFICATIONS AND HAS BEEN CALIBRATED USING STANDARDS TRACEABLE TO THE NATIONAL INSTITUTE OF STANDARDS AND TECHNOLOGY (NIST) OR OTHER STANDARDS ACCEPTED BY NIST IN ACCORDANCE WITH **ISO 10012:2003**

Issued To: _____
Certificate No: 655738-001
Model Name: PD300-UV-SH,RoHS

Serial No: 655738
Catalog No: 7Z02413

CALIBRATION DATA

Filter Setting	Wavelength Range	Accuracy
Filter OUT	200nm to 1100nm	See datasheet *
Filter IN	220nm to 1100nm	See datasheet *

* Data sheets with accuracy specs are enclosed for new sensors. For sensors sent for recalibration or repair, please refer to the data sheets that were originally sent with the sensors. For information about uncertainty of measurement, please refer to "Ophir Power/Energy Meter Calibration Procedure and Traceability/Error Analysis" at www.ophiropt.com.

CALIBRATION STANDARDS TRACEABILITY DATA

This sensor has been calibrated using one or more of the following standards:

Manufacturer	Model	Serial #	Test #	Uncertainty	Last Cal Date	Next Cal Due
OPHIR, NIST CAL	30A-SH	KM6724	814997	1.2%	3/2011	3/2013
OPHIR, NIST CAL	FL250A-SH	KM6723	814996	1.2%	2/2011	2/2013
OPHIR, NIST CAL	PD300-IR-SH	KM6772	685/280894-11/2	1.4%	1/2012	1/2014
OPHIR, NIST CAL	PD300-UV-SH	KM6773	685/280894-11/1	0.4%,400-950nm 1.5%,200-400nm 2.2%,950-1064nm	1/2012	1/2014
OPHIR,NIST CAL	3A-P-SH-V1	KM6742	686006	1.2%	6/2011	6/2013
Labsphere NIST	SRS-99-010	KM-6783	AS-01160-010 3747	0.5% 250 -2500nm	2/2012	2/2014
Ocean Optics NIST	STAN-SSH-NIST	KM-6771	A338-MS-1-N - 00251	1.0% 200 - 400nm 0.5% 400 - 2200nm	11/2011	11/2014

Note 1: Source - Traceability Chart Ver39

Performed By: Ludmila Glushko
Reviewed By: Irena Alexandrov - Q.A. 15   **Date:** 24-APR-2012   **Signed:**

Next Calibration Due: OCT 2013

Ophir Optronics Calibration Centers:

USA: Tel: +1-435-753-3729	Fax +1-435-753-5231	Email: service@ophir-spiricon.com
Japan: Tel: +81-48-646-4150	Fax: +81-48-646-4155	Email: info@ophirjapan.co.jp
Europe: Tel: +49-89-890-1350	Fax: +49-89-800-2561	Email: service.de@bfioptilas.com
Israel: Tel +972-2-548-7407	Fax: +972-2-582-2338	Email: customer.support@ophiropt.co.il

www.ophiropt.com
Page 1 of 1

Figure C.18: *Ophir PD300-UV 655738 (PD 38) certificate of calibration* [DS91].

OPHIR
≡ Photonics Group

Certificate Of Calibration

OPHIR OPTRONICS HEREBY CERTIFIES THAT THIS INSTRUMENT MEETS ALL CURRENT PUBLISHED SPECIFICATIONS AND HAS BEEN CALIBRATED USING STANDARDS TRACEABLE TO THE NATIONAL INSTITUTE OF STANDARDS AND TECHNOLOGY (NIST) OR OTHER STANDARDS ACCEPTED BY NIST IN ACCORDANCE WITH **ISO 10012:2003**

Issued To: _____
Certificate No: 655739-001
Model Name: PD300-UV-SH,RoHS

Serial No: 655739
Catalog No: 7Z02413

CALIBRATION DATA

Filter Setting	Wavelength Range	Accuracy
Filter OUT	200nm to 1100nm	See datasheet *
Filter IN	220nm to 1100nm	See datasheet *

* Data sheets with accuracy specs are enclosed for new sensors. For sensors sent for recalibration or repair, please refer to the data sheets that were originally sent with the sensors. For information about uncertainty of measurement, please refer to "Ophir Power/Energy Meter Calibration Procedure and Traceability/Error Analysis" at www.ophiropt.com.

CALIBRATION STANDARDS TRACEABILITY DATA

This sensor has been calibrated using one or more of the following standards:

Manufacturer	Model	Serial #	Test #	Uncertainty	Last Cal Date	Next Cal Due
OPHIR, NIST CAL	30A-SH	KM6724	814997	1.2%	3/2011	3/2013
OPHIR, NIST CAL	FL250A-SH	KM6723	814996	1.2%	2/2011	2/2013
OPHIR, NIST CAL	PD300-IR-SH	KM6772	685/280894-11/2	1.4%	1/2012	1/2014
OPHIR, NIST CAL	PD300-UV-SH	KM6773	685/280894-11/1	0.4%,400-950nm 1.5%,200-400nm 2.2%,950-1064nm	1/2012	1/2014
OPHIR,NIST CAL	3A-P-SH-V1	KM6742	686006	1.2%	6/2011	6/2013
Labsphere NIST	SRS-99-010	KM-6783	AS-01160-010 3747	0.5% 250 -2500nm	2/2012	2/2014
Ocean Optics NIST	STAN-SSH-NIST	KM-6771	A338-MS-1-N - 00251	1.0% 200 - 400nm 0.5% 400 - 2200nm	11/2011	11/2014

Note 1: Source - Traceability Chart Ver39

Performed By:
Reviewed By: Irena Alexandrov - Q.A. 15   **Date:** 24-APR-2012   **Signed:**

Ludmila Glushko

Next Calibration Due: OCT 2013

Ophir Optronics Calibration Centers:

USA: Tel: +1-435-753-3729	Fax +1-435-753-5231	Email: service@ophir-spiricon.com
Japan: Tel: +81-48-646-4150	Fax: +81-48-646-4155	Email: info@ophirjapan.co.jp
Europe: Tel: +49-89-890-1350	Fax: +49-89-800-2561	Email: service.de@bfioptilas.com
Israel: Tel +972-2-548-7407	Fax: +972-2-582-2338	Email: customer.support@ophiropt.co.il

www.ophiropt.com
Page 1 of 1

Figure C.19: *Ophir PD300-UV 655739 (PD 39) certificate of calibration* [DS91].

Certificate Of Calibration

OPHIR OPTRONICS HEREBY CERTIFIES THAT THIS INSTRUMENT MEETS ALL CURRENT PUBLISHED SPECIFICATIONS AND HAS BEEN CALIBRATED USING STANDARDS TRACEABLE TO THE NATIONAL INSTITUTE OF STANDARDS AND TECHNOLOGY (NIST) OR OTHER STANDARDS ACCEPTED BY NIST IN ACCORDANCE WITH **ISO 10012:2003**

Issued To: _____
Certificate No: 651283-001
Model Name: PULSAR-2

Serial No: 651283
Catalog No: 7Z01202

CALIBRATION STANDARDS TRACEABILITY DATA

Manufacturer	Model	Serial #	Test #	Uncertainty	Last Cal Date	Next Cal Due
FLUKE	8845A	KM3603	9112343949	0.1%	9/2011	9/2012

Note 1: Source - Traceability Chart Ver39
Note 2: Instrument calibration is performed using an automated current calibration unit. This calibration unit is periodically calibrated against the Fluke Voltmeter which is traceably calibrated.

Performed By:
Reviewed By: Gennady Estrin
Steve Demri - Q.A. 56   **Date:** 27-FEB-2012   **Signed:** _____

Next Calibration Due: AUG 2013

Ophir Optronics Calibration Centers:

USA: Tel: +1-435-753-3729	Fax +1-435-753-5231	Email: service@ophir-spiricon.com
Japan: Tel: +81-48-646-4150	Fax: +81-48-646-4155	Email: info@ophirjapan.co.jp
Europe: Tel: +49-89-890-1350	Fax: +49-89-800-2561	Email: service.de@bfioptilas.com
Israel: Tel +972-2-548-7407	Fax: +972-2-582-2338	Email: customer.support@ophiropt.co.il

www.ophiropt.com
Page 1 of 1

Figure C.20: *Ophir Pulsar-2* certificate of calibration [DS92].

UNITED STATES DEPARTMENT OF COMMERCE
National Institute of Standards and Technology
Gaithersburg, Maryland 20899-

In reply refer to: 685/280103-11

December 20, 2010

Dr. Bianca Keilhauer
Karlsruher Institut für Technologie KIT
Campus Nord – IK
Zusatz: Geb 425 Raum 345
Hermann-von-Helmholtz-Platz 1
76344 Eggenstein-Leopoldshafen
GERMANY

Purchase Order No.: 4800033197 dated August 25, 2010

Dear Dr. Keilhauer:

Enclosed are the results of the NIST measurement services and associated documentation that
you requested. Please refer to the above file numbers in any later communication concerning
these tests.

Sincerely,

Gerald T. Fraser, Division Chief
Optical Technology Division
Physical Measurement Laboratory

Enclosure: One Report of Calibration

NIST Service ID Number:
1 each 39071C UV Silicon Photodiodes

GTF/jmh

NIST

Figure C.21: Cover letter of the NIST calibration report for the *OSI Optoelectronics* photo-diode *UV-100* [DS111]. The full calibration report with 9 pages is present at the IKP - KIT [110].
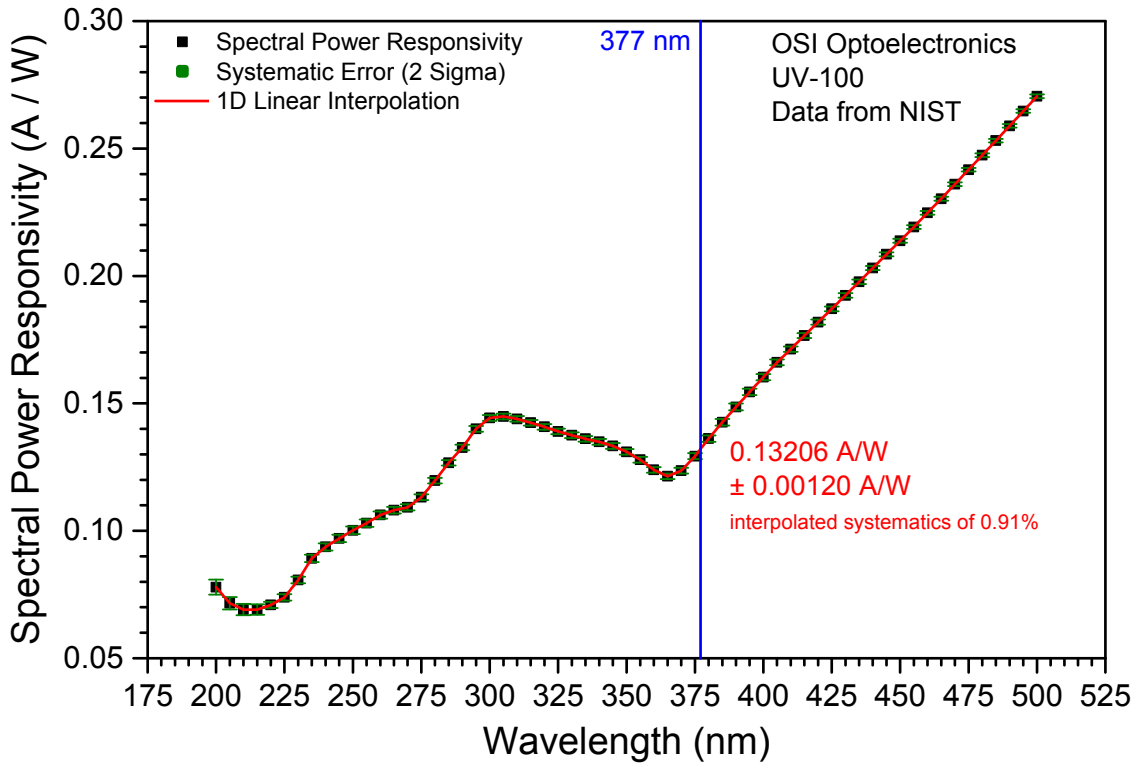
Figure C.22: This graph shows the spectral responsivity of the NIST-photodiode *OSI Opto-electronics UV*-100. This photodiode is read out directly with a *Keithley 6485 Picoammeter* and the responsivity gives the factor for calculating the optical power via the measured current [DS111, DS112]. The responsivity factor at 377 nm and its systematic error were determined via an interpolation of the given values.

C.1.4 *Collimators*
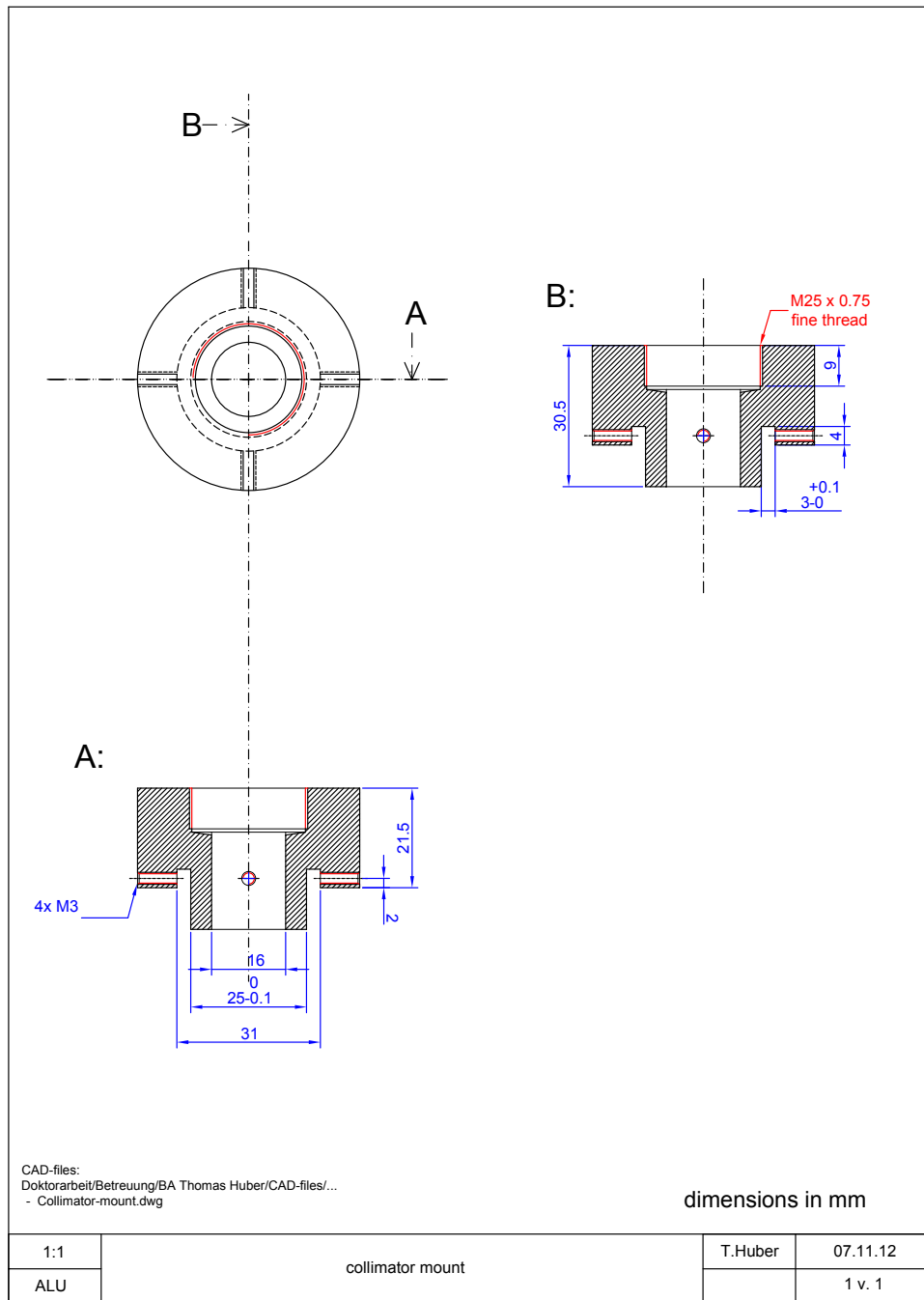
Figure C.23: Mount for the collimators or a round photodiode with an M25 x 0 75 internal fine thread and threads for four headless screws (designed by Thomas Huber) [86].

Plate 1

1mm M25 - M60
Brass

TOP

A

R34
R30
R26
R12.5
R8.5
R0.5

A:

68
25
10
4
17
2.5
0.5
3
4
8
25.5
1
52
4
60
21.5

M25 x 0.75
external fine thread

M60 x 0.75
external fine thread

CAD-files:
Doktorarbeit/Documents/FreeCAD-Projekte/Kollimator/v1.0/export/...
  - Platte1_Step.stp
  - Platte1-sketch.dwg

dimensions in mm

1:1	BRASS collimator plate 1	M.Karus	05.11.12
BRASS			1 v. 1
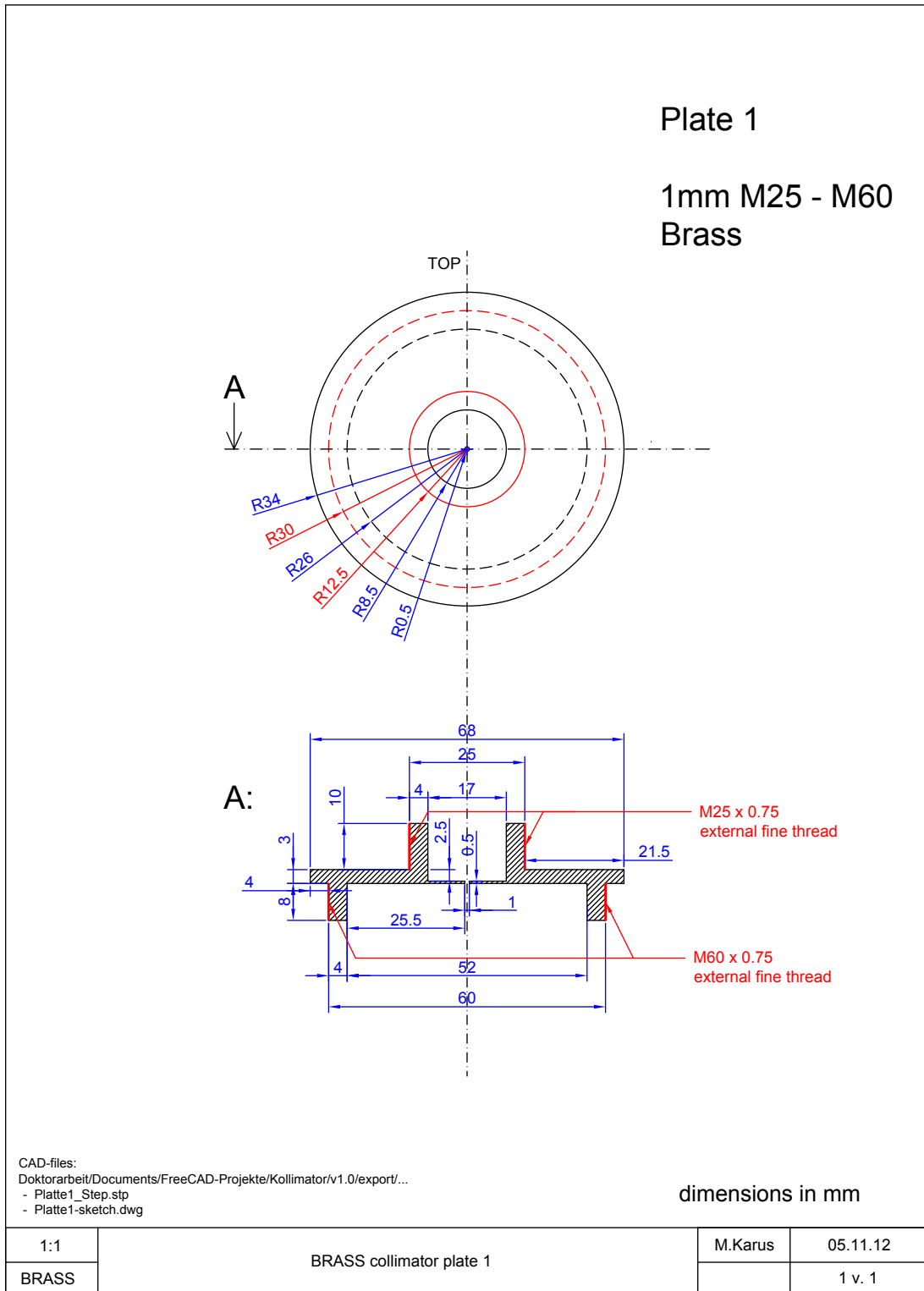
Figure C.24: Plate 1 of the alu-collimator made of brass, with a 1 mm hole, an M25 x 0 75 external fine thread (sphere-side), and an M60 x 0 75 external fine thread (output-side).
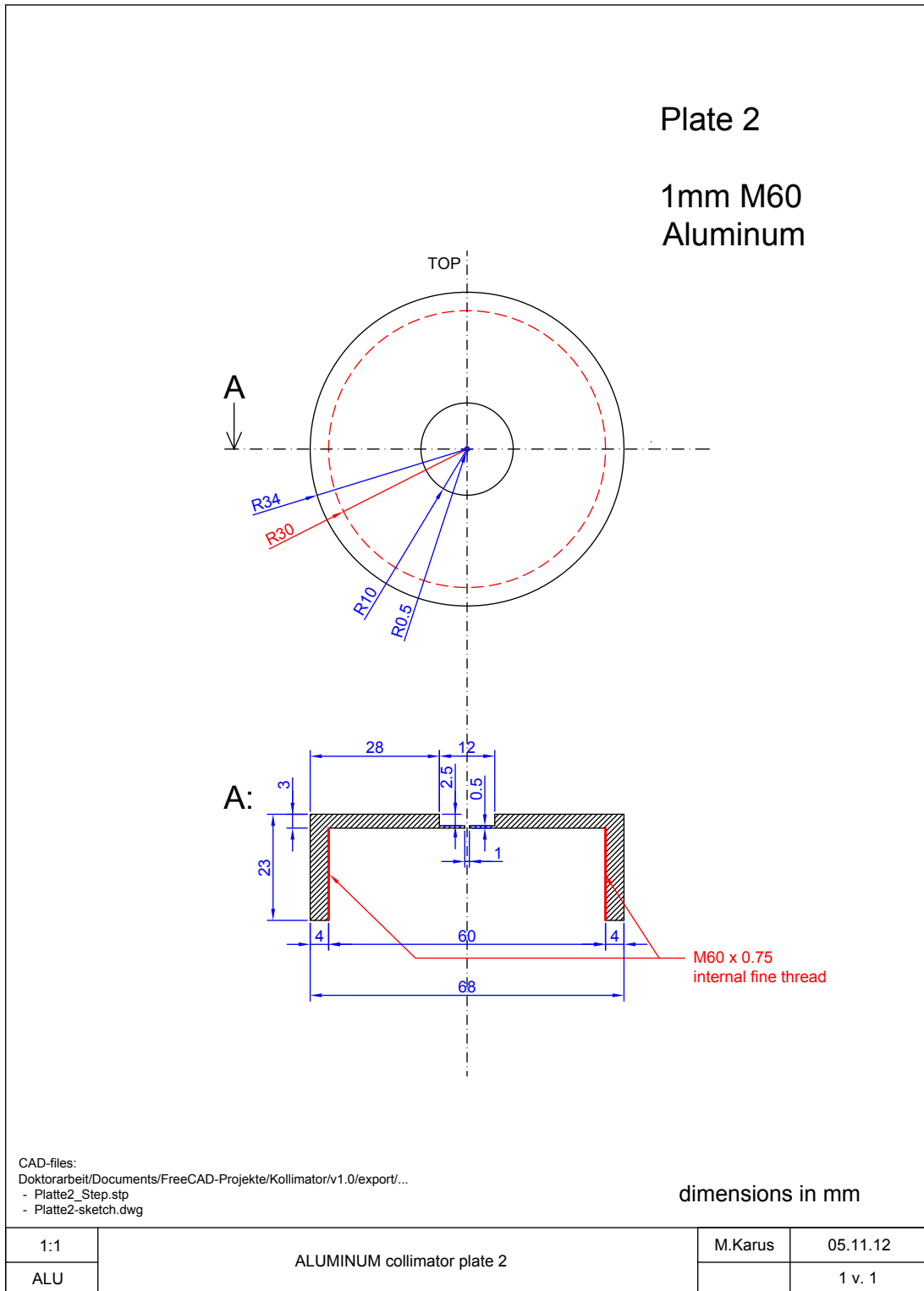
Figure C.25: Plate 2 of the alu-collimator made of aluminum, with a 1 mm hole and an M60 x 0.75 internal fine thread.
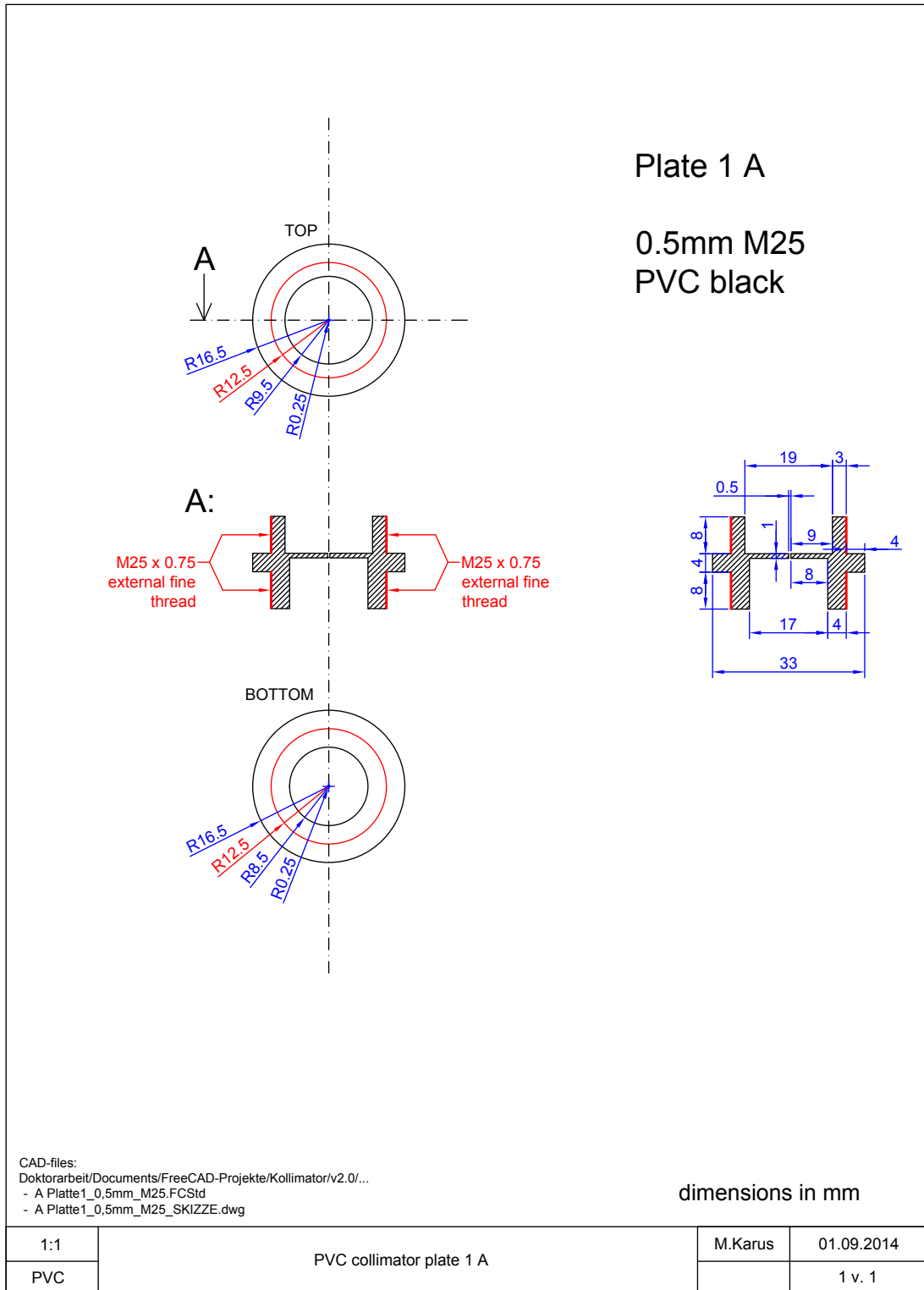
Figure C.26: Plate 1A of the PVC-collimator made of PVC, with a 0.5 mm diameter hole and two M25 x 0.75 external fine threads. The short side goes towards the integrating sphere.
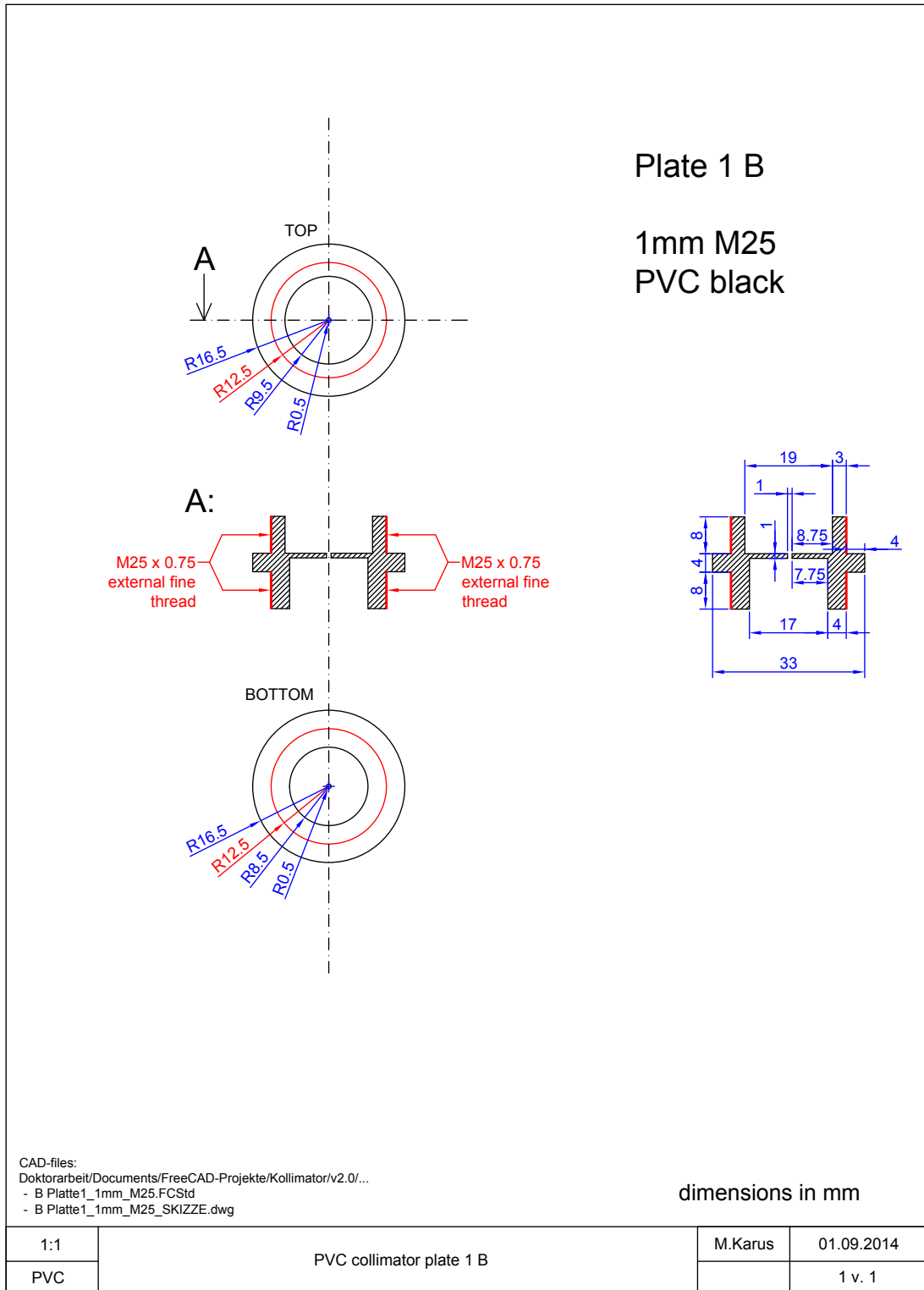
Figure C.27: Plate 1B of the PVC-collimator made of PVC, with a 1 mm diameter hole and two M25 x 0.75 external fine threads. The short side goes towards the integrating sphere.
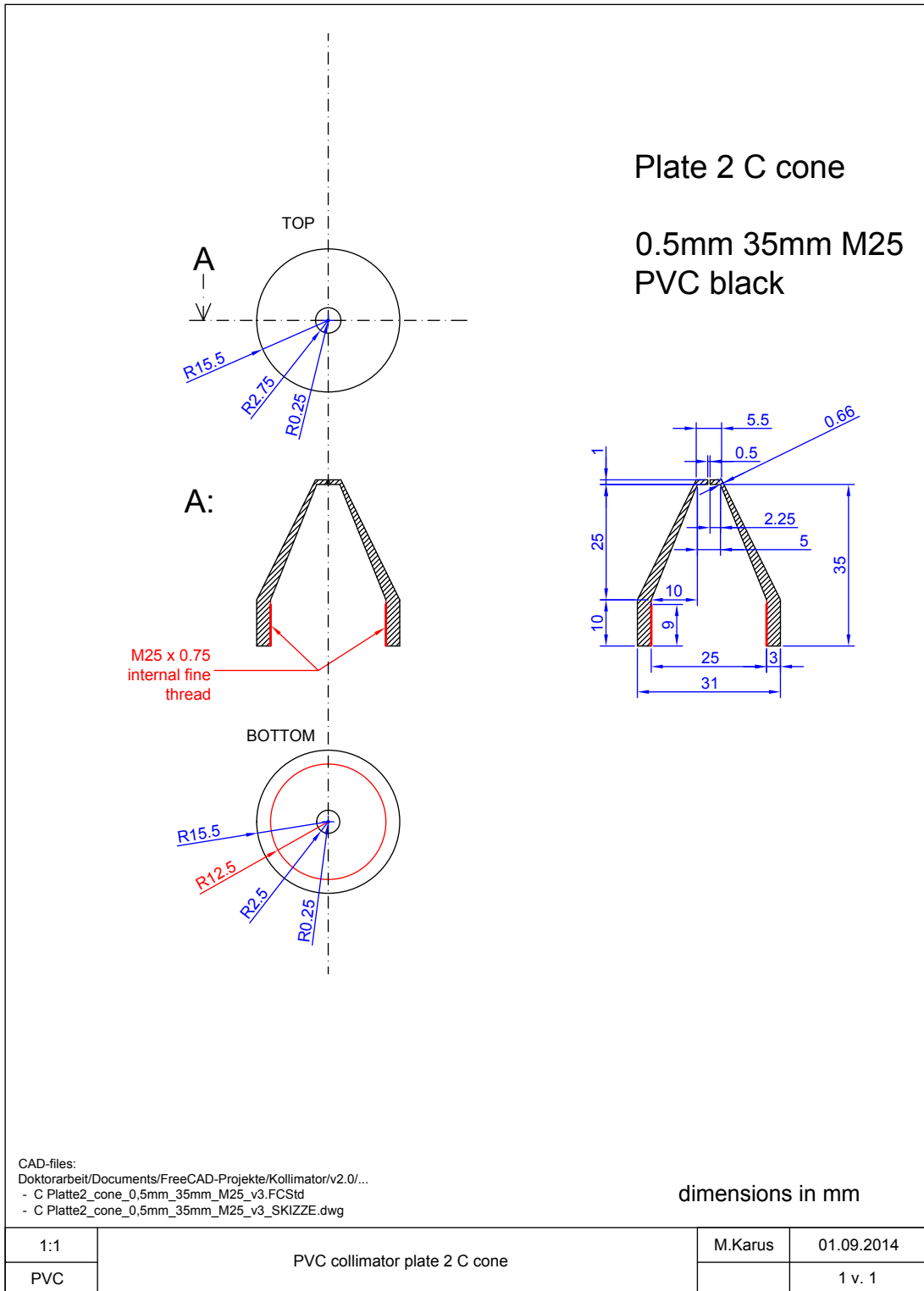
Figure C.28: Plate 2C of the PVC-collimator made of PVC, with a 0.5 mm diameter hole, a height of 35 mm, and a M25 x 0.75 internal fine thread.
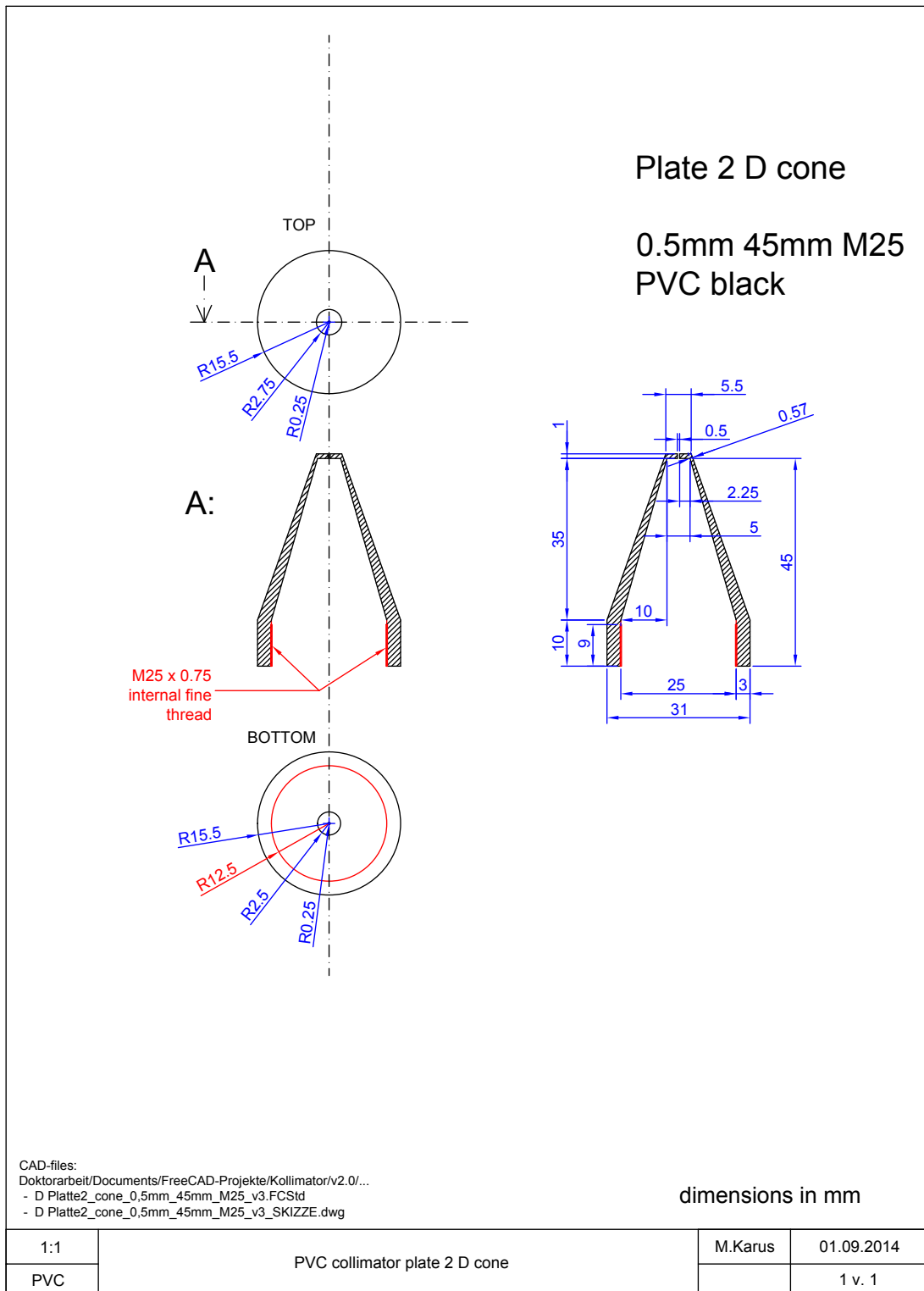
Figure C.29: Plate 2D of the PVC-collimator made of PVC, with a 0.5 mm diameter hole, a height of 45 mm, and a M25 x 0.75 internal fine thread.

C.2 MAPMT

HAMAMATSU	PHOTOMULTIPLIER TUBE
for Jem-Euso collaboration Nov. 2011	R11265-113-M64 MOD2

1 inch Square, 8×8 Multianode, Fast Time Response
UV window, Bialkali Photocathode, Metal Channel Dynode 12-Stage, Head-on Type
\<Pin length of 6.6mm\>

General

Parameter		Description	Unit
Spectral Response Range		185 to 650	nm
Window Material / Thickness		UV glass / 0.8	mm
Photocathode	Material	Bialkali	-
	Minimum Effective Area	23×23	mm^2
Dynode Structure		Metal channel Dynode	-
Number of Stages		12	-
Weight		TBD	g
Operating Ambient Temperature		-30 to +50	deg C
Storage Temperature		-30 to +50	deg C

Maximum Ratings (Absolute Maximum Values)

Parameter	Value	Unit
Supply Voltage Between Anode and Cathode	1100	V
Average Anode Output Current in Total	0.1	mA

Characteristics at 25 deg C

Parameter		Min.	Typ.	Max.	Unit
Cathode Sensitivity	Luminous (2856K)	90	105	-	uA/lm
Anode Sensitivity	Luminous (2856K)	-	105	-	A/lm
Gain		-	1×10^6	-	-
Anode Dark Current (Each anode)		-	0.4	4	nA
Time Response	Rise Time	-	0.6	-	ns
	Transit Time	-	5.1	-	ns
	Transit Time Spread (FWHM)	-	0.35	-	ns
Uniformity Between Each Anode		-	1 : 3	1 : 5	-
Pulse Linearity	at ±2% Deviation	-	0.2	-	mA
(Each Anode)	at ±5% Deviation	-	0.4	-	mA

NOTE: Anode characteristics are measured with a voltage distribution ratio shown below :

Voltage Distribution Ratio and Supply Voltage

Electrodes	K	Dy1	Dy2	Dy3	Dy4	Dy5	Dy6	Dy7	Dy8	Dy9	Dy10	Dy11	Dy12	G.R	P
Ratio	2.3	1.2	1	1	1	1	1	1	1	1	1	1	1		0.5

Supply Voltage : 1000 V   K : Cathode   Dy : Dynode   G.R : Guard Ring   P : Anode

Figure C.30: Datasheet of the Hamamatsu R11265-113-M64 MOD2 - MAPMT. The datasheet was included with the delivery of the device.
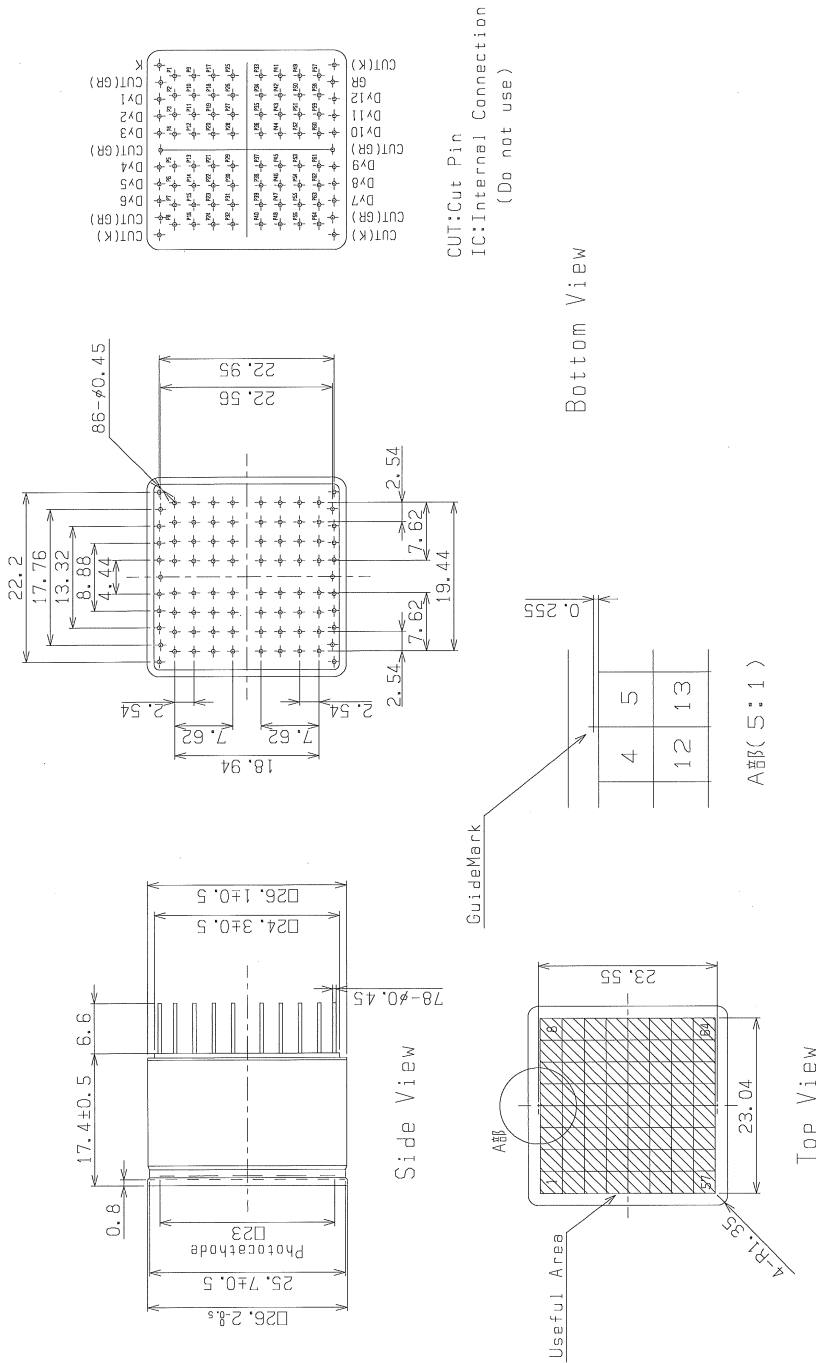
Figure C.31: Sketch of the Hamamatsu R11265-113-M64 MOD2 - MAPMT. The sketch was included with the delivery of the device.

MAPMT voltage divider
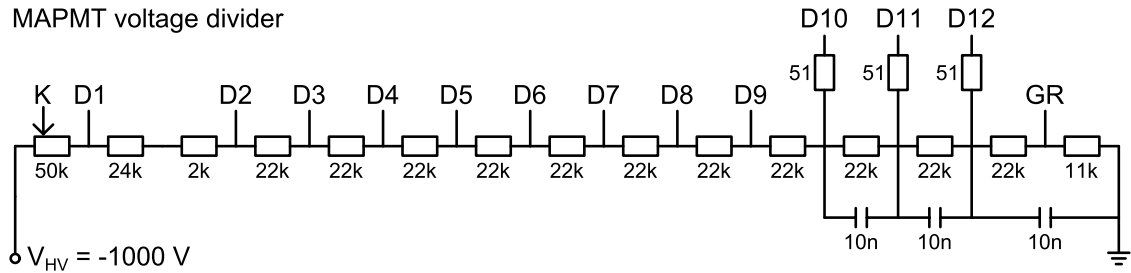
$R_{tot} = 329\ k\Omega$ at $V_{HV} = -1000\ V$ $I_{tot} = 3.04\ mA$ $I_{D9} = 27.5\ mA$

Dynode voltages relative to ground

Type	K	D1	D2	D3	D4	D5	D6	D7	D8	D9	D10	D11	D12	GR
Voltage	-975	-821	-744	-679	-614	-549	-484	-420	-356	-291	-227	-162	-98	-33

Figure C.32: Sketch of the voltage divider for Hamamatsu R11265-113-M64 MOD2 - MAPMT [114]. The bias voltage is set to $-1000\,V$.
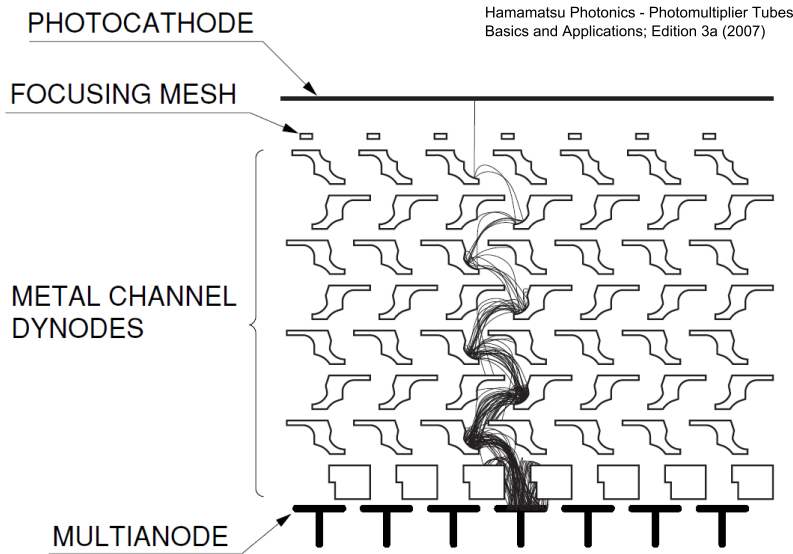
Figure C.33: Sketch of the typical inner structure on a generic MAPMT [126]. The sketch shows the photocathode, the focusing mesh, the inner dynode structure, and the multianode for every pixel. The trajectory of a photoelectron and its cascade is shown. The photocathode has no dead space between the pixels.
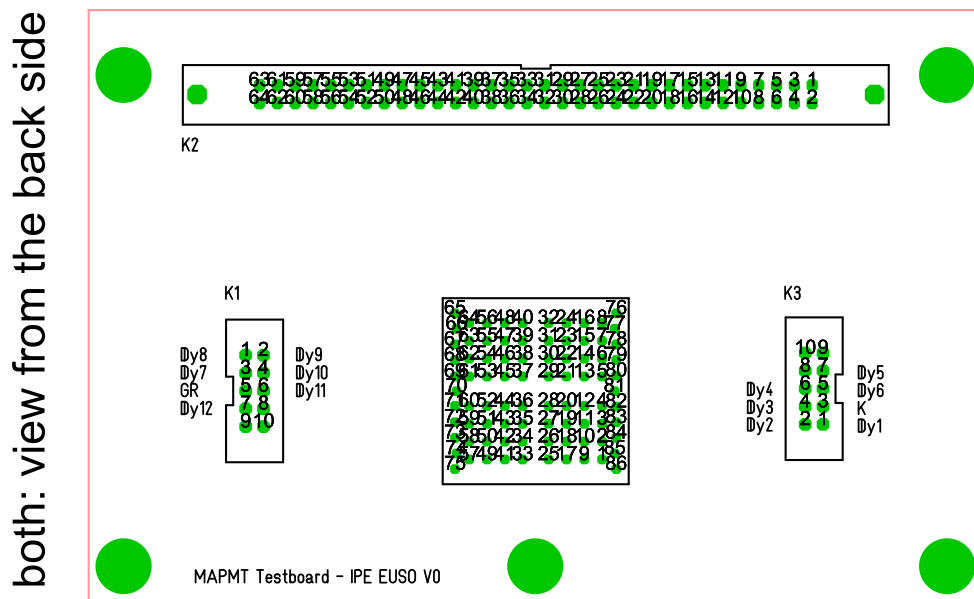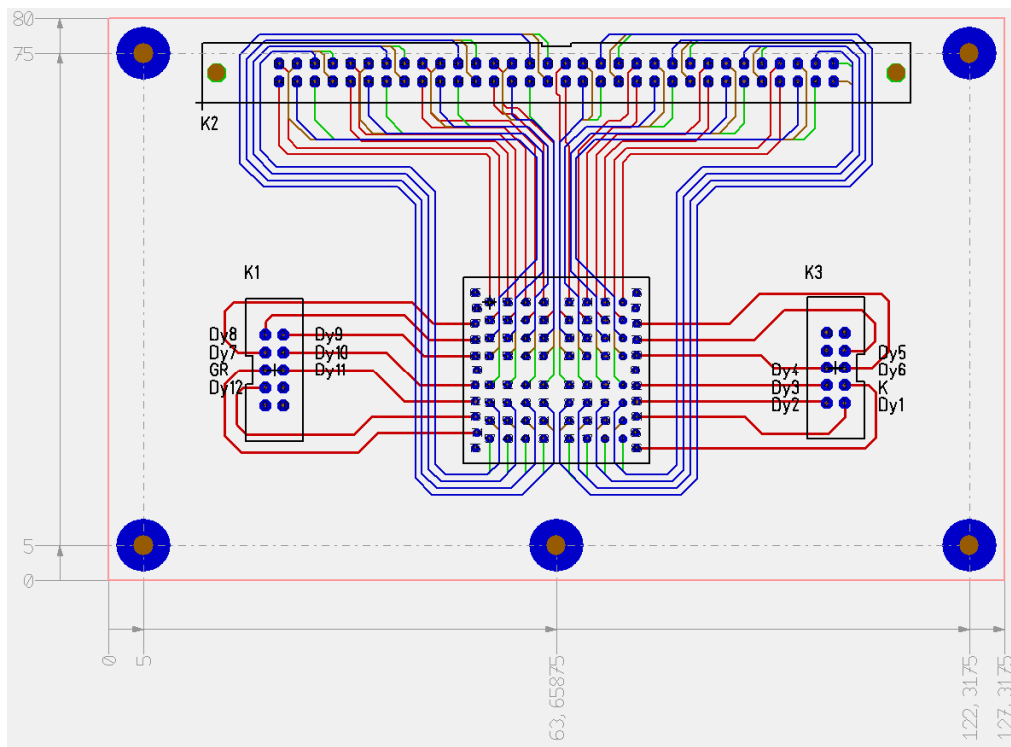
Figure C.34: Sketch of the MAPMT board for Hamamatsu R11265-113-M64 MOD2 - MAPMT, designed by Andreas Ebersoldt (IPE - KIT) [129].
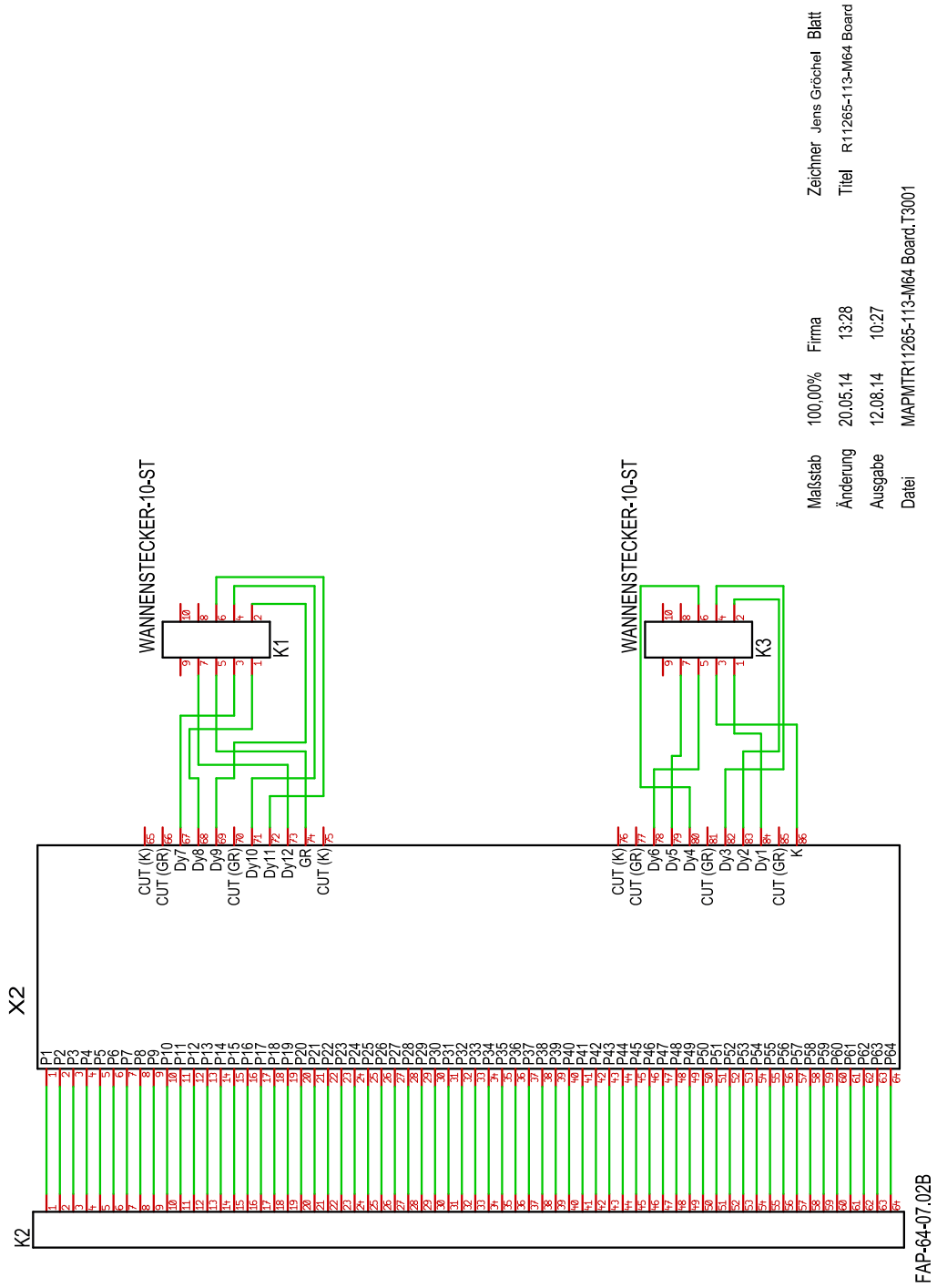
Figure C.35: Sketch of the MAPMT board connections for Hamamatsu R11265-113-M64 MOD2 - MAPMT, designed by Andreas Ebersoldt (IPE - KIT) [129].
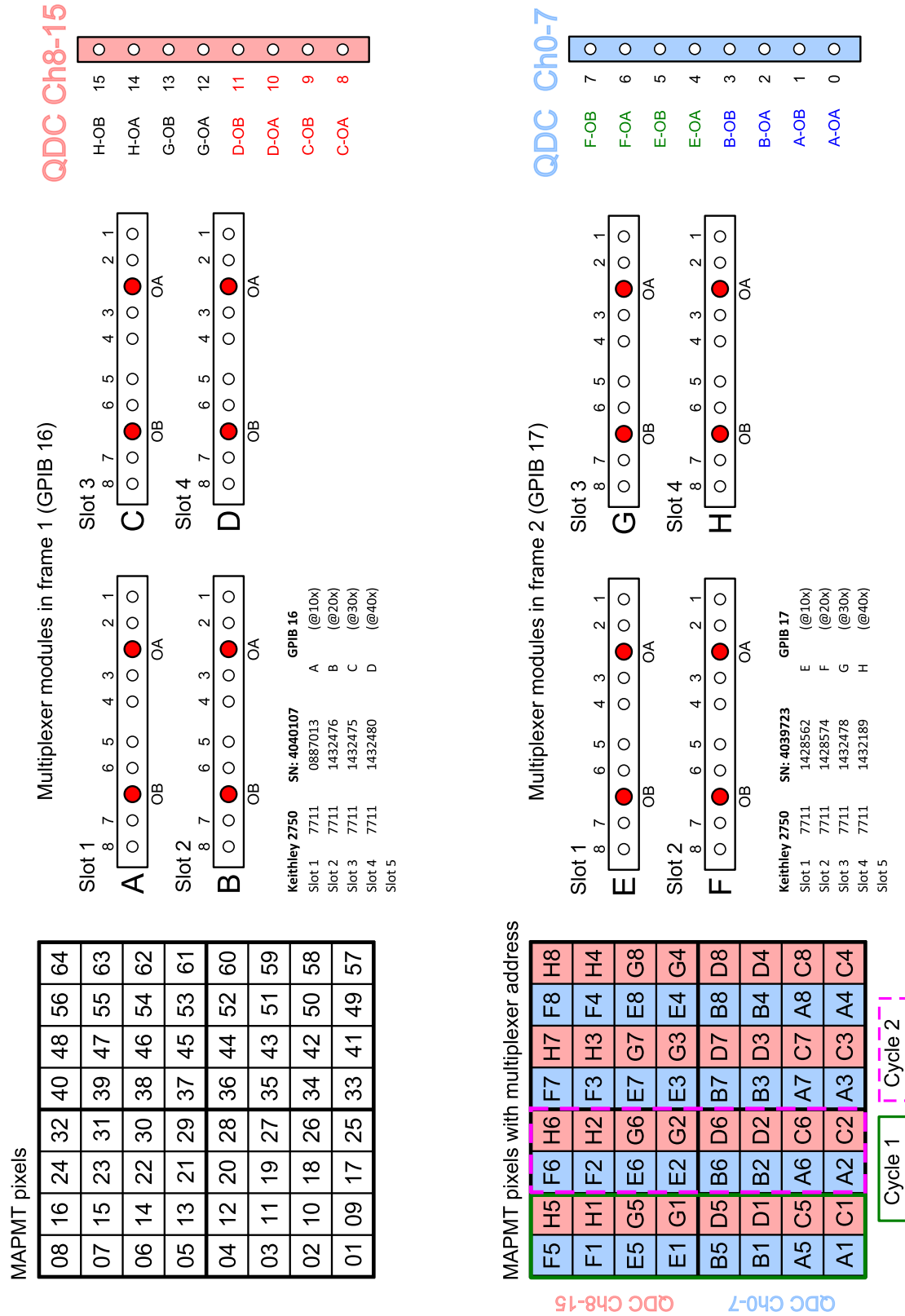
Figure C.36: Scheme of the connections from the MAPMT pixels, through the multiplexer cards, to the QADC channels.

C.3 VARIOUS
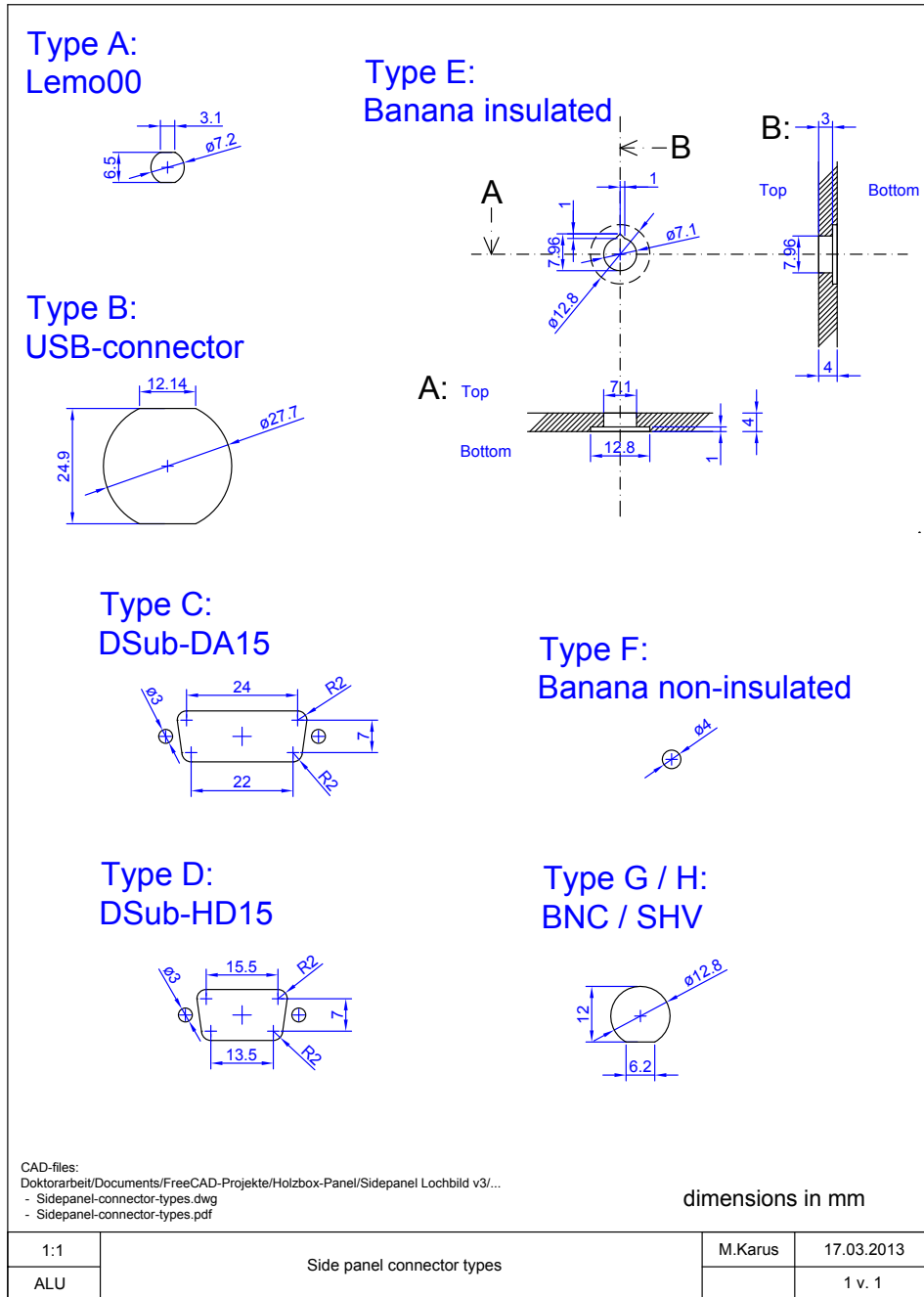
Figure C.37: Sketch of the connector types used for the side panel.
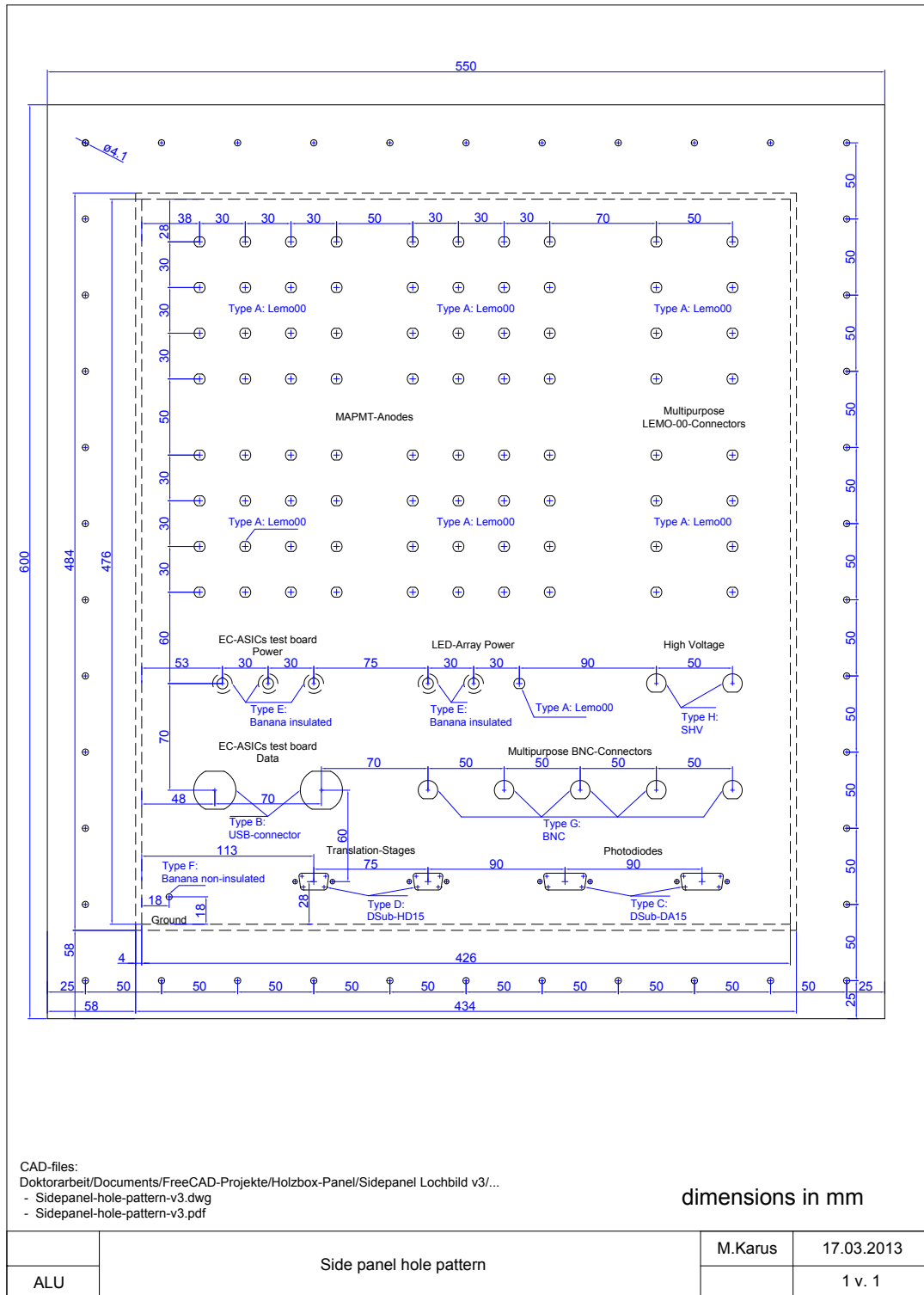
Figure C.38: Sketch of the side panel hole pattern.
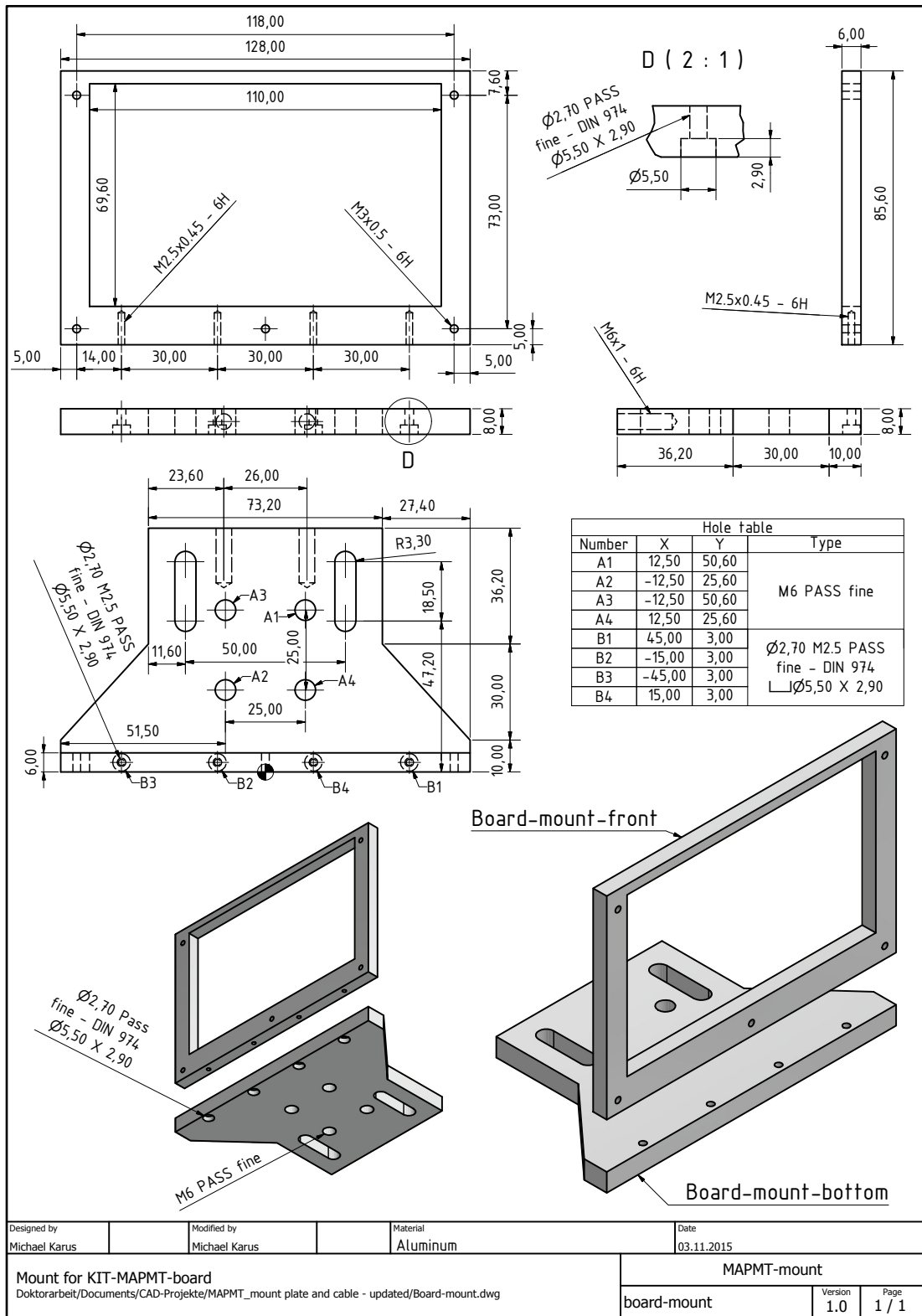
Figure C.39: Construction sheet of the mount for the MAPMT-board.
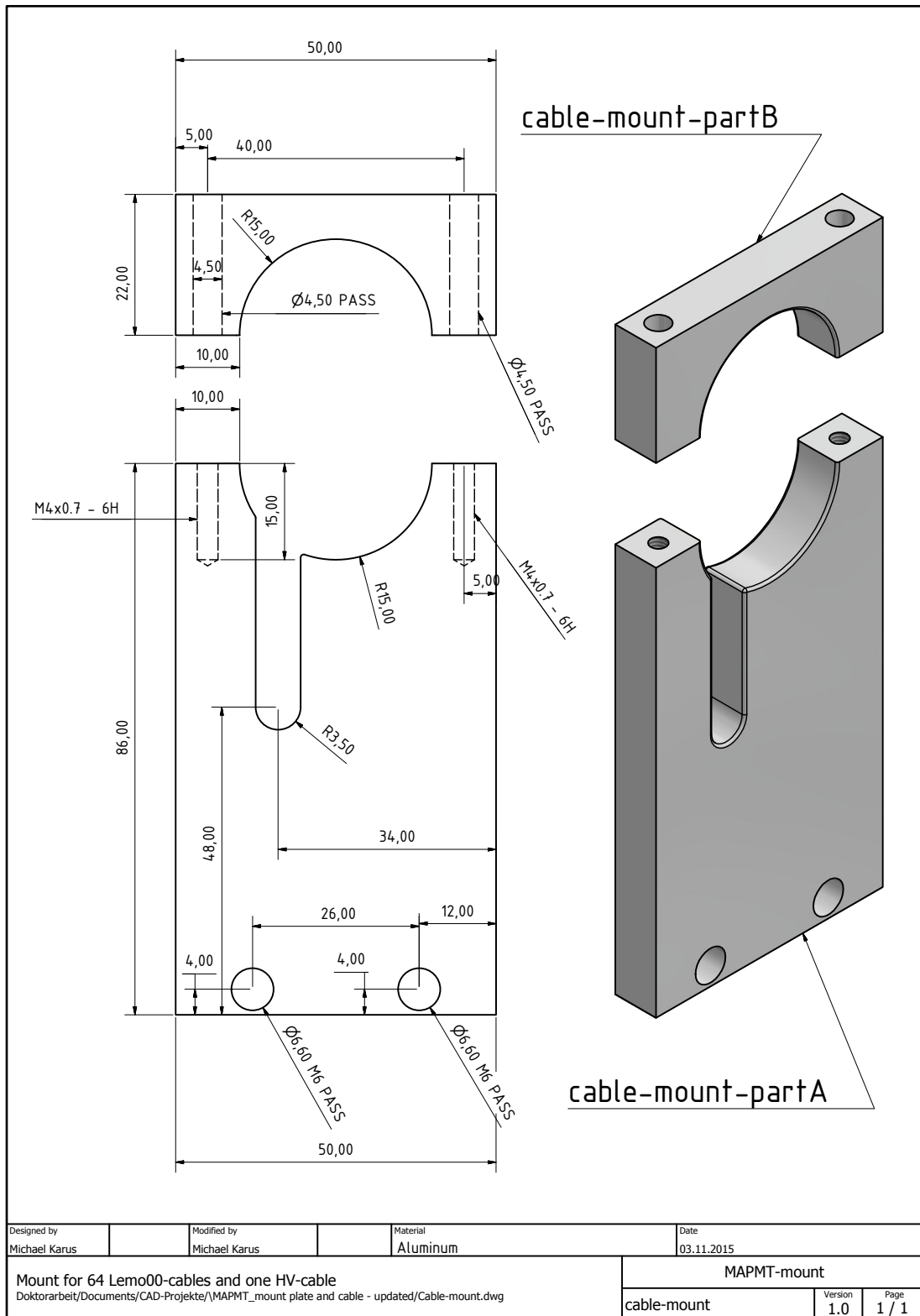
Figure C.40: Construction sheet of the cable-mount for the MAPMT-board.

C.3.1 *NIM-pulse*

Table C.5: NIM-pulse for a termination of 50 Ω.

LOGIC LEVEL	CURRENT	VOLTAGE
Logic 0	$0\,\text{mA}$	$0\,\text{V}$
Logic 1	$-12\,\text{mA}$ to $-32\,\text{mA}$	$-0.6\,\text{V}$ to $-1.6\,\text{V}$

Figure C.41: Sketch of a NIM-pulse and an inverted NIM-pulse.

C.3.2 *TTL-pulse*

Table C.6: TTL-pulse for a termination of 50 Ω.

LOGIC LEVEL	INPUT VOLTAGE	OUTPUT VOLTAGE
Logic 0 (low)	$\leqslant 0.8\,\text{V}$	$\leqslant 0.4\,\text{V}$
Logic 1 (high)	$\geqslant 2.0\,\text{V}$	$\geqslant 2.4\,\text{V}$

C.3.3 *CAEN V965 QADC*

The VME-module CAEN V965 QADC is a 16 channel 12 bit QADC with two ranges: high range (HR) and low range (LR) [DS117].

Table C.7: Ranges of the CAEN V965 QADC.

	RANGE	RESOLUTION
HR	$0\,\text{pC}$ to $900\,\text{pC}$	$200\,\text{fC LSB}$
LR	$0\,\text{pC}$ to $100\,\text{pC}$	$25\,\text{fC LSB}$

D

ACRONYMS

ADC	analogue-digital converter
AGN	Active Galactic Nuclei
AMS	Atmospheric Monitoring System
ASCII	American Standard Code for Information Interchange
ASIC	application-specific integrated circuit
BNC	Bayonet Neill–Concelman (a coaxial cable quick connector)
CCB	Cluster Control Board
CERN	European Organization for Nuclear Research (derived from: Conseil Européen pour la Recherche Nucléaire)
CMB	cosmic microwave background
CNES	Centre national d'études spatiales (French federal space agency)
CR	cosmic rays
DAQ	Data Acquisition
EAS	extensive air showers
EC	elementary cell
EECR	extreme energy cosmic ray
ELS	electron light source (compact electron linear accelerator at TA site)
ESA	European Space Agency
ESAF	EUSO Simulation and Analysis Framework
EUSO	Extreme Universe Space Observatory
EUSO-TA	EUSO prototype at the Telescope Array site

EUSO-Balloon	EUSO prototype onboard a balloon
FOV	field of view
APD	avalanche photodiode
G-APD	Geiger-mode avalanche photodiode
GLS	Global Light System
GRB	Gamma Ray Bursts
GTU	Gate Time Unit
GZK	Greisen-Zatsepin-Kuz'min
HECR	high energy cosmic rays
HV	high voltage
HVPS	high voltage power source
IKP	Institute for Nuclear Physics (Institut für Kernphysik)
IR	infrared
ISS	International Space Station
JAXA	Japan Aerospace Exploration Agency (Japanese federal space agency)
JEM-EUSO	Extreme Universe Space Observatory onboard the Japanese Experiment Module
KASCADE	Karlsruhe Shower Core and Array Detector
KIT	Karlsruhe Institute of Technology
LDD	light diode driver
LED	light-emitting diode
LHC	Large Hadron Collider
LIDAR	Light Detection and Ranging
LPM	Landau-Pomeranchuk-Migdal
LSB	least significant bit
MAPMT	multianode photomultiplier tube

Mini-EUSO	autonomous miniature prototype of the Extreme Universe Space Observatory
MPPC	multi-pixel photon counter
NASA	National Aeronautics and Space Administration (US American federal space agency)
NIM	Nuclear Instrumentation Module (report DOE/ER-0457T)
NIST	National Institute of Standards and Technology (US American measurement standards laboratory)
PC	personal computer
PDE	photo detection efficiency
PDM	photo-detector module
PMMA	polymethyl-metacrylate (UV transmitting)
PMT	photomultiplier tube (teflon)
PVC	polyvinyl chloride
QADC	charge-integrating analog-digital converter
HR	high range 0 pC to 900 pC (200 fC least significant bit (LSB))
LR	low range 0 pC to 100 pC (25 fC LSB)
R&D	research and development
ROSCOSMOS	Russian Federal Space Agency
SNR	supernova remnants
SPACIROC	Spatial Photomultiplier Array Counting and Integrating Chip
SPB	super pressure balloon
SPOCK	Single PhOton Calibration stand at KIT
SiPM	silicon photomultiplier
TA	Telescope Array
TLE	transient luminous events
TSV	through-silicon via

TTL   transistor–transistor logic

UHE   ultra-high energy

UHECR   ultra-high energy cosmic rays

USB   Universal Serial Bus

UV   ultraviolet

VME   Versa Module Eurocard (computer bus standard ANSI/IEEE 1014-1987)

Xe-flasher   Xenon flash lamp

DATASHEETS

[DS62] SCHOTT AG *Schott BG3 - band pass filter* 2015 URL: http://www.schott.com/advanced_optics/english/download/schott-bandpass-bg3-oct-2015-en.pdf

[DS79] HAMAMATSU PHOTONICS K.K. *MPPC and MPPC module for precision measurement* Nov. 2014 URL: https://www.hamamatsu.com/resources/pdf/ssd/mppc_kapd0002e.pdf

[DS80] LABSPHERE INC. *Modular Integrating Spheres* 231018v002 042008 2012 URL: https://www.labsphere.com/wp-content/uploads/2015/05/GenPurposeIntegratingSpheres.pdf

[DS87] THORLABS INC. *Thorlabs MB60120/M - Optical Breadboard* 2012 URL: https://www.thorlabs.com/thorcat/13800/MB60120_M-AutoCADPDF.PDF

[DS88] OWIS GMBH *S 90-1000-LL - SYS 90 System Rail* 9012.0042 / 07.03.2011 2013 URL: http://www.owis.eu/fileadmin/user_upload/owis.eu/products/pdf/pi_s_90ll.pdf

[DS89] OWIS GMBH *RT 90 - SYS 90 System Rail Slides* 9012.0171 / 04.07.2011 2013 URL: http://www.owis.eu/fileadmin/user_upload/owis.eu/products/pdf/rt_90.pdf

[DS90] THORLABS INC. *Thorlabs AP90 - Right-Angle Mounting Plate* 2013 URL: http://www.thorlabs.de/thorcat/0000/AP90-AutoCADPDF.pdf

[DS91] OPHIR OPTRONICS SOLUTIONS LTD *PD300-UV - Photodiode* 2012 URL: http://www.ophiropt.com/laser--measurement/sites/default/files/PD300-UV_PD300-UV-193_PD300-IR_PD300-IRG.pdf

[DS92] OPHIR OPTRONICS SOLUTIONS LTD *Pulsar 2 - Multichannel USB-Interface* 2012 URL: http://www.ophiropt.com/laser--measurement/sites/default/files/pulsar_catalog.pdf

[DS93] OWIS GMBH *PS 10-32-SM - Position Control* 9012.0181 / 11.02.2011 2011 URL: http://www.owis.eu/fileadmin/user_upload/owis.eu/products/pdf/pi_ps10.pdf

[DS94] OWIS GMBH *LTM 80-300-HSM - Precision Linear Stage* 9012.0272 / 25.03.2011 2011 URL: http://www.owis.eu/fileadmin/user_upload/owis.eu/products/pdf/pi_ltm_80.pdf

[DS95] OCEAN OPTICS INC. *S2000 Miniature Fiber Optic Spectrometers and Accessories* 203-00000-DW-02-0505 2005 URL: http://oceanoptics.com/wp-content/uploads/S2000_Operating_Manual2.pdf

[DS96]   OCEAN OPTICS INC. *ADC1000-USB A/D Converter Operating Instructions* Rev. 2.03 05062005 2005 URL: http://oceanoptics.com///wp-content/uploads/ADC1000-USB-Operating-Instructions.pdf

[DS98]   TEKTRONIX INC. *PWS2323 - DC Power Supply* 3GW-25620-3 2011 URL: http://tektronix.calplus.de/pdf/2898/

[DS107] LABSPHERE INC. *Optical-grade Spectralon Reflectance Material* PB-13021-000 Rev.00 2015 URL: https://www.labsphere.com/wp-content/uploads/2015/06/Spectralon-Optical-Grade.pdf

[DS111] OSI OPTOELECTRONICS *UV100 - UV Enhanced Series* 2013 URL: http://www.osioptoelectronics.com/Libraries/Datasheets/UV-Enhanced-Inversion-Layer-Photodiodes.sflb.ashx

[DS112] KEITHLEY INSTRUMENTS INC. *6485 5-1/2 digit Picoammeter* 2015 URL: http://www.keithley.com/data?asset=6199

[DS116] HEWLETT-PACKARD *HP Pulse Generator 8082A* 1983 URL: https://www.valuetronics.com/Manuals/HP_8082A.PDF

[DS117] CAEN S.P.A. *V965 datasheet* 2015 URL: http://www.caen.it/csite/CaenProd.jsp?parent=11&idmod=398#

[DS118] CAEN S.P.A. *V965 Technical Information Manual* Revision 8 2008 URL: http://www.caen.it/servlet/checkCaenManualFile?Id=5333

[DS119] CAEN S.P.A. *V1718 datasheet* 2015 URL: http://www.caen.it/csite/CaenProd.jsp?idmod=417&parent=11#

[DS120] CAEN S.P.A. *V1718 Technical Information Manual* Revision 9 2009 URL: http://www.caen.it/servlet/checkCaenManualFile?Id=5385

[DS121] TELEDYNE LECROY INC. *WaveStation2012 Function/Arbitrary Waveform Generators* wavestation-ds-09apr15 2015 URL: http://cdn.teledynelecroy.com/files/pdf/wavestation_datasheet.pdf

[DS122] TELEDYNE LECROY INC. *WaveRunner 610 Zi Oscilloscopes* waverunner6zi-ds-06apr15 2015 URL: http://cdn.teledynelecroy.com/files/pdf/waverunner-6zi-datasheet.pdf

[DS124] HAMAMATSU PHOTONICS K.K. *Silicone layered TSV MPPC array S13361-3050xx* Mai 2015 URL: http://www.hamamatsu.com/jp/en/product/new/S13361-3050AE-08/index.html

[DS131] KEITHLEY INSTRUMENTS INC. *2750 Multimeter-Switch System* 2013 URL: http://www.keithley.com/products/switch/dmmswitch/?mn=2750

[DS132] KEITHLEY INSTRUMENTS INC. *7711 2GHz 50Ohm RF Module* 2013 URL: http://www.keithley.com/products/switch/dmmswitch/?mn=7711

[DS141]   HAMAMATSU PHOTONICS K.K. *Datasheet for TSV MPPC array S12642-xxxx* KSX-I50014-E S12642 Series Provided by C. Kramer (Hamamatsu Germany) Dec. 2015

[DS144]   HAMAMATSU PHOTONICS K.K. *Datasheet for MPPC S12572-100C* Dec. 2015 URL: http://www.hamamatsu.com/resources/pdf/ssd/s12572-025_etc_kapd1043e.pdf

[DS145]   HAMAMATSU PHOTONICS K.K. *Datasheet for C12332-01 Driver Circuit for MPPC* Dec. 2015 URL: https://www.hamamatsu.com/resources/pdf/ssd/c12332-01_kacc1233e.pdf

[DS147]   TELEDYNE LECROY INC. *428F Quad Linear Fan-In/Fan-Out* 1995 URL: http://teledynelecroy.com/lrs/dsheets/428.htm

[DS149]   TELEDYNE LECROY INC. *WaveJet 324A Oscilloscope* WJADS-12feb13 2013 URL: http://cdn.teledynelecroy.com/files/pdf/lecroy_wavejet-a_oscilloscope_datasheet.pdf

[DS150]   ROITHNER LASERTECHNIK GMBH *DUV-FW5 - 310 nm and 340 nm LEDs* 2015 URL: http://www.roithner-laser.com/datasheets/led_deepuv/duv-fw5_rev%202.0.pdf

[DS151]   SENSOR ELECTRONIC TECHNOLOGY INC. *UVCLEAN - 315 nm 330 nm LEDs* 2015 URL: http://www.s-et.com/uvclean-sheets/high-power-uv-lamp-1-3mw.pdf

[DS152]   ROITHNER LASERTECHNIK GMBH *XSL-355-5E - 357 nm LED* 2010 URL: http://www.roithner-laser.com/datasheets/led_div/uv/xsl-355-5e.pdf

[DS153]   ROITHNER LASERTECHNIK GMBH *UVLED365-110E - 365 nm LED* 2010 URL: http://www.roithner-laser.com/datasheets/led_div/uv/uvled365-110e.pdf

[DS154]   ROITHNER LASERTECHNIK GMBH *XSL-370-TB-4 - 373 nm LED* 2010 URL: http://www.roithner-laser.com/datasheets/led_div/uv/xsl-370-tb-4.pdf

[DS155]   ROITHNER LASERTECHNIK GMBH *XSL-375-3E - 378 nm LED* 2010 URL: http://www.roithner-laser.com/datasheets/led_div/uv/xsl-375-3e.pdf

[DS156]   ROITHNER LASERTECHNIK GMBH *VL380-5-15 - 380 nm LED* 2011 URL: http://www.roithner-laser.com/datasheets/led_div/uv/vl380-5-15.pdf

[DS157]   ROITHNER LASERTECHNIK GMBH *VL390-5-15 - 390 nm LED* 2011 URL: http://www.roithner-laser.com/datasheets/led_div/uv/vl390-5-15.pdf

[DS158]   ROITHNER LASERTECHNIK GMBH *HUUV-5102L - 395 nm LED* 2010 URL: http://www.roithner-laser.com/datasheets/led_div/uv/huuv_5102l.pdf

[DS159]   ROITHNER LASERTECHNIK GMBH *LED405-30M32 - 405 nm LED* 2010 URL: http://www.roithner-laser.com/datasheets/led_div/violet/led405_30m32.pdf

[DS160]   ROITHNER LASERTECHNIK GMBH *VL425-5-15 - 425 nm LED* 2012 URL: http://www.roithner-laser.com/datasheets/led_div/violet/vl425-5-15.pdf

BIBLIOGRAPHY

[1] NOBELPRIZE.ORG The Nobel Prize in Physics 2015 in: *Nobel Media AB 2014 - Web 04 Nov 2015*, (2015) URL: http://www.nobelprize.org/nobel_prizes/physics/laureates/2015/

[2] R. ENGEL, D. HECK, and T. PIEROG Extensive Air Showers and Hadronic Interactions at High Energy in: *Annual Review of Nuclear and Particle Science*, **61**:1 (2011), 467–489 DOI: 10.1146/annurev.nucl.012809.104544

[3] I. ALLEKOTTE ET AL. The surface detector system of the Pierre Auger Observatory in: *Nuclear Instruments and Methods in Physics Research Section A: Accelerators, Spectrometers, Detectors and Associated Equipment*, **586**:3 (2008), 409–420 DOI: 10.1016/j.nima.2007.12.016

[4] J.N. MATTHEWS First results from the Telescope Array in: *Nuclear Physics B - Proceedings Supplements*, **212-213**: (2011) Proceedings of the Cosmic Ray International Seminars (CRIS 2010) 100 years of Cosmic Ray Physics: from pioneering experiments to physics in space, 79–86 DOI: 10.1016/j.nuclphysbps.2011.03.011

[5] W. D. APEL ET AL. Kneelike Structure in the Spectrum of the Heavy Component of Cosmic Rays Observed with KASCADE-Grande in: *Phys. Rev. Lett.*, **107**: (17 Oct. 2011), 171104 DOI: 10.1103/PhysRevLett.107.171104

[6] W.D. APEL ET AL. KASCADE-Grande measurements of energy spectra for elemental groups of cosmic rays in: *Astroparticle Physics*, **47**: (2013), 54–66 DOI: http://dx.doi.org/10.1016/j.astropartphys.2013.06.004

[7] A. CHIAVASSA ET AL. Latest results from the KASCADE-Grande experiment in: *Nuclear Instruments and Methods in Physics Research Section A: Accelerators, Spectrometers, Detectors and Associated Equipment*, **742**: (2014) 4th Roma International Conference on Astroparticle Physics, 10–15 DOI: http://dx.doi.org/10.1016/j.nima.2013.11.045

[8] G.T. ZATSEPIN and V.A. KUZ'MIN Upper Limit of the Spectrum of Cosmic Rays in: *Soviet Journal of Experimental and Theoretical Physics Letters*, **4**: (Aug. 1966), 78 URL: http://www.jetpletters.ac.ru/ps/1624/article_24846.shtml

[9] J.A. CHINELLATO and THE AUGER COLLABORATION Reviewing recent results from Pierre Auger Observatory in: *Journal of Physics: Conference Series*, **485**:1 (2014), 012033 DOI: 10.1088/1742-6596/485/1/012033

[10] R. ENGEL Private communication in: *Institute for Nuclear Physics (IKP) - Karlsruhe Institute of Technology (KIT)*, (2015) URL: ralph.engel@kit.edu

[11] E.S. SEO ET AL. Cosmic-ray energetics and mass (CREAM) balloon project in: *Advances in Space Research*, **33**:10 (2004), 1777–1785 DOI: 10.1016/j.asr.2003.05.019

[12] E.S. SEO ET AL. Cosmic Ray Energetics And Mass for the International Space Station (ISS-CREAM) in: *Advances in Space Research*, **53**:10 (2014) Cosmic Ray Origins: Viktor Hess Centennial Anniversary, 1451–1455 DOI: http://dx.doi.org/10.1016/j.asr.2014.01.013

[13] I. GEBAUER ET AL. "Direction and time dependent fluxes with AMS-02" in: vol. Proceedings of the ICRC 2015, The Hague (The Netherlands) Aug. 2015, PoS(ICRC2015)404 URL: http://pos.sissa.it/archive/conferences/236/404/ICRC2015_404.pdf

[14] J. BLÜMER, R. ENGEL, and J.R. HÖRANDEL Cosmic rays from the knee to the highest energies in: *Progress in Particle and Nuclear Physics*, **63**:2 (2009), 293–338 DOI: 10.1016/j.ppnp.2009.05.002

[15] T.K. GAISSER *Cosmic Rays and Particle Physics* Cambridge University Press, 1991

[16] G. GIACINTI, M. KACHELRIESS, and D. V. SEMIKOZ The escape model for Galactic cosmic rays in: *Journal of Physics: Conference Series*, **632**:1 (2015), 012094 DOI: 10.1088/1742-6596/632/1/012094

[17] V. BEREZINSKY "Transition from galactic to extragalactic cosmic rays" in: *Proceedings, 30th International Cosmic Ray Conference (ICRC 2007)* vol. 6 2007, 21–33 arXiv: 0710.2750 [astro-ph]

[18] A. M. HILLAS The Origin of Ultra-High-Energy Cosmic Rays in: *Annual Review of Astronomy and Astrophysics*, **22**:1 (1984), 425–444 DOI: 10.1146/annurev.aa.22.090184.002233

[19] J. BLÜMER and K.-H. KAMPERT Die Suche nach den Quellen der kosmischen Strahlung: Antworten versprechen die Luftschauerexperimente KASCADE und AUGER in: *Physik Journal*, **56**:3 (2000), 39–45 DOI: 10.1002/phbl.20000560311

[20] R. U. ABBASI ET AL. First Observation of the Greisen-Zatsepin-Kuzmin Suppression in: *Phys. Rev. Lett.*, **100**: (10 Mar. 2008), 101101 DOI: 10.1103/PhysRevLett.100.101101

[21] K. GREISEN End to the Cosmic-Ray Spectrum? in: *Phys. Rev. Lett.*, **16**: (17 Apr. 1966), 748–750 DOI: 10.1103/PhysRevLett.16.748

[22] M. KACHELRIESS, E. PARIZOT, and D. V. SEMIKOZ The GZK horizon and constraints on the cosmic ray source spectrum from observations in the GZK regime in: *JETP Lett.*, **88**: (2009), 553–557 DOI: 10.1134/S0021364008210017

[23] A. AAB ET AL. The Pierre Auger Cosmic Ray Observatory in: *Nucl. Instrum. Meth.*, **A798**: (2015), 172–213 DOI: 10.1016/j.nima.2015.06.058

[24] P. TINYAKOV Latest results from the telescope array in: *Nuclear Instruments and Methods in Physics Research Section A: Accelerators, Spectrometers, Detectors and Associated Equipment*, **742**: (2014) 4th Roma International Conference on Astroparticle Physics, 29–34 DOI: 10.1016/j.nima.2013.10.067

[25] I. VALINO (FOR THE PIERRE AUGER COLLABORATION) "The flux of ultra-high energy cosmic rays after ten years of operation of the Pierre Auger Observatory" in: vol. Proceedings of the ICRC 2015, The Hague (The Netherlands) Aug. 2015, PoS(ICRC2015)271 URL: http://pos.sissa.it/archive/conferences/236/271/ICRC2015_271.pdf

[26] D. IVANOV (FOR THE TELESCOPE ARRAY COLLABORATION) "TA Spectrum Summary" in: vol. Proceedings of the ICRC 2015, The Hague (The Netherlands) Aug. 2015, PoS(ICRC2015)349 URL: http://pos.sissa.it/archive/conferences/236/349/ICRC2015_349.pdf

[27] THE PIERRE AUGER COLLABORATION Measurement of the cosmic ray spectrum above 4×10^{18} eV using inclined events detected with the Pierre Auger Observatory in: *Journal of Cosmology and Astroparticle Physics*, **2015**:08 (2015), 049 DOI: http://dx.doi.org/10.1088/1475-7516/2015/08/049

[28] R. ABBASI ET AL. Report of the Working Group on the Composition of Ultra High Energy Cosmic Rays in: *ArXiv e-prints*, (Mar. 2015) arXiv: 1503.07540 [astro-ph.HE]

[29] A. HAUNGS, H. REBEL, and M. ROTH Energy spectrum and mass composition of high-energy cosmic rays in: *Reports on Progress in Physics*, **66**:7 (2003), 1145 DOI: 10.1088/0034-4885/66/7/202

[30] J. MATTHEWS A Heitler model of extensive air showers in: *Astroparticle Physics*, **22**:5-6 (2005), 387–397 DOI: 10.1016/j.astropartphys.2004.09.003

[31] P. A. CHERENKOV Visible Radiation Produced by Electrons Moving in a Medium with Velocities Exceeding that of Light in: *Phys. Rev.*, **52**: (4 Aug. 1937), 378–379 DOI: 10.1103/PhysRev.52.378

[32] W.D. APEL ET AL. LOPES-3D: An antenna array for full signal detection of air-shower radio emission in: *Nuclear Instruments and Methods in Physics Research Section A: Accelerators, Spectrometers, Detectors and Associated Equipment*, **696**: (2012), 100–109 DOI: http://dx.doi.org/10.1016/j.nima.2012.08.082

[33] J. SCHULZ (FOR THE PIERRE AUGER COLLABORATION) "Status and Prospects of the Auger Engineering Radio Array" in: vol. Proceedings of the ICRC 2015, The Hague (The Netherlands) Aug. 2015, PoS(ICRC2015)615 URL: http://pos.sissa.it/archive/conferences/236/615/ICRC2015_615.pdf

[34] D. Kostunin et al. "The Tunka Radio Extension: reconstruction of energy and shower maximum of the first year data" in: vol. Proceedings of the ICRC 2015, The Hague (The Netherlands) Aug. 2015, PoS(ICRC2015)285 URL: http://pos.sissa.it/archive/conferences/236/285/ICRC2015_285.pdf

[35] R. Smida et al. First Experimental Characterization of Microwave Emission from Cosmic Ray Air Showers in: *Phys. Rev. Lett.*, **113**: (22 Nov. 2014), 221101 DOI: 10.1103/PhysRevLett.113.221101 URL: http://link.aps.org/doi/10.1103/PhysRevLett.113.221101

[36] M. Ave et al. Spectrally resolved pressure dependence measurements of air fluorescence emission with AIRFLY in: *Nuclear Instruments and Methods in Physics Research Section A: Accelerators, Spectrometers, Detectors and Associated Equipment*, **597**:1 (2008) Proceedings of the 5th Fluorescence Workshop, 41–45 DOI: 10.1016/j.nima.2008.08.052

[37] B. Keilhauer et al. Nitrogen fluorescence in air for observing extensive air showers in: *EPJ Web of Conferences*, **53**: (2013), 01010 DOI: 10.1051/epjconf/20135301010

[38] B. Keilhauer et al. Impact of varying atmospheric profiles on extensive air shower observation: fluorescence light emission and energy reconstruction in: *Astropart.Phys.*, **25**: (2006), 259–268 DOI: 10.1016/j.astropartphys.2006.02.005

[39] B. Keilhauer et al. Altitude dependence of fluorescence light emission by extensive air showers in: *Nuclear Instruments and Methods in Physics Research Section A: Accelerators, Spectrometers, Detectors and Associated Equipment*, **597**:1 (2008) Proceedings of the 5th Fluorescence Workshop, 99–104 DOI: 10.1016/j.nima.2008.08.060

[40] J.H. Adams Jr. et al. Ultra high energy photons and neutrinos with JEM-EUSO English in: *Experimental Astronomy*, (Oct. 2013), 1–19 DOI: 10.1007/s10686-013-9353-2

[41] J.H. Adams Jr. et al. Performances of JEM-EUSO: angular reconstruction English in: *Experimental Astronomy*, (Feb. 2014), 1–25 DOI: 10.1007/s10686-013-9371-0

[42] J.H. Adams Jr. et al. JEM-EUSO observational technique and exposure English in: *Experimental Astronomy*, (Mar. 2014), 1–18 DOI: 10.1007/s10686-014-9376-3

[43] J.H. Adams Jr. et al. JEM-EUSO: Meteor and nuclearite observations English in: *Experimental Astronomy*, (Apr. 2014), 1–27 DOI: 10.1007/s10686-014-9375-4

[44] J.H. Adams Jr. et al. The JEM-EUSO observation in cloudy conditions English in: *Experimental Astronomy*, (July 2014), 1–18 DOI: 10.1007/s10686-014-9377-2

[45] J.H. ADAMS JR. ET AL. The atmospheric monitoring system of the JEM-EUSO instrument English in: *Experimental Astronomy*, (July 2014), 1–16 DOI: 10.1007/s10686-014-9378-1

[46] J.H. ADAMS JR. ET AL. The infrared camera onboard JEM-EUSO English in: *Experimental Astronomy*, (Sept. 2014), 1–29 DOI: 10.1007/s10686-014-9402-5

[47] J.H. ADAMS JR. ET AL. The JEM-EUSO instrument English in: *Experimental Astronomy*, (Oct. 2014), 1–26 DOI: 10.1007/s10686-014-9418-x

[48] J.H. ADAMS JR. ET AL. Ground-based tests of JEM-EUSO components at the Telescope Array site, "EUSO-TA" English in: *Experimental Astronomy*, (May 2015), 1–14 DOI: 10.1007/s10686-015-9441-6

[49] J.H. ADAMS JR. ET AL. Performances of JEM–EUSO: energy and X_{max} reconstruction English in: *Experimental Astronomy*, (July 2015), 1–32 DOI: 10.1007/s10686-014-9427-9

[50] J.H. ADAMS JR. ET AL. Calibration aspects of the JEM-EUSO mission English in: *Experimental Astronomy*, (July 2015), 1–26 DOI: 10.1007/s10686-015-9453-2

[51] J.H. ADAMS JR. ET AL. Science of atmospheric phenomena with JEM-EUSO English in: *Experimental Astronomy*, (July 2015), 1–13 DOI: 10.1007/s10686-014-9431-0

[52] J.H. ADAMS JR. ET AL. Erratum to: Performances of JEM-EUSO: angular reconstruction English in: *Experimental Astronomy*, (July 2015), 1–3 DOI: 10.1007/s10686-014-9420-3

[53] J.H. ADAMS JR. ET AL. Erratum to: Ultra high energy photons and neutrinos with JEM-EUSO English in: *Experimental Astronomy*, (July 2015), 1–3 DOI: 10.1007/s10686-015-9470-1

[54] J.H. ADAMS JR. ET AL. The JEM-EUSO Mission: Contributions to the ICRC 2013 in: *ArXiv e-prints*, (July 2013) ICRC2013 arXiv: 1307.7071 [astro-ph.IM]

[55] C. BLAKSLEY ET AL. Ultra-high-energy cosmic ray source statistics in the GZK energy range in: *A&A*, **552**: (Oct. 2013), A125 DOI: 10.1051/0004-6361/201220178

[56] B. ROUILLÉ D'ORFEUIL ET AL. Anisotropy expectations for ultra-high-energy cosmic rays with future high-statistics experiments in: *A & A*, **567**: (July 2014), A81 DOI: 10.1051/0004-6361/201423462

[57] S. FALK *Atmospheric Influences on Space-Based Observations of Extremely High-Energy Cosmic Rays*. PhD thesis Karlsruhe Institute of Technology (KIT), Dec. 2014 URL: http://nbn-resolving.org/urn:nbn:de:swb:90-447887

[58] J.H. ADAMS JR. ET AL. The JEM-EUSO Mission: Status and Prospects in 2011 in: *ArXiv e-prints*, (Apr. 2011) ICRC2011 arXiv: 1204.5065 [astro-ph.IM]

[59] J.H. ADAMS JR. ET AL. An evaluation of the exposure in nadir observation of the JEM-EUSO mission in: *Astroparticle Physics*, **44**: (Apr. 2013), 76–90 DOI: 10.1016/j.astropartphys.2013.01.008

[60] A.V. OLINTO Cosmic Rays of Extreme Energies in: *Nuclear Physics B - Proceedings Supplements*, **243-244**: (2013) Proceedings of the IV International Conference on Particle and Fundamental Physics in Space, 108–115 DOI: 10.1016/j.nuclphysbps.2013.09.015

[61] J.H. ADAMS JR. ET AL. *The JEM-EUSO Purple Book: Report on the Phase A Study* JEUSO-110025-01-E-TR-ZZZ Purple Book May 2010 URL: http://euso-balloon.lal.in2p3.fr/IMG/pdf/PurpleBook_2010_v-5_MCM_lightreso.pdf

[63] *Omega MICRO - SPACIROC Front-end Chip* May 2015 URL: http://omega.in2p3.fr/index.php/products/spaciroc.html

[64] P. VON BALLMOOS ET AL. A balloon-borne prototype for demonstrating the concept of JEM-EUSO in: *Advances in Space Research*, **53**:10 (2014) Cosmic Ray Origins: Viktor Hess Centennial Anniversary, 1544–1550 DOI: 10.1016/j.asr.2013.11.049

[65] P. PICOZZA JEM-EUSO Program in: *AMS DAYS AT CERN - The Future of Cosmic Ray Physics and Latest Results*, (Apr. 16 Apr 2015) URL: https://indico.cern.ch/event/381134/contribution/16/material/slides/1.pdf

[66] B. MOT and S. DAGORET *EUSO-Balloon Assembly, Integration and Tests* tech. rep. PLAN VERSION 2 (JUNE 2014) EUSO-AI-INST-251-LAL_V2.8 IRAP, LAL, June 2014 URL: http://euso-balloon.lal.in2p3.fr/IMG/pdf/EUSO-AI-INST-251-LAL_V2-8.pdf

[67] *JEM-EUSO Italian Collaboration Website* Apr. 2015 URL: http://jem-euso.roma2.infn.it/?page_id=155

[68] F. BISCONTI EUSO-TA prototype telescope in: *Nuclear Instruments and Methods in Physics Research Section A: Accelerators, Spectrometers, Detectors and Associated Equipment*, (2015) DOI: http://dx.doi.org/10.1016/j.nima.2015.09.105

[69] *JEM-EUSO Italian Collaboration Website* Apr. 2015 URL: http://jem-euso.roma2.infn.it/?page_id=818

[70] J. ABRA ET AL. Properties and performance of the prototype instrument for the Pierre Auger Observatory in: *Nuclear Instruments and Methods in Physics Research Section A: Accelerators, Spectrometers, Detectors and Associated Equipment*, **523**:1-2 (2004), 50–95 DOI: 10.1016/j.nima.2003.12.012

[71] R.M. BALTRUSAITIS ET AL. The Utah Fly's Eye detector in: *Nuclear Instruments and Methods in Physics Research Section A: Accelerators, Spectrometers, Detectors and Associated Equipment*, **240**:2 (1985), 410–428 DOI: 10.1016/0168-9002(85)90658-8

[72] T. ABU-ZAYYAD ET AL. The prototype high-resolution Fly's Eye cosmic ray detector in: *Nuclear Instruments and Methods in Physics Research Section A: Accelerators, Spectrometers, Detectors and Associated Equipment*, **450**:2-3 (2000), 253–269 DOI: 10.1016/S0168-9002(00)00307-7

[73] A. HAUNGS (FOR THE JEM-EUSO COLLABORATION) "Towards a SiPM based fluorescence camera for JEM-EUSO" in: vol. Proceedings of the ICRC 2015, The Hague (The Netherlands) Aug. 2015, PoS(ICRC2015)643 URL: http://pos.sissa.it/archive/conferences/236/643/ICRC2015_643.pdf

[74] M. KARUS, F. BISCONTI, and T. HUBER (FOR THE JEM-EUSO COLLABORATION) "Ground calibration of MAPMT and SiPM for JEM-EUSO" in: vol. Proceedings of the ICRC 2015, The Hague (The Netherlands) Aug. 2015, PoS(ICRC2015)612 URL: http://pos.sissa.it/archive/conferences/236/612/ICRC2015_612.pdf

[75] C. BLAKSLEY and P. GORODETZKY A setup for the precision measurement of multianode photomultiplier efficiency in: *Nuclear Instruments and Methods in Physics Research Section A: Accelerators, Spectrometers, Detectors and Associated Equipment*, **764**: (2014), 198–205 DOI: 10.1016/j.nima.2014.07.033

[76] C. BLAKSLEY *Photodetection Aspects of JEM-EUSO and Studies of the Ultra-High Energy Cosmic Ray Sky*. PhD thesis Université Paris 7 - Denis Diderot, June 2014 arXiv: 1406.5818 [astro-ph.IM]

[77] G. LEFEUVRE *Precise measurement of the Absolute Yield of the Fluorescence of Nitrogen in the Air. Effects on the Detection of the Cosmic rays of Ultra-high Energy*. PhD thesis Université Paris 7 - Denis Diderot, July 2006 URL: http://home.fnal.gov/~para/These_Gwenaelle.doc

[78] M. KARUS Calibration of photo sensors for the space-based cosmic ray telescope JEM-EUSO in: *AIP Conference Proceedings*, **1645**: (2015), 353–357 DOI: 10.1063/1.4909600

[81] LABSPHERE INC. *Technical Guide: Integrating Sphere Theory and Applications* 2012 URL: https://www.labsphere.com/wp-content/uploads/2015/02/a-guide-to-integrating-sphere-theory-and-applications.pdf

[82] HAMAMATSU PHOTONICS K.K. *Opto-semiconductor Handbook* 2014 URL: http://www.amatsu.com/jp/en/amatsu/overview/bsd/solid_state_division/related_documents.html

[83] K. VALERIUS ET AL. A UV LED-based fast-pulsed photoelectron source for time-of-flight studies in: *New Journal of Physics*, **11**:6 (2009), 063018 DOI: 10.1088/1367-2630/11/6/063018

[84] R. GASKA and J. ZHANG *Deep-UV LEDs: physics, performance, and applications* 2005 DOI: 10.1117/12.638266

[85] M. SHATALOV ET AL. Time-resolved electroluminescence of AlGaN-based light-emitting diodes with emission at 285 nm in: *Applied Physics Letters*, **82**:2 (2003), 167–169 DOI: 10.1063/1.1536729 URL: http://scitation.aip.org/content/aip/journal/apl/82/2/10.1063/1.1536729

[86] T. HUBER *Entwicklung und Test einer Referenzlichtquelle zur Kalibrierung der Multianoden-Photomultiplierröhren von JEM-EUSO*. Bachelor thesis Karlsruhe Institute of Technology, Apr. 2013

[97] N. HAMPE *Erstellung einer monochromatischen Lichtquelle für JEM-EUSO*. Bachelor thesis Karlsruhe Institute of Technology, Dez 2015

[99] E. HONG and N. NARENDRAN *A method for projecting useful life of LED lighting systems* 2004 DOI: 10.1117/12.509682

[100] N. NARENDRAN ET AL. *Performance characteristics of high-power light-emitting diodes* 2004 DOI: 10.1117/12.515647

[101] X.A. CAO, S.F. LEBOEUF, and T.E. STECHER Temperature-dependent electroluminescence of AlGaN-based UV LEDs in: *Electron Device Letters, IEEE*, **27**:5 (May 2006), 329–331 DOI: 10.1109/LED.2006.873763

[102] LEDS MAGAZINE Driving LED lamps – some simple design guidelines in: **4**: (8 Aug. 2007) URL: http://www.ledsmagazine.com/articles/print/volume-4/issue-8/features/driving-led-lamps-some-simple-design-guidelines.html

[103] OSRAM GMBH *LED Fundamentals - Thermal Characteristics of LEDs* 2015 URL: http://ledlight.osram-os.com/wp-content/uploads/2013/01/OSRAM-OS_LED-FUNDAMENTALS_Thermal-Characteristics-of-LEDs_v2_08-16-11_SCRIPT.pdf

[104] H. Y. FAN Temperature Dependence of the Energy Gap in Monatomic Semiconductors in: *Phys. Rev.*, **78**: (6 June 1950), 808–809 DOI: 10.1103/PhysRev.78.808.2

[105] Y.P. VARSHNI Temperature dependence of the energy gap in semiconductors in: *Physica*, **34**:1 (1967), 149–154 DOI: 10.1016/0031-8914(67)90062-6

[106] LABSPHERE INC. *Technical Guide: Reflectance Materials and Coatings* 2012 URL: https://www.labsphere.com/wp-content/uploads/2015/02/a-guide-to-reflectance-materials-and-coatings.pdf

[108] P.Y. BARNES, E.A. EARLY, and A.C. PARR *NIST Measurement Services: Spectral Reflectance* tech. rep. Optical Technology Division - NIST, Mar. 1998 URL: http://www.nist.gov/calibrations/upload/sp250-48.pdf

[109] H. H. KU Notes on the use of propagation of error formulas in: *Journal of Research of the National Bureau of Standards (National Bureau of Standards)*, **70C**:4 (Oct. 1966), 263–273 DOI: 10.6028/jres.070c.025

[110] K. DAUMILLER Private communication in: *Institute for Nuclear Physics (IKP) - Karlsruhe Institute of Technology (KIT)*, (2014) URL: Kai.Daumiller@kit.edu

[113] F.E. Grubbs Sample Criteria for Testing Outlying Observations in: *Ann. Math. Statist.*, **21**:1 (Mar. 1950), 27–58 DOI: 10.1214/aoms/1177729885

[114] P. Grordetzky Private communication in: *AstroParticule et Cosmologie (APC) - Paris Diderot University (Paris7)*, (2013) URL: Philippe.Gorodetzky@cern.ch

[115] A. Weindl Private communication in: *Institute for Nuclear Physics (IKP) - Karlsruhe Institute of Technology (KIT)*, (2015) URL: andreas.weindl@kit.edu

[123] S. Ehnle *QADC Kalibration und MAPMT Messungen*. Bachelor thesis Karlsruhe Institute of Technology, Dez 2015

[125] C. Kramer Private communication in: *Hamamatsu Photonics Deutschland GmbH*, (2014) URL: ckramer@hamamatsu.de

[126] Hamamatsu Photonics K.K. *Photomultiplier Tubes - Basics and Applications* 3a 2007 URL: http://www.amatsu.com/resources/pdf/etd/PMT_handbook_v3aE.pdf

[127] *Encyclopedia of Mathematics - Poisson distribution* Dec. 2015 URL: https://www.encyclopediaofmath.org/index.php?title=Poisson_distribution&oldid=28559

[128] K. A. Olive et al. Review of Particle Physics in: *Chin. Phys.*, **C38**: (2014), 090001 DOI: 10.1088/1674-1137/38/9/090001

[129] A. Ebersoldt Private communication in: *Institute for Data Processing and Electronics (IPE) - Karlsruhe Institute of Technology (KIT)*, (2014) URL: andreas.ebersoldt@kit.edu

[130] B. Hoffmann Private communication in: *Institute of Experimental Nuclear Physics (IEKP) - Karlsruhe Institute of Technology (KIT)*, (2015) URL: bernd.hoffmann@kit.edu

[133] T. Huber Private communication in: *Institute of Experimental Nuclear Physics (IEKP) - Karlsruhe Institute of Technology (KIT)*, (2013) URL: thomas.huber@student.kit.edu

[134] M. Renschler Private communication in: *Institute for Nuclear Physics (IKP) - Karlsruhe Institute of Technology (KIT)*, (2015) URL: max.renschler@student.kit.edu

[135] N. Sakaki Private communication in: (2014) URL: sakaki@sci.osaka-cu.ac.jp

[136] V. Catalano et al. "The ASTRI SST-2M Prototype: Camera and Electronics" in: *Proceedings, 33rd International Cosmic Ray Conference (ICRC2013)* 2013 arXiv: 1307.5142 [astro-ph.IM]

[137] D. Mazin et al. Towards SiPM camera for current and future generations of Cherenkov telescopes in: (2014) arXiv: 1410.5070 [astro-ph.IM]

[138] J.E. Mackewn et al. PET Performance Evaluation of a Pre-Clinical SiPM-Based MR-Compatible PET Scanner in: *Nuclear Science, IEEE Transactions on*, **62**:3 (June 2015), 784–790 DOI: 10.1109/TNS.2015.2392560

[139] P. ECKERT ET AL. Characterisation studies of silicon photomultipliers in: *Nuclear Instruments and Methods in Physics Research A*, **620**: (Aug. 2010), 217–226 DOI: 10.1016/j.nima.2010.03.169

[140] S.S. PIATEK Physics and Operation of an MPPC in: (Feb. 2014) URL: http://www.hamamatsu.com/us/en/community/optical_sensors/tutorials/physics_of_mppc/index.html

[142] N. AKIL ET AL. A multimechanism model for photon generation by silicon junctions in avalanche breakdown in: *Electron Devices, IEEE Transactions on*, **46**:5 (May 1999), 1022–1028 DOI: 10.1109/16.760412

[143] R. PAGANO ET AL. "Optimized silicon photomultipliers with optical trenches" in: *Solid-State Device Research Conference (ESSDERC), 2011 Proceedings of the European* Sept. 2011, 183–186 DOI: 10.1109/ESSDERC.2011.6044204

[146] S.-A. SANDKUHL *Untersuchungen mit Einzelphotonen von Siliziumphotomultipliern*. Bachelor thesis Karlsruhe Institute of Technology, Dez 2015

[148] W. PAINTER Private communication in: *Institute of Experimental Nuclear Physics (IEKP) - Karlsruhe Institute of Technology (KIT)*, (2015) URL: william.painter@kit.edu

> There is a theory which states that
> if ever anyone discovers exactly what the
> Universe is for and why it is here,
> it will instantly disappear and be replaced by
> something even more bizarre and inexplicable.
>
> There is another theory which states
> that this has already happened.
>
> — DOUGLAS ADAMS
> *The Restaurant at the End of the Universe*

ACKNOWLEDGMENTS

DECLARATION

Michael Karus
Berckmuellerstrasse 22
76131 Karlsruhe
michael.karus@kit.edu

Karlsruhe, den 07.01.2016

**Erklärung der selbständigen Anfertigung meiner
Dissertationsschrift**

Hiermit versichere ich, dass ich die Dissertationsschrift mit dem Titel

**Development of a Calibration Stand for
Photosensors for Extremely High-Energy Cosmic Ray Research**

selbständig und ohne unerlaubte fremde Hilfe verfasst habe. Dabei
habe ich keine anderen, als die von mir angegebenen Hilfsmittel be-
nutzt.

Michael Karus

Karlsruhe (Baden), 07. Januar 2016